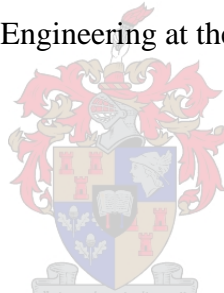


PERFORMANCE OF A  
PARABOLIC TROUGH SOLAR COLLECTOR

by

Michael John Brooks

Thesis presented in partial fulfillment of the requirements for the degree of  
Master of Science in Engineering at the University of Stellenbosch



Thesis supervisor:

Associate Professor T.M. Harms

February 2005

## DECLARATION

I, Michael John Brooks, submit this thesis in partial fulfillment of the requirements of the degree MScEng at the University of Stellenbosch and hereby declare that the work contained in this thesis is my own original work and that I have not previously, in its entirety or in part, submitted it at any university for a degree.

Signed: \_\_\_\_\_

(M. J. Brooks)

Date: \_\_\_\_\_

## ABSTRACT

Parabolic trough solar collectors (PTSCs) constitute a proven source of thermal energy for industrial process heat and power generation, although their implementation has been strongly influenced by economics. In recent years, environmental concerns and other geopolitical factors have focused attention on renewable energy resources, improving the prospects for PTSC deployment. Further work is needed to improve system efficiencies and active areas of research include development of advanced heat collecting elements and working fluids, optimisation of collector structures, thermal storage and direct steam generation (DSG).

A parabolic trough collector, similar in size to smaller-scale commercial modules, has been developed locally for use in an ongoing PTSC research programme. The aim of this study was to test and fully characterise the performance of the collector.

Specialised logging software was developed to record test data and monitor PTSC performance in real-time. Two heat collecting elements were tested with the collector, one unshielded and the other with an evacuated glass cover. Testing was carried out according to the ASHRAE 93-1986 (RA 91) standard, yielding results for the thermal efficiency, collector acceptance angle, incidence angle modifier and collector time constant. Peak thermal efficiency was 55.2 % with the unshielded receiver and 53.8 % with the glass-shielded unit. The evacuated glass shield offered superior performance overall, reducing the receiver heat loss coefficient by 50.2 % at maximum test temperature. The collector time constant was less than 30 s for both receivers, indicating low thermal inertia. Thermal loss tests were conducted and performance of the trough's tracking system was evaluated. The measured acceptance angles of  $0.43^\circ$  (unshielded) and  $0.52^\circ$  (shielded) both exceeded the tracking accuracy of the PTSC, ensuring that the collector operated within 2 % of its optimal efficiency at all times.

Additionally, experimental results were compared with a finite-volume thermal model, which showed potential for predicting trough performance under forced convection conditions.

## OPSOMMING

Paraboliese trog sonkollekteerders is een van die belowende tegnologiese ontwikkelings wat sonenergie op industriële vlak kan gebruik vir die vervaardiging van hitte en elektriese krag. Alhoewel die grootskaalse implementasie van sonenergie as 'n alternatiewe energiebron deur ekonomiese oorwegings beïnvloed word het die verhoogde omgewingsbewustheid en geopolitieke faktore, gedurende die afgelope jare, die klem verskuif na hernubare energiebronne. Die vooruitsig om sonkollekteerders op groot skaal te ontplooi het drasties verbeter. Die aandag is nou gevestig op die verbetering van sisteem effektiwiteit en aktiewe navorsing fokus op gevorderde hitte elemente, werkbare vloeistowwe, optimisering van hitteversameling strukture, storting van hitte energie en direkte stoom vervaardiging.

'n Paraboliese trog sonkollekteerder, vergelykbaar met die grootte van kleiner kommersiële eenhede, is plaaslik ontwikkel vir gebruik in die paraboliese trog sonkollekteerder navorsingsprojek. Die doel van die studie was die toets en karakterisering van die effektiwiteit van die paraboliese trog sonkollekteerder.

Gespesialiseerde data vasleggings programme is ontwikkel ten einde 'n ware-tyd werkverrigtings analise van die paraboliese trog sonkollekteerder te doen. Twee potensiële elemente vir hitteversameling is vervaardig en vergelyk. Die eerste element is onbeskud terwyl die tweede element deur 'n glasbuis onder vakuum beskerm word. Vergelyking van die elemente is volgens die ASHRAE 93-1986 (RA91) standaard gedoen, wat resultate van die prestasie van hitte effektiwiteit, aanvaardingshoeke van die kollekteerder, hoek van inval modifiseerder, en tydkonstante waardes insluit. Die best termiese effektiwiteit van die sonkollekteerder is bereken as 55.2 % met die onbeskutte ontvanger en 53.8 % met die glasomhulsel. Resultate wys dat die glasomhulsel in die algemeen beter werkverrigting lewer aangesien die hitteverlies koëfisient onder vakuum en maksimum toets temperatuur met 50.2 % verminder het. Die tydkonstante waardes was minder as 30s vir beide ontvangers wat op lae termiese inersie dui. Hitteverlies is bepaal en die werkverrigting van die sonopsporingstelsel van die trog is geëvalueer. In beide gevalle is die akuraatheid van die aanvaardingshoeke,  $0.43^\circ$  (onbeskud) en  $0.52^\circ$  (glasomhulde ontvanger), beter as die sonopsporing van die paraboliese trog kollekteerder. Dit verseker dat die sonkollekteerder te alle tye binne 2 % van optimale effektiwiteit kan werk.

Eksperimentele resultate is ook vergelyk met resultate van 'n eindige volume termiese model. Die gevolgtrekking van hierdie vergelyking bevestig dat die model potensiaal toon vir die skatting van termiese werkverrigting gedurende geforseerde konveksie toestande.

To my parents, for their love, patience and sense of humour...

*...et in honorem Mariae, sedis sapientiae, quae nos ducit ad Christum.*

*Ora pro nobis, Sancta Mater Dei!*

## ACKNOWLEDGEMENTS

Many people have supported and contributed to this project – their efforts are acknowledged and sincerely appreciated. Special thanks to the following:

### Mangosuthu Technikon:

- Mrs. Ewa Zawilska, Head of Mechanical Engineering, whose professionalism and untiring support of this project and those involved, enabled it to take place
- Dr. Anette van der Mescht, Research Director, for enabling the development of the test facility, steering the research project through numerous challenges and providing invaluable support and advice
- Mr. Ian Mills, Senior Laboratory Technician, for his hard work and technical expertise
- Prof. E. C. Zingu and senior management of Mangosuthu Technikon
- Messrs. Andrew Nunn, Teddy Singh and all staff in the Department of Mechanical Engineering
- Messrs. Mike Maree and Julian Thompson and their staff in the departments of Maintenance and Information Technology
- Messrs. Ralph Naidoo, Magan Moodley, John van Rensburg, Cannon Maxongo and Chris Presmeg and the staff and students in the Department of Civil Engineering and Surveying

### University of Stellenbosch:

- A/Prof. Thomas Harms, for support, advice and supervision of this project
- Mrs. Ilse du Toit, Mr. Cobus Zietsman and the academic and administrative staff in the Department of Mechanical Engineering
- Messrs. Meiring Beyers, Johan Potgieter, Rhydar Harris and Paul Wipplinger of M303

The support of the following is acknowledged and greatly appreciated:

- Mr. Ryan Botha, AfricaBlue and Autodesk, for graphical renditions of the collector
- The United States Agency for International Development (USAID)
- Mrs. Meena Dhavraj-Lysko, Prof. Jørgen Lovseth (Norwegian University for Science and Technology) and Mr. Robert van den Heetkamp (University of KwaZulu-Natal)

Finally, thanks to friends and family for their encouragement and support.

## TABLE OF CONTENTS

	Page
TITLE PAGE.....	i
DECLARATION.....	ii
ABSTRACT .....	iii
OPSOMMING.....	iv
DEDICATION.....	vi
ACKNOWLEDGEMENTS.....	vii
TABLE OF CONTENTS .....	viii
LIST OF TABLES.....	x
LIST OF FIGURES .....	xii
LIST OF SYMBOLS.....	xv
1. INTRODUCTION .....	1
2. MOTIVATION.....	3
3. DESCRIPTION OF TEST APPARATUS .....	7
3.1 Parabolic Trough Collector Structure.....	7
3.2 Heat Collecting Elements .....	7
3.3 Fluid Circulation System.....	8
3.4 Drive, Tracking and Control System (DTCS).....	9
4. TEST METHODOLOGY.....	11
4.1 Introduction .....	11
4.2 The ASHRAE 93-1986 (RA 91) Testing Standard .....	11
4.2.1 Thermal efficiency test procedure .....	13
4.2.2 Collector time constant test procedure .....	17
4.2.3 Incidence angle modifier test procedure.....	18
4.2.4 Collector acceptance angle test procedure.....	19
4.3 PTSC Test Schedule .....	20
4.3.1 Planned schedule .....	20
4.3.2 Completed test schedule .....	22
4.4 Development of Data Logging Software Applications .....	25
4.4.1 SolarStation .....	25
4.4.2 SCATTAscan and SCATTALog .....	27
4.5 Summary.....	29

5. EXPERIMENTAL RESULTS .....	30
5.1 Introduction .....	30
5.2 Tracking Performance .....	30
5.2.1 Fixed rate tracking .....	30
5.2.2 PSA Algorithm-based tracking.....	33
5.3 PTSC Performance Results .....	34
5.3.1 Collector time constant.....	35
5.3.2 Collector acceptance angle .....	41
5.3.3 Thermal efficiency.....	44
5.3.4 Incidence angle modifier .....	48
5.4 Receiver Thermal Loss Tests .....	52
5.5 Summary.....	56
6. THERMAL MODELLING OF PTSC PERFORMANCE.....	58
6.1 Introduction .....	58
6.2 Thermal Model of Collector Performance.....	59
6.3 Results .....	62
6.4 Summary.....	69
7. DISCUSSION.....	71
7.1 Experimental Results.....	71
7.2 Thermal Modelling of PTSC Performance.....	79
8. SUMMARY.....	83
9. RECOMMENDATIONS.....	85
REFERENCES .....	88
APPENDIX A DESIGN AND CONSTRUCTION OF PTSC .....	A1
APPENDIX B MATLAB CODE FOR PTSC INTERCEPT FACTOR.....	B1
APPENDIX C THE PSA ALGORITHM: CALCULATIONS AND DATA.....	C1
APPENDIX D LABVIEW SOFTWARE: SCATTALOG DATA SAMPLE .....	D1
APPENDIX E SUMMARY OF EXPERIMENTAL TEST DATA .....	E1
APPENDIX F THERMAL MODEL DATA.....	F1

## LIST OF TABLES

	Page
2.1 Comparison of performance and other key parameters for three solar thermal technologies (* Schlaich, 1996; ** SolarPACES, 1999).....	3
3.1 PTSC key features and material properties .....	8
4.1 Planned PTSC test schedule .....	22
4.2 Schedule of completed PTSC tests.....	23
5.1 Key data from time constant tests.....	40
5.2 Key data from thermal efficiency tests.....	47
5.3 Key data from incidence angle modifier tests .....	51
5.4 PTSC performance summary.....	57
A.1 Comparison of reflective surface options.....	A8
A.2 Error sets used to determine absorber diameter in figure A.5.....	A12
A.3 Error sets used in PTSC analysis of Güven et al. (1986) .....	A16
A.4 Intercept factor for PTSC with rim angle of 82° and aperture width of 1.5 m.....	A17
A.5 Operating modes for the DTCS .....	A31
A.6 Summary of key features of PTSC.....	A35
C.1 Solar zenith and azimuth data for a range of days covering one year, generated using the PSA Algorithm (MATLAB programme “psa_16days.m”) and compared with output from the Multi-Year Interactive Computer Almanac (MICA) of the U.S. Naval Observatory .....	C8
D.1 Extract from Excel spreadsheet showing processed output from LabVIEW application SCATTALog for collector acceptance angle test .....	D2
D.2 List of columns from table E1 and description of data types .....	D4
E.1 Summary of data for collector time constant tests .....	E2
E.2 Thermal efficiency test data for glass-shielded receiver (19 February 2004).....	E3
E.3 Summary of data for thermal efficiency tests with unshielded receiver .....	E6
E.4 Summary of data for thermal efficiency tests with glass-shielded receiver.....	E6
E.5 Summary of data for collector acceptance angle tests with unshielded and glass-shielded receiver.....	E7
E.6 Summary of data for incidence angle modifier tests with unshielded receiver.....	E7
E.7 Summary of data for incidence angle modifier tests with glass-shielded receiver .....	E7

F.1	Output from MATLAB thermal modelling programme for unshielded receiver (wind speed of 4.8 m/s, inlet temperature of 27.12 °C and beam irradiance of 928.23 W/m <sup>2</sup> ) .....	F2
F.2	Loss output from MATLAB thermal modelling programme for unshielded receiver (wind speed of 1.34 m/s, inlet temperature of 29.77 °C, ambient temperature of 21.2 °C and zero beam irradiance).....	F3
F.3	Output from MATLAB thermal modelling programme for glass-shielded receiver (wind speed of 4.6 m/s, inlet temperature of 27.27 °C and beam irradiance of 841.73 W/m <sup>2</sup> ) .....	F4

## LIST OF FIGURES

	Page
2.1 Solar Electric Generating Systems (SEGS) collector field (www.kjcsolar.com, 2004) .....	4
2.2 Parabolic trough test loop, Plataforma Solar de Almeria (www.psa.es, 2004) .....	5
3.1 Parabolic trough collector module.....	7
3.2 Schematic layout of fluid circulation system with PTSC structure removed and (inset) three-dimensional sketch .....	9
3.3 PTSC with glass-shielded receiver during operation and vacuum pump visible in foreground .....	10
4.1 Solar map for Mangosuthu Technikon Solar Energy Test Facility with morning and afternoon threshold irradiance times .....	21
4.2 Solar map indicating completed ASHRAE 93 tests .....	24
4.3 Front panel GUI of LabVIEW application SolarStation .....	25
4.4 Schematic diagrams of (a) main block diagram and (b) structural hierarchy of LabVIEW application SolarStation.....	26
4.5 Front panel GUI of LabVIEW application SCATTALog .....	28
5.1 PTSC performance for fixed rate tracking (mode 2) based on VSD on-time .....	31
5.2 PTSC performance for combination of fixed rate tracking (mode 2) and manual adjustment.....	32
5.3 PTSC performance for fixed pulse tracking (mode 2) .....	33
5.4 PTSC performance for PSA Algorithm-based tracking (mode 3).....	34
5.5 Time constant quotient for unshielded receiver (cooling test) .....	35
5.6 Time constant quotient for unshielded receiver (heating test) .....	36
5.7 Time constant for unshielded receiver (cooling and heating tests) .....	36
5.8 Time constant quotient for glass-shielded receiver (cooling test).....	37
5.9 Time constant quotient for glass-shielded receiver (heating test).....	38
5.10 Time constant for glass-shielded receiver (cooling and heating tests).....	38
5.11 Comparison of time constants for glass-shielded and unshielded receivers .....	39
5.12 Collector acceptance angle results for unshielded receiver.....	41
5.13 Collector acceptance angle results for glass-shielded receiver .....	42
5.14 Collector acceptance angle results for unshielded and glass-shielded receivers.....	43
5.15 Thermal efficiency with unshielded receiver .....	44
5.16 Thermal efficiency with glass-shielded receiver .....	45

5.17	Comparison of thermal efficiencies.....	46
5.18	Incidence angle modifier for unshielded receiver .....	49
5.19	Incidence angle modifier for glass-shielded receiver .....	49
5.20	Incidence angle modifier for unshielded and glass-shielded receivers .....	50
5.21	Temperature data from thermal loss test for unshielded receiver .....	53
5.22	Thermal loss and wind data for unshielded receiver .....	54
5.23	Temperature data for glass-shielded receiver .....	55
5.24	Thermal loss and wind data for glass-shielded receiver.....	55
5.25	Thermal loss for glass-shielded and unshielded receivers.....	56
6.1	Heat transfer model for unshielded receiver (Lamprecht, 2000).....	60
6.2	Heat transfer model for glass-shielded receiver (Lamprecht, 2000) .....	60
6.3	Segment control volume for absorber with liquid flow (Lamprecht, 2000).....	60
6.4	Unshielded model results for a range of receiver inlet temperatures .....	63
6.5	Free and forced convection models with experimental data (unshielded) .....	63
6.6	Output from forced convection model for varying wind speed (unshielded).....	64
6.7	Off-sun thermal loss from forced convection model (unshielded).....	65
6.8	Fluid and glass temperatures for two wind speeds .....	66
6.9	Free and forced convection models with experimental data (glass-shielded) .....	67
6.10	Output from forced convection model for varying wind speed (glass-shielded) .....	68
6.11	Off-sun thermal loss from forced convection model (glass-shielded receiver).....	69
7.1	PTSC system on rooftop of test facility with prevailing wind directions .....	81
A.1	PTSC macro- and micro-level design stages proposed by Güven et al. (1986) .....	A3
A.2	PTSC torque-tube collector structure with parabolic ribs .....	A4
A.3	Polypropylene parabolic rib.....	A5
A.4	Parabolic rib attachment method .....	A6
A.5	PTSC collector structure.....	A7
A.6	(a) stainless steel substrate prior to installation (b) assuming parabolic shape .....	A9
A.7	Solar intercept angle due to sun width and image spread due to optical errors .....	A10
A.8	Absorber diameter for $\gamma = 0.95$ using error analysis of Stine and Harrigan (1985) .	A13
A.9	Intercept factor $\gamma$ as a function of $\beta^*$ and $d^*$ for $\sigma^* = 0.0$ .....	A18
A.10	Intercept factor $\gamma$ as a function of $\beta^*$ and $d^*$ for $\sigma^* = 0.1798$ (error set B3 indicated) .....	A19
A.11	Intercept factor as a function of $\beta^*$ for fixed $d^*$ and six values of $\sigma^*$ .....	A20
A.12	Intercept factor as a function of $d^*$ for fixed $\beta^*$ and six values of $\sigma^*$ .....	A20

A.13	Intercept factor as a function of $d^*$ for fixed $\beta^*$ and $\sigma^*$ and six rim angles.....	A21
A.14	Intercept factor as a function of receiver diameter $D$ for fixed $\sigma^*$ and $\beta^*$ and six values of $(d_r)_y$ .....	A22
A.15	(a) general dimensions of receiver (b) receiver drive end (c) non-drive end with instrumentation sections (d) three-dimensional view of drive end instrumentation section.....	A25
A.16	(a) detailed view of ring holder and positioning bolts (b) attachment of receiver to the collector structure .....	A26
A.17	(a) glass shield, absorber, vacuum vent and o-ring seal arrangement at drive end (b) and (c) o-ring seal (d) vacuum seal arrangement at drive end of PTSC .....	A27
A.18	(a) Samples of tube with $\text{Cu}_2\text{S}$ coating obtained after exposure to $\text{NH}_4\text{S}$ for (left to right) 20 s, 40 s, 60 s, 120 s and 5 min (b) $\text{CuO}$ surface coating showing blue-black finish.....	A28
A.19	Schematic diagram of incidence angle $\theta_i$ at solar noon on solstices and equinoxes for a PTSC located in Durban, South Africa, and aligned in the N-S direction (adapted from Stine and Harrigan, 1985).....	A30
A.20	Development of tracking error as sun moves through PTSC focus .....	A32
A.21	Schematic diagram of the solar vector ( $\theta_z$ and $A$ ) and tracking angle ( $\rho$ ) for an N-S aligned PTSC rotated through $\rho_T$ degrees to the east.....	A34

## LIST OF SYMBOLS

### Nomenclature

A	Area, [m <sup>2</sup> ] or solar azimuth angle, [rad]
C	Geometric concentration ratio
c <sub>p</sub>	Specific heat at constant pressure, [J/kgK]
D	Absorber tube diameter, [m]
d	Aperture width of parabola, [m] or day number of the month
(d <sub>r</sub> ) <sub>y</sub>	Receiver mislocation along the optical axis of the reflector, [cm]
d*	Universal nonrandom error parameter due to receiver mislocation
ε <sub>p</sub>	Obliquity of the ecliptic, [rad]
F <sub>R</sub>	Heat removal factor
f	Focal length of parabola, [m] or friction factor
G	Irradiance, [W/m <sup>2</sup> ]
g	Mean anomaly of the sun, [rad]
gmst	Greenwich mean sidereal time, [h]
h	Height of parabola, [m] or convective heat transfer coefficient, [W/m <sup>2</sup> K]
hour	Hour of the day in Universal Time and decimal format, [h]
jd	Julian Day, [days]
K <sub>ατ</sub>	Incidence angle modifier
k	Thermal conductivity, [W/mK]
L	Mean longitude of the sun, [rad] or litres
l	Ecliptic longitude of the sun, [rad]
lmst	Local mean sidereal time, [h]
long	Geographical longitude, [deg]
m	Month of the year or mass flow rate, [kg/s]
n	Number of standard deviations or difference between the current Julian Day and Julian Day corresponding to 1 January 2000
Q	Volumetric flow rate, [L/h] or heat flow [W]
Q <sub>o</sub>	Off-sun thermal loss per unit area of receiver, [W/m <sup>2</sup> ]
Q <sub>+</sub>	On-sun thermal loss per unit area of receiver, [W/m <sup>2</sup> ]
R <sup>2</sup>	Coefficient of determination
r	Distance from reflector surface to focal point of parabola, [m]
ra	Right ascension, [rad]

s	Arc length, [m]
T	Torque, [Nm] or time, decimal [h] or [s]
$t_a$	Ambient air temperature, [°C]
$t_{f,i}$	Fluid temperature at inlet to receiver, [°C]
$t_{f,o}$	Fluid temperature at outlet from receiver, [°C]
U	Overall heat transfer coefficient, [W/m <sup>2</sup> K]
V	Air velocity, [m/s]
v	Fluid velocity, [m/s]
y	Gregorian year

#### Greek symbols

$\alpha$	Absorptance
$\beta$	Reflector misalignment and tracking error angle, [rad]
$\beta^*$	Universal nonrandom error parameter due to angular errors, [rad]
$\gamma$	Intercept factor
$\delta$	Dispersion angle, [rad], declination angle, [rad] or beam deflection, [m]
$\Delta T$	Time difference or sampling interval, [s]
$\Delta t$	Difference between receiver inlet temperature and ambient, [°C]
$\Delta t_{ave}$	Difference between average receiver fluid temperature and ambient, [°C]
$\Delta t_r$	Difference between receiver outlet and inlet temperatures, [°C]
$\varepsilon$	Thermal emittance
$\eta_g$	Thermal efficiency
$\eta_o$	Optical efficiency
$\theta_i$	Angle of incidence of central solar ray with collector aperture, [deg]
$\theta_z$	Solar zenith angle, [rad]
$\mu$	Dynamic viscosity, [kg/ms]
$\rho$	Density, [kg/m <sup>3</sup> ] or reflectance
$\rho_T$	Collector tracking angle, [deg]
$\sigma$	Random optical error, [rad]
$\sigma^*$	Universal random error parameter, [rad]
$\sigma_{contour \perp}$	Rms transverse deviation of contour from design direction, [mrad]
$\sigma_{contour \parallel}$	Rms longitudinal deviation of contour from design direction, [mrad]
$\sigma_{displacement}$	Equivalent rms angular spread from receiver misplacement, [mrad]
$\sigma_{drive}$	Standard deviation of tracker drive errors, [mrad]

$\sigma_{\text{optical}}$	Rms angular spread caused by all optical errors, [mrad]
$\sigma_{\text{rec}}$	Standard deviation of receiver location errors, [mrad]
$\sigma_{\text{refl}}$	Standard deviation of mirror specularity errors, [mrad]
$\sigma_{\text{sensor}}$	Standard deviation of tracking sensor errors, [mrad]
$\sigma_{\text{slope}}$	Standard deviation of mirror slope errors, [mrad]
$\sigma_{\text{specular} \perp}$	Rms transverse deviation of contour from design direction, [mrad]
$\sigma_{\text{specular} \parallel}$	Rms longitudinal deviation of contour from design direction, [mrad]
$\sigma_{\text{sun}}$	Standard deviation equivalent to sun's width, [mrad]
$\sigma_{\text{tot}}$	Weighted standard deviation of collector errors or total rms beam spread, [mrad]
$\sigma_{\text{tracking}}$	Rms tracking error, [mrad]
$\sigma_{1D}$	Standard deviation of one-dimensional collector errors, [mrad]
$\sigma_{2D}$	Standard deviation of two-dimensional collector errors, [mrad]
$\tau$	Transmittance
$\Phi$	Geographical latitude, [deg]
$\psi$	Angle between parabolic axis and point on mirror surface, [deg]
$\psi_{\text{rim}}$	Rim angle, [deg]
$\omega$	Hour angle, [rad]

### Subscripts

a	aperture or ambient
ave	average
bp	beam in plane
ce	convective external
DN	direct normal
e	effective
f	fluid
G	glass
g	gross
i	inlet or internal
inst	instantaneous
initial	initial
L	loss
MAX	maximum

n	index value or normal
o	outlet or optical
r	receiver
T	time
t	total
U	unshielded
z	zenith

#### Dimensionless groups

Nu	Nusselt number, $hD/k$
Pr	Prandtl number, $\mu c_p/k$
Re	Reynolds number, $\rho VD/\mu$

#### Abbreviations

AC	Alternating current
ASHRAE	American Society of Heating, Refrigerating and Air-Conditioning Engineers
AWJ	Abrasive water-jet
CAD	Computer-aided design
CAM	Computer-aided manufacturing
CD	Compact disc
DOE	Department of energy
DTCS	Drive, tracking and control system
E	East
EDEP	Energy deposition
GUI	Graphical user interface
HCE	Heat collecting element
HT	High temperature
IST	Industrial Solar Technology
KJC	Kramer Junction Company
LT	Low temperature
MICA	Multi-year interactive computer almanac
N	North
NIP	Normal incidence pyrhelimeter
NREL	National Renewable Energy Laboratory

NSTTF	National Solar Thermal Test Facility
PLC	Programmable logic controller
PSA	Plataforma Solar de Almeria
PSP	Precision spectral pyranometer
PTSC	Parabolic trough solar collector
S	South
Sandia	Sandia National Laboratories
SEGS	Solar Electric Generating System
SAST	South African Standard Time
ST	Solar time
TC	Thermocouple
U.S.	United States of America
USNO	United States Naval Observatory
VSD	Variable speed drive
W	West

## 1. INTRODUCTION

Solar thermal systems play an important role in providing non-polluting energy for domestic and industrial applications. Concentrating solar technologies, such as the parabolic dish, compound parabolic collector and parabolic trough can operate at high temperatures and are used to supply industrial process heat, off-grid electricity and bulk electrical power. In a parabolic trough solar collector, or PTSC, the reflective profile focuses sunlight on a linear heat collecting element (HCE) through which a heat transfer fluid is pumped. The fluid captures solar energy in the form of heat that can then be used in a variety of applications. Key components of a PTSC include the collector structure, the receiver or HCE, the drive system and the fluid circulation system, which delivers thermal energy to its point of use.

The use of concentrating solar energy collectors dates back to the late 19<sup>th</sup> century. The technology was originally used for pumping water although more unusual applications included a steam-powered printing press exhibited at the 1902 Paris Exposition (Duffie and Beckman, 1991). It was not until the mid-1970s that large-scale development of PTSCs began in the United States under the Energy Research and Development Administration (ERDA), later the Department of Energy (DOE) (U.S. Department of Energy, 2004). This development was strongly influenced by geopolitical factors, such as the oil crisis, and focused on the provision of industrial process heat rather than electrical power. Typical applications of trough technology included laundry processing, oil refining and steam production for sterilisation of medical instruments (Stine and Harrigan, 1985).

The first trough-based Solar Electric Generating Systems (SEGS I) power plant was constructed in 1984 in the U.S. state of California. Eight further plants followed, the last being completed in 1991. Together, SEGS I to IX represent a total of 354 MW of installed electrical capacity and all the plants are still operational. A tenth plant was planned but abandoned when the development company failed to secure financing for construction and went bankrupt (U.S. Department of Energy, 2004). Cheap and stable oil supplies through the 1980s meant no new parabolic trough power plants have been constructed since.

In recent years, a new momentum in PTSC research has developed, fuelled by climate concerns, dwindling oil reserves and political instability in some oil-producing countries. An

attractive feature of the technology is that PTSCs are already in use in great numbers and research output is likely to find immediate application. Parabolic trough technology has made the crucial leap from pure concept to working solution, offering a real alternative to fossil fuel energy sources. This demonstrated capability gives credibility to trough research, which is now focused on ways to advance PTSC technology and lower the costs of constructing and operating trough-based power plants.

For researchers interested in contributing to the development of PTSCs it is important to be able to test new collector components. To this end, the construction of a parabolic trough collector is vital and a number of such PTSCs have been constructed for research institutions, ranging in size from 1 m<sup>2</sup> to 100 m<sup>2</sup>. Smaller-scale PTSCs can be used to test advances in receiver design, reflective materials, control methods, structural design, thermal storage, testing and tracking methods (Thomas, 1994; Bakos et al., 1999; Almanza et al., 1997). One such PTSC of aperture area 7.5 m<sup>2</sup> has been developed at Mangosuthu Technikon.

The aim of this study is to test the newly developed PTSC and characterise its performance. This is to be done using a suitable solar collector test standard and the results compared with a thermal model of the PTSC.

The results of this study will allow the performance of new parabolic trough components such as heat collecting elements, surface materials and tracking systems to be measured when the collector becomes a test-rig in an ongoing solar thermal research programme.

## 2. MOTIVATION

Faced with shrinking fossil fuel resources, growing global energy demands and increasing CO<sub>2</sub> levels in the Earth's atmosphere (Sayigh, 1999), the “global village” urgently needs to reassess how it generates and consumes power. Renewable energy technologies such as geothermal, hydro-power, biomass conversion and wind energy all offer potential for replacing conventional coal-, gas- and oil-fired power-plants, though not yet on the same scale or for the same cost.

Solar thermal energy systems are among the most promising of the renewable technologies. Three such concepts for bulk electricity production are the central receiver, the solar chimney and parabolic trough solar collector. Table 2.1 presents a comparison of key parameters for the three technologies. The parabolic trough data are based on actual commercial plant performance.

**Table 2.1** Comparison of performance and other key parameters for three solar thermal technologies (\* Schlaich, 1996; \*\* SolarPACES, 1999)

	<b>Solar Chimney *</b>	<b>Central Receiver **</b>	<b>Parabolic Trough **</b>
<b>Capacity (MW)</b>	< 200	30 - 200	30 - 80
<b>Levelized energy cost (c/kWh)</b>	50 - 105	70 - 100	85
<b>Installed capacity (MW)</b>	-	10	354
<b>Efficiency (%)</b>	2	23 (peak), 14-19 (annual)	21 (peak), 14-18 (annual)
<b>Next hurdle?</b>	First commercial station. 1000m high stack.	Volumetric receiver. Molten salts. Heliostats. Storage	Advanced collector. Direct Steam Generation (DSG). Storage.

While each of the technologies shown in Table 2.1 has its advantages, only the parabolic trough system has been commercialised. The central receiver concept has a potentially higher

operating efficiency and the solar chimney has built-in thermal storage but neither concept has a commercial track record. In contrast, the first SEGS plant has been operating successfully for over 20 years.



**Figure 2.1** Solar Electric Generating Systems (SEGS) collector field ([www.kjcsolar.com](http://www.kjcsolar.com), 2004)

With the performance of SEGS I to IX and the experience gained in operating and maintaining them, research into the next generation of PTSC systems has commenced. The two most prominent large-scale PTSC test facilities are Sandia National Laboratories (Sandia) in the U.S. state of New Mexico and the Plataforma Solar de Almeria (PSA) in Spain.

The National Solar Thermal Test Facility (NSTTF) at Sandia was established in 1976 and is operated by the U.S. DOE through its business unit SunLab. The NSTTF covers 45 hectares of land and includes a central receiver test facility with a central tower and 222 heliostats, a 16 kW solar furnace, a rotating azimuth-tracking platform for parabolic trough research (Dudley et al., 1995) and a Distributed Receiver Test Facility with two 75 kW parabolic dishes. The technology that made it possible to commercialise parabolic troughs was originally developed at Sandia's NSTTF (SunLab, 2000).

At the commercial level, trough research in the U.S. is now focused on thermal storage and the development of “next generation” collectors and components (Energy Efficiency and Renewable Energy Network, 2003). Key areas identified in the Parabolic-Trough Technology Roadmap, compiled by Price and Kearney (1999), include development of an advanced collector structure, heat collecting element (HCE), mirrors and thermal storage. The document acknowledges the need for international collaboration in research as well as the possibility of U.S. industry losing its competitive edge in trough production in the face of greater funding of research efforts in Europe.

The centre of parabolic trough research in Europe is the PSA in Spain, managed by the Research Centre for Energy, Environment and Technology (CIEMAT) and DLR, the German Aerospace Centre (CIEMAT, 2003). It is home to the European DISS (Direct Solar Steam) project consisting of a full-scale parabolic trough solar steam generator of length 500 m and thermal power of 2 MW, two central receiver prototypes and dish/stirling systems. The trough collector loop consists of eleven modified Luz LS-3 collectors of the same type designed for use in the Californian SEGS VII, VIII and IX power plants. The DISS project has proven the feasibility of direct steam generation (DSG), which is widely considered to be the next step in parabolic trough power production (Eck et al., 2003 and Energy Efficiency and Renewable Energy Network, 2003).



**Figure 2.2** Parabolic trough test loop, Plataforma Solar de Almería (www.psa.es, 2004)

Research into advanced collector structures (the so-called “torque-box” design) is also under way at the PSA through the EuroTrough initiative. This is a collaborative venture aimed at developing a high-performance European collector. Initial tests carried out at the PSA have shown a performance improvement over existing designs of 3 %. A 50 MW power plant with 549 000 m<sup>2</sup> of these collectors is planned for southern Spain – the first commercial plant to be constructed since 1991 (Geyer et al., 2002).

With abundant levels of solar irradiance and an inevitable move away from fossil-fuel based power stations, South Africa is well positioned to take advantage of solar thermal energy. Power producer Eskom is considering the construction of a 100 MW power plant in the Northern Cape, based on the central receiver concept. They anticipate a high degree of local content in the plant’s manufacture (up to 90 %). A fully imported plant would have a capital cost of approximately R 24 000 per kilowatt compared with R 10 000 per kilowatt for a coal-fired power station, leading to an estimated electricity cost of 60 c/kWh. Notwithstanding the higher cost, Eskom is giving serious consideration to the project (Engineering News Online, 2003).

The age of the “fossil-fuel economy” is coming to an end and the development of new sources of power is becoming a priority. Against a backdrop of renewed global interest in solar thermal power generation, this study is motivated by the desire to further develop South Africa’s research capacity in alternative energy systems, with particular emphasis on parabolic trough solar collectors.

### 3. DESCRIPTION OF TEST APPARATUS

#### Parabolic Trough Collector Structure

The equipment tested in this study consisted of a locally developed parabolic trough solar collector. The PTSC has a torque-tube structure with a length of 5 m, aperture width of 1.5 m and a rim angle of  $82^\circ$  (see figure 3.1). The reflective surface consists of stainless steel sheets covered with SA-85 aluminised acrylic reflective film and clamped into the profile formed by parabolic ribs. Aspects of the design and construction of the collector are given in Appendix A.

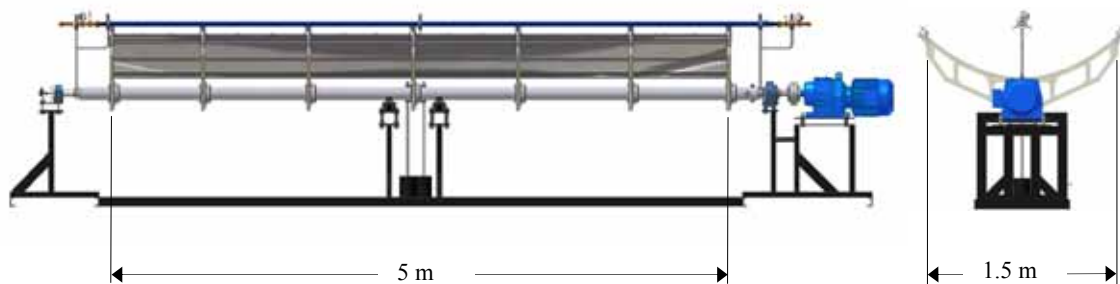


**Figure 3.1** Parabolic trough collector module

#### 3.2 Heat Collecting Elements

Two HCEs, or receivers, were tested - one an unshielded copper tube and the other a similar tube enclosed in an evacuated glass shield. Both absorber tubes are coated with a commercial selective coating (Solkote) to reduce thermal emittance and increase absorptance. Table 3.1 summarises the key parameters of the PTSC for both receivers. The optical efficiencies ( $\eta_o$ ) were obtained from an error analysis conducted to determine the intercept factor ( $\gamma$ ), details of which are given in Appendix A, together with diagrams of the receivers.

**Table 3.1** PTSC key parameters and material properties

Feature / Parameter	Value
Collector dimensions	5.0 m x 1.5 m
Rim angle, $\psi_{rim}$	82.2°
Absorber diameter, $D$	28.6 mm
Concentration ratio, $C$	16.7
Intercept factor, $\gamma$	0.823
Surface reflectance, $\rho$	0.83
Receiver absorptance, $\alpha$	0.88
Receiver emittance, $\epsilon$	0.49
Glass-shield transmittance, $\tau$	0.92
$\eta_o$ (unshielded receiver)	0.601
$\eta_o$ (glass-shielded receiver)	0.553

### 3.3 Fluid Circulation System

The fluid driver is a 960 rev/min Howden GF positive displacement (helical element) pump with flange-mounted 0.75 kW motor and a high-temperature Viton stator. Maximum output ranges from 700 L/hr at 100 kPa to 400 L/hr at 500 kPa. Pump speed is controlled by a Siemens 6SE6440 variable speed drive (VSD) to provide variable flow rate via a manual dial in the control room of the solar energy test facility (Brooks, 2005). High-temperature (HT) and low-temperature (LT) tanks enable water to be supplied for testing purposes up to a maximum of 85 °C. A Tecfluid SC-250 variable area flow meter (100 L/hr to 1000 L/hr) provides flow data. Ten type-K thermocouple (TC) probes enable temperatures to be recorded during testing of the PTSC.

A test flow rate of 300 L/h was used to ensure turbulent conditions in the receiver throughout the expected temperature range. Fluid density fluctuations were accommodated during data processing using the water temperature to calculate mass flow rate for each datum point. During testing, flow meter readings were checked by physical measurement. Small variations in mass flow rate were allowed between low and high temperature tests, but properly accounted for in the processing of test data. Figure 3.2 shows the layout of the fluid circulation system.

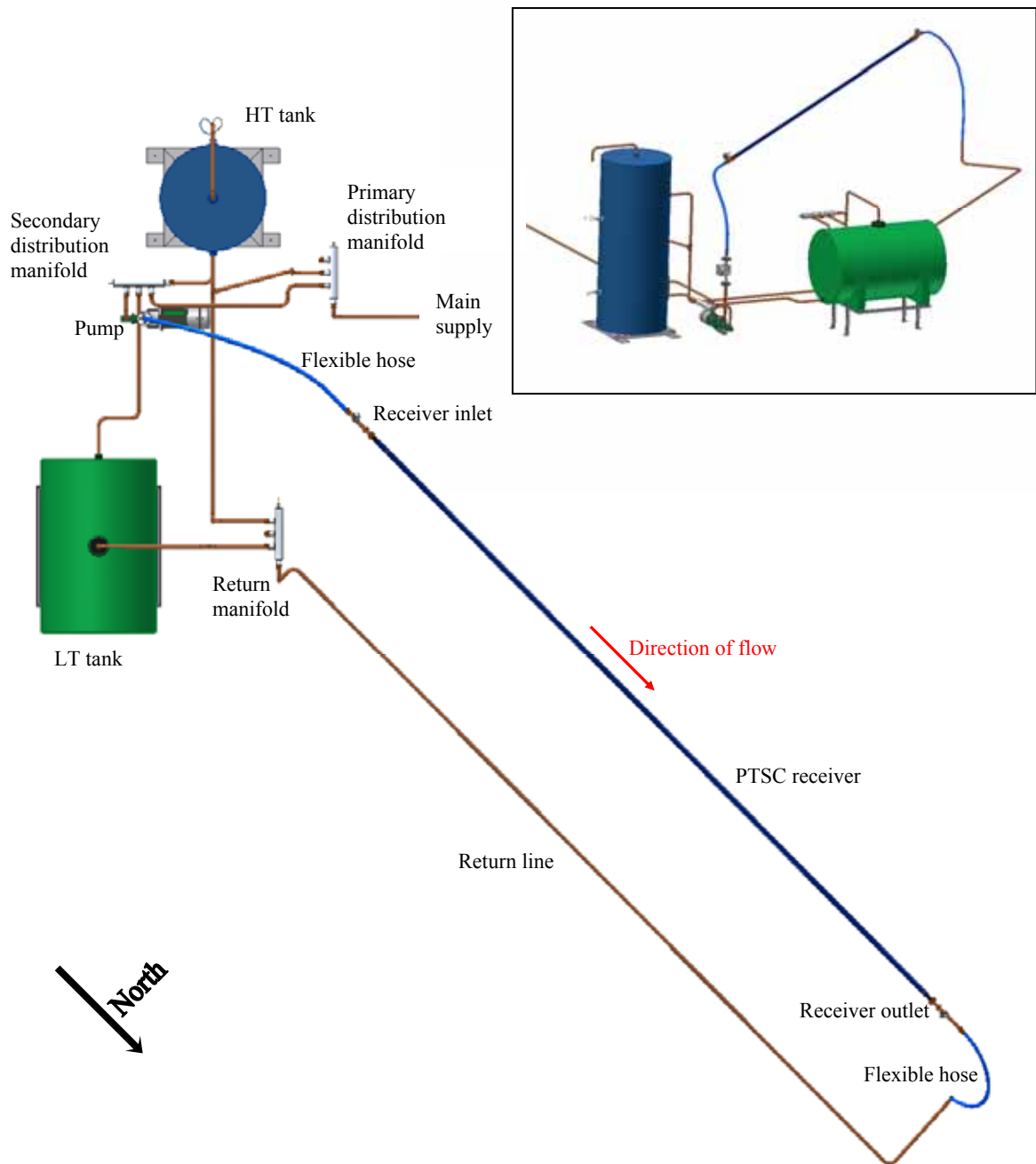


**Figure 3.2** Schematic layout of fluid circulation system with PTSC structure removed and (inset) three-dimensional sketch

### 3.4 Drive, Tracking and Control System (DTCS)

The PTSC is aligned along a true-north line and employs single-axis tracking. The tracking hardware consists of a Siemens 0.25 kW, 685 rev/min, 8-pole AC motor with electromechanical brake and a 463:1 high-reduction helical gearbox. A Siemens VSD enables the system to operate at trough rotational speeds of between 1.5 rev/min and zero rev/min.

The control hardware consists of a 2500-pulse rotary encoder mounted on the shaft of the PTSC to provide angular feedback information, and a Siemens S7 programmable logic controller (PLC). Tracking of the collector is exercised via PLC-control of the VSD. Three tracking modes were available during this study: manual jogging of the collector, fixed-rate angular corrections based on the sun's apparent motion ( $0.25^\circ/\text{min}$ ) and virtual tracking using solar angle information from the implementation of the PSA Algorithm (Blanco-Muriel et al., 2001). Appendix A includes further information on the DTCS, while a sample calculation using the PSA Algorithm is given in appendix C. The tracking system is described in detail by Naidoo (2005). A photograph of the parabolic trough in operation is shown in figure 3.3.



**Figure 3.3** PTSC with glass-shielded receiver during operation and vacuum pump visible in foreground

## 4. TEST METHODOLOGY

### 4.1 Introduction

To ensure the quality of results and to allow for comparison of performance with other collectors, the PTSC was tested according to a recognised solar collector standard. This chapter describes the chosen standard, the planned and completed test schedules and the software applications developed to log test data.

The formalisation of collector test procedures is a recent development. Duffie and Beckmann (1991) note that this became necessary in the mid-1970s when many new designs appeared on the commercial market. Standard tests were required to provide operating data, especially with respect to energy absorption, heat loss, effects of incidence angle and heat capacity. In the U.S. the National Bureau of Standards devised a test procedure that was modified by the American Society of Heating, Refrigerating and Air-conditioning Engineers (ASHRAE). This eventually became the ASHRAE Standard 93-1986, which is used in this study and described in 4.2.

Of those making use of ASHRAE 93, Kalogirou (1996) has published full results of a parabolic trough collector test using the standard. Although Dudley et al. (1995) do not refer to the standard in their description of the Industrial Solar Technology (IST) parabolic trough tests at Sandia, they follow the same principles as ASHRAE 93 in their procedures. A significant difference is their definition of collector efficiency using a second order polynomial in  $\Delta t$  (fluid inlet temperature above ambient or  $(t_{f,i} - t_a)$ ), and not a linear function.

The extensive international use of ASHRAE 93 for commercial purposes, its accessibility and the comprehensive manner in which it describes the various test procedures, supported its use in this study.

### 4.2 The ASHRAE 93-1986 (RA 91) Testing Standard

ASHRAE Standard 93-1986 (RA 91), first published in 1977 and updated in 1991, applies to those concentrating and nonconcentrating collectors in which a fluid enters through a single

inlet and leaves through a single outlet. A separate standard (ASHRAE 96-1990) is used for collectors in which the heat transfer fluid changes phase, such as DSG trough systems (ASHRAE, 1991).

The four tests included under the ASHRAE 93 standard are:

- Thermal efficiency,  $\eta_g$
- Collector time constant
- Incidence angle modifier,  $K_{\tau\alpha}(\theta_i)$
- Collector acceptance angle

The standard defines the allowed variation in system operating parameters to ensure steady state conditions during testing. These prescribed limits may be categorised as either fluid-related, climatological or radiometric and are listed below.

#### Fluid constraints

- The working fluid temperature and flow rate of the collector at receiver inlet should remain constant to within  $\pm 1$  °C and 0.000315 L/s respectively for 15 min prior to the start of data logging (that is, the system should be properly stabilised)
- The receiver inlet temperature of the fluid should be controlled to within  $\pm 0.05$  °C of the desired test value throughout the test period
- For the collector acceptance angle test (only), the receiver inlet temperature should preferably be controlled to within  $\pm 1$  °C of the ambient air temperature

#### Climatological constraints

- The maximum ambient air temperature during testing should not exceed 30 °C
- Ambient temperature should not vary by more than  $\pm 1.5$  °C during a 15-minute interval prior to the start of data logging
- For thermal efficiency and incident angle modifier tests, the average wind velocity should be between 2.2 m/s and 4.5 m/s (4.3 knots and 8.7 knots) during the test period and for 10 min prior to the start of data logging

### Radiometric constraints

- Average normal beam irradiance should exceed  $790 \text{ W/m}^2$  and should not vary by more than  $\pm 32 \text{ W/m}^2$  during the data logging period and for 10 min prior to it
- During testing the collector should be maintained within  $2.5^\circ$  of the angle of incidence for which the test is conducted
- During collector acceptance angle tests, normal beam irradiance should exceed  $800 \text{ W/m}^2$  and remain as constant as possible

In addition to the above, the collector reflective surface should be checked prior to testing for pollution or dust deposits and cleaned.

#### 4.2.1 Thermal efficiency test procedure

Thermal efficiency ( $\eta_g$ ) is obtained by measuring  $\Delta t_r$ , the temperature increase of the working fluid through the receiver ( $\Delta t_r = (t_{f,o} - t_{f,i})$ ). Together with the fluid properties and mass flow rate, this gives the rate of thermal energy input. Dividing this by the solar radiation falling on the collector gives a measure of the collector's efficiency. By repeating the test for increasing  $\Delta t$ , a linear model of the collector efficiency can be obtained. From ASHRAE 93, the efficiency equation has the form

$$\begin{aligned}\eta_g &= -\left(\frac{A_r U_L F_R}{A_g}\right)\left(\frac{\Delta t}{G_{bp}}\right) + \left(\frac{A_a}{A_g}\right)F_R \eta_o \\ &= -\left(\frac{A_r U_L F_R}{A_a}\right)\left(\frac{\Delta t}{G_{bp}}\right) + F_R \eta_o \quad (\text{for } A_a = A_g)\end{aligned}\tag{4.1}$$

In equation 4.1,  $A_r$ ,  $A_g$  and  $A_a$  are the receiver area, the collector gross area (“footprint” of the whole collector including support structure) and the collector aperture area respectively,  $U_L$  is an overall heat loss coefficient,  $F_R$  is a heat removal factor and  $G_{bp}$  represents the component of the normal beam irradiance in the plane of the collector aperture. Equation 4.2 may be used to determine  $G_{bp}$  from calculated angles of incidence ( $\theta_i$ ) and values of  $G_{DN}$  obtained by measurement, using a pyrheliometer.

$$G_{bp} = G_{DN} \cos\theta_i \quad [\text{W/m}^2]\tag{4.2}$$

In this study, the collector gross area was taken to equal the aperture area, since the module under test was a research prototype, not a commercial unit, and the “footprint” area occupied by the support frame was almost the same as the aperture area. The minor difference caused by the frame’s two end bearing-supports was negligible.

The straight line represented by equation 4.1 has a gradient of  $-(A_r U_L F_R / A_a)$  [W/m<sup>2</sup>K] and y-intercept of  $(F_R \eta_o)$ . The optical efficiency can be obtained from equation A.1, enabling the calculation of the heat removal factor,  $F_R$ . Alternatively, with accurate knowledge of the conditions under which heat transfer takes place from the receiver to the surrounding atmosphere, a value for  $U_L$  can be calculated from heat transfer theory and  $F_R$  can be obtained from the gradient of equation 4.1

ASHRAE 93 requires that all thermal efficiency tests be conducted at normal or near-normal angles of incidence, which contributes to the difficulty of running such tests using a single-axis tracking system, since  $\theta_i$  cannot be held constant over the course of a day or even throughout a season. In this project it was planned to schedule efficiency tests for the time of year when incidence angle was at its minimum so as to restrict  $\theta_i$  to a maximum value of 10° (see 4.3). For the glass-shielded receiver, which was installed after the unshielded unit, it was not possible to complete all efficiency tests before  $\theta_i$  had risen to 15°. This was unavoidable because of poor weather over the summer rainfall season.

In practice, the efficiency of the PTSC is determined by dividing the energy absorbed by the working fluid as it passes through the receiver, by the solar energy falling on the collector aperture. This can be expressed as follows:

$$\begin{aligned} \eta_g &= \frac{mc_p(t_{f,o} - t_{f,i})}{A_a G_{bp}} \\ &= \frac{mc_p \Delta t_r}{A_a G_{bp}} \end{aligned} \quad (4.3)$$

Equation 4.3 is used to process the experimental data gathered during tests. The linear model of  $\eta_g$  given by equation 4.1 is imposed on the graph obtained from the experimental data after processing.

Equation 4.1 requires that the difference between the working fluid inlet temperature and the ambient air temperature ( $\Delta t$ ) be varied to determine PTSC performance. Inlet temperatures should span the normal operating range of the collector. In this project, the receiver inlet temperature was limited by the fluid circulation system, which could supply water at a maximum temperature of approximately 85 °C, thus the inlet range was from 20 °C to 85 °C.

During efficiency tests, the standard requires that at least four data points be obtained for each value of  $\Delta t$ , with two each obtained symmetrically before and after solar noon. This is to ensure that transient effects do not bias the results. The efficiency curve described by equation 4.1 must be established using at least 16 points, or four sets of four data points. To compute the thermal efficiency for each data point, ASHRAE 93 gives the following equation:

$$\eta_g = \frac{\int_{T_1}^{T_2} m c_p (t_{f,o} - t_{f,i}) dT}{A_a \int_{T_1}^{T_2} G dT} \quad (4.4)$$

where  $T_1$  and  $T_2$  represent the start and finish times for the test period and  $G$  is the beam irradiance in the plane of the collector aperture. In the original form of the equation  $A_g$  replaces  $A_a$ , although here the aperture area is used for the reasons described above. In practice, each integral in equation 4.4 is converted to a summation of discrete values since data samples of temperatures and irradiance are logged at fixed time intervals. The time interval chosen for this study was 6 s, giving 10 readings per minute. The integrals were thus determined using numerical integration with an element “width” of 6 s.

According to the test standard, the duration of each thermal efficiency trial must equal one collector time constant, or five minutes, whichever is larger. For example, where the trial lasts five minutes (300 s) consisting of 50 intervals of 6 s each, equation 4.4 becomes:

$$\begin{aligned}
\eta_g &= \frac{\sum_{n=1}^{50} m_n (c_p)_n (t_{f,o} - t_{f,i})_n \Delta T_n}{A_a \sum_{n=1}^{50} G_n \Delta T_n} \\
&= \frac{m_1 (c_p)_1 (\Delta t_r)_1 \Delta T_1 + m_2 (c_p)_2 (\Delta t_r)_2 \Delta T_2 + \dots + m_{50} (c_p)_{50} (\Delta t_r)_{50} \Delta T_{50}}{A_a [(G_1 \Delta T_1 + G_2 \Delta T_2 + \dots + G_{50} \Delta T_{50})]} \\
&= \frac{\phi [m_1 (c_p)_1 (\Delta t_r)_1 + m_2 (c_p)_2 (\Delta t_r)_2 + \dots + m_{50} (c_p)_{50} (\Delta t_r)_{50}]}{\phi A_a [(G_1 + G_2 + \dots + G_{50})]} \quad (\Delta T_n = 6s) \\
&= \frac{\sum_{n=1}^{50} m_n (c_p)_n (\Delta t_r)_n}{A_a \sum_{n=1}^{50} G_n} \tag{4.5}
\end{aligned}$$

In this study, the receiver inlet and outlet temperatures in equation 4.5 were measured using the TC probes described in appendix A.3.2 and shown in figure A.15. The mass flow rate was determined by multiplying the volumetric flow rate of the working fluid (300 L/h) by its density. Both density and specific heat were calculated for each time step using the average measured receiver temperature. The aperture area was constant at 7.5 m<sup>2</sup>. Although the value of the time step disappears from equation 4.5, it is not irrelevant in the calculation. By setting the time step too large, stabilising the system becomes difficult and compromises the accuracy of the results. Too small a time step does not meaningfully improve the quality of the efficiency results beyond a certain point and complicates data processing by generating too much unnecessary information.

Dudley et al. (1995) used a time step of 20 s for the IST tests conducted at Sandia. The fluid residence time in the receiver was approximately 15 s giving a rate of 0.75 samples per receiver pass. In this study, the fluid residence time was 33 s giving a rate of 5.5 samples per receiver pass. This higher rate was considered necessary to accurately monitor the tracking performance of the PTSC and to ensure steady state operation. All sub-calculations in equation 4.5 were done in real-time during testing by the data acquisition software written for this project and checked for accuracy during processing of the data in Microsoft Excel. A sample calculation of efficiency is given in appendix E.

#### 4.2.2 Collector time constant test procedure

The collector time constant measures transient behaviour of the PTSC, or thermal inertia, and is obtained:

- a) by running the PTSC system in focused, steady-state mode and then abruptly withdrawing the incident solar energy (the cooling test), or
- b) by running the PTSC system in a defocused state and abruptly bringing it into focus (the heating test).

Dudley et al. (1995) and Kalogirou (1996) published results using both variations of the time constant test, even though ASHRAE 93 refers only to the cooling test in which solar energy is withdrawn. In both variations of the test the step change in energy input is normally achieved by de-focusing the collector for case (a) and by swiftly focusing it for case (b).

The time constant is determined by measuring the time taken for the time constant quotient (TCQ), a pre-defined system parameter based on temperature, to change by an amount of 0.632. For the cooling test, the receiver inlet and outlet temperatures are monitored as a function of time until:

$$\frac{t_{f,o,T} - t_{f,i}}{t_{f,o,initial} - t_{f,i}} < 0.30 \quad (4.6)$$

where  $t_{f,o,T}$  is the receiver outlet temperature [°C] at time T and  $t_{f,o,initial}$  is the outlet temperature [°C] at the start of the test, just prior to removal of the solar energy source. The actual time constant is the time T [s] required for the TCQ  $[(t_{f,o,T} - t_{f,i}) / (t_{f,o,initial} - t_{f,i})]$  to change from 1 to 0.368. For the heating test, the left hand side of equation 4.6 starts at zero and must be monitored until  $t_{f,o,T}$  stabilises at the steady state outlet temperature of the system. The time constant is then obtained from the time (T) taken for the TCQ to change from zero to 0.632. The time constant test must be performed at the same flow rate used for all the other ASHRAE tests, though for interest it was performed for a range of flow rates in this study from 75 L/h to 750 L/h, including the formal test flow rate of 300 L/h.

### 4.2.3 Incidence angle modifier test procedure

The incidence angle modifier,  $K_{\alpha\tau}$ , enables the performance of the collector to be predicted for solar angles of incidence other than  $0^\circ$ . This is important in commercial systems that operate throughout the year and experience a reduction in performance during winter when the sun is lower in the sky.

Incidence angle modifier tests are run essentially the same way as normal thermal efficiency tests, with PTSC performance measured for a receiver inlet temperature near the ambient air temperature. Data are processed as before using equation 4.5, however each test is conducted at a set value of  $\theta_i$  and  $K_{\alpha\tau}$  is then calculated using equation 4.7.

$$\begin{aligned}
 K_{\alpha\tau} &= \frac{\eta_g}{(A_a/A_g)F_R [(\tau\alpha)_c \rho\gamma]_n} & (4.7) \\
 &= \frac{\eta_g}{F_R [(\tau\alpha)_c \rho\gamma]_n} & (\text{for } A_a = A_g) \\
 &= \frac{\eta_g}{F_R \eta_o}
 \end{aligned}$$

ASHRAE 93 recommends that the value of  $\theta_i$  be increased from zero to a maximum of  $60^\circ$  for the incidence angle modifier tests and that a total of four data points be generated with one each at  $0^\circ$ ,  $30^\circ$ ,  $45^\circ$  and  $60^\circ$ . A curve-fitting exercise can be applied to the resulting graph to yield an equation for  $K_{\alpha\tau}$  in terms of  $\theta_i$ . Kalogirou (1996) presents  $K_{\alpha\tau}$  as a polynomial in  $(\theta_i)^3$  while Dudley et al. (1995) use a mixed equation in  $(\cos(\theta_i))$  and  $(\theta_i)^2$ .

The denominator in equation 4.7 is a constant and is equal to the y-intercept of the thermal efficiency curve obtained from equation 4.1 for the PTSC at normal or near-normal angles of incidence. The incidence angle modifier is thus a dimensionless measure of the performance of a solar collector at a set value of  $\theta_i$  compared with its optimum performance at normal or near-normal incidence. The determination of  $K_{\alpha\tau}$  takes place after thermal efficiency tests have been completed.

Because of the need to fix  $\theta_i$  during testing, determining  $K_{at}$  normally requires that the collector be capable of two-axis tracking. In two-axis tracking systems the PTSC is mounted on a movable test rack (altazimuth collector mount) so that its horizontal axis can be rotated for azimuth control and the collector can track the sun about two axes, thereby maintaining any desired  $\theta_i$  accurately and continuously. Alternatively the tilt of the collector should be adjustable. Being able to set and maintain a desired value of  $\theta_i$  enables the PTSC operator to complete the ASHRAE incidence angle modifier tests within one or two days.

Owing to the size of the PTSC, costs, the scope of the project and weight restrictions on the roof of the test facility, a two-axis tracking capability could not be provided in this study. Instead, the PTSC test programme was extended and the natural seasonal change in  $\theta_i$  was used to generate a curve of  $K_{at}$ . The disadvantage was having to wait for the seasonal change in  $\theta_i$  to take effect. Careful scheduling was required to avoid excessive handling of the fragile glass-shielded receiver. Instead of repeatedly swapping receivers, tests with the glass-shielded HCE were completed first and the unshielded unit was then reinstalled to complete all outstanding tests by the end of July 2004. This prolonged testing but reduced the risk of destroying the glass shield midway through the test programme.

#### 4.2.4 Collector acceptance angle test procedure

The collector acceptance angle defines the sensitivity of the collector to tracking misalignment. The collector is positioned ahead of the sun and its performance continuously measured as the sun moves into and out of focus. By monitoring thermal efficiency as a function of tracking angle ( $\rho_T$ ), the maximum allowable focal misalignment of the collector can be obtained. This is useful for determining the accuracy required of the tracking system.

To start the test, the PTSC is rotated to a position between  $7.5^\circ$  and  $10^\circ$  west of the sun and the tracking system is disengaged. Fluid flow rate is set at the normal test value, receiver inlet temperature is maintained as close as possible to ambient temperature and the thermal efficiency is recorded normally, though the standard suggests measurements be taken once per minute during the time when the sun is within 5 min of the plane of focus of the collector. In this study, measurements were taken at 6-second intervals and each efficiency point was based on 10 such intervals, giving a continuous series of 1-minute rolling average efficiency

values. This was to damp out minor spikes in the instantaneous efficiency values, caused by small variations in temperature and irradiance point-measurements.

After the sun has traversed through the PTSC's focal position, thermal efficiency values are divided by the peak efficiency recorded at zero angle of incidence, as measured in a plane perpendicular to the receiver (the plane in which tracking angle is measured). This yields a form of incidence angle modifier or efficiency factor between zero and 1, which is a function of  $\rho_T$ , not  $\theta_i$ . ASHRAE 93 defines the collector acceptance angle as the range of incident angles in which the modifier varies by no more than  $\pm 2\%$  from the normal incident value.

### 4.3 PTSC Test Schedule

#### 4.3.1 Planned schedule

The test programme was scheduled to run from the end of December 2003 to the end of February 2004, with only the incidence angle modifier tests continuing beyond February to June. Without the capacity to set and maintain a zero angle of incidence, the timetable for thermal efficiency tests had to be planned to accommodate daily and seasonal changes in incidence angle. The main objective was to schedule all tests in an appropriate order to fulfill the ASHRAE 93 requirements regarding minimum threshold beam irradiance ( $790 \text{ W/m}^2$ ) and incidence angle. It was also necessary to meet the requirements regarding wind and ambient temperature. From the monitoring exercise done at the solar energy test facility since February 2003, some idea of the expected rainfall, temperature and wind patterns had been obtained (Brooks, 2005). Nevertheless general weather conditions were less predictable than threshold irradiance levels and disruptions to testing caused by cloudy and windy conditions were plentiful and had to be tolerated.

To assist with scheduling, the PSA Algorithm was used to generate a graph of the daily change in  $\theta_i$  for a range of dates from 22 December 2003 to the winter solstice on 21 June 2004 (the expected PTSC test period). This was transformed into a 6-month solar map of the test facility using a solar irradiance profile developed by Brooks (2005) to describe the morning time at which normal beam irradiance first exceeds  $790 \text{ W/m}^2$ . This map, shown in figure 4.1, gave each day's expected "test window" during which the angle of incidence was

determined and the normal beam irradiance conformed to the ASHRAE minimum threshold value.

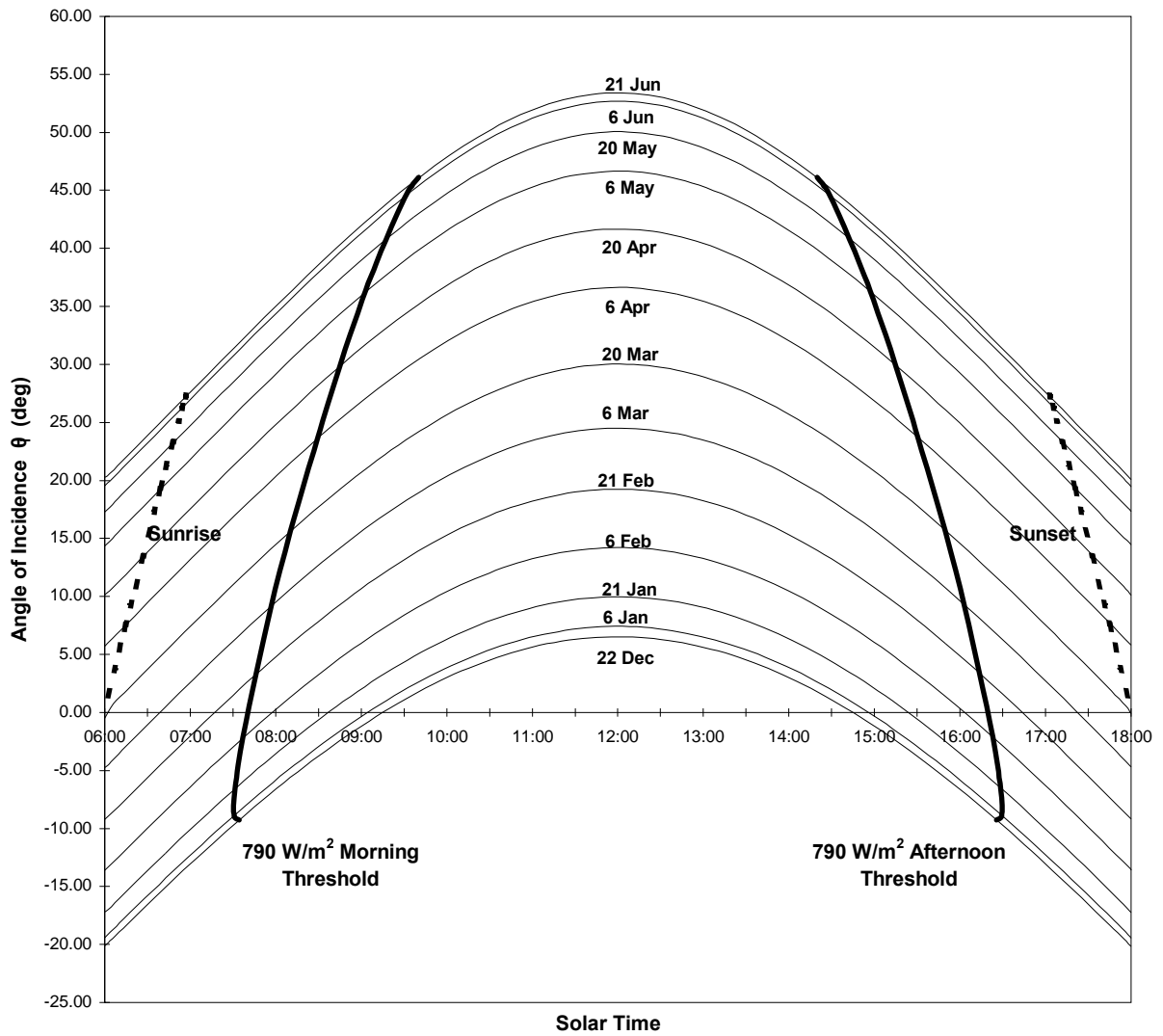


**Figure 4.1** Solar map for Mangosuthu Technikon Solar Energy Test Facility with morning and afternoon threshold irradiance times

To finish the test programme by the end of July, the final test point for the incidence angle modifier for the unshielded receiver had to be obtained at an incidence angle of 37° (according to figure 4.1), not the recommended 30°. This was not problematic since the resulting curve for  $K_{at}$  (a fitted regression polynomial) would be negligibly affected by

shifting one data point by 7°. The planned test schedule for both receivers is shown in table 4.1.

**Table 4.1** Planned PTSC test schedule

Date	Unshielded receiver				Glass-shielded receiver			
	Thermal efficiency	Time const.	Accept. angle	Inc. angle mod.	Thermal efficiency	Time const.	Accept. angle	Inc. angle mod.
22 Dec 2003 to 15 Jan 2004	X	X	X	$\theta_i \approx 0^\circ$				
16 Jan 2004	Change from unshielded receiver to glass-shielded receiver.							
17 Jan 2004 to 31 Jan 2004					X	X	X	$\theta_i \approx 0^\circ$
20 Mar 2004								$\theta_i \approx 30^\circ$
6 May 2004								$\theta_i \approx 45^\circ$
6 June 2004								$\theta_i \approx 50^\circ$
7 June 2004	Change from glass-shielded receiver to unshielded receiver.							
8 June 2004				$\theta_i \approx 50^\circ$ and $45^\circ$ )				
31 July 2004				$\theta_i \approx 38^\circ$				

#### 4.3.2 Completed test schedule

Deviations from the schedule shown in table 4.1 were caused by periods of poor weather during January and February 2004. This led to numerous delays in completing the thermal efficiency tests for the unshielded receiver. It was particularly difficult to obtain results symmetrically before and after noon because of deteriorating afternoon weather conditions typical of the summer weather pattern in Kwazulu-Natal. Although a full set of 20 tests was completed for the shielded receiver, the morning/afternoon requirement was dropped for the shielded receiver so that the test programme could be completed before  $\theta_i$  became too large. As a result, only 10 tests were conducted for the unshielded HCE, though these spanned the full receiver inlet temperature range. In addition, weather delays meant some of the tests for the shielded HCE had to be conducted at  $\theta_i$  values as high as 15°. On average, the angle of incidence for the unshielded receiver efficiency tests was 7.09° while for the glass-shielded

efficiency tests it rose to  $11.42^\circ$  (see chapter 5). Table 4.2 gives the actual completed test schedule, while figure 4.2 shows all eight series of ASHRAE 93 tests, as they occurred, superimposed on the solar map from figure 4.1.

**Table 4.2** Schedule of completed PTSC tests

Date	Unshielded receiver				Glass-shielded receiver			
	Thermal efficiency	Time const.	Accept. angle	Inc. angle mod.	Thermal efficiency	Time const.	Accept. angle	Inc. angle mod.
Marker symbol for figure 5.2	$\triangle$	*	$\blacklozenge$	x	$\bigcirc$	+	$\bullet$	$\square$
22 Dec 2003 to 2 Feb 2004	X	X	X	$\theta_i \approx 0^\circ$				
10 Feb 2004	Change from unshielded receiver to glass-shielded receiver.							
11 Feb 2004 to 19 Feb 2004					X	X	X	$\theta_i \approx 0^\circ$
28 Mar to 21 Apr 2004								$\theta_i \approx 30^\circ$
19 Apr to 1 May 2004								$\theta_i \approx 45^\circ$
22 May to 9 Jun 2004								$\theta_i \approx 50^\circ$
11 Jun 2004	Change from glass-shielded receiver to unshielded receiver.							
11 Jun to 12 Jul 2004				$\theta_i \approx 50^\circ$ and $45^\circ$				
29 July 2004				$\theta_i \approx 37^\circ$				

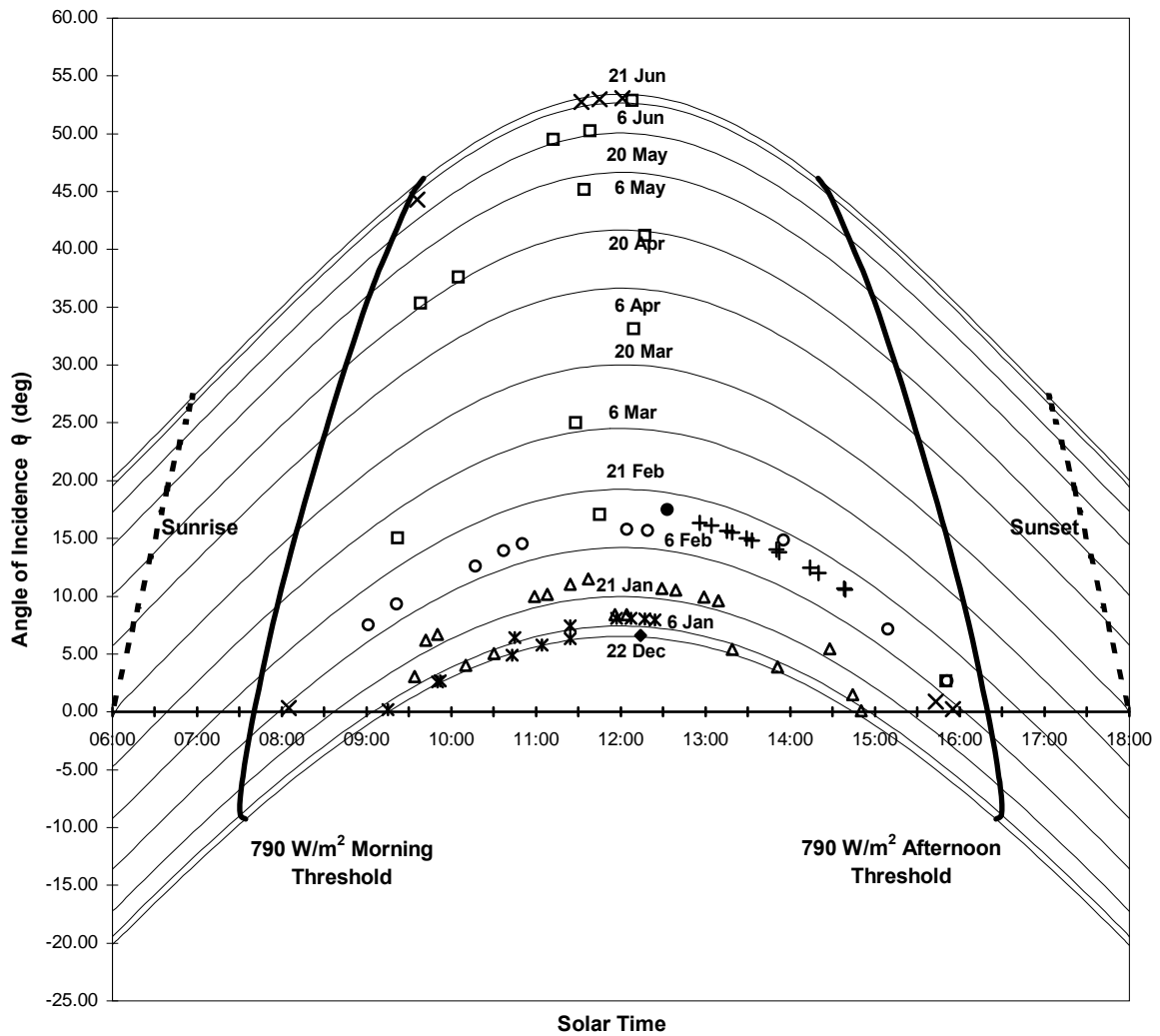


**Figure 4.2** Solar map indicating completed ASHRAE 93 tests

Set up tests were also conducted to ensure the PTSC system functioned as expected. These included:

- Tests of fluid system flow rates versus pressure to verify pump performance
- Tank heating and cooling tests to determine the time taken to raise water in the HT tank to its maximum temperature, as well as the rate at which heat was lost (this was to help plan the high-temperature tests)
- Thermal loss tests to determine the heat transfer characteristics of the glass-shielded and unshielded receivers
- DTCS tests to determine tracking performance

## 4.4 Development of Data Logging Software Applications

Three software applications were developed for data monitoring and acquisition. These were created using National Instruments LabVIEW 7.0 Express and made it possible to:

- Plan daily PTSC tests by verifying the sun's position and monitoring the change in crucial solar angles (in real-time) using SolarStation,
- Operate the PTSC system, monitor its behaviour and stabilise it properly before starting a formal test (using SCATTAscan), and
- Acquire and log PTSC test data during formal ASHRAE 93 tests using SCATTALog.

### 4.4.1 SolarStation

SolarStation provided the PTSC operator located in the test facility control room with a real-time stream of values for the solar azimuth angle  $A$ , the zenith angle  $\theta_z$  and the PTSC angle of incidence  $\theta_i$ . This allowed quick decisions to be made as to whether PTSC tests should be run or not. The application provided date and time information (both SAST and solar time), the sun's declination angle and the PTSC's required tracking angle  $\rho_T$  (the tracking angle was for information only – the data acquisition PC was not connected to the trough's DTCS). The application was intended to float on top of other Microsoft Windows applications running on the control room PCs and the graphical user interface (GUI), or front panel, was sized to make it unobtrusive. A screen-captured image of the front panel is shown in figure 4.3.

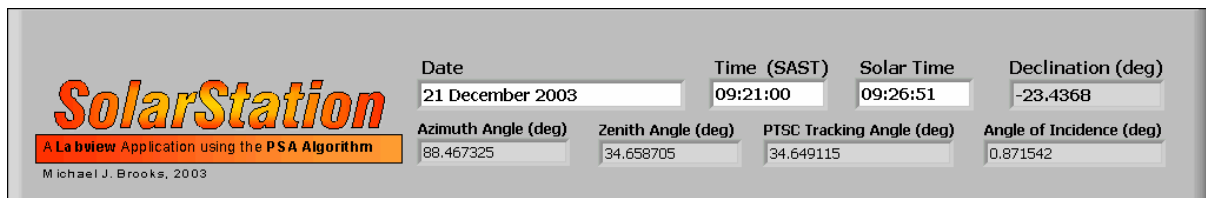


**Figure 4.3** Front panel GUI of LabVIEW application SolarStation

At the core of SolarStation is a sub-VI (virtual instrument) implementing the PSA Algorithm. This accesses the PC clock-time at 1-second intervals to generate updates of the variables.

During execution, the PSA sub-VI calls a further seven sub-VIs, each implementing stages of the algorithm. Figure 4.4 (a) shows the main block diagram of SolarStation. The PSA sub-VI is visible at the top left of the block with its output consisting of time and date information (top centre) and a cluster containing the internal variables from the PSA Algorithm (for example mean longitude, mean anomaly and ecliptic longitude). The variable cluster is wired to display only those variables from the PSA Algorithm that appear on the front panel shown in figure 4.3. Figure 4.4 (b) shows the sub-VI building blocks in the structural hierarchy of the application.

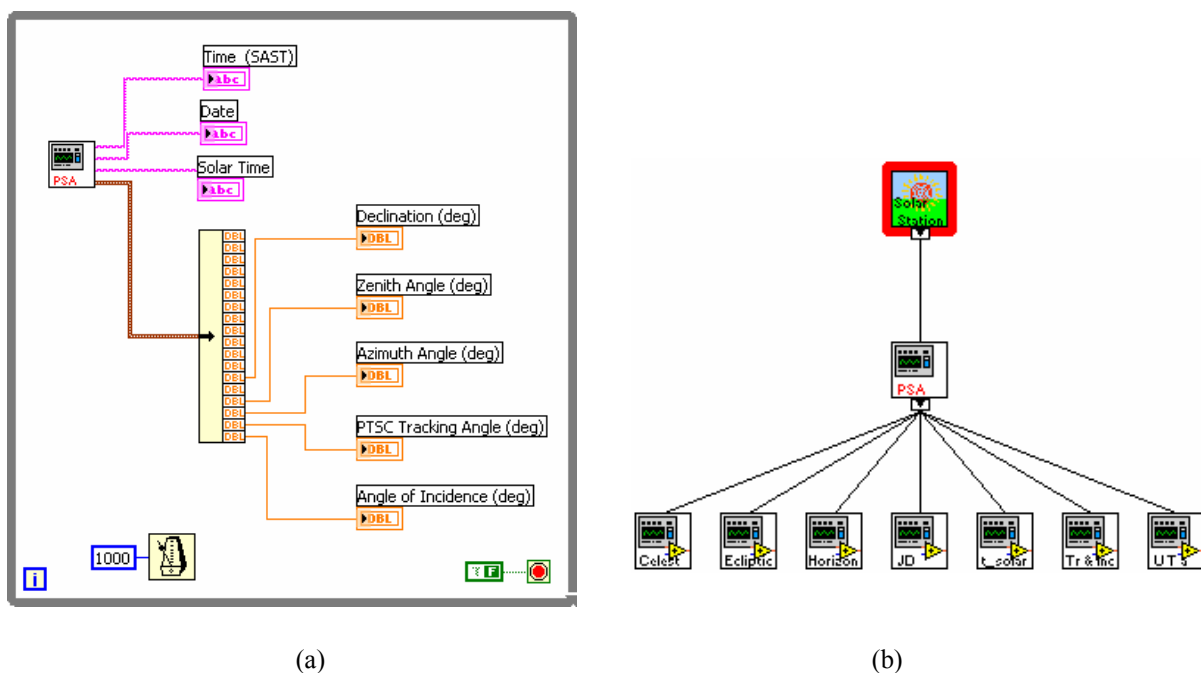


**Figure 4.4** Schematic diagrams of (a) main block diagram and (b) structural hierarchy of LabVIEW application SolarStation

Each of the sub-VIs shown below the PSA sub-VI in figure 4.4 (b) consists of a block diagram similar to that in figure 4.4 (a). These are not shown, although the SolarStation application is included on the computer disc submitted with this study.

#### 4.4.2 SCATTAScan and SCATTALog

The LabVIEW scanning and logging applications used to monitor PTSC performance were almost identical, except for additions in SCATTALog to write the data to file. A description of the logging application is given here.

The main purpose of SCATTALog was to sample and log temperature and irradiance data during PTSC testing. The programme's functionality was extended to include processing of data and to generate real-time thermal efficiency values. This was to help the operator stabilise the system during testing. A range of information and trough performance variables was provided for, including:

- PSA solar position data, updated once per second
- ASHRAE 93 thermal efficiency (as given by equation 4.4)
- Instantaneous thermal efficiency
- Collector time constant quotient (as given by equation 4.5)
- Temperature output from TC probes
- Irradiance values from the pyranometer and pyrliometer
- Receiver fluid temperature, density, viscosity, specific heat and thermal conductivity
- Theoretical Reynolds, Prandtl and Nusselt numbers, fluid mass flow rate, friction factor and convective heat transfer coefficient

In SCATTALog the above information is presented numerically. Three sets of axes are also positioned on the front panel to provide a real-time graphing function of the behaviour of the ASHRAE 93 thermal efficiency (equation 4.5), the instantaneous thermal efficiency and the collector time constant (equation 4.6). The programme requires the user to enter the fluid volumetric flow rate and the sampling interval in seconds. The thermophysical properties of the working fluid (water) are based on its average temperature through the receiver and calculated from equations given by Kröger (1998).

On start-up the application requests a filename under which to save the logged data. This allows data to be catalogued and facilitates processing. The programme opens a tab-delimited file and writes data to it each time values are sampled at the user-defined interval (6 s for most

of the tests conducted). On completion of the test the files can be opened in Microsoft Excel for data processing. Each batch of values written to file during the PTSC test is date- and time-stamped with the local clock time and solar time. Figure 4.5 shows the front panel of SCATTALog. An extract from a logged data file is given in appendix D.

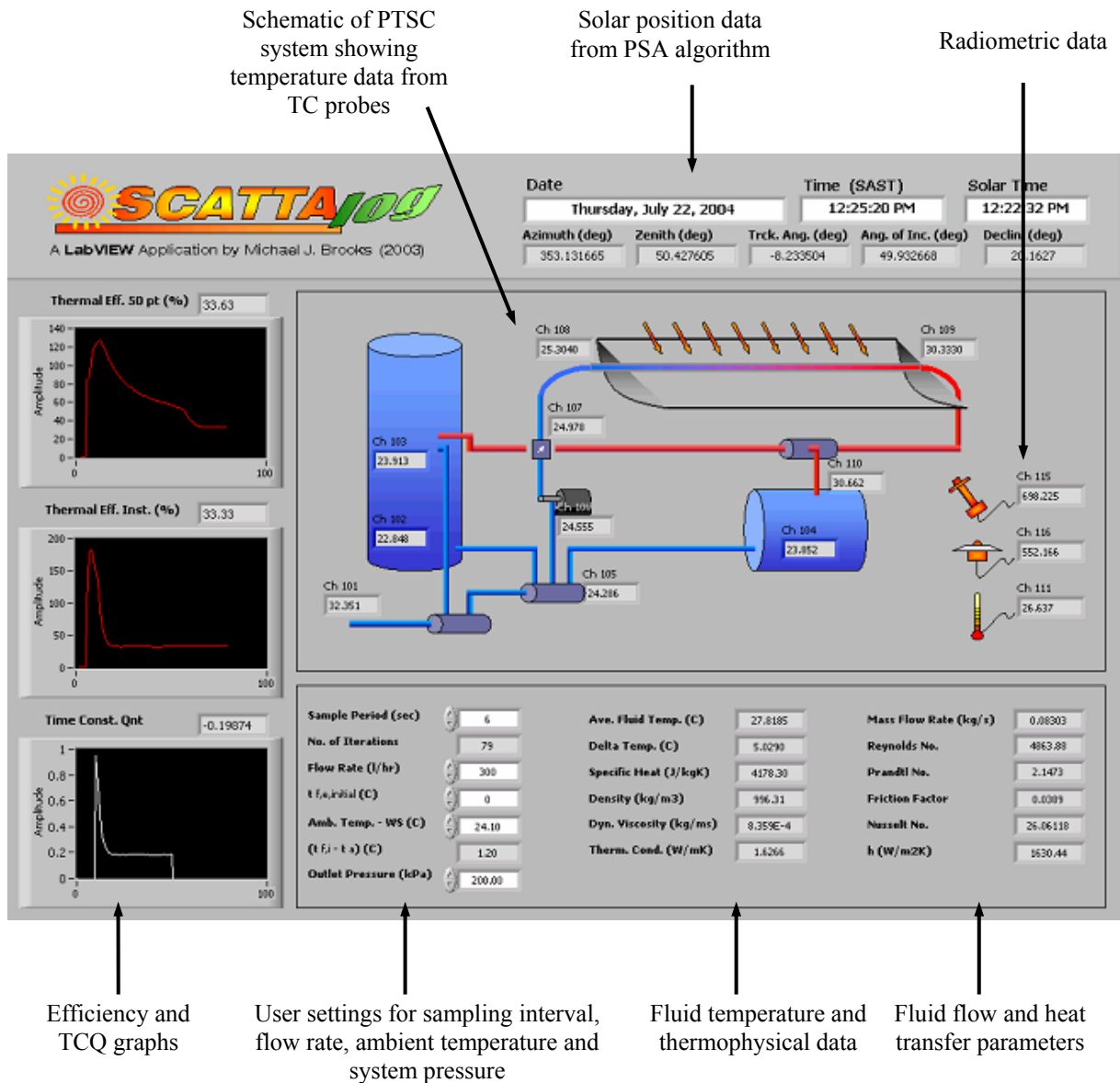


**Figure 4.5** Front panel GUI of LabVIEW application SCATTALog

The development of SCATTALog was an ongoing project and was successful in facilitating the logging and processing of test data. Two faults were discovered in the application during

the course of the project – the first was a minor error in the calculation of the difference between the receiver fluid inlet temperature and ambient temperature ( $\Delta t$ ). This was manually corrected during processing of the data in Microsoft Excel. The second fault occurred in a later update of the software and was caused by an error in the processing sequence of certain internal variables. In all cases the errors were manually corrected. The unprocessed temperature and radiometric data were unaffected by the problem, as were the PSA solar position data. The extract from a SCATTALog data file shown in appendix D is from an early version of the software and contains no errors. Copies of SCATTALog and SCATTAscan are included on the computer disc submitted as part of this study.

#### 4.5 Summary

Conducting the PTSC test programme was difficult at times because of the weather conditions that forced the postponement of numerous tests and caused several violations of ASHRAE 93 test conditions (see chapter 5). This was unavoidable and compromises had to be made to finish testing. Despite delays, the programme proceeded well and generated a significant amount of performance data. Approximately 120 individual tests were run from December 2003 to July 2004 representing 130 hours of testing time and generating 25 megabytes of unprocessed information. This produced over 30 000 lines of processed spreadsheet data. Coordinating and executing the test programme was helped by the following:

- Access to a well-equipped, dedicated and secure solar energy test facility
- Results from the radiometric and meteorological monitoring programmes conducted during 2003
- The implementation of the ASHRAE 93 testing standard
- Comprehensive instrumenting of the PTSC system
- The development of flexible data acquisition software for conducting tests and logging data

## 5. EXPERIMENTAL RESULTS

### 5.1 Introduction

Performance results are presented from the PTSC test programme described in chapter 4 and cover both receivers. These were generated from two types of tests:

- Tracking tests to verify performance of the DTCS
- PTSC performance tests as described by the ASHRAE 93-1986 (RA 91) standard (including receiver heat loss)

### 5.2 Tracking Performance

Results of the DTCS performance are discussed in detail by Naidoo (2005) and are restricted here to a brief summary.

#### 5.2.1 Fixed rate tracking

Early tests to measure PTSC efficiency under fixed rate tracking conditions, showed the DTCS could not maintain focus without fine, manual adjustments being made. With the PLC programmed to jog the VSD at 5.6 rev/min for exactly 4 s every 69.2 s (see appendix A), the PTSC would lag behind the sun, as shown in figure 5.1, which gives tracking performance in terms of an instantaneous efficiency factor:

$$\text{Efficiency factor} = \frac{\eta_{\text{inst},T}}{\eta_{\text{inst},\text{MAX}}} \quad (5.1)$$

$\eta_{\text{inst},T}$  is the instantaneous thermal efficiency of the collector at time T and  $\eta_{\text{inst},\text{MAX}}$  is the maximum measured instantaneous efficiency from the test. Equation 5.1 is helpful in comparing tracking performance from different tests as it eliminates variations that arise from tests being performed at different receiver inlet temperatures. Instantaneous efficiency is the point efficiency of the collector, determined using equation 4.3, not equation 4.5. See appendix E for a sample calculation. To obtain the results shown in figure 5.1, the collector

was positioned slightly ahead of the sun and Mode 2 tracking was engaged using the above VSD on-time settings.

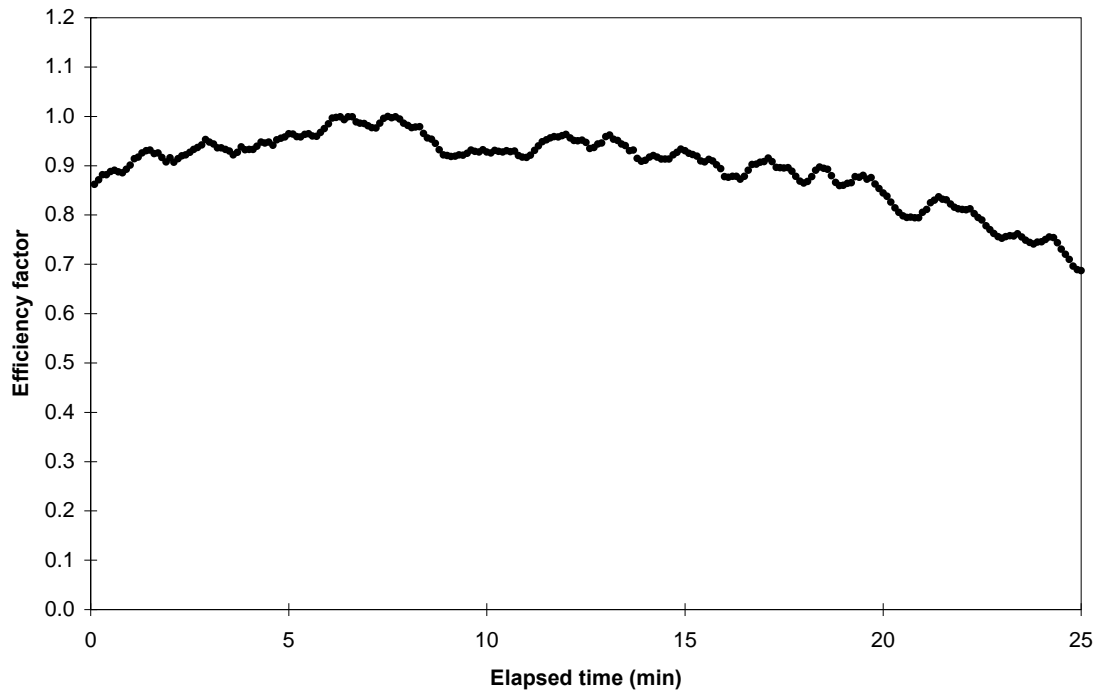


**Figure 5.1** PTSC performance for fixed rate tracking (Mode 2) based on VSD on-time

The increase and subsequent decrease in performance was due to the collector entering and leaving focus, as the frequency and duration of jog pulses were incapable of keeping pace with the sun. The lag was the result of a time delay in the VSD caused by the ramping up of the speed from zero to the set value of 5.6 rev/min as well as shorter timing delays in the switchgear. To improve tracking performance, the VSD on-time was manipulated until a value was found that enabled the PTSC to maintain the sun in focus. To prevent the maximum tracking error of  $0.2^\circ$  being exceeded, the time interval between jog periods was reduced to 32 s and a VSD on-time of 2.4 s employed. Combined with fine, manual adjustment of the collector based on a visual assessment of the receiver light pattern and close monitoring of the receiver outlet temperature, it was possible to maintain the trough in focus. This method of control was facilitated by the LabVIEW data acquisition system which provided real-time temperature data and the positioning of the PTSC control panel, which enabled the operator to observe the light focus pattern on the receiver, monitor the collector

performance on SCATTAscan and make fine adjustments to the fixed rate tracking system. Figure 5.2 illustrates the improvement in tracking performance with this method.

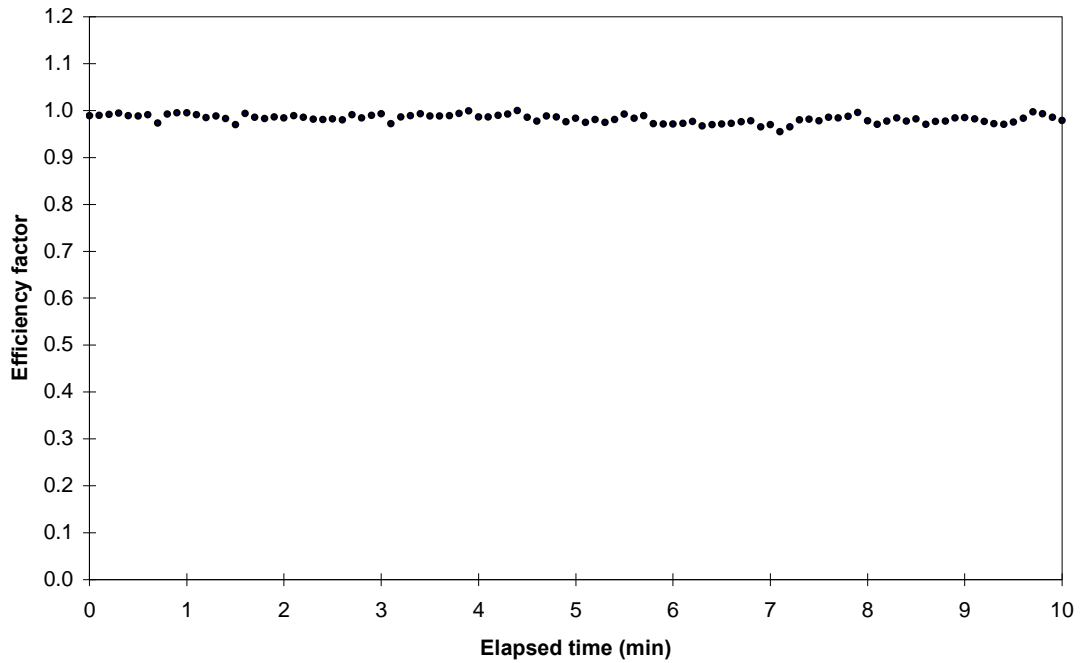


**Figure 5.2** PTSC performance for combination of fixed rate tracking (Mode 2) and manual adjustment

The method of counting VSD on-time was changed to counting individual pulses from the rotary encoder instead. Tests showed that the PLC/VSD combination was able to start, turn and stop the collector accurately through a single pulse, or  $0.144^\circ$ , as indicated on the PLC (Naidoo, 2005). This enabled the fixed rate tracking method to be changed from counting VSD on-time to counting 1 pulse on the encoder at a fixed time interval of 34.56 s, giving the required angular velocity of  $0.25^\circ/\text{min}$ .

Figure 5.3 shows the performance of the collector for fixed pulse tracking. The successful operation of the tracking system is visible in the consistent performance of the collector, as measured by the efficiency factor.

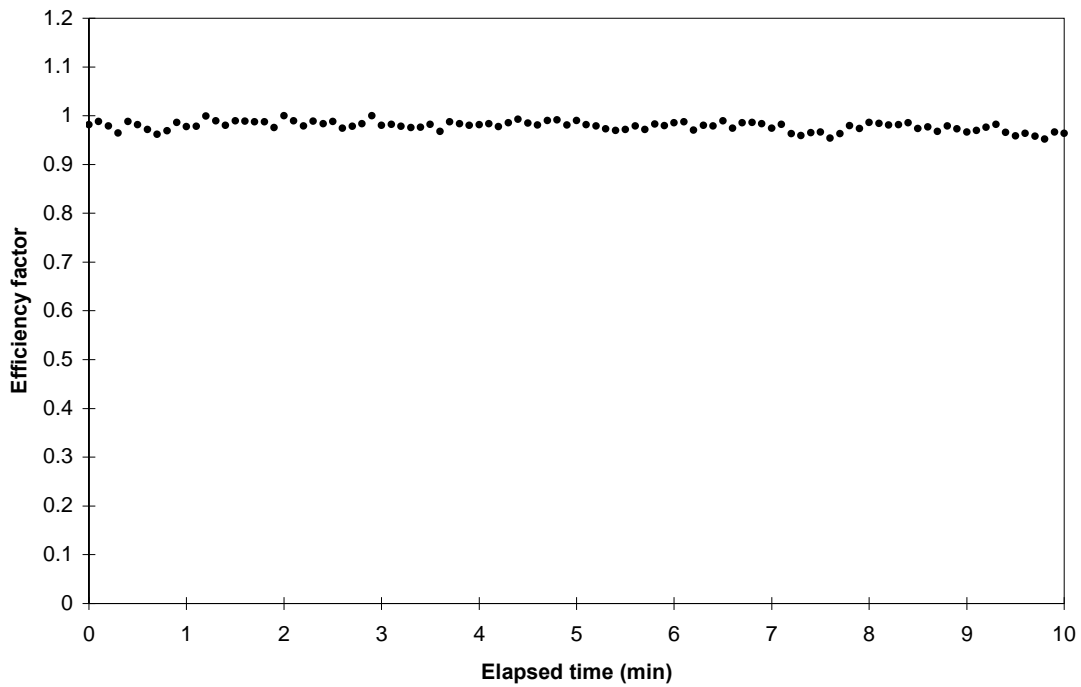


**Figure 5.3** PTSC performance for fixed pulse tracking (Mode 2)

### 5.2.2 PSA Algorithm-based tracking

PSA Algorithm-based tracking (Mode 3) became operational by mid-February 2004, seven weeks into the PTSC test programme. Under Mode 3 control, the DTCS was able to rotate the trough to locate the position of the sun and keep it focused using continuous positioning updates via the PLC, VSD and drive system. These updates were triggered when the difference between the calculated angular position of the collector (output from the PSA Algorithm) and the actual position (read from the rotary encoder) exceeded 1 pulse on the encoder ( $0.144^\circ$ ). Thus Mode 3 tracking had a similar level of accuracy to Mode 2, but could also locate the sun and accurately follow it independently of weather conditions (cloud) and the PTSC operator.

Figure 5.4 shows Mode 3 tracking in operation, with the collector initially defocused and then brought into focus by the DTCS. During commissioning it was necessary to introduce a constant offset value of  $1^\circ$  to the PLC code to enable the collector to focus optimally. This was most likely due to the presence of inaccuracies in the physical orientation of the collector as well as receiver mislocation and reflector misalignment.

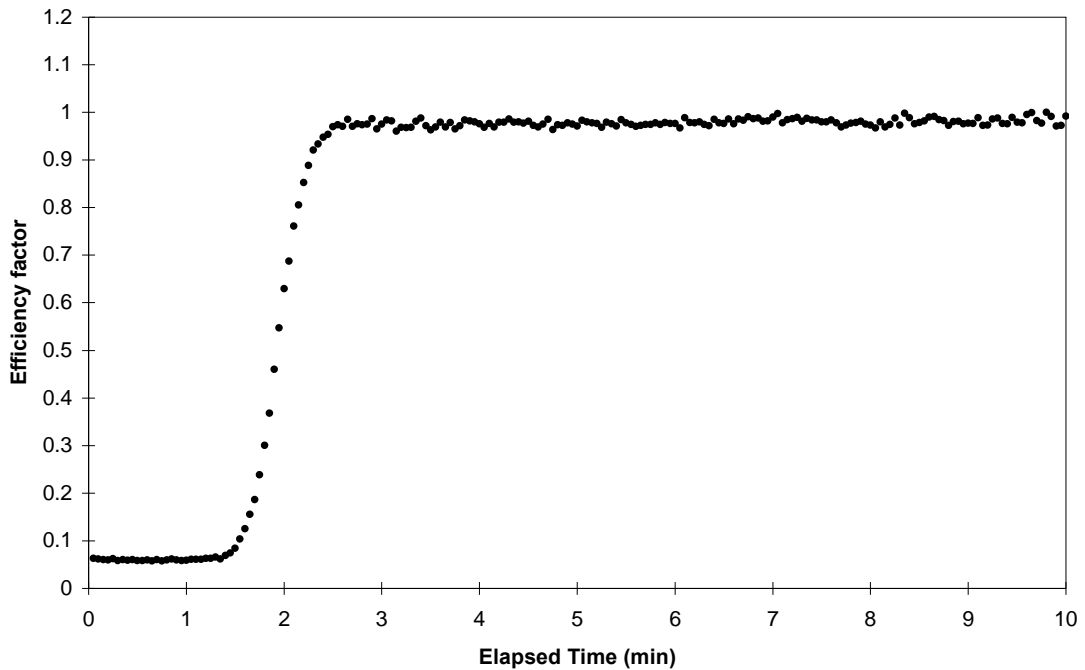


**Figure 5.4** PTSC performance for PSA Algorithm-based tracking (Mode 3)

The system worked correctly once the offset factor had been introduced. The offset had to be modified several months later once the unshielded receiver had been replaced by the glass-shielded unit. It is believed that the change of receivers, together with the increase in winter solar angles of incidence, led to a change in the way beam irradiance interacted with errors in the collector’s construction and set up, as compared with summertime conditions. Seasonal variability in tracking performance thus remained an area requiring further study.

Although some problems were experienced with the DTCS, the system worked progressively better as the test programme continued and initial problems were gradually eliminated. Showing excellent potential for expansion into a comprehensive tracking and control system, the DTCS remained under development on completion of this project.

### 5.3 PTSC Performance Results

Results are presented for the four ASHRAE 93 tests conducted to determine the performance characteristics of the PTSC.

### 5.3.1 Collector time constant

#### Unshielded receiver

Results from the collector time constant tests are shown graphically in figures 5.5 and 5.6. Table E.1 (appendix E) gives a full summary of the results, including meteorological, radiometric and fluid system data from the each test.

For the set of flow rates used, the time constant for the unshielded receiver ranged from 12.1 s to 97.1 s for the cooling tests and from 15.6 s to 98.0 s for the heating tests. At the formal test flow rate of 300 L/h the time constant was 30.5 s for the cooling test and 27.7 s for the heating test, giving an overall average of 29.1 s. In both cases (cooling and heating) the time constant was less than 300 s, which meant that all thermal efficiency tests had to be conducted over a 5-minute period (see 4.2.1). Figure 5.7 compares the heating and cooling results for the unshielded receiver. At higher flow rates the heating time constant was marginally greater although overall the values were similar.

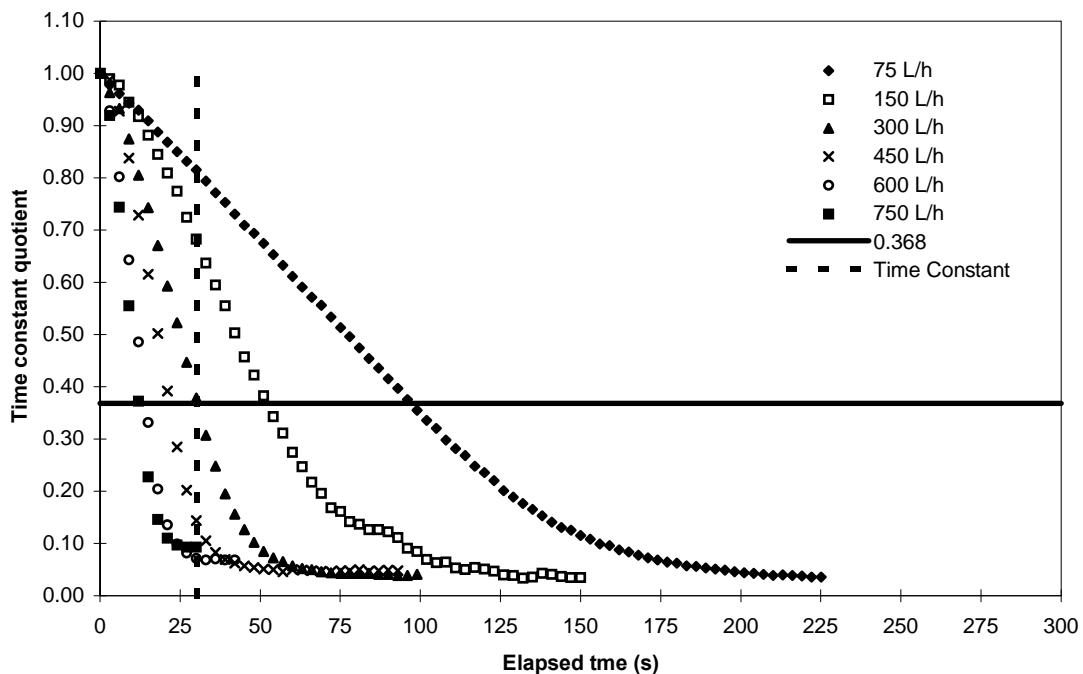


**Figure 5.5** Time constant quotient for unshielded receiver (cooling test)

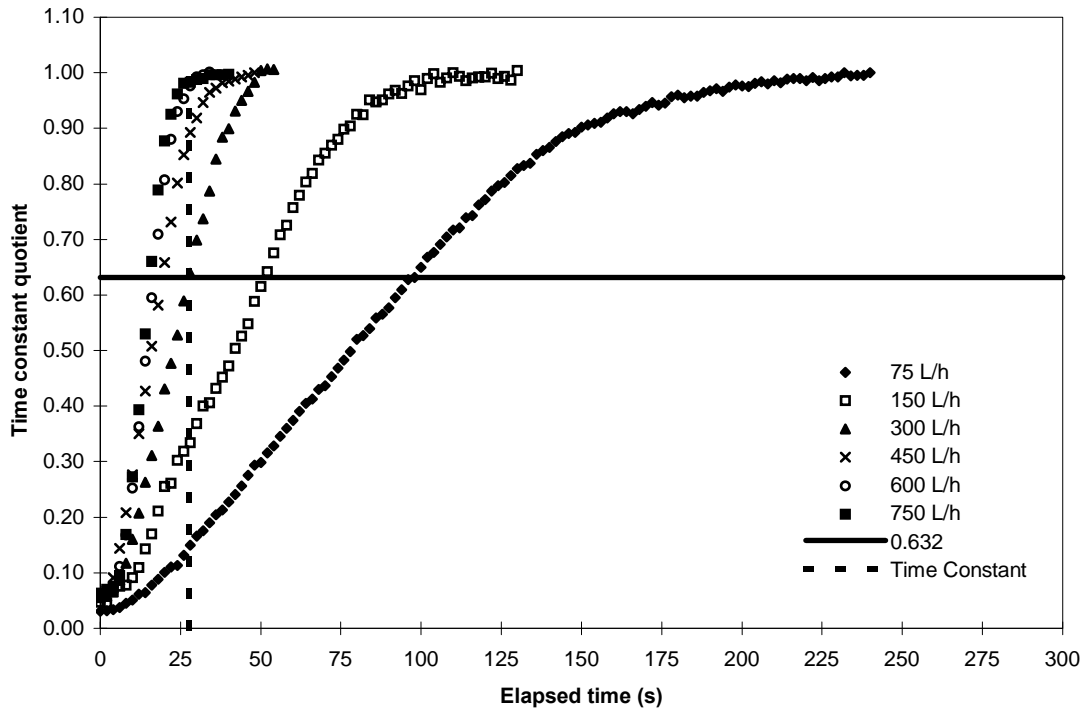


**Figure 5.6** Time constant quotient for unshielded receiver (heating test)

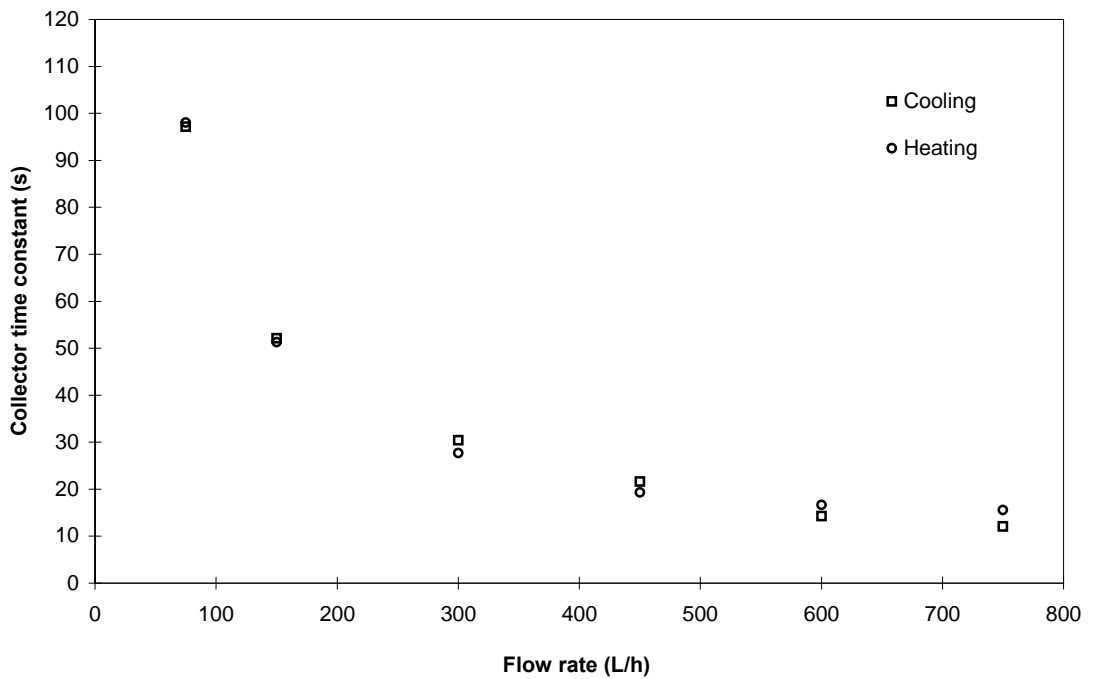


**Figure 5.7** Time constant for unshielded receiver (cooling and heating tests)

### Glass-shielded receiver

Results from time constant tests for the glass-shielded receiver are shown in figures 5.8 and 5.9. The time constant varied from 10.8 s to 108.7 s for the cooling tests and from 12.3 s to 103.2 s for the heating tests across the range of test flow rates (75 L/h to 750 L/h). At the chosen the test flow rate of 300 L/h the time constant was 28.6 s for the cooling test and 26.4 s for the heating test giving an average for both tests of 27.5 s. As with the unshielded receiver, the time constants at 300 L/h were both below 300 s, confirming the duration of thermal efficiency tests at 5 min.

Figure 5.10 provides a comparison between cooling and heating results. At the higher flow rates there was no significant difference between results, but at 75 L/h and 150 L/h the cooling time constants were 5.3 % and 10.8 % higher respectively than the heating values.

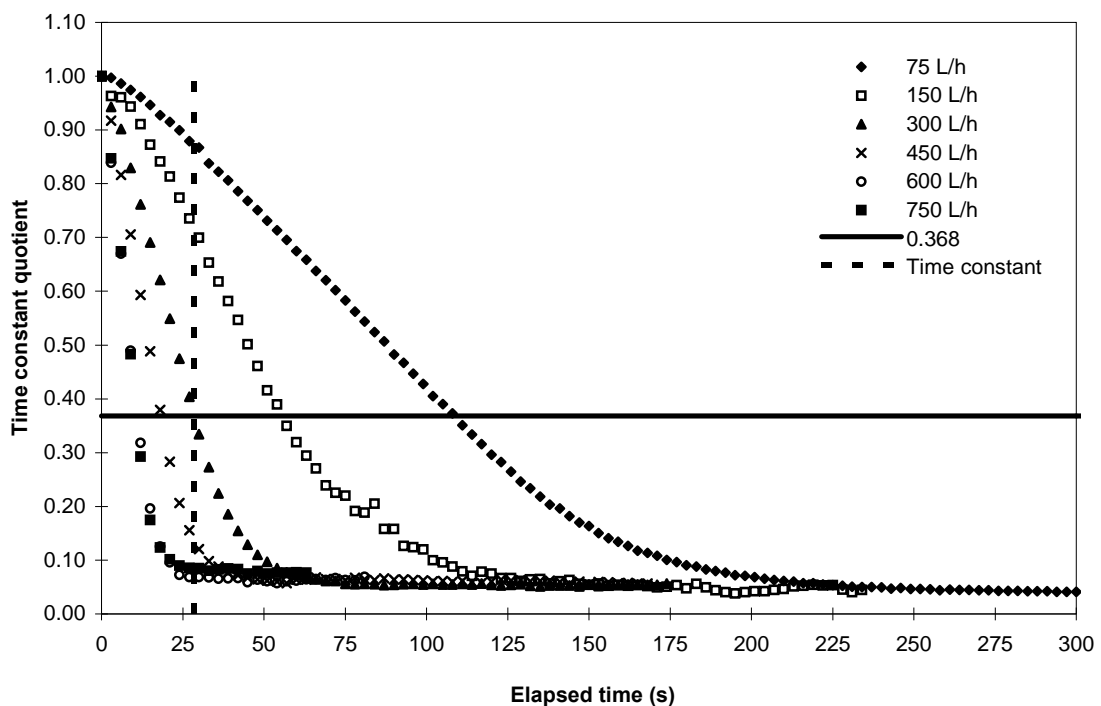


**Figure 5.8** Time constant quotient for glass-shielded receiver (cooling test)

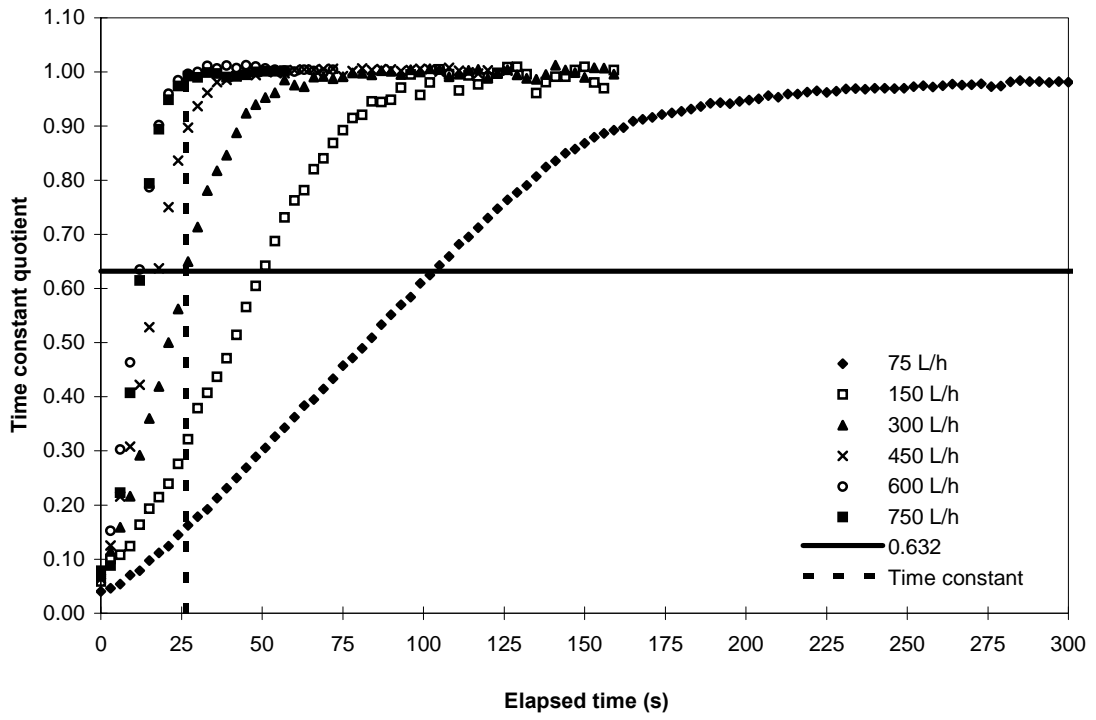


Figure 5.9 Time constant quotient for glass-shielded receiver (heating test)

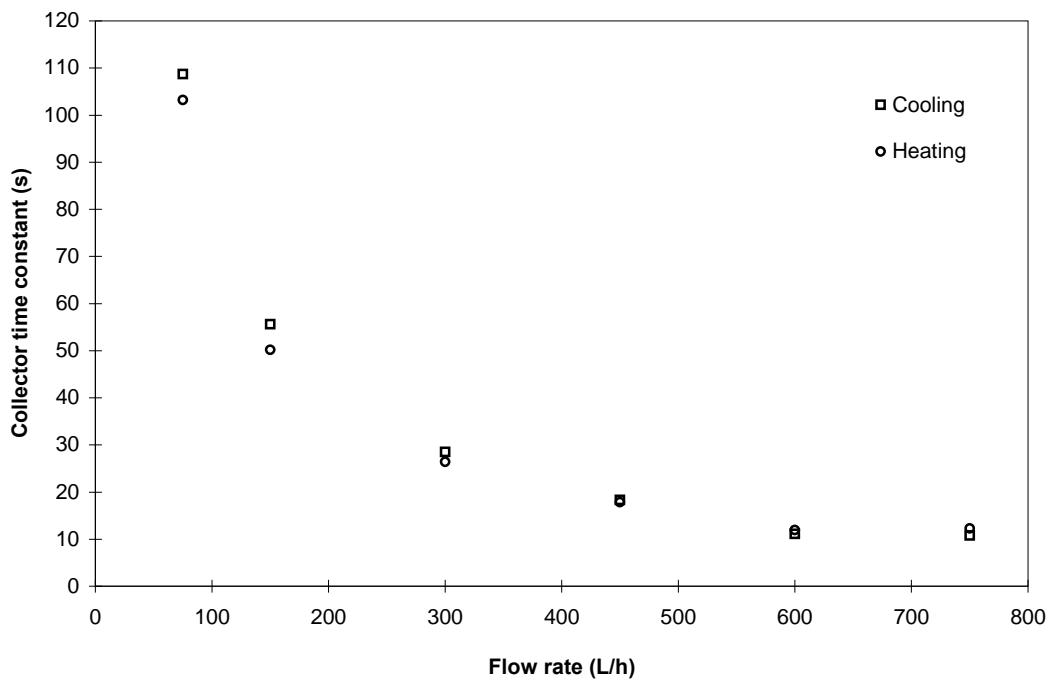
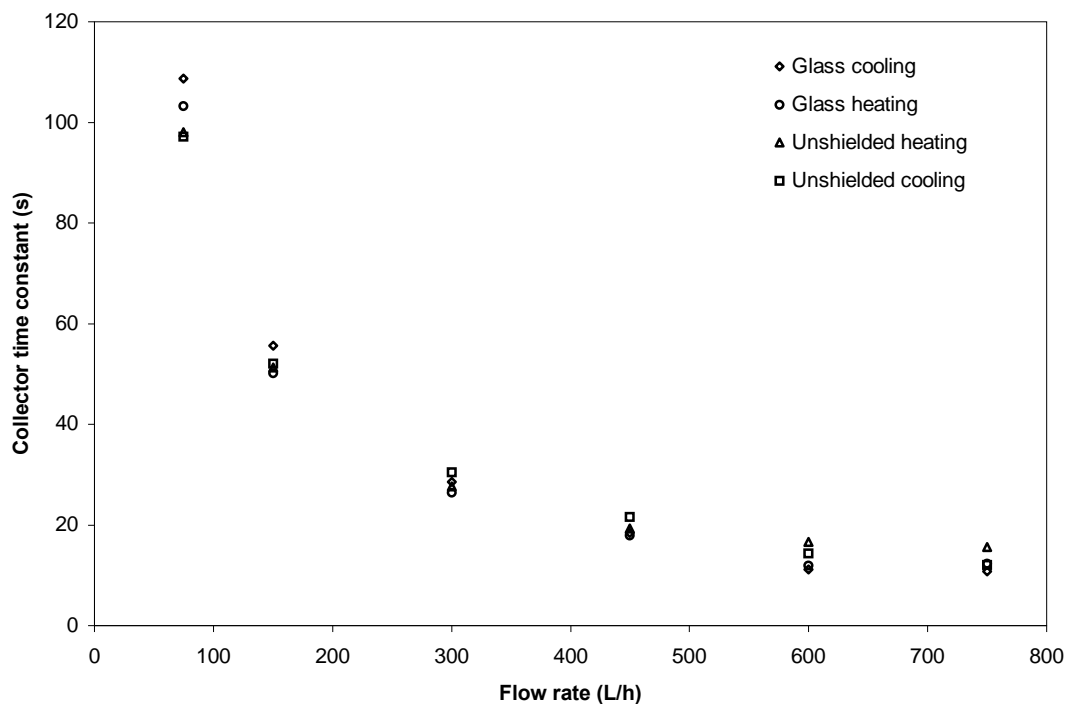


Figure 5.10 Time constant for glass-shielded receiver (cooling and heating tests)

## Comparison of results

Figure 5.11 compares the heating and cooling results for both HCE types. Results were similar with the only significant difference occurring at the lower flow rates of 75 L/h and 150 L/h, where the time constants for the glass-shielded receiver were noticeably higher.

At the lowest flow rate, the time constants for the shielded receiver were 108.7 s and 103.2 s respectively. During cooling at this flow rate, the time constant was 11.4 % higher than the average of the results for the unshielded receiver (97.6 s), while the time constant for the glass receiver under heating was 5.8 % higher. At maximum flow rate the highest time constant was measured for the unshielded receiver during heating.



**Figure 5.11** Comparison of time constants for glass-shielded and unshielded receivers

## ASHRAE 93 compliance

Meteorological, radiometric and fluid system variables were monitored to assess compliance with the ASHRAE 93 test conditions described in chapter 4. A summary of key variables is given in table 5.1. The data are given in detail in appendix E.

**Table 5.1** Key data from time constant tests

	$(t_{f,i} - t_a)$ (°C)	Max. $\Delta(t_{f,i})$ (°C)	Ave. $G_{DN}$ (W/m <sup>2</sup> )	Ave. $\theta_i$ (deg)	$t_a$ (°C)	Ave. wind vel. (m/s)
<b>Unshielded (cooling)</b>	3.08	0.05	869.08	3.75	24.72	5.1
<b>Unshielded (heating)</b>	2.36	0.09	907.79	7.67	26.03	4.7
<b>Glass-shielded (cooling)</b>	4.33	0.09	891.10	13.96	26.82	5.4
<b>Glass-shielded (heating)</b>	4.28	0.07	887.76	13.88	26.83	5.4
<b>AVERAGE</b>	3.51	0.08	888.93	9.82	26.1	5.2

On average, it was not possible to maintain the fluid receiver inlet temperature ( $t_{f,i}$ ) to within  $\pm 1$  °C of the ambient air temperature, which was an average of 3.5 °C lower than that of the fluid. For consistency, the ambient temperature was measured throughout the test programme using the test facility’s weather station and entered manually in the SCATTALog application during testing. Although no formal tests were conducted to compare the weather station temperature readings with those of a stand-alone thermometer, measurements taken near the trough suggested that the weather station tended to under-read temperature. This was probably due to its position on the edge of the rooftop test facility, where winds appeared stronger than at the trough collector position, providing a cooling effect to the instruments contained within the station’s sensor suite. To avoid introducing variations in the test procedure, no adjustments were made to the ambient temperature readings, nor was any adjustment made to account for the violation of ASHRAE requirements regarding  $\Delta t$ .

The variation in receiver fluid inlet temperature ( $t_{f,i}$ ) was well controlled, with the maximum variation restricted to an average of 0.08 °C, within the ASHRAE 93 limit of 0.1 °C ( $\pm 0.05$  °C of the chosen set-point). Although less important during time constant tests, the average normal beam irradiance was also monitored and remained above the minimum required value of 790 W/m<sup>2</sup> during the focused period of the tests. Ambient temperature remained below the ASHRAE 93 limit of 30 °C.

On average, wind velocity exceeded the prescribed limit of 4.5 m/s (8.7 knots). Care was taken to avoid running tests on excessively windy days and a test was abandoned if the velocity exceeded 6.7 m/s (13 knots).

As with ambient temperature, qualitative observations suggested that wind speeds were higher where the anemometer was located than near the PTSC receiver, though no portable equipment was available to confirm this at the time and, for consistency, no attempt was made to adjust the wind velocity during data logging to account for differences.

### 5.3.2 Collector acceptance angle

#### Unshielded receiver

Results from the collector acceptance angle test for the unshielded receiver are shown graphically in figure 5.12.

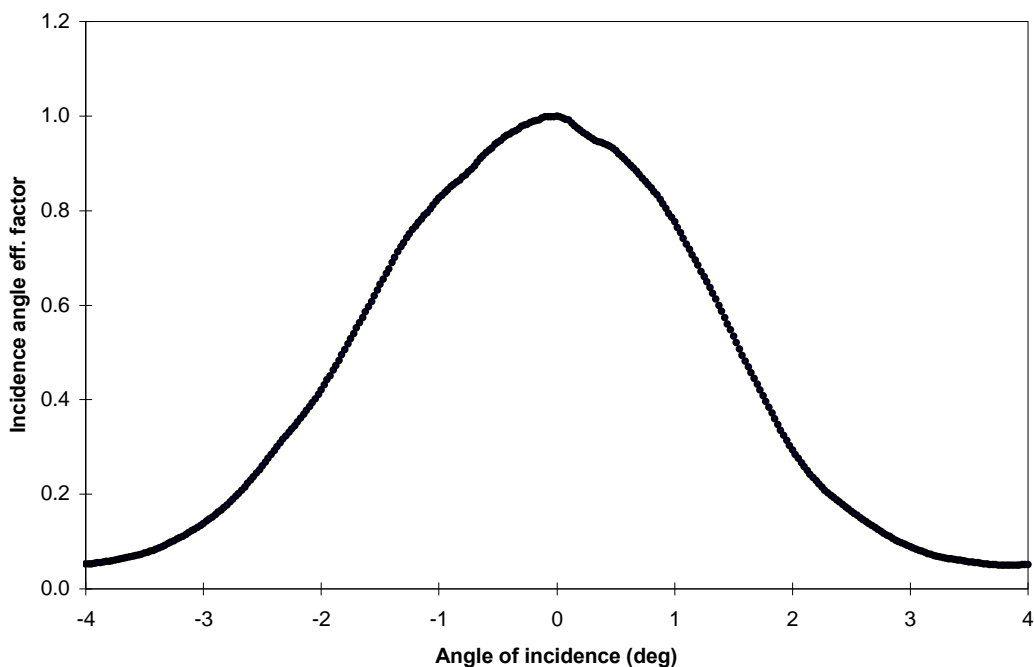


**Figure 5.12** Collector acceptance angle results for unshielded receiver

The efficiency factor is calculated in the same way as tracking efficiency factor, except that a 10-point average is used (see 4.2.4 and appendix E for a sample calculation). The values are plotted against angle of incidence, which is measured in a plane perpendicular to the receiver and represents the angle through which the collector must be turned to focus properly at any moment. For the unshielded receiver, the collector acceptance angle was  $0.43^\circ$ , this being the

angular interval in which thermal performance of the PTSC remained within 2 % of peak performance.

#### Glass-shielded receiver

The collector acceptance angle results for the glass-shielded receiver are shown in figure 5.13. For this configuration, the acceptance angle was measured at  $0.52^\circ$ .

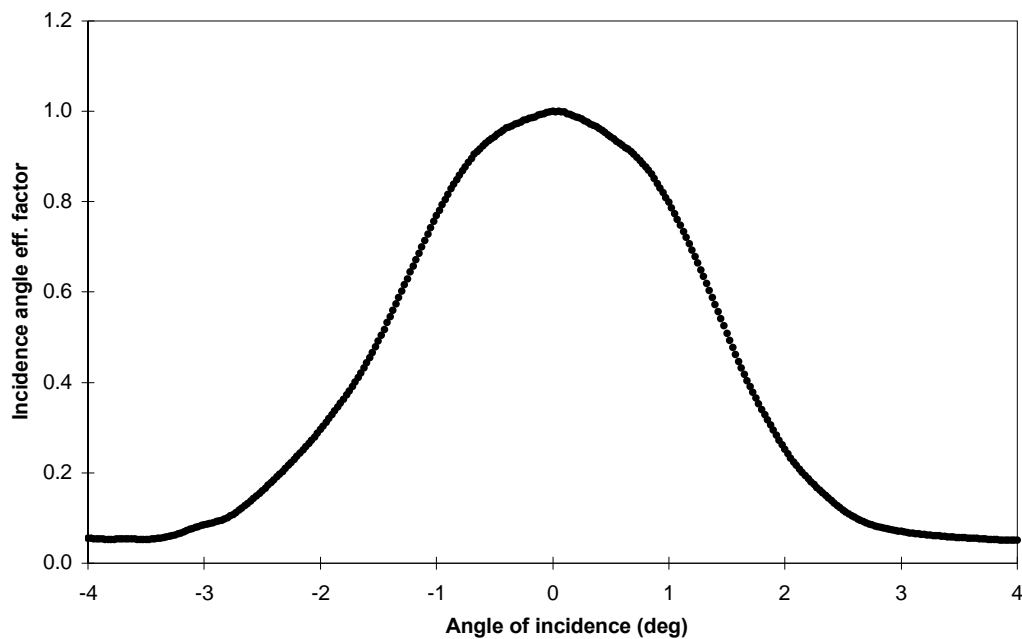


**Figure 5.13** Collector acceptance angle results for glass-shielded receiver

#### Comparison of results

In figure 5.14, data from both the collector acceptance angle tests (unshielded and glass-shielded) are shown on the same set of axes, which have been scaled to illustrate the 2 % band in which collector performance is permitted to fluctuate. Overall, the glass-shielded receiver was slightly more tolerant of being in an out-of-focus position than the unshielded receiver, though the results were similar.

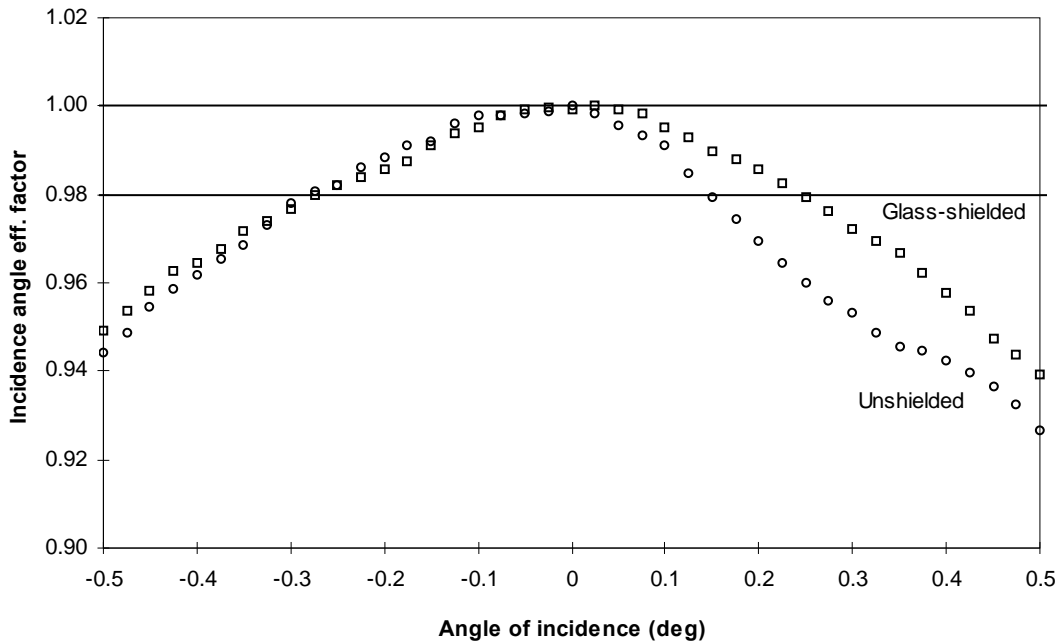


**Figure 5.14** Collector acceptance angle results for unshielded and glass-shielded receivers

ASHRAE 93 compliance

Table E.4 (appendix E) contains data used to determine compliance with ASHRAE 93 limits.

The test for the unshielded receiver took place on 28 December 2003 shortly after solar noon. Average wind velocity was within ASHRAE 93 limits at 4.1 m/s (8.0 knots), as were the normal beam irradiance average and variation as well as the variation in receiver fluid inlet temperature. The average angle of incidence was 6.62°. The only violation of the ASHRAE 93 limit occurred with regard to the difference between receiver inlet temperature and ambient air temperature,  $\Delta t$ . This was measured at an average of 2.62 °C for the test. The test standard prescribes an inlet temperature of  $t_a \pm 1$  °C.

For the glass-shielded receiver, violations of the ASHRAE 93 limit occurred with regard to average wind velocity (5.7 m/s or 11 knots),  $\Delta t$  (3.38 °C) and variation in receiver fluid inlet temperature (0.18 °C). These violations were not excessive. The average angle of incidence was 17.52°, which was somewhat higher than ideal. The need to conduct the collector acceptance angle test at solar noon precluded reducing the value of  $\theta_i$  since the test was performed during February, by which time  $\theta_i$  had increased appreciably from its mid-summer low.

### 5.3.3 Thermal efficiency

#### Unshielded receiver

Twenty tests were conducted to generate the thermal efficiency curve of the PTSC, which is shown in figure 5.15.

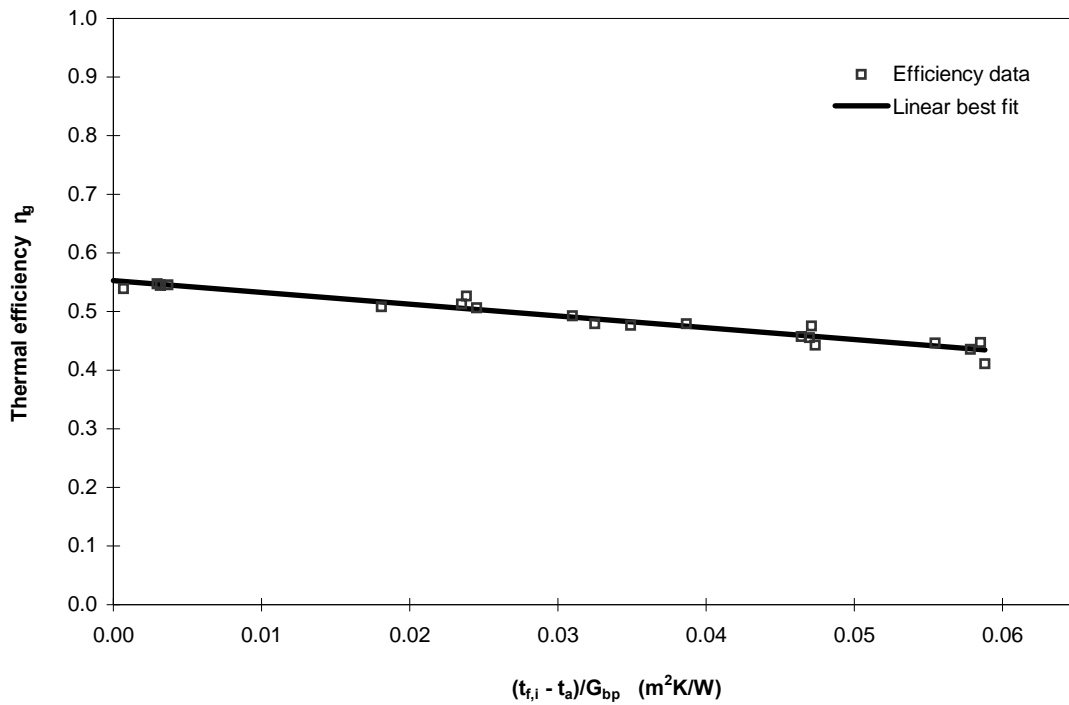


**Figure 5.15** Thermal efficiency with unshielded receiver

The best fit curve in figure 5.15 was obtained from a regression analysis using the method of least squares. This yielded equation 5.2, the thermal performance equation for the collector with the unshielded receiver.

$$\eta_g = -2.0099 \left( \frac{\Delta t}{G_{bp}} \right) + 0.5523 \quad (5.2)$$

The coefficient of determination ( $R^2$ ) for equation 5.2 was 0.934, indicating a good fit with the data. From equation 5.2,  $(A_r U_L F_R / A_a) = 2.0099$  W/m<sup>2</sup>K and  $F_R \eta_0 = 0.5523$ .

For a geometric concentration ratio ( $A_a/A_r$ ) of 16.70 the gradient of equation 5.2 gives  $U_L F_R = 33.57 \text{ W/m}^2\text{K}$ . The optical efficiency can be calculated from equation A.1, for which  $\eta_o = 0.601$  at near-normal angles of incidence. This results in a heat removal factor ( $F_R$ ) of 0.919. The heat removal factor represents the ratio of actual useful energy gain of the collector to the useful gain if the whole receiver were at the fluid inlet temperature. This in turn yields an overall heat loss coefficient ( $U_L$ ) of  $36.53 \text{ W/m}^2\text{K}$ .

### Glass-shielded receiver

Due to weather delays, the test programme for the glass-shielded HCE was shortened and 10 tests were conducted to determine the thermal efficiency curve, which is shown in figure 5.16.

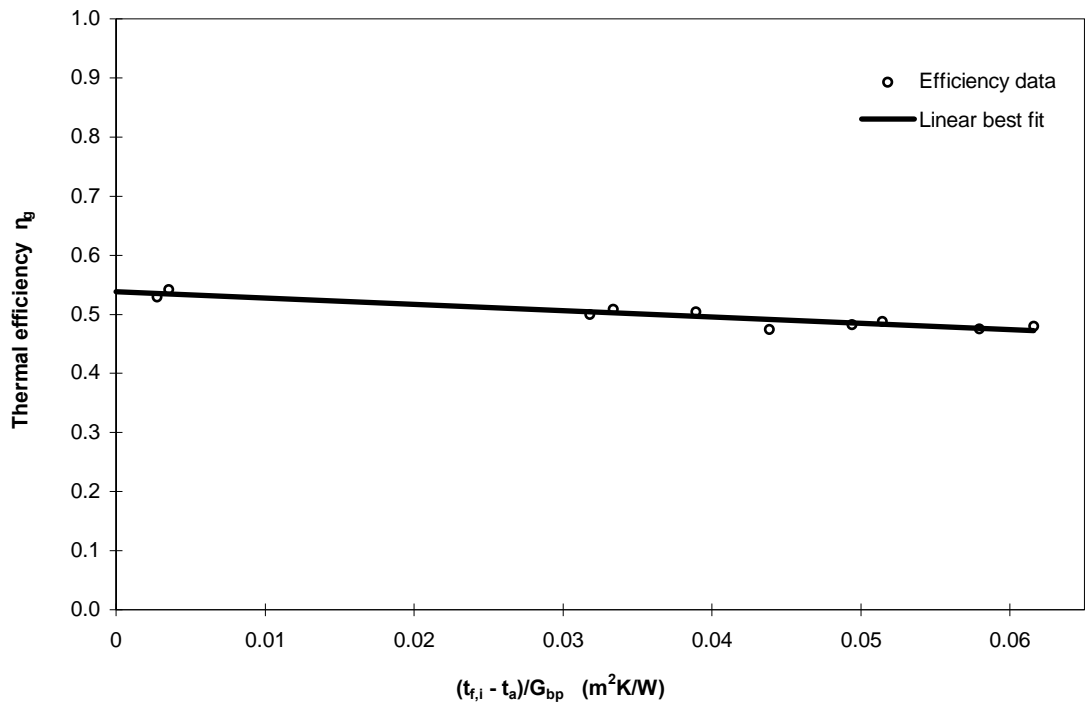


**Figure 5.16** Thermal efficiency with glass-shielded receiver

A regression analysis yielded the following performance equation for the collector with the glass-shielded receiver:

$$\eta_g = -1.0595 \left( \frac{\Delta t}{G_{bp}} \right) + 0.5381 \quad (5.3)$$

For equation 5.3,  $R^2$  was 0.922. From equation 5.3,  $(A_r U_L F_R / A_a) = 1.0595 \text{ W/m}^2\text{K}$  and  $F_R \eta_o = 0.5381$ . For a concentration ratio of 16.70, the gradient of equation 5.3 gives  $U_L F_R = 17.69 \text{ W/m}^2\text{K}$ . As with the unshielded receiver, the optical efficiency can be calculated from equation A.1. The presence of the glass shield reduces  $\eta_o$  from 0.601 to 0.553 at near-normal angles of incidence. This results in a heat removal factor ( $F_R$ ) for the shielded receiver of 0.973 and an overall heat loss coefficient ( $U_L$ ) of  $18.18 \text{ W/m}^2\text{K}$ .

### Comparison of results

Data from both sets of thermal efficiency tests are consolidated in figure 5.17. The point at which the performance curves cross corresponds to a thermal efficiency of 52.23 %, with  $(\Delta t / G_{bp}) = 0.0149 \text{ m}^2\text{K/W}$ . For a normal beam irradiance value of  $900 \text{ W/m}^2$  this equates to a fluid inlet temperature  $13.45 \text{ }^\circ\text{C}$  above ambient. For fluid temperatures greater than this, the glass-shielded receiver performs better than the unshielded unit.

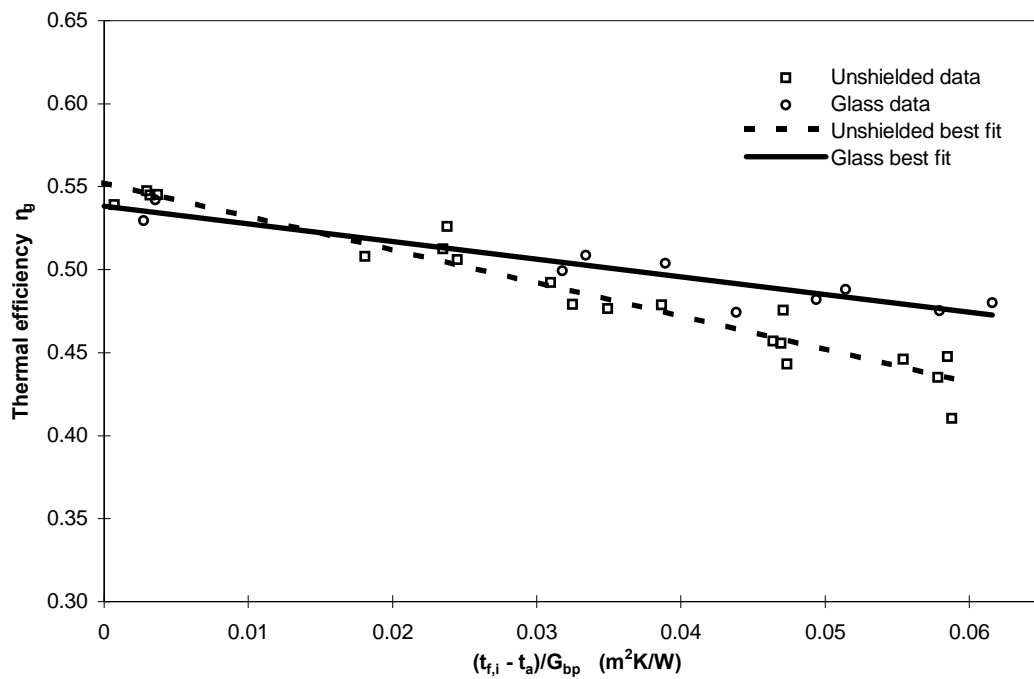


**Figure 5.17** Comparison of thermal efficiencies

### ASHRAE 93 compliance

Tables E.2 and E.3 give key data from all 20 thermal efficiency tests conducted for the PTSC with the unshielded receiver and the 10 tests conducted with the glass-shielded receiver. A summary of the data is given in table 5.2.

**Table 5.2** Key data from thermal efficiency tests

	$t_a$ (°C)	Ave. $G_{DN}$ (W/m <sup>2</sup> )	Max. $\Delta(G_{DN})$ (W/m <sup>2</sup> )	Max. $\Delta(t_{f,i})$ (°C)	Ave. $\theta_i$ (deg)	Max. $\Delta(\theta_i)$ (deg)	Ave. wind vel. (m/s)
<b>Unshielded AVERAGE</b>	27.12	937.17	11.51	0.52	7.08	0.20	4.8
<b>Glass-shielded AVERAGE</b>	27.27	861.58	10.11	0.52	10.11	0.26	4.6

At no time during the tests with the unshielded receiver did the ambient air temperature exceed the ASHRAE 93 limit of 30 °C, and the average test temperature was 27.12 °C. Likewise, the standard's requirement of normal beam irradiance greater than 790 W/m<sup>2</sup> was met in all tests, with an average for the batch of 937.17 W/m<sup>2</sup>. The average maximum variation in beam irradiance across all 20 tests was 11.51 W/m<sup>2</sup>, well within the prescribed limit of  $\pm 32$  W/m<sup>2</sup>, and no violations of this limit occurred in any of the tests. The calculated average angle of incidence was 7.08°, with a minimum value of 0.10° and a maximum of 11.53°. The maximum variation during any one test was 0.38°, with an average variation of 0.20°.

Violations of the ASHRAE 93 test limits occurred with respect to variation of  $t_{f,i}$  and measured wind speed. The average maximum variation in  $t_{f,i}$  was 0.52 °C, considerably higher than the limit of 0.1 °C ( $\pm 0.05$  °C). The ASHRAE 93 limit was exceeded in 15 of 20 tests and was more pronounced at higher fluid inlet temperatures, where accurate temperature control was more difficult.

Average wind velocity exceeded the ASHRAE 93 maximum limit of 4.5 m/s. Violations occurred in just over half the tests, although they were minor in magnitude and wind speed never exceeded 6.7 m/s (13.0 knots).

For the glass-shielded receiver, the average air temperature was 27.27 °C with no violations of the ASHRAE 93 upper limit. Average normal beam irradiance was lower than the unshielded tests at 861.58 W/m<sup>2</sup>, reflecting the expected seasonal reduction with the passing of summer. Variations in G<sub>DN</sub> were minimal and within limits.

As with the unshielded receiver tests, controlling  $t_{f,i}$  proved difficult and the variation of this parameter was 0.52 °C, identical to the unshielded tests. With the tests having been conducted later in the year, the average angle of incidence was 10.11°, with a minimum value of 2.71° and a maximum of 15.80°. The maximum, minimum and average wind speeds were 5.2 m/s (10.0 knots), 3.6 m/s (7.0 knots) and 4.6 m/s (8.9 knots) respectively.

#### 5.3.4 Incidence angle modifier

##### Unshielded receiver

Data for the unshielded receiver are presented graphically in figure 5.18 with a fitted curve obtained from regression analysis.

The data were obtained using equation 4.7 and the y-intercept of the linear curve fitted to the data in figure 5.15. This gave a value for  $F_R\eta_0$  of 0.5523, representing the peak performance of the PTSC at near-normal angles of incidence. Values of  $K_{\alpha\tau}$  at increased angles of incidence were obtained by dividing efficiency values into the peak value. A regression analysis provided the following equation for  $K_{\alpha\tau}$  as a function of  $\theta_i$ :

$$K_{\alpha\tau} = -2.032 \times 10^{-6} (\theta_i)^3 + 1.199 \times 10^{-4} (\theta_i)^2 - 3.940 \times 10^{-3} (\theta_i) + 1.005 \quad (5.4)$$

For this regression analysis,  $R^2 = 0.966$ , indicating a very good fit with the data.

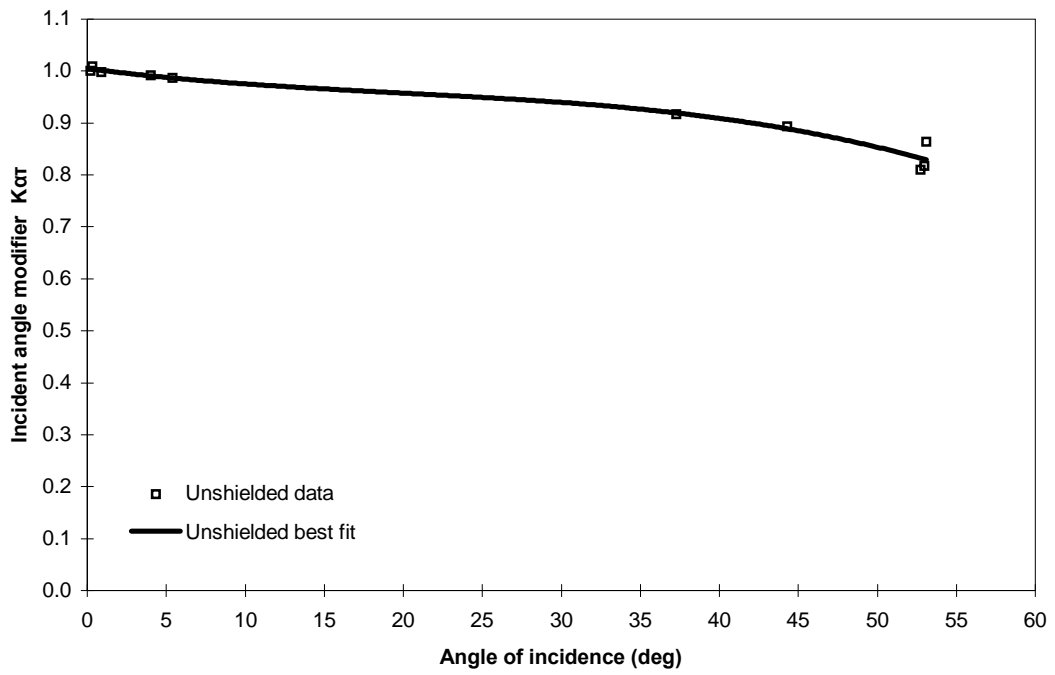


**Figure 5.18** Incidence angle modifier for unshielded receiver

Glass-shielded receiver

Figure 5.19 illustrates the performance of the PTSC with the glass-shielded HCE installed.

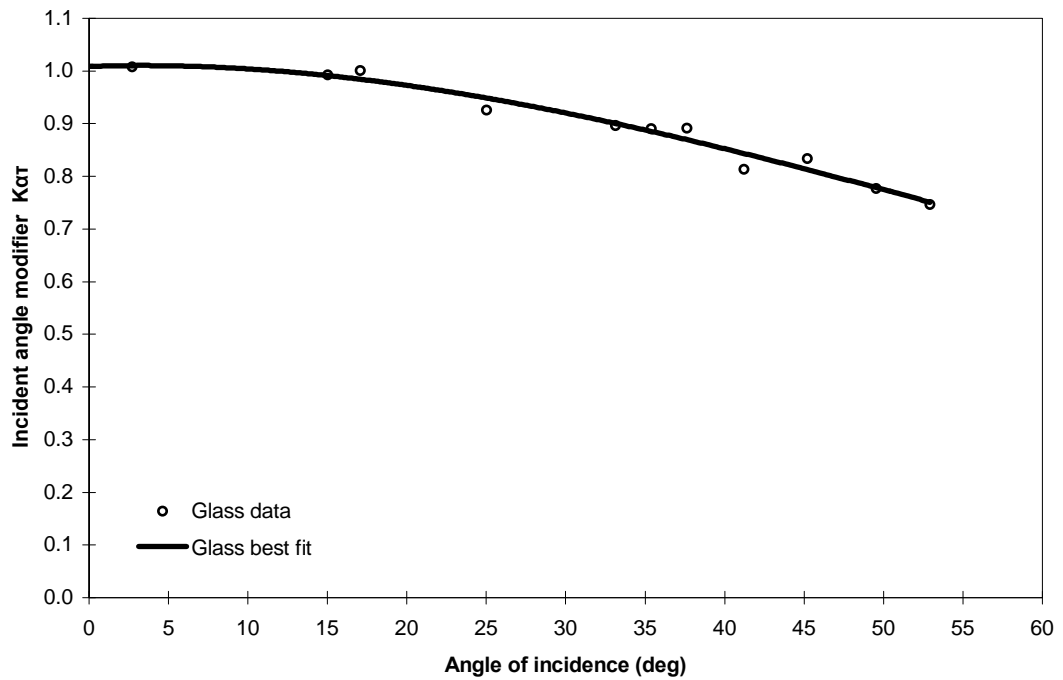


**Figure 5.19** Incidence angle modifier for glass-shielded receiver

Equation 5.5 was obtained for  $K_{\alpha\tau}$  by linear regression.

$$K_{\alpha\tau} = 9.360 \times 10^{-7} (\theta_i)^3 - 1.616 \times 10^{-4} (\theta_i)^2 + 1.061 \times 10^{-3} (\theta_i) + 1.009 \quad (5.5)$$

As for the unshielded receiver, the coefficient of determination confirmed a very good fit with the data ( $R^2 = 0.967$ ).

### Comparison of results

Figure 5.20 shows equations 5.4 and 5.5 plotted on the same axes. For interest, a cosine plot is included to illustrate the difference between the experimental equations and a much simpler model for the incidence angle modifier,  $K_{\alpha\tau}$ .

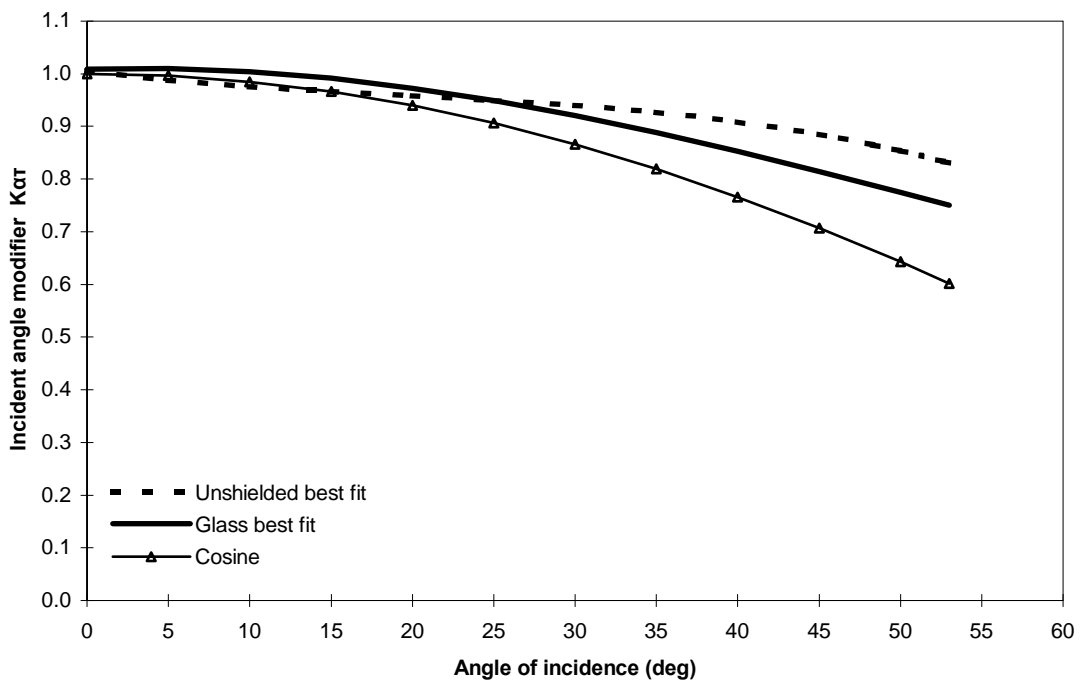


**Figure 5.20** Incidence angle modifier for unshielded and glass-shielded receivers

Up to an incidence angle of approximately  $25^\circ$  the glass-shielded receiver performed slightly better, but beyond that its performance declined more rapidly and was inferior to that of the unshielded receiver. From figure 5.20, the calculated value of  $K_{\alpha\tau}$  was 0.75 for the glass-shielded receiver at the maximum tested incidence angle of  $53^\circ$ . This was 9.6 % lower than

for the unshielded receiver, which had an incidence angle modifier of 0.83, as calculated from equation 5.4. At the same maximum angle of incidence, the simplified cosine model under-predicted  $K_{\text{gr}}$  by 27.5 % for the unshielded receiver and by 19.8 % for the glass-shielded unit.

### ASHRAE 93 compliance

Table 5.3 contains summarised data from both sets of incidence angle modifier tests. The source data are given in appendix E.

Ten thermal efficiency tests were used to determine the incidence angle modifier for the unshielded receiver. Violations of ASHRAE 93 prescribed limits occurred with respect to receiver fluid inlet temperature, both in absolute value above ambient air temperature and in variation. On average  $\Delta t$  was 3.02 °C. This was greater than the allowable variation of  $\pm 1$  °C above or below  $t_a$ . The average variation in  $t_{f,i}$  of 0.32 °C was also over the prescribed limit, which was exceeded in 7 out of 10 tests. Apart from this, normal beam irradiance levels were acceptable, as was their variation. Average wind speed was also within limits, though in three tests it exceeded the maximum limit of 4.5 m/s slightly and in four tests it was either borderline or lower than the minimum of 2.2 m/s. In two of the tests there were no wind data available due to a weather station failure.

Eleven tests were used to determine  $K_{\text{gr}}$  for the glass-shielded receiver. As can be seen from table 5.3 and tables E.5 and E.6, the extent of ASHRAE 93 compliance and transgression was similar. Average recorded wind speed was within limits, although in two tests it was measured at 6.2 m/s (12 knots) and in three tests it fell below the minimum level of 2.2 m/s. As with all testing, there was nothing that could be done to alter wind conditions other than abandon a test if the wind speed became unreasonably high. With little time to reschedule tests, minor violations of ASHRAE 93 with were disregarded.

**Table 5.3** Key data from incidence angle modifier tests

	$t_a$ (°C)	$(t_{f,i} - t_a)$ (°C)	Ave. $G_{\text{DN}}$ (W/m <sup>2</sup> )	Max. $\Delta(t_{f,i})$ (°C)	Max. $\Delta(G_{\text{DN}})$ (W/m <sup>2</sup> )	Max. $\Delta(\theta_i)$ (deg)	Ave. wind vel. (m/s)
<b>Unshielded AVERAGE</b>	23.32	3.02	826.67	0.32	14.38	0.30	3.2
<b>Glass-shielded AVERAGE</b>	26.34	2.90	859.37	0.30	13.18	0.20	3.8

#### 5.4 Receiver Thermal Loss Tests

The aim of these tests was to determine steady state heat loss as a function of operating temperature (Dudley et. al, 1995). Two tests were conducted, one each for the unshielded and glass-shielded receivers. Before each test the HT tank was filled and heated to its maximum temperature of approximately 85 °C. At sunset, the PTSC fluid circulation pump was started and the flow rate set at 300 L/h. Temperature data were then logged at regular intervals, specifically the temperature drop as the hot water passed through the receiver. The system was left to run overnight, during which the fluid was constantly recirculated through the PTSC, gradually cooling as heat was lost. By monitoring  $(t_{f,i} - t_{f,o})$  versus  $(t_{f,i} - t_a)$ , a measure of the thermal loss in Watts per square metre of receiver area was obtained, this being the “off-sun” loss  $Q_0$ . Off-sun loss differs from the “on-sun” loss experienced during daytime focusing of the PTSC. On-sun loss per unit receiver area,  $Q_+$ , is determined from the heat gain difference between the operating efficiency and the optical efficiency, and is equal to the product  $U_L F_R$ , as determined from the thermal efficiency curve, and the receiver fluid inlet temperature above ambient. Off-sun loss, which contributes to the total thermal loss under normal operating conditions, is lower than on-sun loss because during normal operation of the collector the sun’s energy causes the external surface of the receiver to heat up, increasing heat loss via the normal mechanisms of conduction, convection and radiation (Dudley et. al, 1995). Losses can be calculated from equations 5.6 and 5.7.

$$\text{Off – sun loss} = Q_0 = \frac{mc_p(t_{f,i} - t_{f,o})}{A_r} \quad [\text{W/m}^2] \quad (5.6)$$

$$\text{On – sun loss} = Q_+ = U_L F_R \Delta t_{\text{ave}} \quad [\text{W/m}^2] \quad (5.7)$$

In equation 5.7,  $\Delta t_{\text{ave}}$  represents the average receiver fluid temperature above ambient and  $U_L F_R$  is 33.57 W/m<sup>2</sup>K for the unshielded receiver and 17.69 W/m<sup>2</sup>K for the glass-shielded receiver. The on-sun loss is an approximation, since  $U_L F_R$  is obtained from the thermal efficiency curve which is determined using  $(t_{f,i} - t_a)$ , not  $\Delta t_{\text{ave}}$ . Since the actual temperature drop through the receiver for the loss tests ranged from zero at receiver temperatures close to ambient to less than 3 °C at maximum inlet temperature, the difference between  $(t_{f,i} - t_a)$  and  $\Delta t_{\text{ave}}$  was negligible.

By conducting thermal loss tests at night, all energy input to the collector was eliminated enabling true measurement of the off-sun loss (running thermal loss tests during the day with the PTSC defocused does not completely eliminate heat input to the receiver).

### Unshielded receiver

In figure 5.21, the average receiver fluid temperature  $((t_{f,i} + t_{f,o})/2)$ , the ambient air temperature ( $t_a$ ) and the fluid temperature drop across the receiver ( $t_{f,i} - t_{f,o}$ ) are shown over the duration of the nighttime loss test for the unshielded receiver. Since heat loss can be severely affected by wind conditions during testing, wind data for the night of the test were logged and are presented in figure 5.22.

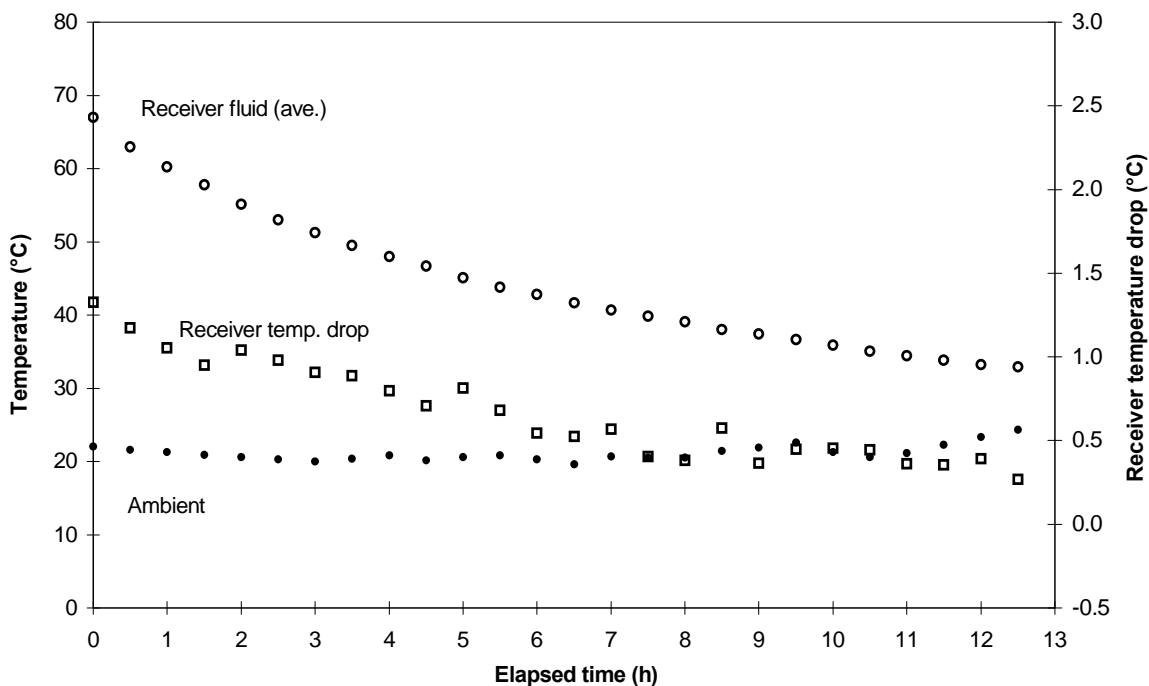


**Figure 5.21** Temperature data from thermal loss test for unshielded receiver

Figure 5.22 compares the measured off-sun thermal loss,  $Q_{0U}$ , and on-sun loss,  $Q_{+U}$ , for the unshielded receiver, as determined from figure 5.21 and equations 5.6 and 5.7. Following the approach of Dudley et. al (1995) and Stine and Harrigan (1985), the calculated data points for off-sun loss for the unshielded HCE were used to generate a third order polynomial curve describing thermal loss as a function of average receiver fluid temperature above ambient:

$$Q_{0U} = 0.0033 (\Delta t_{ave})^3 - 0.1935 (\Delta t_{ave})^2 + 23.2746 (\Delta t_{ave}) \quad [W/m^2] \quad (5.8)$$

For this equation,  $R^2 = 0.936$ . The average value of  $G_{bp}$  for the 20 thermal efficiency tests from which the on-sun curve was obtained, was  $928.23 \text{ W/m}^2$ .

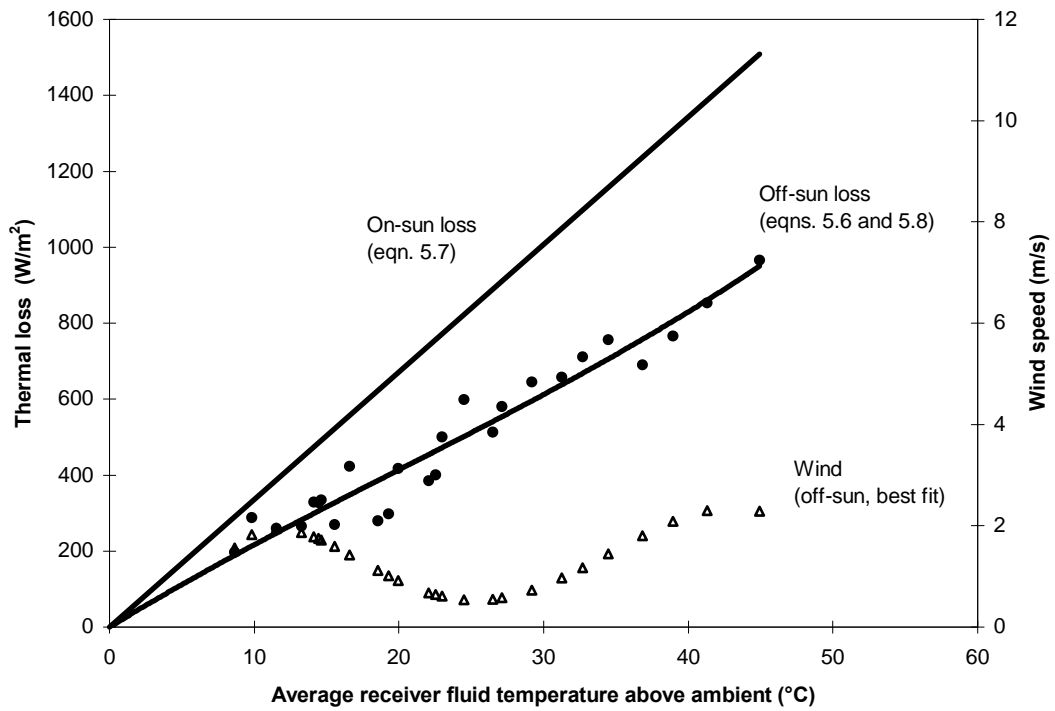


**Figure 5.22** Thermal loss and wind data for unshielded receiver

### Glass-shielded receiver

Results from the thermal loss test for the glass-shielded receiver are shown graphically in figures 5.23 and 5.24. The curve describing heat loss as a function of average receiver fluid temperature above ambient is given as:

$$Q_{0G} = -0.0036 (\Delta t_{ave})^3 + 0.3511 (\Delta t_{ave})^2 + 0.3392 (\Delta t_{ave}) \quad [W/m^2] \quad (5.9)$$

For this equation,  $R^2 = 0.995$ . The average value of beam irradiance ( $G_{bp}$ ) for the 10 tests, from which the on-sun curve in figure 5.24 was obtained, was  $841.73 \text{ W/m}^2$ .

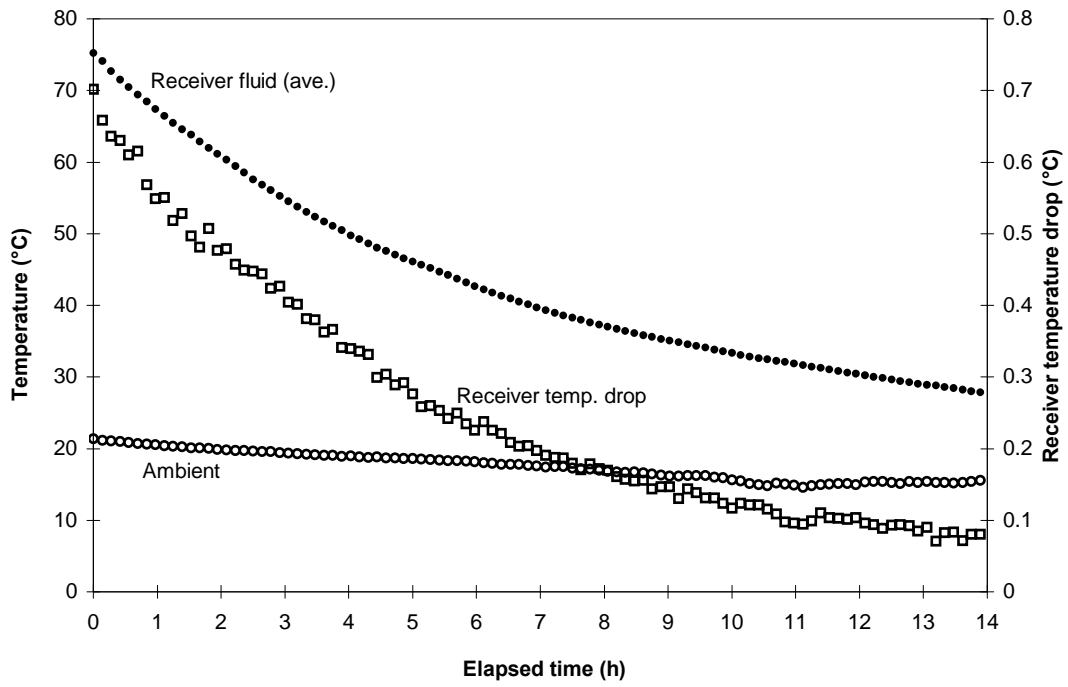


Figure 5.23 Temperature data for glass-shielded receiver

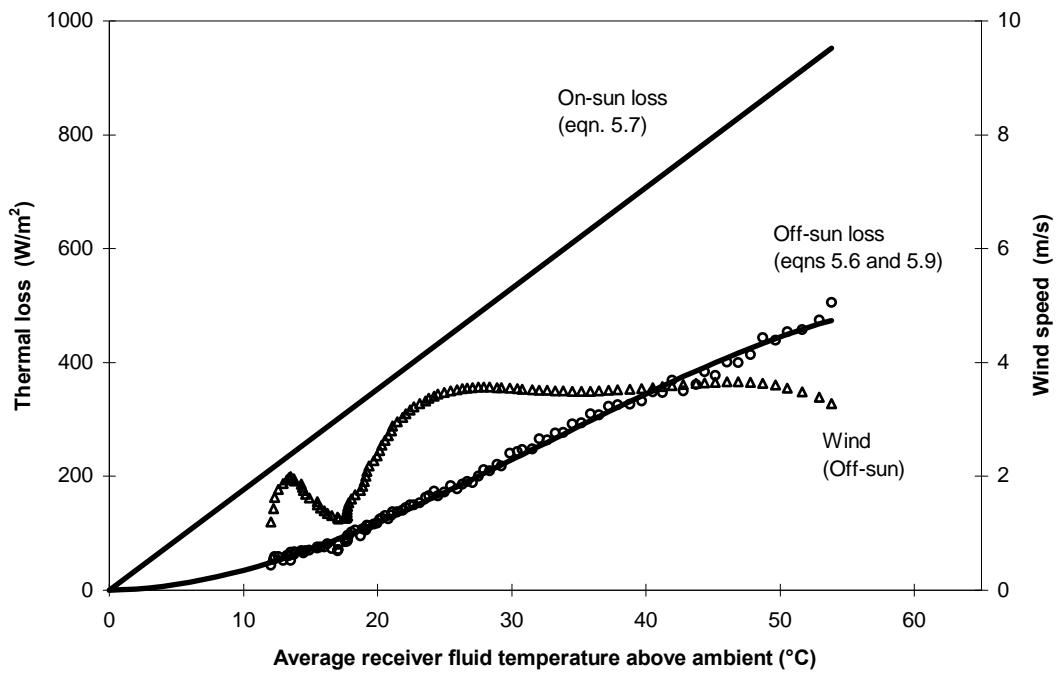
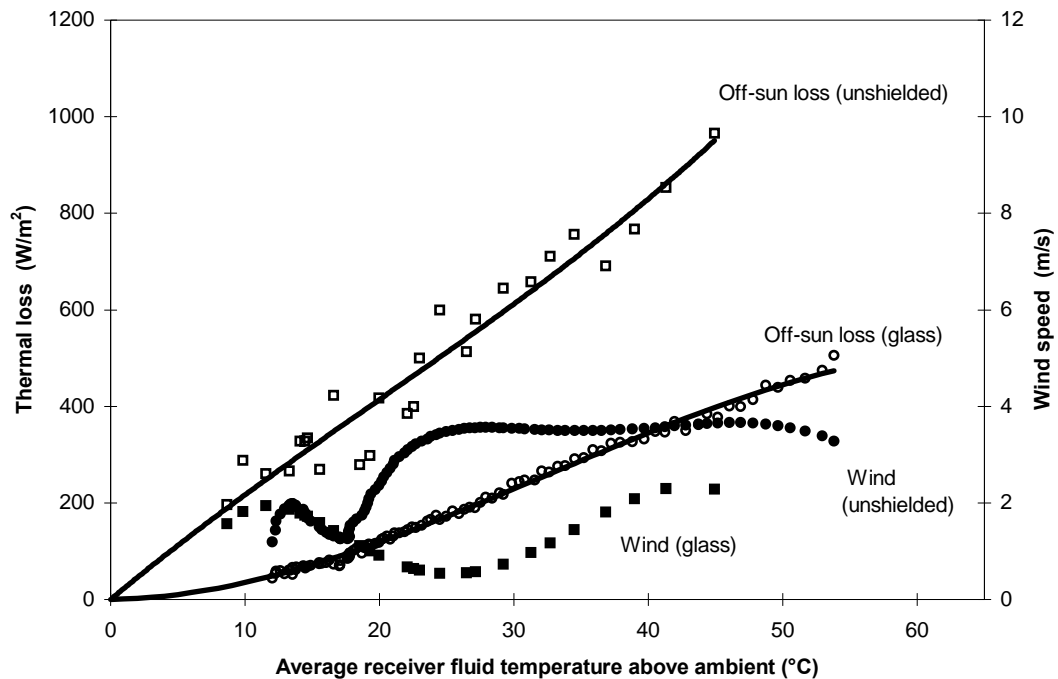


Figure 5.24 Thermal loss and wind data for glass-shielded receiver

## Comparison of results

Figure 5.25 compares thermal loss results for both receivers, including the wind conditions under which tests were conducted.



**Figure 5.25** Thermal loss for glass-shielded and unshielded receivers

Compared to figure 5.22, the off-sun loss data in figure 5.24 showed considerably less scatter. This is discussed further in chapter 7.

## 5.5 Summary

A summary of the thermal performance of the PTSC is presented in table 5.4 for both receiver types, as determined from the ASHRAE 93 tests and thermal loss tests conducted on the collector.

**Table 5.4** PTSC performance summary

<b>Parameter</b>	<b>Unshielded receiver</b>	<b>Glass-shielded receiver</b>
<b>Time constant (s)</b>	30.5 (cooling) 27.7 (heating) 29.1 (average)	28.6 (cooling) 26.4 (heating) 27.5 (average)
<b>Collector acceptance angle (deg)</b>	0.43	0.52
<b>Thermal efficiency</b>	$\eta_g = -2.0099(\Delta t/G_{bp}) + 0.5523$ $\eta_o = 0.601$ $F_R = 0.919$ $U_L = 36.53 \text{ W/m}^2\text{K}$	$\eta_g = -1.0595(\Delta t/G_{bp}) + 0.5381$ $\eta_o = 0.553$ $F_R = 0.973$ $U_L = 18.18 \text{ W/m}^2\text{K}$
<b>Incidence angle modifier</b>	$K_{\alpha r} = -2.032 \times 10^{-6} (\theta_i)^3 + 1.199 \times 10^{-4} (\theta_i)^2 - 3.940 \times 10^{-3} (\theta_i) + 1.005$	$K_{\alpha r} = 9.360 \times 10^{-7} (\theta_i)^3 - 1.616 \times 10^{-4} (\theta_i)^2 + 1.061 \times 10^{-3} (\theta_i) + 1.009$
<b>Off-sun loss (W/m<sup>2</sup>)</b>	$Q_{0U} = 0.0033(\Delta t_{ave})^3 - 0.1935(\Delta t_{ave})^2 + 23.2746(\Delta t_{ave})$	$Q_{0G} = -0.0036(\Delta t_{ave})^3 + 0.3511(\Delta t_{ave})^2 + 0.3392(\Delta t_{ave})$

## 6. THERMAL MODELLING OF PTSC PERFORMANCE

### 6.1 Introduction

Conventional PTSC models treat the receiver as a single unit into and out of which energy is transferred (Stine and Harrigan, 1985; Incropera and DeWitt, 1990; Duffie and Beckman, 1991; Bakos et al., 1999). The principle source of energy is solar irradiance reflected from the mirror surface of the collector to the absorber, through which a heat transfer fluid is pumped. Several heat loss mechanisms are active as a result of the absorber's raised temperature, mainly radiation and residual gas conduction from the absorber to the glass shield (if present), convection from the outer surface of the receiver to atmosphere, conduction through end connections and radiation loss to the sky (Odeh et al., 1998). Heat "loss" to the working fluid is the intended aim of the PTSC.

The magnitudes of thermal losses change depending on operating conditions. Convective losses are strongly dependent on ambient wind conditions and whether or not the absorber is shielded, conductive losses are usually small and radiation heat loss is a strong function of the receiver temperature. Under steady state conditions, the energy flows into and out of the receiver are balanced enabling the calculation of parameters such as the absorber wall temperature and rise in fluid temperature. The temperature rise causes a positive gradient in the receiver wall temperature from inlet to outlet. In the conventional modelling approach, this lengthwise gradient is either ignored by using averaged temperature values for the wall of the receiver and the working fluid (Stine and Harrigan, 1985), or it is circumvented by introducing a heat removal factor ( $F_R$ ) to account for the reduction in effectiveness of the absorber (Duffie and Beckman, 1991).

As an alternative to the conventional modelling approach, the receiver is divided into short lengths or segments and an energy balance is performed on each segment, leading to a solution for the temperature of the fluid and that of the absorber wall within each segment, from inlet to outlet of the receiver. This finite volume approach is followed by Odeh et al. (1998) and Lamprecht (2000), and is used in this study to model the thermal efficiency of the PTSC. In this chapter, a brief description of the model presented by Lamprecht (2000) is

given. Results from the implementation of the model are presented and a comparison is made between the model's results and those obtained by experiment.

## 6.2 Thermal Model of Collector Performance

In implementing the PTSC performance model of Lamprecht (2000), the following assumptions and constraints were adopted:

- Steady state operation was assumed
- Only single phase (liquid) flow was considered in the absorber
- Circumferential temperature gradients in the absorber wall were ignored
- Fluid pressure was assumed constant through the absorber
- Heat transfer between absorber and glass-shield was by radiation only
- Heat conduction along the length of the absorber was ignored
- Turbulent flow in the absorber was assumed
- Forced convection was assumed from the receiver to atmosphere
- For calculation purposes, the length of the receiver was set at 5 m
- During simulation of the performance of the unshielded and glass-shielded receivers, average ambient conditions (wind speed, irradiance, fluid and air temperatures) from the completed PTSC test programme were used as inputs to the model so as to enable meaningful comparison between model and experiment

To accommodate the unshielded and glass-shielded receivers used in this project, the model configurations shown in figures 6.1 and 6.2 were used. In figure 6.1 the energy flows and temperatures for the unshielded receiver are shown, while those applicable to the glass-shielded receiver are illustrated in figure 6.2. Heat flows in [W] to the control volume in figure 6.1 include beam radiation from the sun ( $Q_{q-a}$ ) and radiation from the sky ( $Q_{sky-a}$ ), while losses from the absorber include radiation to the sky ( $Q_{rad(a-s)}$ ) and convection to the atmosphere ( $Q_{conv(a-s)}$ ), which is at ambient temperature  $t_a$ . The absorber wall temperature is  $t_{wa}$ , fluid enters the segment at temperature  $t_i$  and leaves at  $t_{i+1}$ , with an average bulk value of  $t_b$ . Heat flow from the wall to the working fluid is  $Q_{wall}$ .

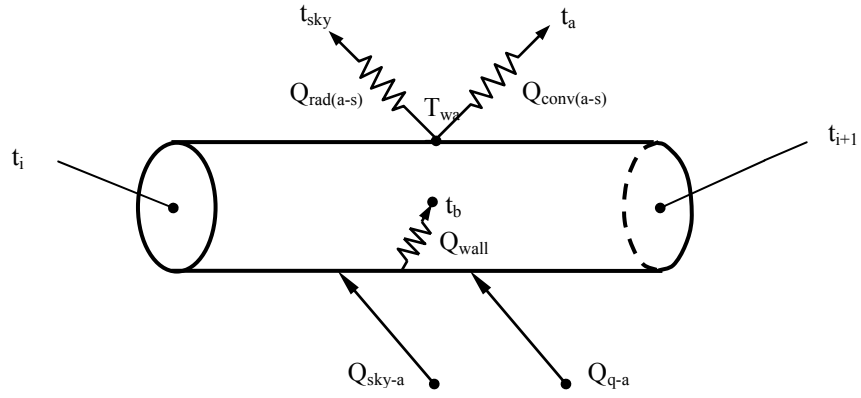


**Figure 6.1** Heat transfer model for unshielded receiver (Lamprecht, 2000)

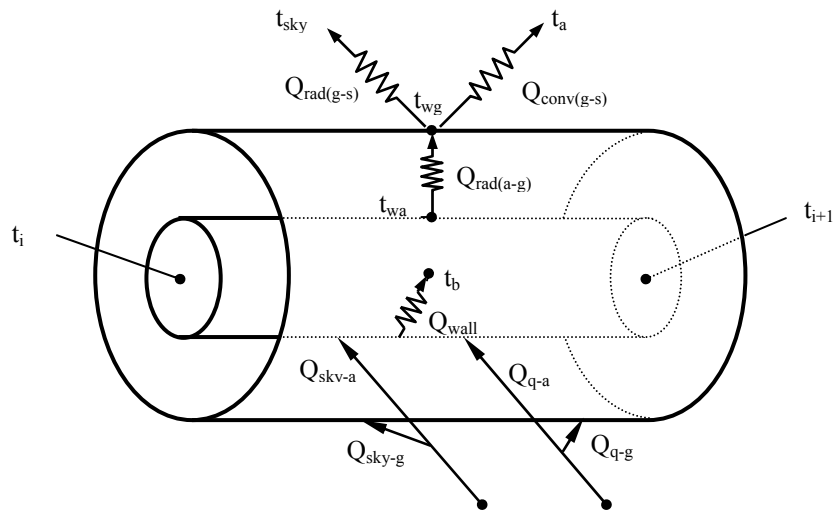


**Figure 6.2** Heat transfer model for glass-shielded receiver (Lamprecht, 2000)

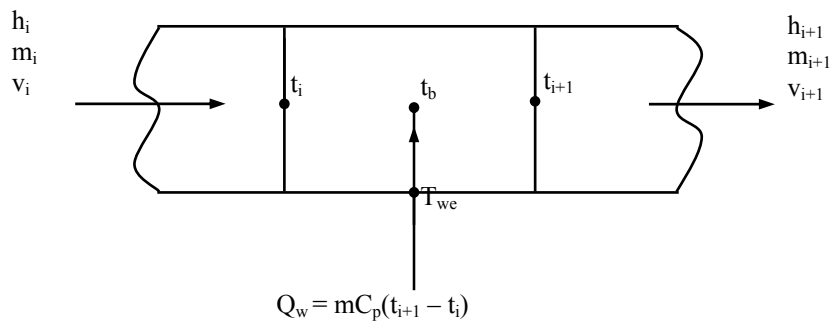


**Figure 6.3** Segment control volume for absorber with liquid flow (Lamprecht, 2000)

In figure 6.2, additional energy flows include absorption of beam and sky radiation by the glass shield ( $Q_{q-g}$  and  $Q_{sky-g}$ ), net radiation exchange between the absorber and the glass shield ( $Q_{rad(a-g)}$ ), radiation loss from the glass to the sky ( $Q_{rad(g-s)}$ ) and convective loss from the glass to atmosphere ( $Q_{conv(g-s)}$ ).

In the sketch of the control volume (figure 6.3), the working fluid enters the segment with specific enthalpy  $h_i$  [J/kg], velocity  $v_i$  [m/s] and at a mass flow rate of  $m_i$  [kg/s]. The rate at which energy is absorbed by the fluid ( $Q_w = mc_p(t_{i+1} - t_i)$ ) is equal to the heat transfer-rate through the absorber wall ( $Q_{wall}$ ), changing the fluid properties at outlet to  $t_{i+1}$  and  $h_{i+1}$  ( $v_{i+1}$  and  $m_{i+1}$  are assumed to remain constant from the inlet).

In Lamprecht's model, only free convection is assumed in the calculation of the external convective heat transfer coefficient,  $h_{ce}$ . The model was therefore modified to reflect more accurately the conditions experienced during testing in this study when the average recorded wind speed was 4.8 m/s for the unshielded receiver tests and 4.6 m/s for the glass-shielded receiver. Under these conditions, the free convection model would have under-predicted heat loss. Duffie and Beckman (1991) recommend the following equations for determining the Nusselt number for flow across a single tube exposed to wind in an outdoor environment:

$$Nu = 0.40 + 0.54 Re^{0.52} \quad \text{for } 0.1 < Re < 1000 \quad (6.1)$$

$$Nu = 0.30 Re^{0.6} \quad \text{for } 1000 < Re < 50\,000 \quad (6.2)$$

where  $Re$  is the Reynolds number based on the outer diameter of the absorber or, if applicable, the glass-shield. Once the Nusselt number is known, the convective heat transfer coefficient can be obtained from equation 6.3.

$$h_{ce} = Nu \frac{k_a}{D} \quad [W/m^2K] \quad (6.3)$$

Here,  $k_a$  is the thermal conductivity of the air [W/mK] at a mean film temperature determined for each control volume of the model and  $D$  is the outer diameter of the tube [m] from which heat is lost. This heat transfer coefficient is then used in the calculation of the convective heat

loss terms  $Q_{\text{conv(a-s)}}$  and  $Q_{\text{conv(g-s)}}$ , which form part of the energy balance equations that emerge from the thermal model of the receiver.

To produce a solution, the model proceeds from the receiver inlet, where fluid conditions are known, and the energy balance equations that are graphically illustrated in figures 6.1 and 6.2 are solved for each successive control volume. Two MATLAB programmes based on a Visual Basic application by Lamprecht (2000) were used to implement the solution scheme for both receiver types. Inputs include fluid inlet temperature, ambient air temperature, wind velocity, beam irradiance, PTSC dimensions and material properties. Outputs include inlet, outlet and bulk fluid temperature for each segment and the absorber wall temperature and glass shield temperature (if applicable) for each segment.

The model configurations were used to predict the total rise in temperature through the unshielded and glass-shielded receivers ( $\Delta t_r$ ) for the same conditions under which the experimental PTSC efficiency tests were conducted. Equation 4.3 was then used to calculate efficiency in the same way as during physical testing. To produce thermal performance graphs such as those in figures 5.15 and 5.16, a range of receiver inlet temperatures was used to simulate actual conditions.

## Results

### Unshielded receiver

Output from the finite volume model is shown in figure 6.4. This gives receiver fluid temperatures for each of the model segments for a range of inlet values. Inlet temperatures were chosen to give an even spread comparable to the values used in testing. Values of wind speed and beam irradiance equal to actual test averages (4.8 m/s and 928.23 W/m<sup>2</sup>) were used. Table F.1 contains raw data from a single run of the MATLAB programme written to implement the thermal model for the unshielded receiver. Using the temperature gains shown in figure 6.4, thermal efficiency data were derived for the receiver and these appear in figure 6.5. This graph includes results from the free convection model of Lamprecht (2000), the modified forced convection model and experimental test data from figure 5.15.

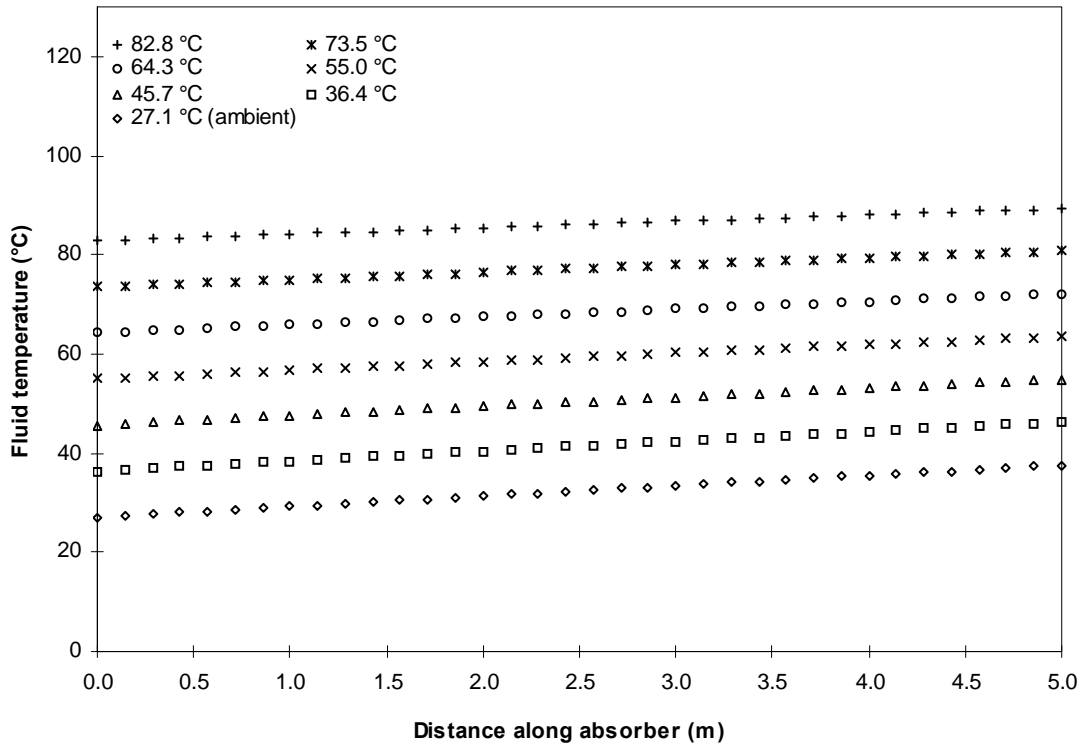


**Figure 6.4** Unshielded model results for a range of receiver inlet temperatures

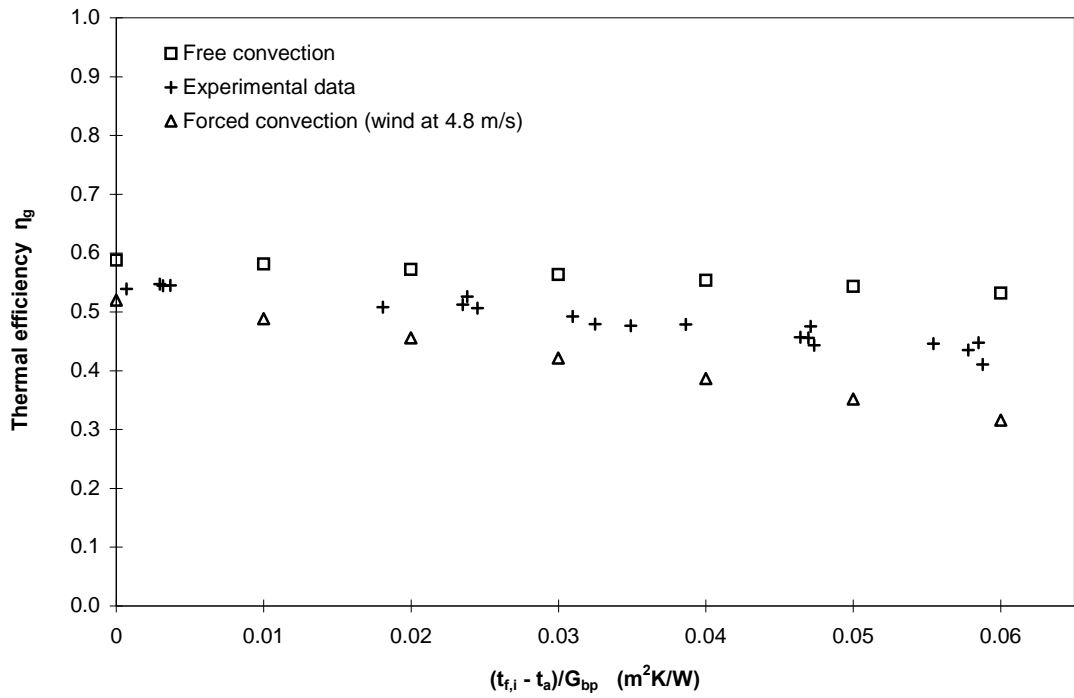


**Figure 6.5** Free and forced convection models with experimental data (unshielded)

From figure 6.5, the performance data of the free and forced convection models intercept the efficiency axis at 0.588 and 0.520 respectively, with the experimental value at 0.552 obtained from the best fit curve (equation 5.2).  $F_R\eta_0$  is 6.5 % higher than the test result for the free convection model and 5.8 % lower for the forced convection model. At the maximum inlet temperature tested, the free and forced convection models give efficiency results that are 22.6 % higher and 27.2 % lower respectively. Since the gradient of the efficiency curve is dependent on the system's overall heat loss coefficient ( $U_L$ ), it can be concluded that the free convection model under-predicts heat loss and the forced convection model, with an input wind speed of 4.8 m/s, over-predicts it.

To investigate the effect of wind speed on the predicted performance of the unshielded receiver, the forced convection model was tested for a range of wind speeds, from near-zero to 4.8 m/s. A velocity of 0.001 m/s was entered for the near-zero condition to ensure  $Re > 0.1$  (see equation 6.1). The results are shown in figure 6.6.

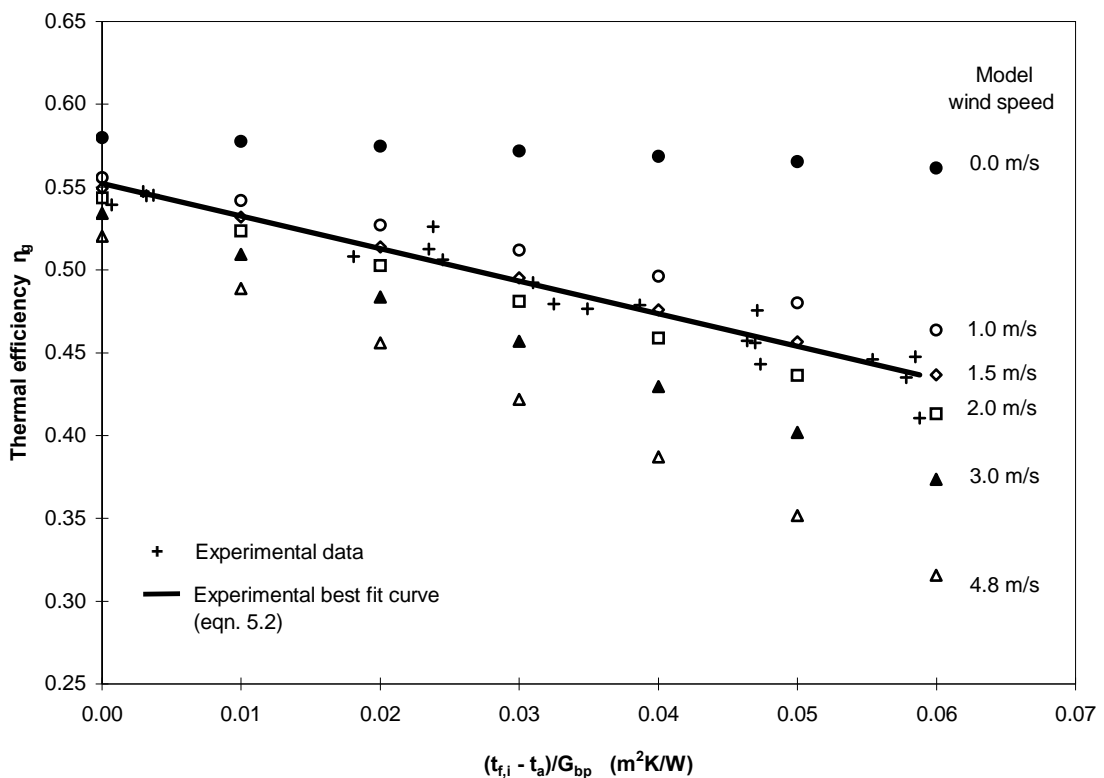


**Figure 6.6** Output from forced convection model for varying wind speed (unshielded)

Although the average recorded wind speed during testing was 4.8 m/s, the forced convection model shows excellent agreement with the experimental data at a wind speed of 1.5 m/s.

Lamprecht’s model was not intended to be used to determine thermal loss under zero irradiance conditions but for interest the MATLAB programme developed for this project was run with a beam irradiance value ( $G_{bp}$ ) of 0 W/m<sup>2</sup> to simulate conditions during the off-sun loss tests described in 5.4. The output from one such run is given in table F.2. The results of implementing the forced convection model at zero beam irradiance over a range of wind speeds are shown in figure 6.7. A wind speed of 1.34 m/s and ambient temperature of 21.2 °C were used to simulate actual test conditions. Experimental data are also shown with predicted values for near-zero wind speed. As in figures 6.5 and 6.6, the experimental values fall between the free convection data and those at the average recorded wind speed.

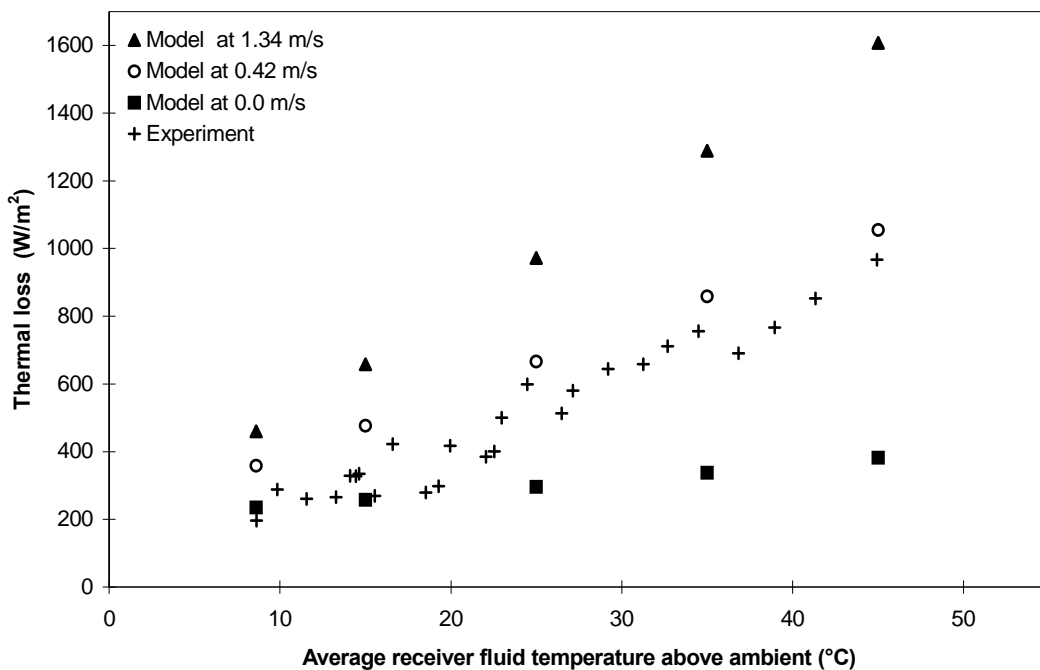


**Figure 6.7** Off-sun thermal loss from forced convection model (unshielded)

In figure 6.6, the thermal performance model showed excellent agreement with experimental data for a wind speed of 1.5 m/s, or 31.3 % of the recorded average from the test facility’s anemometer. For interest, the same scaling factor (0.313) was applied to the average wind speed measured during off-sun loss tests (1.34 m/s), to yield an adjusted wind speed of

0.42 m/s. This speed was used in the performance model to produce the third set of data shown in figure 6.7. Under these conditions, agreement between the model and the experimental data is close.

Glass-shielded receiver

Results from two runs of the programme written to implement the forced convection model for the glass-shielded receiver are given in figure 6.8. Fluid and glass shield temperatures are presented for wind speeds of 4.6 m/s and 1.0 m/s. In both cases, the fluid temperature rise from an inlet value of 27.3 °C is similar, but at the higher wind speed, the glass temperature is lower reflecting the increased heat loss to atmosphere due to convection. A sample of data from the implementation of the model is given in appendix F.

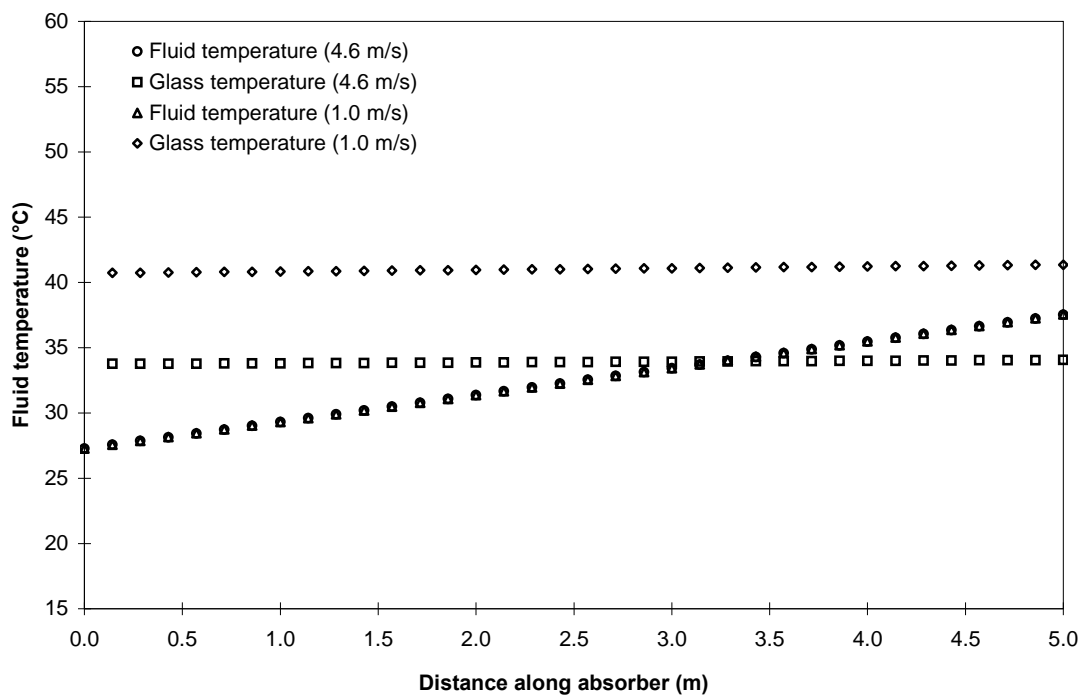


**Figure 6.8** Fluid and glass temperatures for two wind speeds

Efficiency results are shown in figure 6.9. The graph includes output from the free convection model, the modified forced convection model at a wind speed of 4.6 m/s (the average recorded wind speed during testing) and experimental test data from figure 5.16. A beam irradiance value of 841.73 W/m<sup>2</sup> was used to simulate actual test conditions.

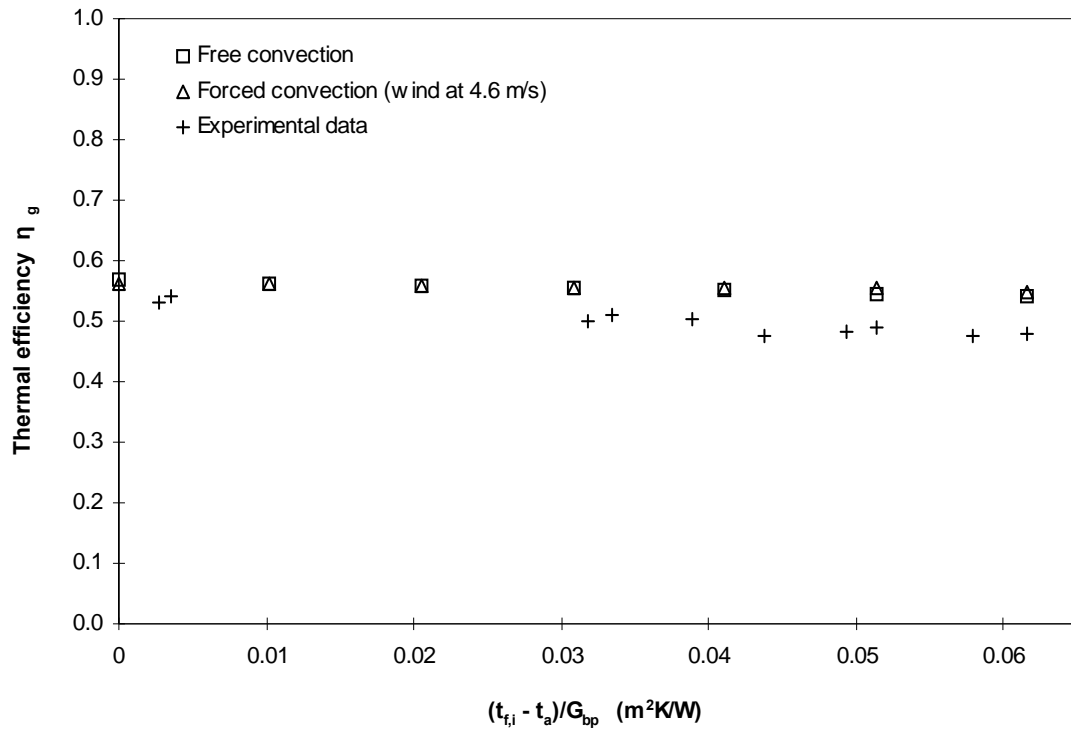


**Figure 6.9** Free and forced convection models with experimental data (glass-shielded)

Results from the free and forced convection models are nearly identical with intercept values at the efficiency axis of 0.568 and 0.563 respectively. The experimental value, representing the product  $F_R\eta_0$ , is 0.538 as obtained from equation 5.3. The value from the free convection model is thus 5.6 % higher than the experimental result and that from the forced convection model is 4.6 % higher. At the maximum receiver inlet temperature tested, the free and forced convection models give efficiency results that are 14.2 % and 16.1 % higher respectively. Both the free and forced convection models therefore under-predict heat loss for this PTSC.

Figure 6.10 gives forced convection results for a range of wind speeds.

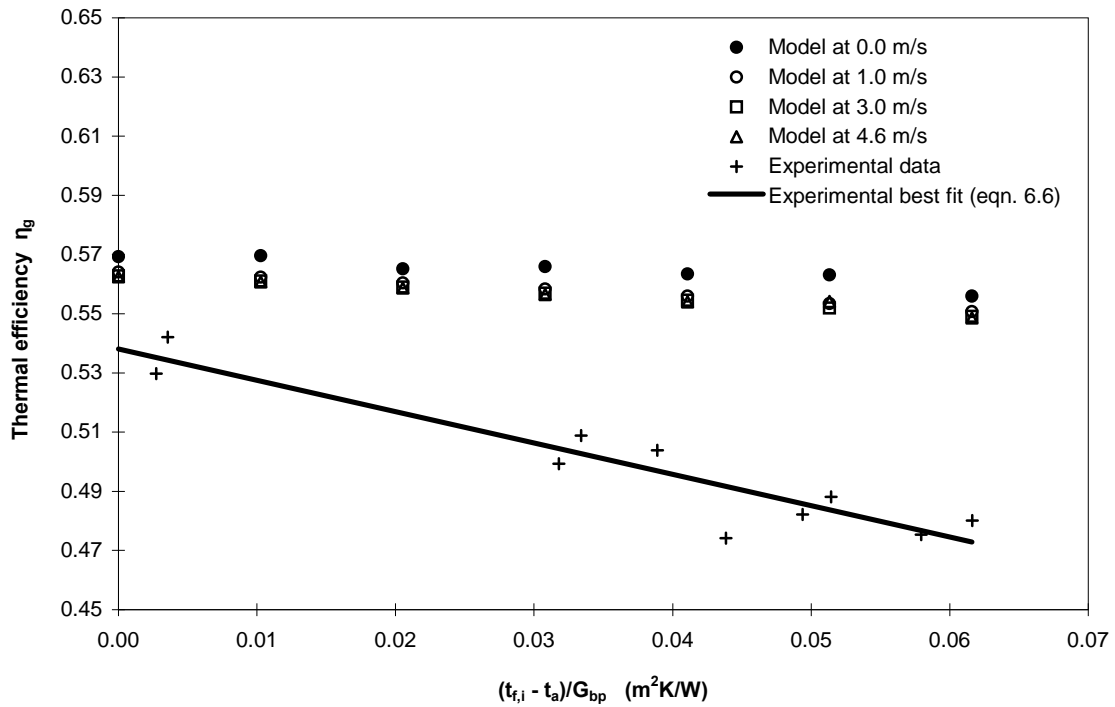


**Figure 6.10** Output from forced convection model for varying wind speed (glass-shielded)

Increasing wind speed has little effect on the predicted efficiency, yet figure 6.8 shows an increase in glass temperature at lower wind speeds. As the receiver fluid temperature is increased, the growing difference between the predicted and measured performance of the PTSC in figure 6.9 suggests that the modelled loss from the absorber to the glass shield is lower than that measured experimentally. The negligible effect of wind speed on thermal efficiency suggests that heat build-up in the glass shield is more a function of absorbed solar energy than of transfer from the absorber. Based on the data in figures 6.9 and 6.10, not all heat loss mechanisms are adequately accounted for in the model of the glass-shielded receiver.

Attempts to use Lamprecht's model to simulate off-sun loss for the glass-shielded receiver (see figure 5.24) were not successful, as shown in figure 6.11. For this investigation, the model was implemented with a  $G_{bp}$  value of  $0 \text{ W/m}^2$ . Although it correctly shows a trend of increasing thermal loss with fluid inlet temperature, the model wrongly predicts a small temperature rise through the receiver for inlet temperatures below  $55 \text{ }^\circ\text{C}$ . Clearly this is incorrect for a zero beam irradiance input. Since the glass-shielded model is considerably

more complex than the unshielded version, employs a different method of solution and is untested for a zero irradiance input, further study of the modelling scheme would be required to explain the anomalous results shown in figure 6.11.

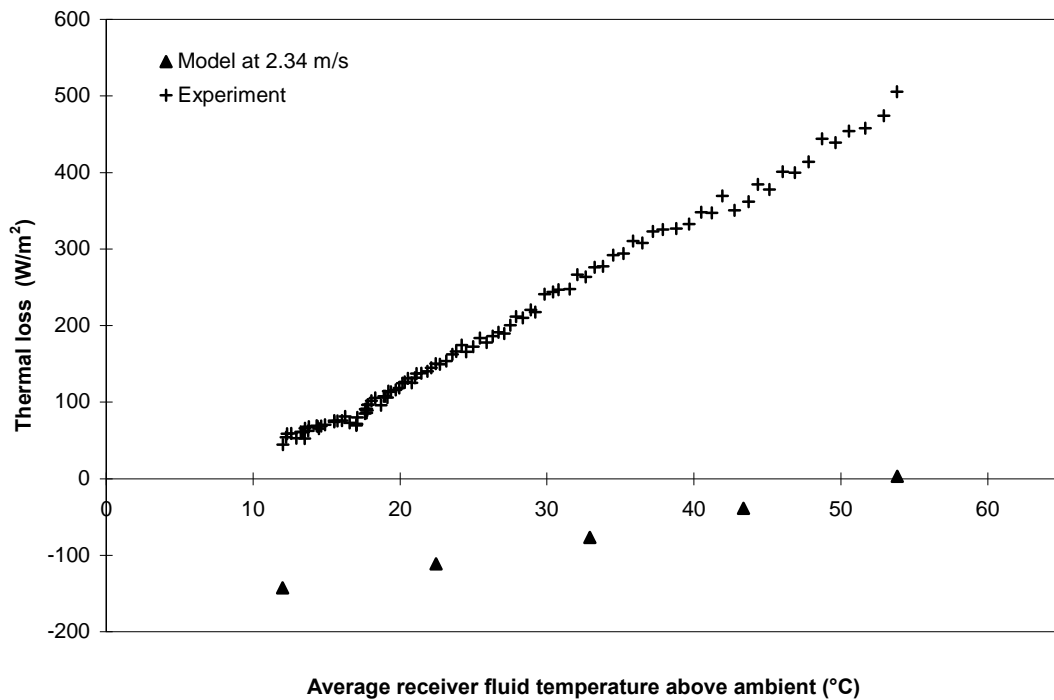


**Figure 6.11** Off-sun thermal loss from forced convection model (glass-shielded)

#### 6.4 Summary

Two thermal models developed in the Department of Mechanical Engineering at the University of Stellenbosch (Lamprecht, 2000) were tested against experimental results from the PTSC test programme. The models, which were adapted to account for forced convection from the receiver, used a finite volume approach in which the receiver was divided into multiple control volumes or segments. The energy balance equations for each segment were then solved yielding temperature data from which thermal efficiency values could be obtained and compared with experimental results. The results for the forced convection, unshielded model showed the following:

- The model was highly sensitive to wind speed
- At the test-average wind speed of 4.8 m/s the predicted thermal efficiency of the PTSC was lower than that determined experimentally
- Excellent agreement was obtained between the model and experimental results for the forced convection model at a wind speed of 1.5 m/s, reinforcing doubts about the accuracy of the measured test wind speed (4.8 m/s)
- After adjusting the wind speed according to results from the thermal efficiency tests, output from the model showed close agreement with data from experimental off-sun thermal loss tests

For the glass-shielded model with forced convection:

- In predicting thermal efficiency, the model showed agreement to within 5 % of experiment at ambient fluid inlet temperature, but results were less accurate at higher inlet temperatures
- The model was insensitive to wind speed with almost no change in thermal efficiency as wind speed increased
- The model under-predicted heat loss and could not accurately predict off-sun thermal loss

## 7. DISCUSSION

### 7.1 Experimental Results

#### Tracking performance

The combined use of fixed rate tracking (Mode 2) and manual adjustment (Modes 1a and 1c) to track the sun early in the test programme was a necessary measure. While not ideal, it proved quite successful as seen in the performance curve of figure 5.2, and enabled the test programme to proceed while work continued on the algorithm-based system. The introduction of fixed pulse tracking was an improvement over the fixed rate method, yielding a tracking accuracy of  $0.144^\circ$ .

As a new method of determining the solar vector, use of the PSA Algorithm is not widely reported in the literature. Development of Mode 3 tracking was therefore a significant milestone in this project. The need for an offset factor indicates that further study is required regarding the accuracy of the PTSC's construction and alignment. Nevertheless the algorithm-based tracking mode worked well and the use of powerful and programmable components such as the Siemens PLC and VSD provided great flexibility in configuring tracking modes.

The use of a high-reduction gearbox and AC motor with electro-mechanical brake was effective. Although other hardware options were possible, such as a highly geared DC motor or linear actuators (mechanical, hydraulic or electric) of the types used on satellite tracking dishes, the chosen equipment was well suited to the needs of the project, considering cost, complexity and time limitations.

Initial plans to include optical feedback in the tracking system were not pursued due to a lack of time and resources. Such a system would have measured the difference in light falling on two accurately positioned light dependent resistors (LDRs) to verify actual focusing and to make fine adjustments to the collector's position. Optical feedback would have improved the accuracy of Mode 2 tracking early in the test programme when effective VSD settings were being developed. Setting up a feedback system would have introduced additional problems, however, such as accurately locating the LDRs and calibrating their response to differential

shading. This would have required time to correct and would have delayed PSA Algorithm-based tracking, which was the more important goal. Optical feedback remains a worthwhile addition to the DTCS and should be pursued as part of the system's ongoing development.

In general, the DTCS functioned sufficiently well to enable trough testing to proceed, although much work remains to transform it into a comprehensive drive, tracking and control system.

#### PTSC performance results

##### i) Collector time constant

Figures 5.5, 5.6, 5.8 and 5.10 show that at higher flow rates the collector time constant was reduced, regardless of heating or cooling. This is because heat transfer is more effective at higher flow rates and the receiver does not heat up as much, so reaching thermal equilibrium whether by adding or removing heat takes less time. The shapes of the curves in figures 5.7 and 5.10 confirm the exponential nature of the time constant with regard to flow rate, as described in ASHRAE 93 (ASHRAE, 1991).

The measured time constants for both receivers (at the test flow rate of 300 L/h) were low at an average of 29.1 s for the unshielded and 27.5 s for the glass-shielded receiver. By comparison, Kalogirou (1996) published results for a PTSC with aperture width of 1.46 m and area of 3.5 m<sup>2</sup> for which the average time constant was 50 s. Comparison with the IST results of Dudley et al. (1995) is not possible because they report the total time taken for the system to stabilise and not a time constant value. This inability to compare results from different programmes makes a good argument for standardising PTSC test methods.

The comparison of results given in figure 5.11 suggests a trend of slightly higher time constants for the glass-shielded receiver during cooling and at low flow rates. A likely explanation is that low flow rates produce higher temperatures in the fluid and the absorber wall. In shedding this heat during the cooling stage of the test, heat loss by convection from the absorber to the surrounding air is retarded by the glass shield, increasing the time constant. At higher flow rates the data are close together and no clear trends are obvious.

ASHRAE 93 compliance was generally good throughout the tests, although it appeared that wind speeds were higher at the weather station's position than at the receiver, an effect that was noticed several times during the programme. For the time constant tests, absolute wind speed was less important than change in speed, which could have introduced variations in the results. The recorded wind speeds shown in table 5.1 were close (all within 10 % of the average), ensuring consistency in the test data.

ii) Collector acceptance angle

The acceptance angles for the unshielded and glass-shielded receivers ( $0.43^\circ$  and  $0.52^\circ$  respectively) were similar. By comparison, Kalogirou (1996) reports a value of  $1^\circ$  for the same collector referred to in the time constant discussion.

A notable feature of figure 5.14 is the slight asymmetry of the unshielded data, compared with the glass-shielded results. This probably indicates mislocation of the receiver or the asymmetrical effects of other optical errors, such as reflector misalignment. The larger acceptance angle and symmetrical data for the glass-shielded receiver possibly suggest that refraction of incoming light rays by the glass helps to “damp out” optical image spread. It is also possible that the insulating effect of the glass acts to smooth the thermal efficiency results that make up the data.

Both ASHRAE 93 (1991) and Kalogirou (1996) link acceptance angle to tracking accuracy. For this PTSC the tracking accuracy is equal to the angular magnitude of 1 pulse on the rotary encoder, since this is the minimum angle through which the DTCS can turn the collector. Therefore the trough has a tracking accuracy of  $0.144^\circ$ . Provided the DTCS maintains its degree of accuracy, the collector will always operate within 2 % of its optimal efficiency since the acceptance angle for both receivers is greater than the angular accuracy of the tracking system.

ASHRAE 93 compliance was generally good during acceptance angle tests, although the angle of incidence recorded for the glass-shielded test ( $\theta_i = 17.52^\circ$ ) was higher than ideal. This was a concern since the amount of reflection from a glass shield increases with  $\theta_i$  (Duffie and Beckman, 1991).

### iii) Thermal efficiency

Thermal efficiency is an important measure of performance. It relates PTSC behaviour to the working fluid temperature and assists in predicting overall performance of large-scale systems. Commercial software packages used to predict the technical and economic performance of planned installations, such as TRNSYS, SOLTES, DELSOL and WATSUN, rely on performance models of the collector field, which are developed from the results of thermal efficiency tests conducted on individual modules (Stine and Harrigan, 1985; Duffie and Beckman, 1991).

For this PTSC, the peak efficiencies were 55.2 % and 53.8 % for the unshielded and glass-shielded receivers respectively. These results are lower than those of commercial trough collectors. For example, the IST collector tested by Dudley et al. (1995) showed a maximum efficiency of between 70.8% and 76.3 %, depending on the type of receiver used. Peak efficiency of the newest Eurotrough collector is approximately 75 % (Geyer et al., 2002). Superior performance in commercial PTSCs is due to several factors, including higher intercept factors (enabling an increase in concentration ratio), highly reflective mirror surfaces and receivers incorporating ceramic-metal coatings with very high solar absorptance.

Efficiency results from this test programme are closer to those of other research troughs, for which peak efficiency values of 63.8 % (Kalogirou, 1996), 62 % (Ibrahim, 1996) and approximately 45 % (Bakos et al., 1999) are reported in the literature.

The gradient of the thermal efficiency equation gives a measure of the overall heat loss coefficient ( $U_L$ ), which was found to be 36.53 W/m<sup>2</sup>K for the unshielded receiver and 18.18 W/m<sup>2</sup>K for the glass-shielded unit. The presence of the evacuated glass-shield therefore reduced  $U_L$  by 50.23 % producing a 9.2 % improvement in performance at maximum test temperature. The results clearly show the benefit of installing a glass-shield.

Few authors provide a performance equation in their results, making it difficult to compare heat loss from different PTSCs. An exception is Kalogirou (1996) who reported a loss coefficient of 8.2 W/m<sup>2</sup>K. Details of the receiver's construction were not given.

For high-temperature PTSCs a linear efficiency model is inadequate because radiation loss is a nonlinear function of temperature-difference and the model becomes progressively less accurate with increasing temperature. Inspection of IST performance graphs (Dudley et al., 1995) suggests nonlinearity of the efficiency curve does not become pronounced until the average receiver fluid temperature exceeds ambient temperature by approximately 100 °C. While this is not necessarily true of other collectors, it gives some indication of the fluid temperature range over which a linear model might be used. Each collector should be evaluated independently to determine the most appropriate model, but the results from this study confirmed the suitability of the linear model.

In figure 5.17 it can be seen that the glass-shielded receiver performs better for fluid temperatures greater than 13.45 °C above ambient. Below this temperature heat loss is low and the glass adversely affects performance by reducing optical efficiency. At higher temperatures performance is dominated by heat loss, which is prevented more effectively by the shielded receiver. In fact, a direct comparison of the thermal efficiency curves is not strictly correct since they were generated using data obtained at different values of  $G_{bp}$  (varying  $G_{bp}$  can result in temperature and heat loss changes). However, the efficiency results of Dudley et al. (1995) show a very weak dependence on irradiance at low receiver temperatures and a comparison was considered acceptable. The results of Lamprecht (2000) also show a crossover point in the performance of a trough with two receivers (shielded and unshielded) built at the University of Stellenbosch.

The temperature range over which a PTSC's efficiency is tested should correspond to the temperatures expected in service, which for commercial units can range from less than 100 °C to over 400 °C. For a research collector such as this, the testing range is dictated by the aims of the programme. In this case, the collector was built to establish a testing capacity for components such as reflective surfaces, tracking systems and receivers, not all of which require high-temperature testing. Thus, although a higher temperature range would have been preferred it was not essential. It should be added that three of the four ASHRAE 93 tests are performed with fluid at ambient temperatures. Also, not all commercial PTSC systems operate at high temperature. At the Campbell Soup Company in California PTSCs provide hot water at 91 °C for can washing (Stine and Harrigan, 1985) and the Phoenix Federal Correctional Institution installed a PTSC system in 1998 to supply hot water for the washing,

kitchen and laundry needs of inmates (National Renewable Energy Laboratory, 2004). Parabolic trough component testing at lower temperatures is therefore necessary and relevant. In time, the scope of testing will be expanded and a possible solution to the limitations of the fluid system may be found in the approach of Dudley et al. (1995), who used water for low-temperature tests on the IST collector at Sandia, and oil for tests conducted up to 400 °C.

ASHRAE 93 compliance was acceptable during efficiency testing except for high wind speed and variations in the receiver inlet temperature, which was difficult to hold constant at higher temperatures. ASHRAE 93 recommends controlling fluid temperatures with an inline heater and heat exchanger (ASHRAE, 1991). With time and cost constraints it was not possible to implement such a system and this remains to be resolved on completion of the project. A more accurate method of recording wind speed nearer to the collector is also needed.

Overall, the thermal efficiency performance of this PTSC was pleasing, given the larger size of this trough relative to most research units.

#### iv) Incidence angle modifier

The behaviour of the incidence angle modifier curves in figures 5.18 and 5.19 is consistent with that described in the literature, with a smooth reduction in collector performance as  $\theta_i$  increases (ASHRAE, 1991). The polynomial equations 5.4 and 5.5 each match the experimental data very well, as shown by the statistical parameter  $R^2$  (coefficient of multiple determination), which indicates the proportion of the data explained by the model (Walpole and Myers, 1990).

Two primary factors are responsible for the decline in performance of a PTSC with increasing  $\theta_i$ : the geometric reduction in irradiance falling on the aperture as  $\theta_i$  increases, called the “cosine effect” (Stine and Harrigan, 1985), and the change in optical efficiency as light interacts differently with the reflective surface of the collector, the glass shield (if present) and the absorber. Nothing can be done to counter the first effect apart from tilting or rotating the PTSC constantly so as to keep it oriented perpendicular to the sun’s rays. In commercial systems this is not possible and the cosine effect must be accounted for when calculating expected energy output from a field of collectors over the course of a year (Stine and Harrigan, 1985). To calculate the thermal efficiency of a solar collector, only that component

of the sun's irradiance normal to the aperture plane should be considered, hence the use of  $G_{bp}$  in equation 4.3 and not  $G_{DN}$  (ASHRAE, 1991). Since the cosine effect is accounted for in the calculation of thermal efficiency, it might be expected that a collector's performance would remain unchanged as  $\theta_i$  increased, yet this does not occur due to the second of the two primary factors mentioned above.

Apart from the cosine effect, the result of increasing  $\theta_i$  is a reduction in the intercept factor  $\gamma$  and changes to the mirror surface reflectance  $\rho$ , glass transmittance  $\tau$  and receiver surface absorptance  $\alpha$ . Practically,  $\gamma$  declines because light rays must travel further from the reflective surface of the trough to the receiver as  $\theta_i$  increases, magnifying the effect of any optical errors present. The material properties change because of the way light interacts with surfaces at different incidence angles. The introduction of the incidence angle modifier  $K_{\alpha\tau}$  allows for the overall effect of changes to  $\gamma$ ,  $\rho$ ,  $\tau$  and  $\alpha$  to be measured.  $K_{\alpha\tau}$  does not account for the cosine effect, which has already been negated in the calculation of  $G_{bp}$ . Interestingly, in publishing results from the IST collector tests at Sandia, Dudley et al. (1995) use  $G_{DN}$  in the calculation of efficiency, not  $G_{bp}$ . This reduces thermal efficiency at high angles of incidence since the larger value of  $G_{DN}$  appears in the denominator of equation 4.3. To accommodate this, their equation for  $K_{\alpha\tau}$  is not a simple polynomial in  $\theta_i$  but includes a  $\cos(\theta_i)$  term as described in 4.2.3.

In this project the PTSC collector structure and reflective surface were identical for both receivers. Assuming the receivers were set up similarly within the ring holders of the PTSC, any change in  $\theta_i$  would produce similar changes in  $\gamma$  for both, and any difference in  $K_{\alpha\tau}$  could then be ascribed to the only major difference between the two receivers, namely the glass shield. Since high angles of incidence increase reflection from the surface of a glass cover (Duffie and Beckman, 1991), the crossover point in figure 5.20 and subsequent decrease in performance of the glass-shielded receiver, is most likely due to reduced transmittance of the glass.

#### v) Thermal loss

The method used to obtain the data shown in figures 5.21 to 5.24 was to conduct continuous, overnight tests. An alternative method would have been to run short tests at specific fluid temperatures, though this would have required repeated adjustment of the water temperature

in the HT tank by introducing cold water, and it was more convenient to leave the system to run and adjust naturally.

Key results to emerge from the thermal loss tests were:

- Performance equations for both receivers for off-sun loss ( $Q_0$ ) as a function of  $\Delta t_{ave}$
- Heat loss sensitivity of the unshielded receiver to variation in wind speed
- Corresponding insensitivity of the glass-shielded receiver

Care must be exercised in interpreting the results from the loss tests. In particular the following must be considered:

- Heat loss is affected by wind speed and since the tests were conducted on different nights, ambient conditions must be considered before drawing general conclusions about the loss performance of the receivers. This is further complicated by the change in ambient conditions over the course of the night-time test period.
- The heat loss equations obtained from both tests (equations 5.8 and 5.9) are not intended to represent an exact model of receiver heat loss, but are an empirical fit of recorded data expressing loss in terms of receiver area.
- The on-sun loss curves in figures 5.22 and 5.24 are only valid for the range of receiver temperatures tested and the average recorded beam irradiance values ( $G_{bp}$ ) from which the thermal efficiency curves (equations 5.2 and 5.3) were generated. Receiver wall temperature is a function of irradiance and increasing  $G_{bp}$  would increase heat loss, changing the curves.
- Equations 5.8 and 5.9 should not be extrapolated to predict PTSC loss performance outside the range of tested temperatures, since heat loss mechanisms change (the equations do not account for increased radiation loss and other effects).

The degree of scatter in the data of figure 5.22 confirms that wind severely affected heat loss performance of the unshielded receiver while the glass-shielded results showed almost no scatter at all. This is shown in the excellent fit with the regression equation, for which  $R^2 = 0.995$ . Clearly, the use of a glass-shield is preferable in reducing heat loss, particularly in high-wind locations.

Figure 5.25 illustrates the considerable difference in loss performance between the two receivers. Wind speed was included because of the sensitivity of the unshielded data to this parameter. With this in mind, it would be better to run repeated thermal loss tests to increase the reliability of the data. Results from night tests with similar ambient conditions could then be isolated for comparison. This is suggested for future tests.

## 7.2 Thermal Modelling of PTSC Performance

Implementing the performance model of Lamprecht (2000) produced encouraging results. These suggested the need for certain refinements, the first of which was carried out early in the modelling process: a forced convection heat transfer coefficient was introduced to sensitise the model to the effects of wind across the receiver.

Although figure 6.5 shows the unshielded model over-predicts heat loss, figure 6.6 suggests that the wind speed used in the simulation was too high. Good agreement is seen between the model and experimental data for a wind speed of 1.5 m/s. While this reinforces suspicions that wind intensity was greater at the edge of the rooftop site than at its centre, it does not necessarily prove the model accurate. As a further complication the heat transfer model assumes a constant wind speed, yet the rooftop location experiences considerable turbulence that the model cannot accommodate. Still, results suggest that the forced convection modification improves the accuracy of the model. In this regard the model confirms what was found experimentally, that heat loss from the unshielded receiver is strongly dependent on wind speed.

The thermal loss results shown in figure 6.7 were produced by applying a scaling factor to the simulated wind speed (0.313), which gave better results. Although this does not confirm the accuracy of the heat transfer model, it again suggests a consistent difference between wind intensity at the receiver and that measured at the edge of the test facility. When tests are done to confirm this, the scaling factor will provide a means of crosschecking the results.

Compared with experimental data, output from the glass-shielded model shows good agreement at ambient inlet temperature (figure 6.9). Of interest is the gradient of the

simulated efficiency curve, which contains the effect of the heat loss coefficient  $U_L$ . For the simulated results this gradient is small (approximately  $-0.2 \text{ W/m}^2\text{K}$ ), while that of the experimental curve is considerably greater ( $-1.06 \text{ W/m}^2\text{K}$  from equation 5.3). These results should be assessed together with figure 6.8, which shows an increased glass temperature at lower wind speeds. By way of explanation, the glass shield receives heat energy both from radiation exchange between the absorber and the glass and from absorption of the sun's energy as it passes from the reflective surface of the PTSC to the absorber. Although the glass temperature clearly increases as the wind speed drops (see figure 6.8), the model shows almost no change in thermal efficiency as wind speed is increased (figure 6.10). This suggests the following:

- The rise in glass temperature at low wind speeds is more the result of retention of absorbed heat from incoming solar radiation, than from absorber-glass heat transfer
- The model under-predicts heat loss from the absorber tube to the glass-shield

With limited heat transfer from absorber to glass, the amount of heat lost via convection from the glass to atmosphere is reduced, neutralising the influence of increased wind speed on thermal efficiency. To improve its accuracy, the model should be adapted to include conduction loss through the ends of the receiver, loss through the annular spacing rings placed along the length of the receiver and loss through the end o-ring seal arrangements shown in figure A.14. Odeh et al. (1998) provide an expression for the heat transfer coefficient in low-density residual gas. Inclusion of an air-conduction loss term would be especially worthwhile given the likelihood that the new generation receivers will have low-conducting gas pumped into the annulus, instead of an evacuated space (Sargent & Lundy LLC Consulting Group, 2003). Ignoring these losses leaves radiation as the only mode heat transfer between absorber and glass. Because radiation loss is low at low receiver temperatures, the model under-predicts absorber-loss, producing a near-flat efficiency curve for the glass-shielded receiver. Rectifying this would improve the forced convection model.

In spite of some shortcomings, the modified heat transfer models tested in this study showed promising results for both receiver types. Results suggest that with some refinement the models should accurately simulate the thermal performance of parabolic trough collectors.

The thermal modelling exercise also highlighted concerns about the accuracy of wind data from PTSC tests. As noted above and in 5.3, wind speed appeared higher at times near the measuring anemometer than at the collector. It is believed this discrepancy resulted from turbulence caused by the size and shape of the building and rooftop obstacles where the test facility is located. The anemometer is located near the edge of the roof and elevated 2 m above it, placing it nearer to the wind free stream and clear of turbulence. The PTSC is located nearer the centre of the rooftop where turbulence is believed to occur (see figure 7.1).

The extent of the discrepancy may have also been affected by the prevailing wind direction, which is normally either south-westerly or north-easterly. A south-westerly wind would likely have caused a greater difference because of the position of the control room. The PTSC structure itself and angle of rotation of the trough would also have had an effect. Generally, the discrepancy between the anemometer and the receiver appeared slight, although observations were qualitative.

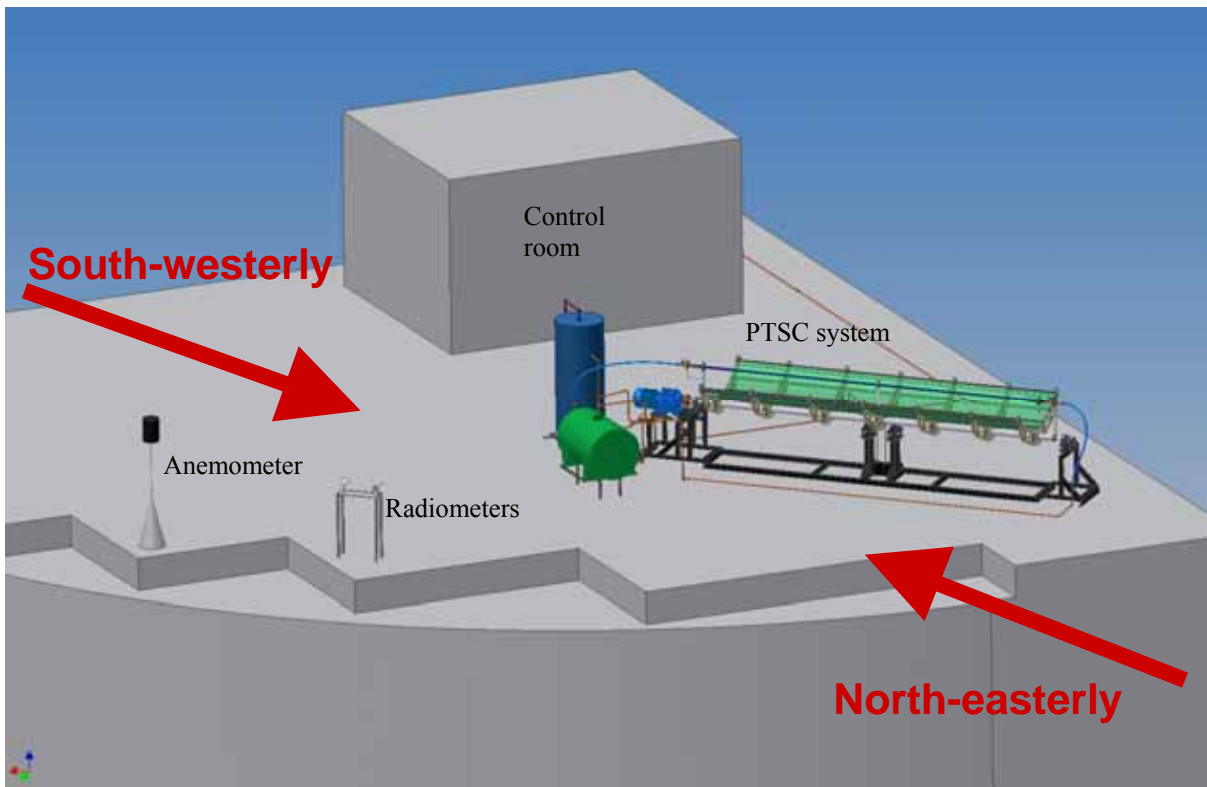


**Figure 7.1** PTSC system on rooftop of test facility with prevailing wind directions

The implications of the wind difference for ASHRAE test results were not considered severe, since wind speed is not a direct factor in any of the calculations, although it is used to determine whether a test should proceed or not (see 4.2). Since the ASHRAE wind speed violations were mostly high, any measurement error would have helped bring test conditions into line with ASHRAE criteria.

Implications for the modelling exercise were more serious since the unshielded receiver is sensitive to forced convection effects and wind speed is an input to the convective heat transfer coefficient through the Nusselt number (equations 6.1 to 6.3). The model also assumes a constant wind velocity although the PTSC may at times have experienced turbulent gusts. This made it difficult to draw conclusions about the models' accuracy, although the scaling factor obtained from figure 6.6 and checked using the data in figure 6.7 suggests heat loss is properly modelled for the unshielded receiver. Little can be said about the effects of the wind measurement discrepancy on the glass-shielded model, which is insensitive to wind and does not appear to account for all heat transfer modes.

Clearly the qualitative analysis above is only a start and further tests are needed to quantify the differences between the measured wind speed and that experienced by the collector. These will be undertaken on completion of the project.

## 8. SUMMARY

A parabolic trough solar collector, developed locally for use in a solar thermal research programme, was tested to characterise its performance. The torque-tube based PTSC was 5 m long with an aperture width of 1.5 m, a rim angle of  $82^\circ$  and a concentration ratio of 16.7. The surface consisted of 3M SA-85 aluminised acrylic film on a stainless steel substrate. The intercept factor of 0.8231 was determined by conducting an optical error analysis. The collector's tracking capability consisted of manual adjustment as well as automatic tracking using the PSA Algorithm to determine the solar vector. Tracking accuracy was  $0.144^\circ$ .

The ASHRAE 93-1986 (RA 91) standard was selected to evaluate performance of the collector. A comprehensive LabVIEW software application was developed to display and log real-time radiometric data, PTSC temperatures and solar angles.

Two receivers were tested, one unshielded and the other with an evacuated glass shield to limit convective heat loss. The absorber tubes were covered with a high-absorptance solar-selective coating, giving optical efficiencies of 0.601 (unshielded) and 0.553 (glass-shielded)

The peak thermal efficiencies obtained during testing were 55.2 % for the unshielded receiver and 53.8 % for the glass-shielded unit. Although the unshielded receiver performed better at ambient fluid temperature, overall heat loss was greater with a measured test slope of  $-2.01 \text{ W/m}^2\text{K}$  versus  $-1.06 \text{ W/m}^2\text{K}$  for the glass-shielded receiver. The presence of the evacuated glass shield reduced the overall heat loss coefficient by 50.2 % producing a 9.2 % improvement in performance at maximum test temperature. The average collector time constants were 29.1 s and 27.5 s for the unshielded and glass-shielded receivers respectively. Acceptance angles were measured at  $0.43^\circ$  (unshielded) and  $0.52^\circ$  (glass-shielded), both of which were greater than the tracking accuracy ( $0.144^\circ$ ) indicating that the PTSC operated within 2 % of its optimum efficiency at all times. The incidence angle modifiers for both receivers were determined empirically and characterised using polynomial equations. Tests conducted to determine off-sun heat loss showed the unshielded receiver to be highly sensitive to wind intensity.

As part of the study, performance of the PTSC was simulated using a finite volume heat transfer model adapted to include forced convection effects. Heat loss was over-predicted at the measured wind speed of 4.8 m/s, although wind speeds are thought to have been higher at the weather station than at the collector. The model showed excellent correlation with experimental data at an adjusted wind speed of 1.5 m/s and confirmed wind-sensitivity in the absence of the glass shield. The heat transfer model under-predicted heat loss from the glass-shielded receiver due to the assumption that absorber-glass heat transfer was by radiation only. Although the results of the simulation exercise suggested a need for some refinement of the model, it showed potential as a tool for predicting the performance of parabolic trough solar collectors.

## 9. RECOMMENDATIONS

The following recommendations are made for expanding on the work done in this project.

1. The PTSC fluid circulation system should be improved to enable high-temperature testing of the collector up to 400 °C. This could be done by installing either a high-pressure/high-temperature water system or an oil heater. The water option is preferable because it would also enable the collector to be used for direct steam generation.
2. Differences between the wind intensity at the edge of the test facility and at other points on the rooftop need to be quantified. A trial is proposed using a second anemometer for comparing wind speed under different conditions – to this end a portable anemometer has already been obtained. This study will help determine the accuracy of the heat transfer model implemented in chapter 6.
3. Based on the discussion in chapter 7, the heat transfer model of Lamprecht (2000) should be refined to accurately account for all heat loss mechanisms. Results from the suggested wind study would be needed before evaluating changes to the model. It would be interesting to investigate the effects of rooftop turbulence on heat loss from the receiver.
4. The trough collector offers an excellent opportunity to test new methods of improving PTSC performance. One possible method is the use of a twisted tape element inside the absorber tube to promote fluid turbulence and enhance heat transfer from the wall to the fluid. Kumar and Prasad (2000) report heat transfer improvements of between 18 % and 70 % for twisted tape inserts in a flat-plate solar water heater, albeit at the cost of a higher pressure drop. Little work has been done relating to similar experiments on concentrating collectors. The analysis of the effects of a twisted tape insert in a PTSC is proposed as the subject of future study.
5. The work done in this project to develop a LabVIEW application for monitoring collector performance presents considerable opportunities. It is recommended that

the SCATTALog programme be expanded into a comprehensive solar collector test application, enabling the user to run performance tests on different types of collectors, including domestic solar hot water units, PTSCs (at different orientations) and solar cookers. Incorporating modified versions of the Parasim software developed by Lamprecht (2000) would add a further dimension to the programme and enable real-time comparison between actual and simulated performance.

6. An analysis of the PTSC structure would be of interest. This would take place with regard to material strength and deformation of the collector and would be useful in quantifying the magnitudes of optical errors that degrade performance. A finite element approach would seem appropriate. The strength and deformation characteristics of the polypropylene ribs would be of particular interest. In this regard, two unused ribs are available for conducting physical tests.
7. The reflective surface of the PTSC should be replaced, given the weathering that is starting to occur. After replacement (preferably with a superior reflective material), it would be advisable to run a series of tests to quantify changes in collector performance.
8. Though it would present a challenge, it would be greatly beneficial to install a rotating platform on the rooftop test site for conducting constant angle of incidence tests. This would considerably expand the capabilities of the solar energy test facility and shorten the duration of future PTSC test programmes.
9. The radiometric equipment available at the test facility presents an excellent opportunity to expand the monitoring programme begun in this project. As a starting point, it is recommended that methods of data collection be improved to conform to accepted international standards. Collaboration with other researchers in this field should also be pursued. A step in this direction has already been taken involving NTNU, but enormous scope exists for data-exchange with other universities and laboratories.

10. It is recommended that a thermal storage component be added to the PTSC project. With the short-term performance of the collector well defined, the next step would be to investigate its performance over extended periods. The integration of an energy-storage system would fit in well and increase the relevance of the research programme. Research into types of storage media and methods of controlling flow rate and fluid outlet temperature should be included.
11. It is recommended that special attention be paid to the emergence of advanced materials that might improve the performance of PTSC components. One such material is the 3M product Vikuiti, which is a non-metallic composite with reflectance greater than 97 %. Although it was not designed for outdoor exposure it shows excellent potential for use on solar collectors, provided it can be protected. Another such material is Aerogel, an extremely lightweight ceramic with very low thermal conductivity. Recent research has shown that aerogels can be produced in a transparent form, leading to their possible use as glass shields in parabolic trough collectors. Depending on the transmittance, this could eliminate the need for complex evacuated tubes and seal arrangements.
12. Other areas of potential study linked to this project include:
- Use of the PTSC to initiate a research project in concentrating photovoltaic collector technology
  - The use of shape memory alloys as thermal actuators in solar energy systems
  - Alternative methods of solar tracking, including development of an optical feedback component to the DTCS

## REFERENCES

Agnihotri O. P. and Gupta B. K. (1981) *Solar selective surfaces*, John Wiley & Sons, Inc., United States

Almanza R., Lentz A. and Jiménez G. (1997) Receiver behavior in direct steam generation with parabolic troughs, *Solar Energy*, vol. 61, no. 4, pp. 275-278

ASHRAE (1991) Standard 93-1986 (RA 91) Methods of testing to determine the thermal performance of solar collectors, American Society of Heating, Refrigerating and Air-conditioning Engineers, Inc.

Bakos G. C., Adamopoulos D., Soursos M. and Tsagas N. F. (1999) Design and construction of a line-focus parabolic trough solar concentrator for electricity generation, *Proceedings of ISES Solar World Congress*, Jerusalem, p. 16

Blanco-Muriel M., Alarcón-Padilla D. C., López-Moratalla T. and Lara-Coira M. (2001) Computing the solar vector, *Solar Energy*, vol. 70, no. 5, pp. 431-441

Brooks M. J. (2005) Development of an outdoor test facility for solar thermal energy research, In preparation

CIEMAT (2003)

Site: [www.ciemat.es/eng/infogral/psolar](http://www.ciemat.es/eng/infogral/psolar)

Dudley V. E., Evans L. R. and Matthews C. W. (1995) Test results. Industrial Solar Technology. Parabolic trough solar collector, SAND94-1117, Sandia National Laboratories

Duffie J. A. and Beckman W. A. (1991) *Solar engineering of thermal processes*, 2<sup>nd</sup> ed., John Wiley & Sons, Inc., United States

Eck M., Zarza E., Eickhoff M., Rheinländer J., Valenzuela L. (2003) Applied research concerning the direct steam generation in parabolic troughs, *Solar Energy*, Article in press, pp. 1-11

Energy Efficiency and Renewable Energy Network (2003)

Site: [www.eere.energy.gov/troughnet](http://www.eere.energy.gov/troughnet)

Engineering News Online (2003)

Site: [www.engineeringnews.co.za](http://www.engineeringnews.co.za)

Geyer M., Lüpfert E., Osuna R., Esteban A., Schiel W., Schweitzer A., Zarza E., Nava P., Langenkamp J. and Mandelberg E. (2002) EuroTrough – Parabolic trough collector developed for cost efficient solar power generation, Paper presented at the 11<sup>th</sup> Int. Symposium on Concentrating Solar Power and Chemical Energy Technologies, Zurich

Güven H. M., Mistree F. and Bannerot R. B. (1986) A conceptual basis for the design of parabolic troughs for different design environments, *Journal of Solar Energy Engineering*, vol. 108, pp. 60-66

Güven H. M. and Bannerot R. B. (1986a) Determination of error tolerances for the optical design of parabolic troughs for developing countries, *Solar Energy*, vol. 36, no. 6, pp. 535-550

Güven H. M. and Bannerot R. B. (1986b) Derivation of universal error parameters for comprehensive optical analysis of parabolic troughs, *Journal of Solar Energy Engineering*, vol. 108, pp. 275-281

Güven H. M. (1994) Optimization of parabolic trough collector design for varying manufacturing tolerances using a closed-form expression for intercept factor, *Journal of Solar Energy Engineering*, vol. 116, pp. 164-166

Ibrahim S. M. A. (1996) The forced circulation performance of a sun tracking parabolic concentrator collector, *Proceedings of the World Renewable Energy Congress*, pp. 568-571

Incropera F. P. and DeWitt D. P. (1990) *Fundamentals of heat and mass transfer*, 3<sup>rd</sup> Ed., John Wiley & Sons, Singapore

Kalogirou S. (1996) Parabolic trough collector system for low temperature steam generation: design and performance characteristics, *Applied Energy*, vol. 55, pp. 1-19

Kalogirou S. (1996a) Design and construction of a one-axis sun-tracking system, *Solar Energy*, vol. 57, no. 6, pp. 465-469

Kalogirou S., Lloyd S. and Ward J. (1996) A simplified method for estimating intercept factor of parabolic trough collectors, *Proceedings of the fourth World Renewable energy Congress*, Denver, vol. 3, pp. 1782-1786

Kröger D. G. (1998) *Air-cooled heat exchangers and cooling towers. Thermal flow performance evaluation and design*, Department of Mechanical Engineering, University of Stellenbosch, South Africa

Kumar A. and Prasad B. N. (2000) Investigation of twisted tape inserted solar water heaters – heat transfer, friction factor and thermal performance results, *Renewable Energy*, vol. 19, pp. 370-398

Lamprecht A. J. (2000) Efficiency improvement of parabolic trough solar collector, Mechanical Project 478, University of Stellenbosch

Naidoo P. (2005) Intelligent control and tracking of a solar parabolic trough, PhD dissertation, Nelson Mandela Metropolitan University, In preparation

National Renewable Energy Laboratory (2004)

*Site:* [www.nrel.gov/docs/fy04osti/33211.pdf](http://www.nrel.gov/docs/fy04osti/33211.pdf)

Neethling A. (2002) Computer simulation for parabolic trough solar collector, Mechanical Project 478, University of Stellenbosch

Odeh S. D., Morrison G. L. and Behnia M. (1998) Modelling of parabolic trough direct steam generation solar collectors, *Solar Energy*, vol. 62, no. 6, pp. 395-406

Price H., Kearney D. (1999) Parabolic-trough technology roadmap: a pathway for sustained commercial development and deployment of parabolic-trough technology, Technology workshop of the U.S. Department of Energy and SunLab

Sargent & Lundy LLC Consulting Group (2003) Assessment of parabolic trough and power tower solar technology cost and performance forecasts, NREL/SR-550-34440, National Renewable Energy Laboratory

Sayigh A. (1999) Renewable energy – the way forward, *Applied Energy*, vol. 64, pp. 15-30

Schlaich, J. (1995) *The solar chimney: electricity from the sun*, Edition Axel Menges, Stuttgart, Germany

Schott-Rohr glass GmbH (2004)

Site: [www.schott.com](http://www.schott.com)

SolarPACES (1999)

Site: [www.solarpaces.org/publications/sp99\\_tec](http://www.solarpaces.org/publications/sp99_tec)

SunLab (2000)

Site: [www.energylan.sandia.gov/sunlab/Snapshot/FACILITY.HTM](http://www.energylan.sandia.gov/sunlab/Snapshot/FACILITY.HTM)

Stine W. B. and Harrigan R. W. (1985) *Solar energy fundamentals and design: with computer applications*, John Wiley & Sons, Inc., United States

Thomas A. (1994) Simple structure for parabolic trough concentrator, *Energy Conversion Management*, vol. 35, no. 7, pp. 569-573

U.S. Department of Energy (2004)

Site: [www.eere.energy.gov/troughnet/](http://www.eere.energy.gov/troughnet/)

U.S. Naval Observatory (2003)

Site: [aa.usno.navy.mil](http://aa.usno.navy.mil)

Walpole R. E. and Myers R. H. (1990) *Probability and statistics for engineers and scientists*,  
4<sup>th</sup> Ed., Macmillan Publishing Company, Singapore

## APPENDIX A

### DESIGN AND CONSTRUCTION OF PTSC

## A.1 Introduction

The development of PTSCs by universities and institutes for research purposes is well documented in the literature. For example, Kalogirou (1996) describes the design of a trough collector with aperture area of  $3.5 \text{ m}^2$ , rim angle of  $90^\circ$  and concentration ratio of 21.2. The performance of the collector is reported in terms of the recommended ASHRAE 93 procedure (ASHRAE, 1991). Ibrahim (1996) reports the performance of a multiple-trough collector, consisting of six connected parabolic troughs, each 1.14 m in length and 0.12 m wide giving a total aperture area of  $0.82 \text{ m}^2$ . Almanza et al. (1997) successfully produced steam in the absorber tubes of an existing 29 m long parabolic trough collector of aperture width 2.5 m and absorber diameter of 25.4 mm. Bakos et al. (1999) describe the construction of a trough with approximately  $12 \text{ m}^2$  of aperture area and the capacity to track the sun about two axes. This is achieved by connecting one end of the parabolic trough to a vertical sliding mechanism and hinged “turret” or pylon.

Key aspects of the design and construction of the structure, heat collecting elements and tracking system of this PTSC are briefly described here.

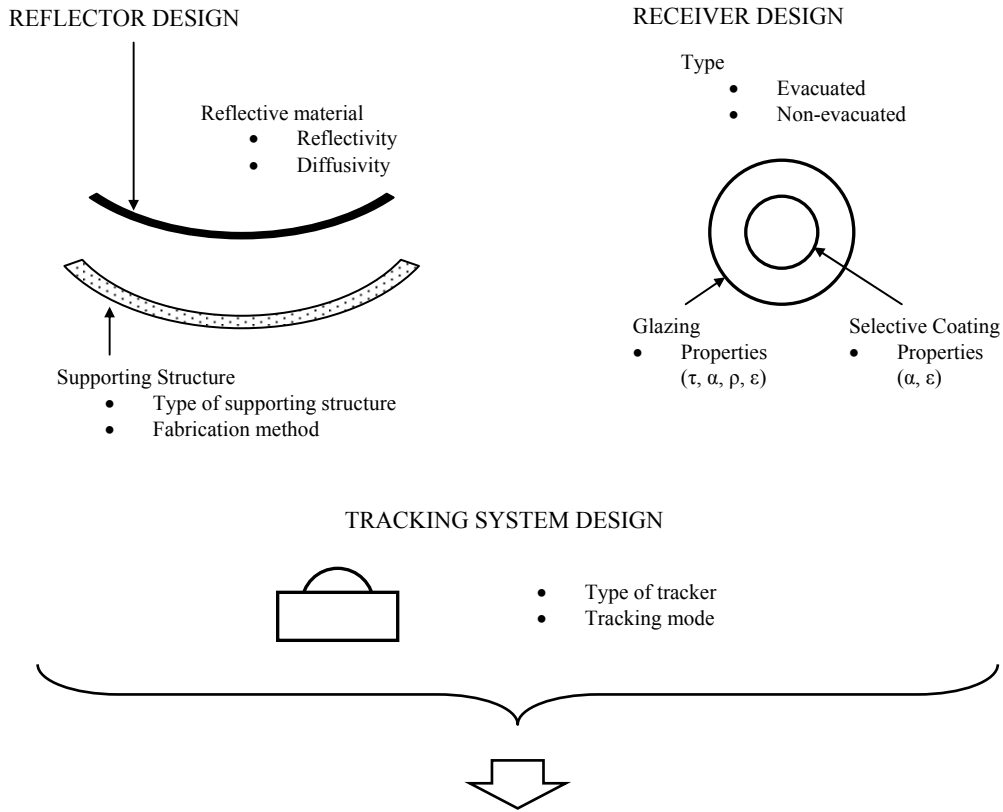
## A.2 Collector Structure

The primary objective in the design and construction of this collector was to ensure that the reflective surface exhibited a stable, accurate parabolic profile. The basics of parabolic geometry (for example, focal length, rim angle, width and height) are readily available in the literature and are omitted here. Factors considered in the construction of this PTSC included optical error tolerance, material cost and availability and manufacturing constraints.

Güven et al. (1986) studied the overall process of parabolic trough design with specific reference to accommodating multiple objectives and working in different design environments. They highlighted the need for a design approach that takes into account the differences between a developed country, like the U.S., and developing nations, where design objectives are not limited to maximising thermal efficiency, but must also favour cheaper, labour-intensive design and production techniques. A schematic diagram of this process of is

shown in figure A.1. The macro-level design stage entails specifying the characteristics of the reflector surface, reflector support structure, receiver and tracking system. In the micro-level stage these subsystem components are integrated.

**MACRO-LEVEL DESIGN: Subsystem design**



**MICRO-LEVEL DESIGN: Subsystem Integration**

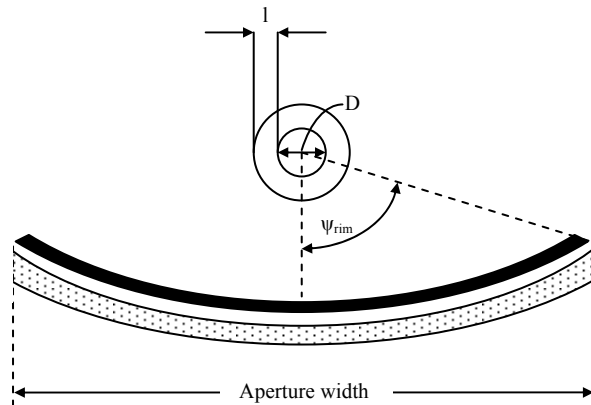


**Figure A.1** PTSC macro- and micro-level design stages proposed by Güven et al. (1986)

The sequence shown in figure A.1 was followed in the design and construction of this PTSC, particularly with regard to the use of universal error parameters in the design of the receiver. Deviations from the process included pre-selecting the rim angle of the collector based on parabolic-rib material constraints and selection of the receiver glass envelope diameter based on availability of Schott tubing, not on the optimum calculated gap width between absorber and glass envelope. These compromises were dictated by material availability and cost and were unavoidable.

Design alternatives for the PTSC structure-type included truss, torque-tube, torque-box, stamped profile and moulded fibre-glass structures. The torque-tube structure (see figure A.2) was selected for simplicity and ease of manufacture.

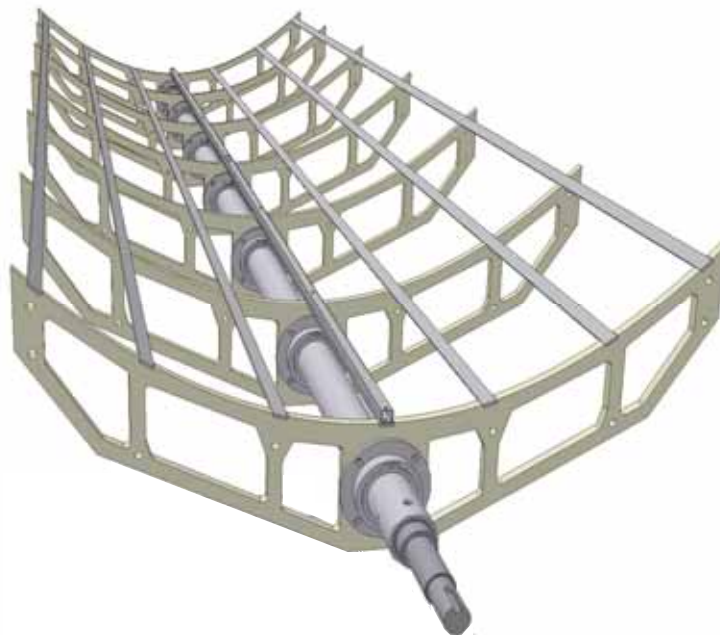


**Figure A.2** PTSC torque-tube collector structure with parabolic ribs

The parabolic ribs were cut from a sheet of polypropylene, to provide the shape of the surface, in a CAD/CAM process using abrasive water jet machining (AWJ). Figures A.3 to A.5 show schematics of the rib, the rib attachment method and the collector structure.

AS

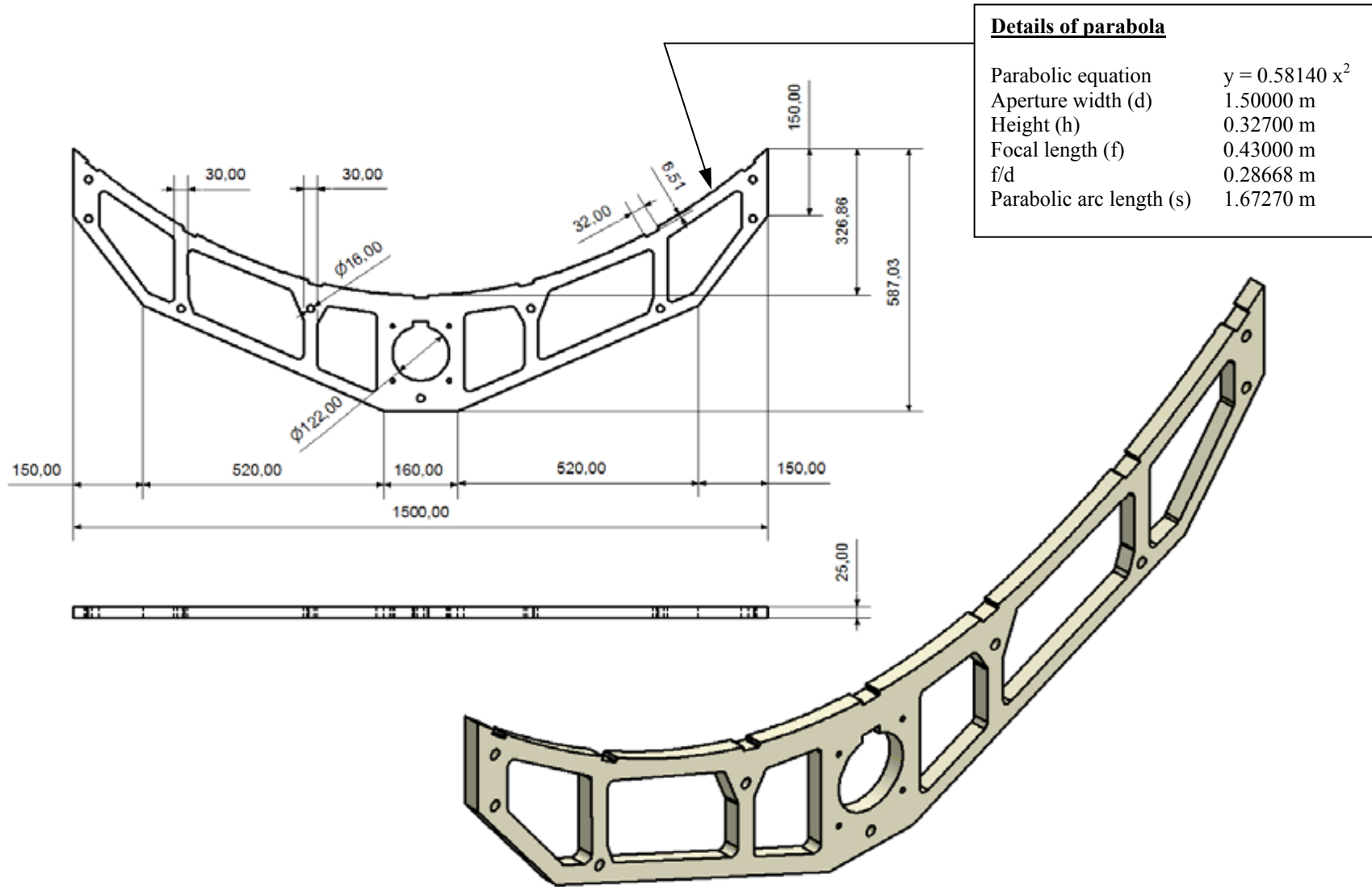


Figure A.3 Polypropylene parabolic rib

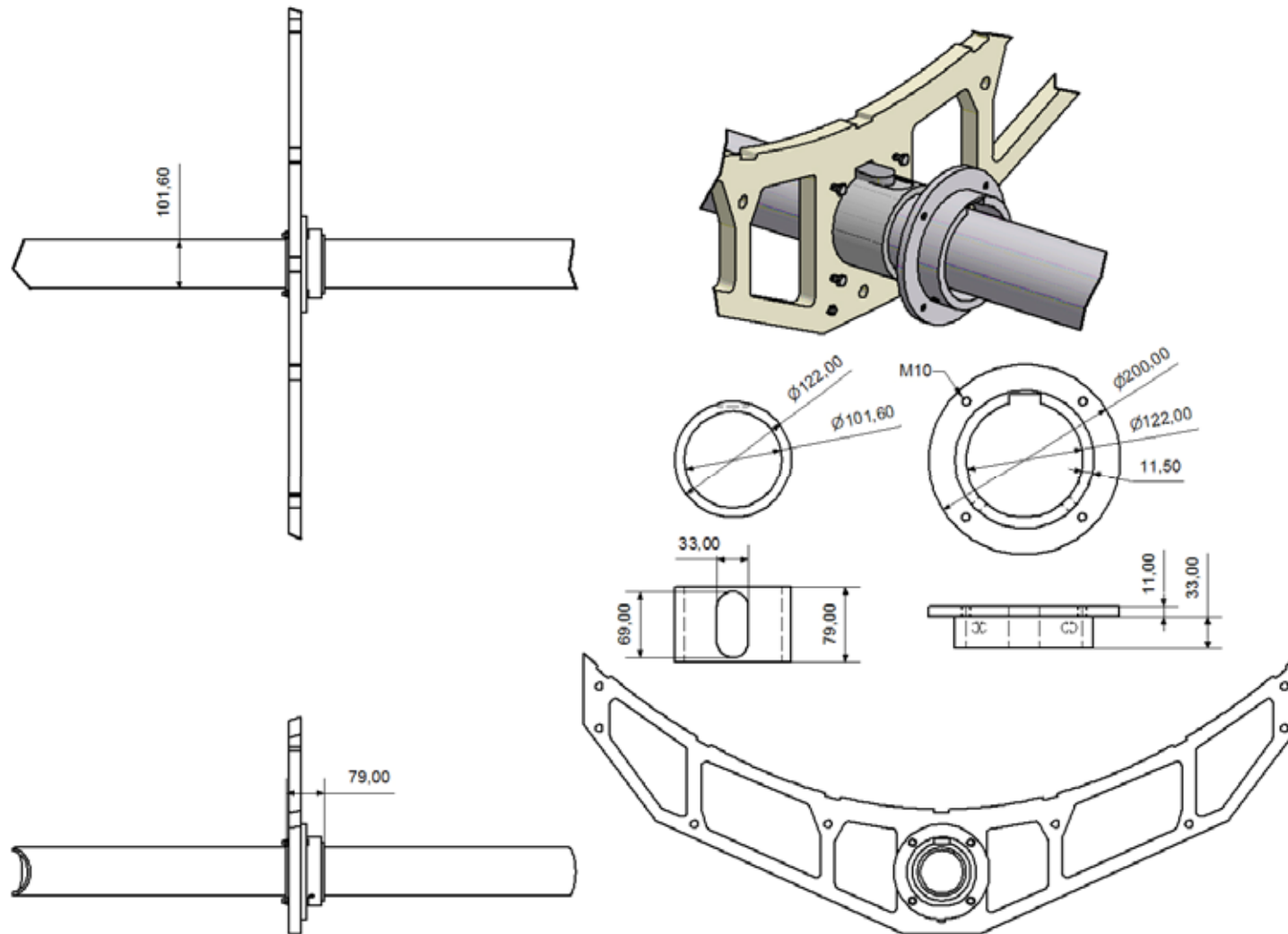
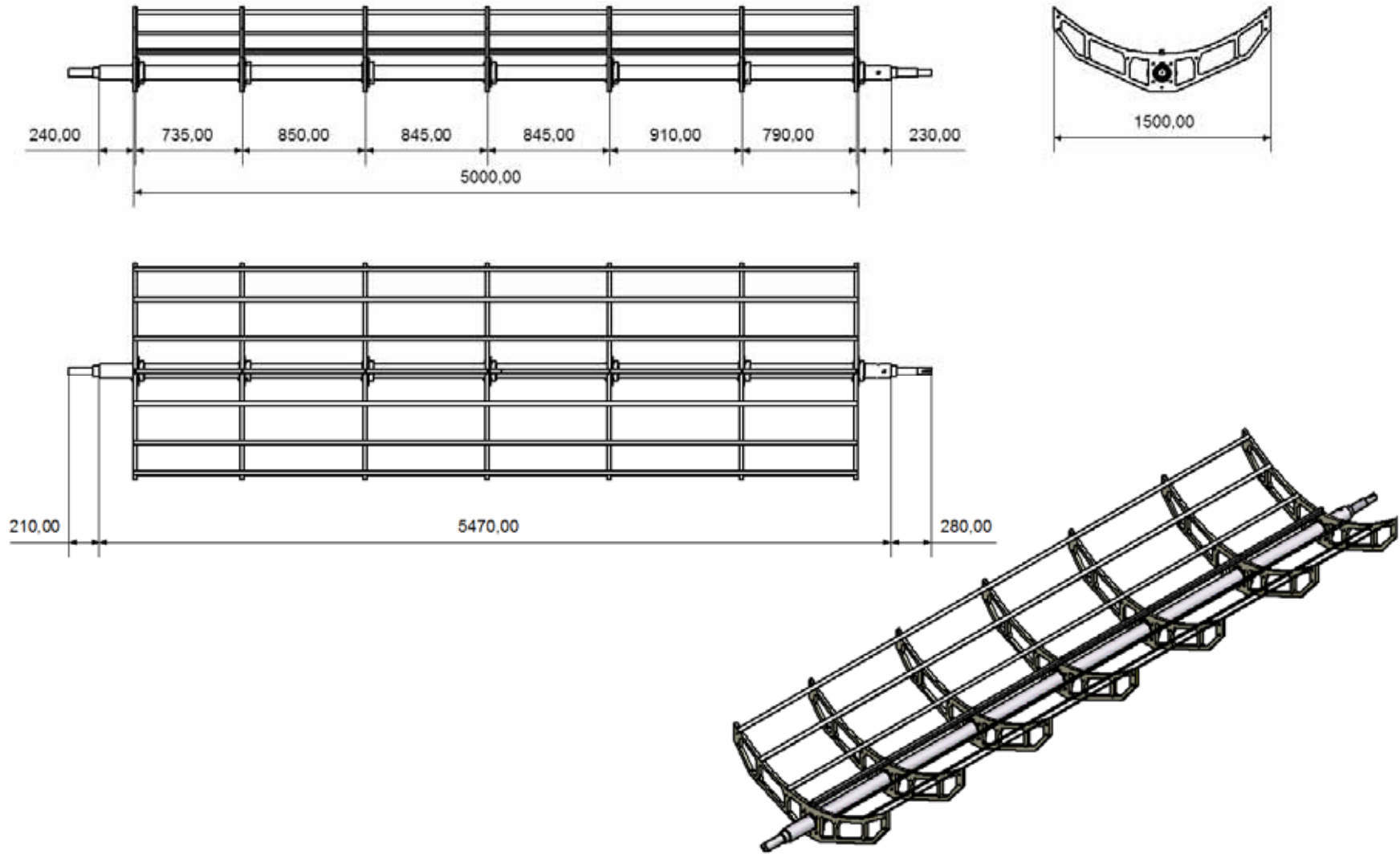


Figure A.4 Parabolic rib attachment method



A7

**Figure A.5** PTSC collector structure

Possible alternatives for the reflective surface of the trough included back-silvered thin glass, bare aluminium, polished stainless steel, aluminised acrylic plastic and advanced composite coatings. Table A.1 provides a comparison of these alternatives.

**Table A.1** Comparison of reflective surface options

<b>Reflective surface</b>	<b>Advantages</b>	<b>Disadvantages</b>
Back-silvered glass	<ul style="list-style-type: none"> <li>• High reflectance</li> <li>• Load carrying capacity</li> <li>• Surface accuracy independent of PTSC structure</li> <li>• Good weathering protection</li> </ul>	<ul style="list-style-type: none"> <li>• Very expensive</li> <li>• Specialised equipment needed for manufacture</li> </ul>
Bare aluminium (eg. Alanod MIRO)	<ul style="list-style-type: none"> <li>• Reflectances up to 95 % possible</li> <li>• Inexpensive</li> <li>• Various gauges available</li> <li>• Lightweight</li> </ul>	<ul style="list-style-type: none"> <li>• No weathering protection</li> <li>• Highly susceptible to abrasion</li> <li>• Requires stable, accurate parabolic structure</li> </ul>
Polished stainless steel	<ul style="list-style-type: none"> <li>• Inexpensive</li> <li>• Various gauges available</li> </ul>	<ul style="list-style-type: none"> <li>• Low reflectance (&lt; 70 %)</li> <li>• Susceptible to abrasion</li> <li>• Requires stable, accurate parabolic structure</li> </ul>
Aluminised acrylic perspex	<ul style="list-style-type: none"> <li>• Reflectance up to 80 % possible</li> <li>• Inexpensive</li> <li>• Lightweight</li> </ul>	<ul style="list-style-type: none"> <li>• Limited weathering protection</li> <li>• Susceptible to abrasion</li> <li>• Requires stable, accurate parabolic structure and substrate</li> <li>• Deforms easily</li> </ul>
Aluminised acrylic film (eg. 3M SA-85)	<ul style="list-style-type: none"> <li>• Reflectance up to 85 % possible</li> <li>• Relatively inexpensive</li> <li>• Some weathering protection</li> </ul>	<ul style="list-style-type: none"> <li>• Susceptible to abrasion</li> <li>• Requires stable, accurate parabolic structure and substrate</li> <li>• Out of production</li> </ul>
Advanced composite film (eg. 3M Vikuiti)	<ul style="list-style-type: none"> <li>• Very high reflectance (&gt; 97 %)</li> <li>• Non-metallic composite</li> </ul>	<ul style="list-style-type: none"> <li>• Susceptible to abrasion</li> <li>• Requires stable, accurate parabolic structure and substrate</li> <li>• No weathering protection</li> <li>• Very expensive</li> </ul>

Early tests with aluminised acrylic Perspex showed high levels of surface distortion. Although it is now out of production, a quantity of SA-85 film was obtained. This was applied to a stainless steel substrate, which was clamped into the profile formed by the parabolic ribs, producing a stable and sufficiently rigid surface (see figure A.6). The clamping system was designed to allow easy swapping of surface sheets for comparative testing of different materials.



(a)



(b)

**Figure A.6** (a) stainless steel substrate prior to installation (b) assuming parabolic shape

### A.3 Heat Collecting Element

The receiver of a PTSC is that element of the system where solar radiation is absorbed and converted primarily into heat. It includes the absorber tube through which the heat transfer fluid flows, the tube transparent cover or envelope, if applicable, and any insulation. In the case of a parabolic trough, which is defined as a linear imaging concentrator, the receiver is located so as to coincide with the focal line of the trough (Duffie and Beckman, 1991).

An optical error analysis was used to determine the size of the absorber for this project. The design and construction of two receivers are briefly described – one unshielded and one with an evacuated glass envelope.

#### A.3.1 Optical error analysis

The design of a receiver must include both optical and thermal considerations. If the optical characteristics of the receiver materials are assumed to be temperature independent, the optical and thermal analyses can be de-coupled and most of the optical design work carried out independently (Güven and Bannerot, 1986a). A good starting point is the definition of collector optical efficiency, which is the ratio of solar energy falling on the surface of the absorber tube (the inner conduit of the receiver) to that which falls on the reflective surface of the collector. It can also be expressed as the product of glass cover transmittance, absorber surface absorptance, collector surface reflectance and the intercept factor.

$$\eta_o = [K_{\alpha\tau}(\theta_i)][(\tau\alpha)_e \rho \gamma]_n \quad (\text{A.1})$$

$K_{\alpha\tau}(\theta_i)$  represents the incidence angle modifier,  $(\tau\alpha)_e$  is the effective transmittance-absorptance factor (relating to the glass shield and absorber surface),  $\rho$  is the reflectance of the mirror surface,  $\gamma$  is the intercept factor and  $[(\tau\alpha)_e \rho \gamma]_n$  represents the product of these factors at or near normal incidence. The intercept factor is defined as the fraction of the reflected radiation that is incident on the absorbing surface of the receiver (Duffie and Beckman, 1991). The factors  $\tau$ ,  $\alpha$  and  $\rho$  represent material properties while the intercept factor  $\gamma$  contains the effects of all optical errors (Güven and Bannerot, 1986a). A good design will maximise the optical efficiency through appropriate material selection and reduction of optical errors.

Optical errors arise from the imperfect reflection of solar radiation off the collector surface and are caused by the finite angular size of the sun (see figure A.7), an inaccurate parabolic profile, non-specular reflectance of the reflective material, imprecise tracking and poor receiver alignment (Stine and Harrigan, 1985).

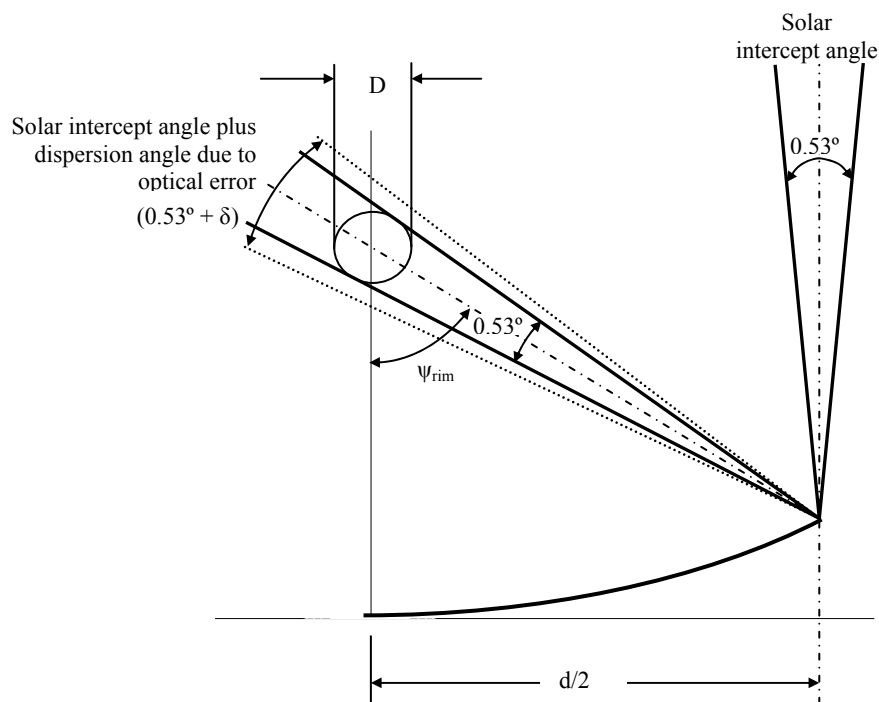


**Figure A.7** Solar intercept angle due to sun width and image spread due to optical errors

The absorber tube should be made large enough to capture as much of the reflected solar energy from the collector surface as possible. Opposing this is the need to minimise absorber diameter to increase the concentration ratio of the collector and cut thermal losses. Sizing the absorber thus becomes a compromise between conflicting requirements. The design process requires knowledge of the intercept factor  $\gamma$ , which in turn requires knowledge of the errors likely to be encountered with the chosen design, construction method, operating loads and the tracking system employed.

Two methods are described in the literature for analysing the nature and effect of optical errors. One treats all optical errors as random and provides a relatively simple method of determining absorber tube diameter  $D$  ('Method A'). A second separates errors into random and nonrandom and allows for the calculation of the PTSC intercept factor ('Method B'). In this study, both were investigated as part of the HCE design process.

#### Method A

In the approach followed by Stine and Harrigan (1985), among others, all errors are treated as independent, random processes with the combined effect determined statistically. Sources of error, quoted in [mrad], are given as: structural (slope imperfections)  $\sigma_{\text{slope}}$ , tracking (sensor and drive non-uniformity)  $\sigma_{\text{tracking}}$ , receiver misalignment  $\sigma_{\text{rec}}$ , mirror specular reflectance  $\sigma_{\text{refl}}$ , and sun width or solar intercept angle  $\sigma_{\text{sun}}$ .

These are either one-dimensional (in the plane of curvature of the parabola) or two-dimensional (out of the plane of curvature) and combined to give a total optical error  $\sigma_{\text{tot}}$  as follows:

$$\sigma_{1D} = \left[ (2\sigma_{\text{slope}})^2 + (\sigma_{\text{sensor}})^2 + (\sigma_{\text{drive}})^2 + (\sigma_{\text{rec}})^2 \right]^{\frac{1}{2}} \quad [\text{mrad}] \quad (\text{A.2})$$

$$\sigma_{2D} = \frac{(\sigma_{\text{sun}}^2 + \sigma_{\text{refl}}^2)^{\frac{1}{2}}}{\cos \theta_i} \quad [\text{mrad}] \quad (\text{A.3})$$

$$\sigma_{\text{tot}} = (\sigma_{1D}^2 + \sigma_{2D}^2)^{\frac{1}{2}} \quad [\text{mrad}] \quad (\text{A.4})$$

The slope error is doubled to account for the implications of Snell's Law. The diameter of the absorber tube  $D$  can be determined from a geometrical analysis of image-spread at the focal point. Thus,

$$D = 2r \tan\left(n \frac{\sigma_{\text{tot}}}{2}\right) \quad [\text{m}] \quad (\text{A.5})$$

where  $r$  is the distance from the reflector surface to the focal point and  $n$  is the number of standard deviations into which the given errors fall (in this approach, the probability associated with the total sum of optical errors falling within  $n$  standard deviations for a standard normal distribution, is effectively the same thing as the intercept factor). By increasing  $n$  the designer can ensure that a higher percentage of the spread image is intercepted ( $n = 1$  guarantees interception of 68.27 % of the image,  $n = 2$  guarantees 95.45 % and  $n = 3$  guarantees 99.73 %). By assuming values for the random errors and selecting a desired intercept factor (probability), the required absorber tube diameter can be calculated. The weakness in this approach is the assumption that all errors are random.

The dimensions of the parabolic trough in this project were used to obtain an approximate absorber diameter from the error analysis of Stine and Harrigan (1985). Based on equation A.5, figure A.8 shows how the required absorber diameter for this PTSC changes with variation in the types and magnitudes of optical errors. Four error sets are considered, as shown in table A.2, ranging from the "best case" scenario (set A1) where the collector contains no errors other than the sun width, to set A5 representing severe imperfections.

**Table A.2** Error sets used to determine absorber diameter in figure A.5

<b>Error Set</b>	<b>Description of Errors</b>
A1 (Best case)	Sun width only – no other errors
A2	Typical PTSC errors as given by Stine and Harrigan (1985)
A3	Errors as reported by Kalogirou for hand-built fiberglass PTSC (1996)
A4	1° tracking error, other errors typical as per set 2
A5 (Worst case)	1° tracking error, twice the structural errors of Set 2, other errors as per set 2

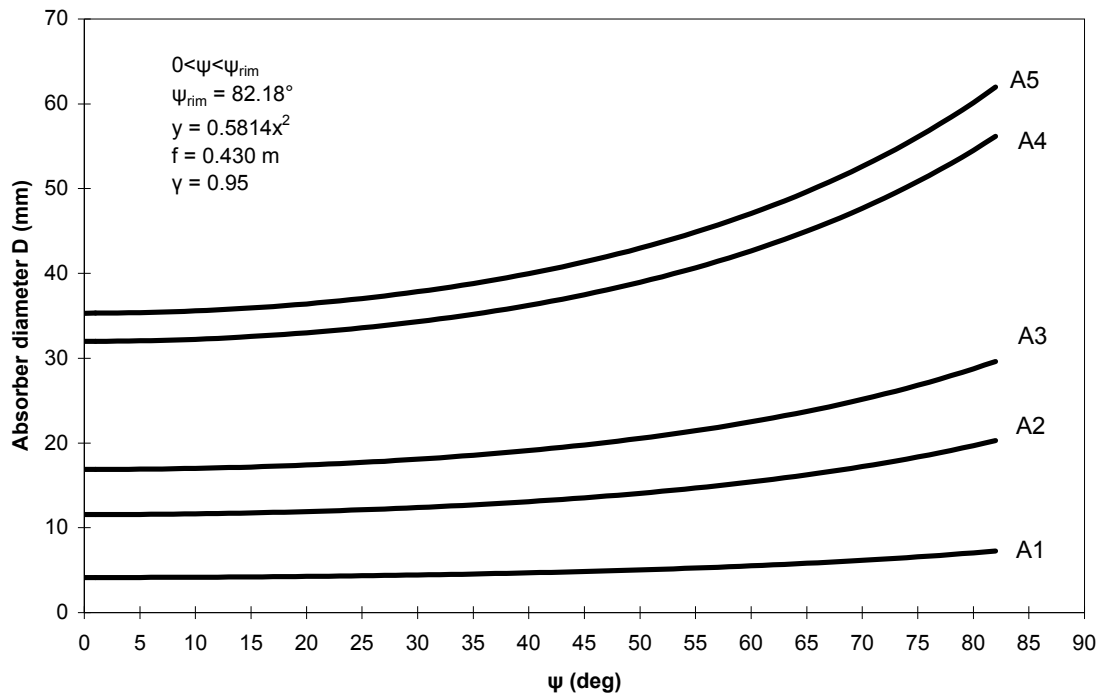


**Figure A.8** Absorber diameter for  $\gamma = 0.95$  using error analysis of Stine and Harrigan (1985)

Figure A.8 is plotted for a statistical capture rate (intercept factor) of 95 % of the total solar radiation falling on the reflector surface. In practice, the absorber diameter must be determined by considering error effects at the extreme value of  $\psi$ , namely the rim angle  $\psi_{rim}$  ( $82.18^\circ$ ), where image spread is greatest.

Assuming errors for the trough in this project similar to those reported by Kalogirou (1996) for a hand-produced fibreglass trough (set A3), figure A.8 gives a required absorber diameter of 30 mm, resulting in a geometric concentration ratio of 15.9. For error sets A4 and A5, D becomes 56 mm and 62 mm respectively. In the best case scenario (set A1) the absorber diameter for this PTSC would be 7.25 mm and the maximum geometric concentration ratio 65.9.

### Method B

In the approach proposed by Güven and Bannerot, (1986b) some optical errors are treated as random (for example light scattering and reflector waviness) and some as nonrandom (for example receiver misalignment and an inaccurate parabolic profile). Whereas in Method A the error values are combined with a chosen intercept factor to generate an absorber diameter,

Method B combines error values (both random and nonrandom) with a chosen absorber diameter to determine the resulting intercept factor. Because optical errors are dealt with more realistically in Method B, it is the more accurate approach, although it is more difficult to implement.

Güven and Bannerot (1986a) argue that not all optical errors are random and although the assumption of normal distributions throughout simplifies the analysis, it is not valid for all practical applications. They propose that scattering effects caused by random slope errors and reflector surface imperfections, as well as transient tracking errors, are random and consequently have normal distributions that can be grouped together in the random error parameter  $\sigma$  (Güven and Bannerot, 1986b).

Nonrandom errors include reflector surface profile errors due to distortion, consistent tracking errors, systematic misalignment of the reflector with respect to the PTSC's intended geographic axis and mislocation of the receiver with respect to the reflector. These are treated as geometric effects. Two independent nonrandom variables are proposed:  $\beta$  in [deg] for the tracking error and reflector misalignment and  $(d_r)_y$  in [cm] for both the receiver mislocation and reflector profile imperfections. It is argued that this method provides a much more realistic approach for:

- one-off projects where errors are not averaged over an entire collector field
- low-technology environments, such as developing countries

The error parameters  $\sigma$ ,  $\beta$  and  $(d_r)_y$  are combined with  $C$  (concentration ratio) and  $D$  (absorber tube diameter) to yield parameters universal to all collector geometries, as given by equations A.6 to A.8.  $\sigma^*$ ,  $\beta^*$  and  $d^*$  are the universal random error parameter in [rad], the universal nonrandom error parameter due to angular errors in [rad] and the universal nonrandom error parameter due to receiver mislocation and reflector profile errors (dimensionless) respectively.

$$\sigma^* = \sigma C \quad [\text{rad}] \quad (\text{A.6})$$

$$\beta^* = \beta C \quad [\text{rad}] \quad (\text{A.7})$$

$$d^* = \frac{(d_r)_y}{D} \quad (\text{A.8})$$

The intercept factor  $\gamma$  is determined numerically using a modified version of the EDEP (Energy DEPosition) code developed at Sandia. This code is not given in the literature although Güven and Bannerot (1986b) provide a closed form expression for  $\gamma$ :

$$\gamma = \frac{1 + \cos \Psi_{\text{rim}}}{2 \sin \Psi_{\text{rim}}} \cdot \int_0^{\Psi_{\text{rim}}} \left[ \text{erf} \left\{ \frac{\sin \Psi_{\text{rim}} (1 + \cos \Psi) (1 - 2d^* \sin \Psi) - \pi \beta^* (1 + \cos \Psi_{\text{rim}})}{\sqrt{2} \pi \sigma^* (1 + \cos \Psi_{\text{rim}})} \right\} \right. \\ \left. - \text{erf} \left\{ \frac{\sin \Psi_{\text{rim}} (1 + \cos \Psi) (1 + 2d^* \sin \Psi) + \pi \beta^* (1 + \cos \Psi_{\text{rim}})}{\sqrt{2} \pi \sigma^* (1 + \cos \Psi_{\text{rim}})} \right\} \right] \frac{d\Psi}{(1 + \cos \Psi)} \quad (\text{A.9})$$

Güven (1994) suggests solving equation A.9 by numerical integration (trapezoidal method). Kalogirou et al. (1996) developed a BASIC computer programme to solve equation A.9 using the Simpson integration method. They present results from their code and compare these with results obtained using a trapezoidal integration method, as well as results from the original EDEP programme. The BASIC programme is found to approximate the EDEP results closely. The approach adopted for this study was as follows:

1. Establish reasonable estimates for the optical errors likely to be encountered during construction of the PTSC, as was done in Method A.
2. Use the absorber diameter and concentration ratio from Method A as a starting point to universalise the random and nonrandom error parameters.
3. Solve equation A.9 for the intercept factor  $\gamma$  using MATLAB code.
4. Investigate the effect of varying error parameters on the intercept factor.
5. Finalise the absorber dimensions, taking into account the results of the analysis, material cost, availability, strength and concentration ratio effects.

Since the error parameters in Method B are defined differently to those in Method A, the literature was consulted to determine reasonable error values for a PTSC constructed under the type of conditions experienced in this project. Güven et al. (1986) give a table of values for three PTSC types: a PTSC typical of the high-technology U.S. trough systems and two lower-technology PTSC types representative of developing country conditions. The developing country values are not measured but estimated by inflating the U.S. high-technology data. (As the authors point out, there were no realistic data available regarding actual hardware for developed countries when the work was published.) These values are shown in table A.3 along with a further 3 error sets, which were modified error values used as estimates for this PTSC project.

**Table A.3** Error sets used in PTSC analysis of Güven et al. (1986)

Parameter	Errors given by Güven et al. (1986)			Error sets for this PTSC		
	U.S. high-tech PTSC	Developing country #1	Developing country #2	Set B1	Set B2	Set B3
$\sigma$ [rad]	0.0064	0.0087	0.0113	0.0087	0.0113	0.0113
$\beta$ [deg]	0.25	0.50	1.00	0.50	1.00	0.375
$(d_r)_y$ [mm]	3.10	6.20	6.20	6.20	6.20	7.75
D [mm]	24.80	24.80	24.80	30.00	30.00	30.00
C	28.00	21.00	16.00	15.92	15.92	15.92
$\sigma^*$ [rad]	0.1792	0.1827	0.1808	0.1385	0.1798	0.1798
$\beta^*$ [rad]	0.1222	0.1833	0.2793	0.1389	0.2778	0.1111
$d^*$	0.125	0.250	0.250	0.2067	0.2067	0.2583

Error set B1 was obtained by using the values from Developing Country #1, together with a starting absorber diameter of 30.00 mm. Set B2 used the values from Developing Country #2 while set B3 used the same random error value  $\sigma$  as set B2, a reduced tracking and reflector misalignment error  $\beta$  and a receiver mislocation error  $(d_r)_y$  inflated by 25 % over the Developing Country #2 case proposed by Güven et al. (1986). The reasons for using these values were as follows:

- It was anticipated that the tracking system for this PTSC would be more accurate than Developing Country #1 owing to the use of sophisticated hardware. Thus the value of  $\beta$  was set midway between the high-technology U.S. case and Developing Country #1
- The set-up of the receiver was undertaken using basic measuring tools, and it was reasoned that  $(d_r)_y$  would likely be greater given the larger size of the collector (increasing the chance of surface distortion) compared to research units described in the literature
- Errors incorporated in  $\sigma$  were likely to be much the same as those proposed by Güven et al. (1986) since the construction of the PTSC was carried out using a mix of basic and advanced fabrication methods and materials (for example, water cutting of the parabolic ribs)

Equation A.9 was solved using a MATLAB programme. The two error function terms in the integral were solved using MATLAB's *erf* function with  $0.5^\circ$  increments. The result was integrated over the total rim angle value using MATLAB's *trapz* trapezoidal numerical integration function. The MATLAB programme was tested prior to use and all variations of the basic "paracept.m" code showed good agreement with values calculated by Güven (also using trapezoidal numerical integration) and reported by Kalogirou et al. (1996). Two of the computer programmes written for the project are included in appendix B. Table A.4 shows the results for  $\gamma$  based on error sets B1, B2 and B3 and determined using the "paracept\_pt.m" code. A starting absorber diameter of 30 mm was used from the Method A analysis.

**Table A.4** Intercept factor for PTSC with rim angle of  $82^\circ$  and aperture width of 1.5 m

	<b>Method B error sets for this PTSC</b>		
<b>Parameter</b>	<b>Set B1</b>	<b>Set B2</b>	<b>Set B3</b>
<b>D [mm]</b>	30.00	30.00	30.00
<b>C</b>	15.92	15.92	15.92
<b><math>\sigma^*</math> [rad]</b>	0.1385	0.1798	0.1798
<b><math>\beta^*</math> [rad]</b>	0.1389	0.2778	0.1111
<b><math>d^*</math></b>	0.2067	0.2067	0.2583
<b><math>\gamma</math></b>	0.8728	0.6148	0.8231

Results for errors sets 1 and 2 showed a sharp reduction in  $\gamma$  from 0.873 to 0.615 as the random, tracking and misalignment errors were increased. Error set B3, which was the best estimate of error parameters for this project, gave an intercept factor of 0.823. This was lower than the 0.95 assumed in Method A but more realistic given the manner in which the error parameters were determined.

Figures A.9 and A.10 illustrate how the error parameters  $\sigma^*$ ,  $\beta^*$  and  $d^*$  combine to degrade  $\gamma$  as they are increased. The graphs are drawn for a rim angle of  $82^\circ$ , representing the PTSC of this project.

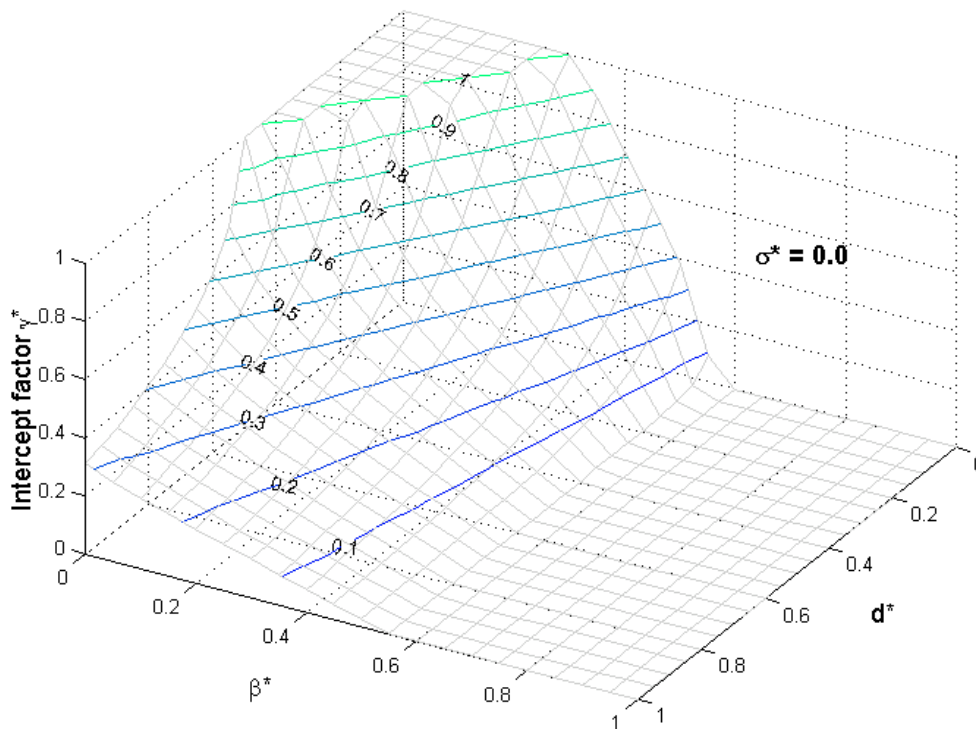


**Figure A.9** Intercept factor  $\gamma$  as a function of  $\beta^*$  and  $d^*$  for  $\sigma^* = 0.0$

The plateau area in figure A.9 shows the PTSC design is fully tolerant of  $\beta^*$  and  $d^*$  values up to 0.30 and 0.45 respectively with no associated reduction in  $\gamma$ . Below  $\sigma^* = 0.10$  the design remains tolerant of  $\beta^*$  and  $d^*$  values up to 0.30 and 0.45, with a reduction in  $\gamma$  of only 10 % from 1.00 to 0.90. The benefit of restricting  $\sigma^*$  (through reduction of random slope errors

during construction) was thus a greater tolerance of systematic profile distortion and misalignment well beyond the levels expected in this project.

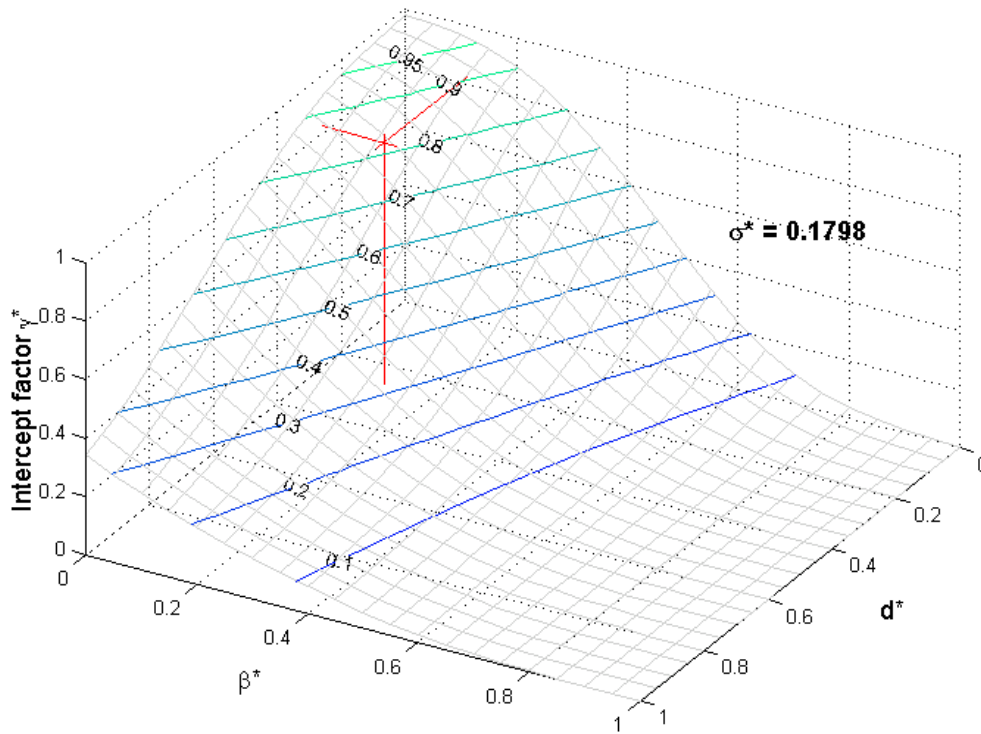


**Figure A.10** Intercept factor  $\gamma$  as a function of  $\beta^*$  and  $d^*$  for  $\sigma^* = 0.1798$  (error set B3 indicated)

Figure A.10 represents the case for the expected value of  $\sigma^* = 0.1798$ . The marker lines for  $\beta^* = 0.1111$  and  $d^* = 0.2583$  indicate the calculated intercept factor of 0.8231. The linearity and gradient of the contour lines ( $\partial\beta^*/\partial d^* \approx 0.64$  for  $\gamma = 0.82$ ) suggested the PTSC design would be more tolerant of receiver mislocation and reflector profile errors than of tracking and misalignment errors. Figure A.11 allows the effect of varying  $\sigma^*$  to be seen on a single graph for constant  $d^* = 0.2583$ . The plateau of figure A.9 where  $\gamma$  remains unaffected by  $\beta^*$  and  $d^*$  is visible for  $\sigma^* = 0.00$ . Also visible is the convergence of the curves for  $\beta^* \approx 0.30$ , indicating that  $\gamma$  becomes independent of  $\sigma^*$  around that value. Figure A.12 shows similar features for  $\beta^* = 0.1111$ , as per error set 3.

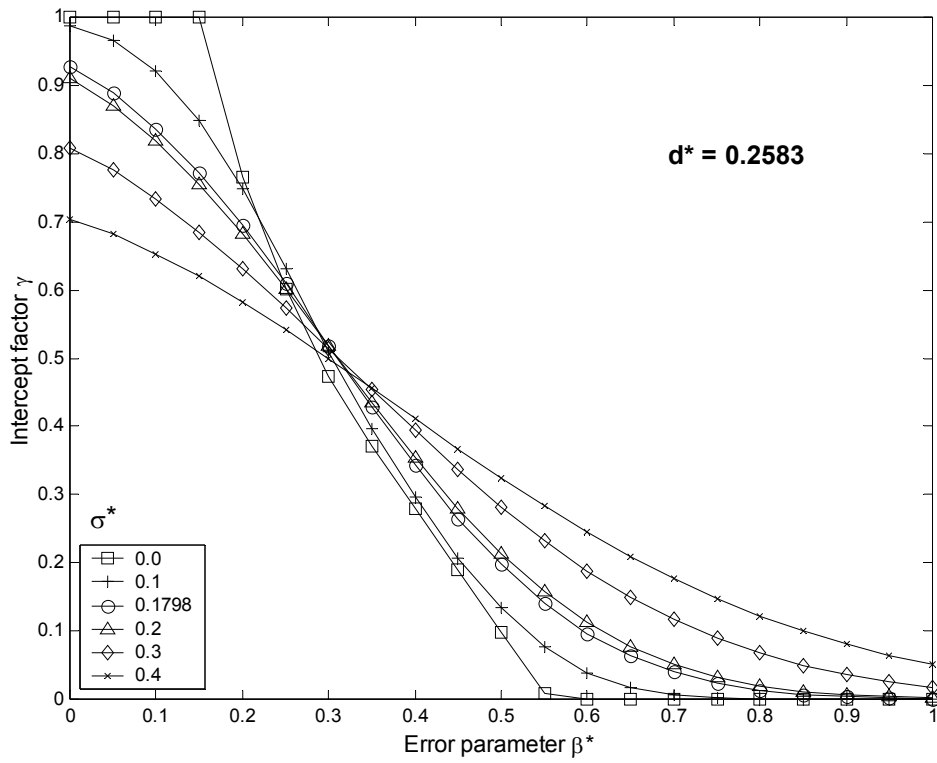


**Figure A.11** Intercept factor as a function of  $\beta^*$  for fixed  $d^*$  and six values of  $\sigma^*$

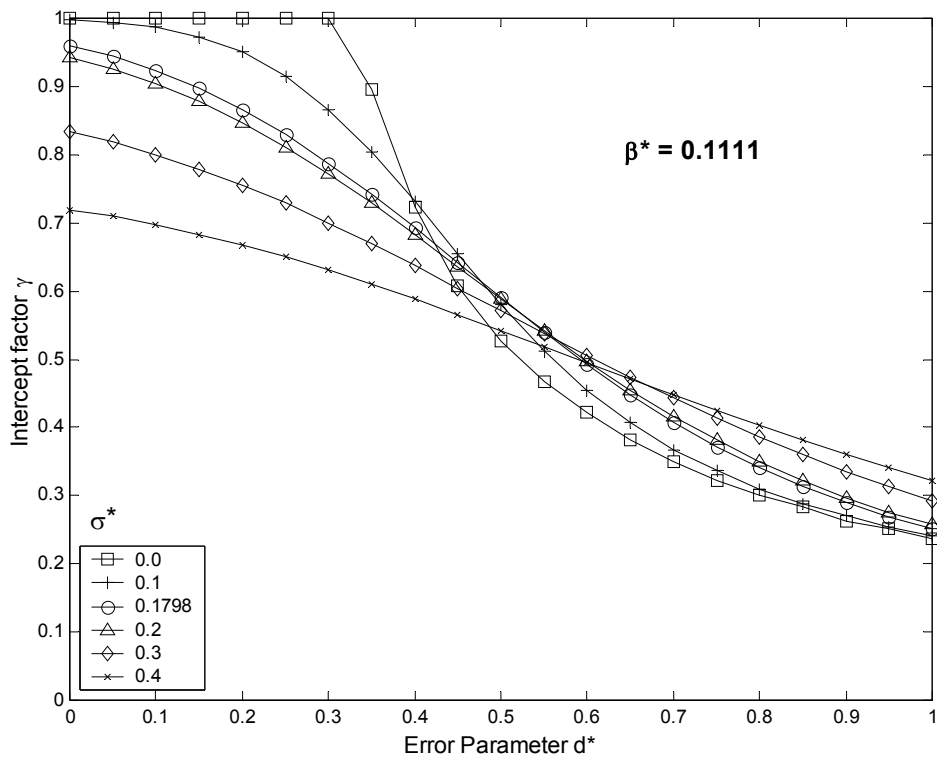


**Figure A.12** Intercept factor as a function of  $d^*$  for fixed  $\beta^*$  and six values of  $\sigma^*$

To evaluate the choice of collector rim angle equation A.9 was solved for a range of rim angles from  $50^\circ$  to  $130^\circ$ . The results are shown in figure A.13. Although concentration ratio is maximised for a rim angle of  $90^\circ$ , the intercept factor increases with increasing rim angle. For a low rim angle of  $50^\circ$ , the maximum possible intercept factor for this PTSC would have been approximately 80 % (assuming zero mislocation error). A rim angle of  $130^\circ$  would have given the best result for  $\gamma$ , but the closeness of the curves for rim angles from  $80^\circ$  to  $130^\circ$  indicates that for the error set used here, the range of optimum rim angles is wide and the chosen value of  $82^\circ$  falls within that range. A higher rim angle would therefore have had little positive effect on the intercept factor.

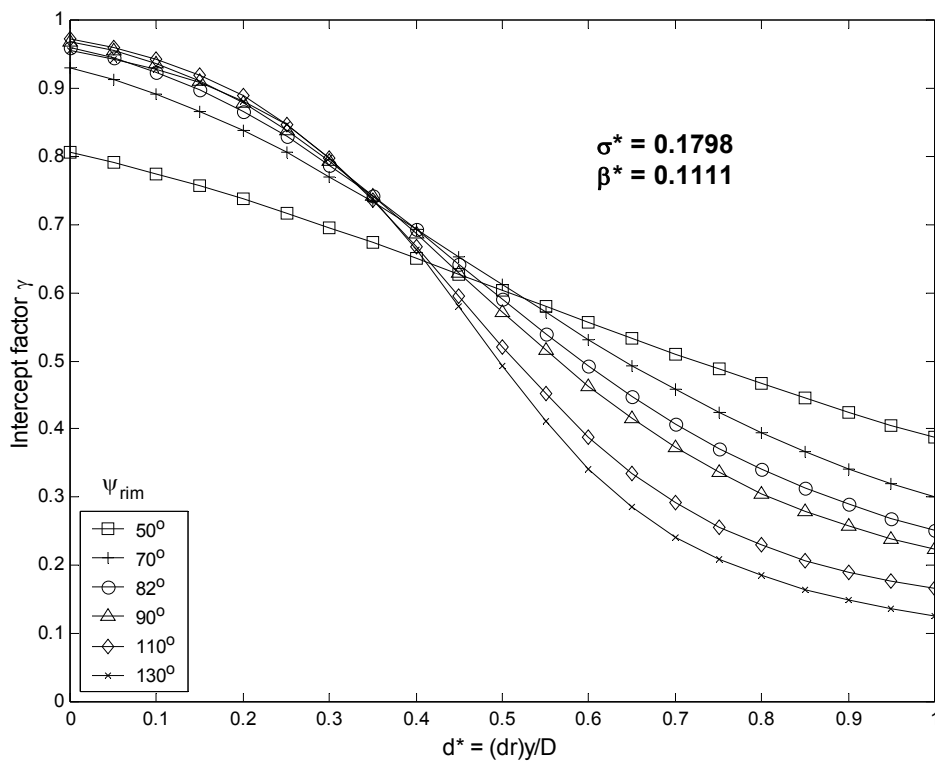


**Figure A.13** Intercept factor as a function of  $d^*$  for fixed  $\beta^*$  and  $\sigma^*$  and six rim angles

Figure A.14 illustrates the relationship between intercept factor and absorber diameter  $D$  for  $\beta^* = 0.1111$ ,  $\sigma^* = 0.1798$  and a range of receiver mislocation values  $(d_r)_y$ . The concentration ratio ( $C$ ) is also shown. Maximising both  $C$  and  $\gamma$  results in opposing requirements, since reducing the diameter to increase  $C$  necessarily implies intercepting less reflected energy from

the surface of the collector, and therefore  $\gamma$  declines. The dominant concern is the intercept factor, however, since this directly affects the optical efficiency of the collector and the final decision on sizing the absorber was made with this in mind. For the error values in set B3 ( $(d_r)_y = 7.75$  mm), increasing the absorber diameter from 30 mm to 45 mm would have increased  $\gamma$  from 82 % to approximately 88 %. At the same time the concentration ratio would have fallen to approximately 11, which was considered unacceptably low. Reducing  $D$  would have driven the operating point in figure 4.37 along the curve to the left and towards a steeper downward trend. This would have placed the PTSC performance at risk had any of the error values been greater in practice than those estimated for error set B3. Based on this, an absorber diameter  $D$  between 27 mm and 32 mm was specified. This ensured that  $\gamma$  and  $C$  remained above 80 % and 15 respectively. Importantly, it maintained a degree of safety had any of the error parameters exceeded their anticipated values.

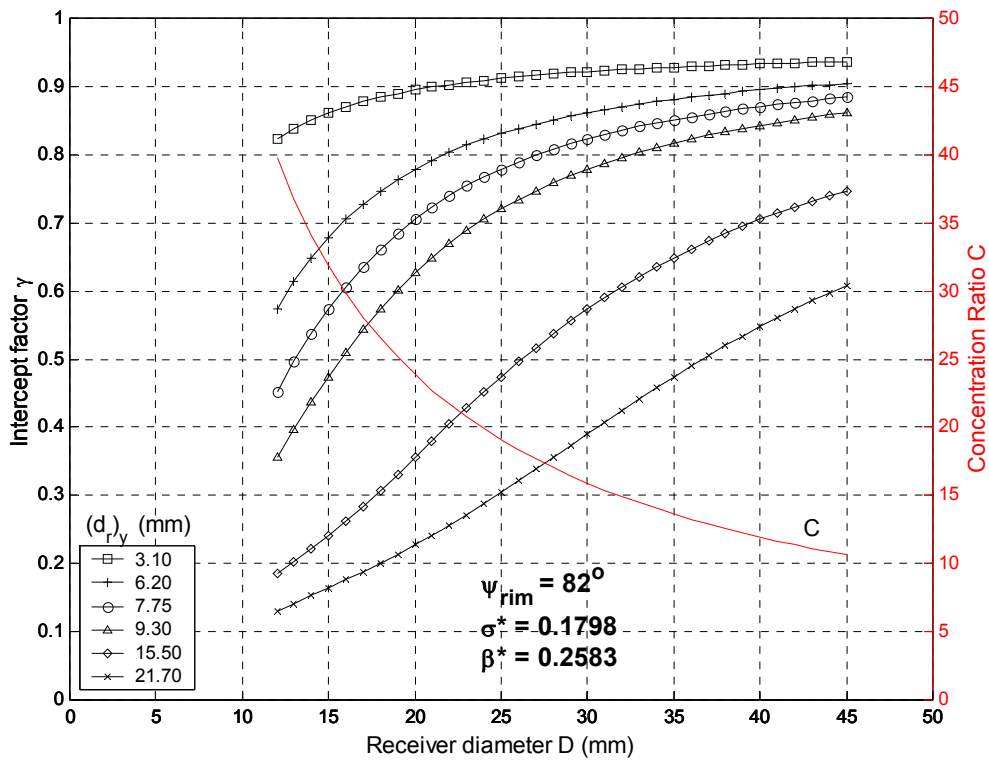


**Figure A.14** Intercept factor as a function of receiver diameter  $D$  for fixed  $\sigma_r^*$  and  $\beta^*$  and six values of  $(d_r)_y$

It should be noted that an obvious shortcoming of all error-based design methods, is that they assume accurate *a priori* knowledge of error magnitudes before the trough has been

constructed. Since very limited data are available for PTSCs built in developing countries, the results obtained for  $\gamma$ , while useful, remain only an approximation. In summary:

- For the error values expected in this project (random and nonrandom) the intercept factor  $\gamma$  was 82.3 %, a reduction from 95 % as determined using the less rigorous method based on random errors only
- By solving equation A.9 for variations in  $\sigma^*$ ,  $\beta^*$  and  $d^*$ , it was possible to identify trends in the behaviour of  $\gamma$  using 3-dimensional and 2-dimensional visualisation
- The region in which the PTSC was expected to operate, showed no serious sensitivity of  $\gamma$  with regards  $\sigma^*$ ,  $\beta^*$  and  $d^*$
- The proposed PTSC design was more tolerant of receiver mislocation and reflector profile errors than of tracking and misalignment errors
- The intercept factor showed a relatively weak dependence on random errors
- The closeness of the  $\gamma$ -curves for rim angles from 80° to 130° indicated that the range of optimum rim angles was wide and included the value of 82° chosen for this PTSC
- An absorber diameter of between 27 mm and 32 mm ensured the intercept factor  $\gamma$  remained above 80 % and the concentration ratio above 15

### A.3.2 Receiver design

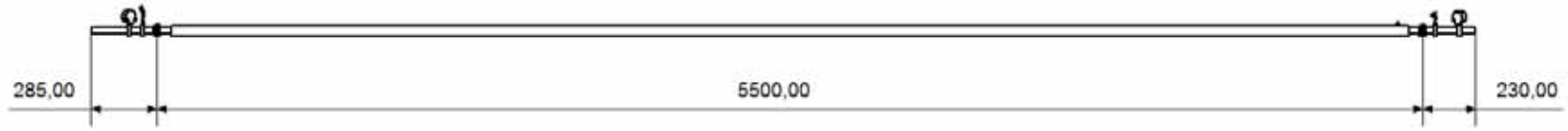
Almanza et al. (1997) showed that steel receivers can bend during operation due to poor thermal conduction and the creation circumferential thermal gradients. They changed their design material to copper. For similar reasons copper was used in this project. The only grade of SABS tubing that fell within the range of diameters determined from the optical error analysis had an outer diameter of 28.58 mm and wall thickness of 1.02 mm. The resulting concentration ratio of the PTSC was 16.70.

To measure the performance of the PTSC, two lengths of piping were designed to accommodate TC probes and pressure gauges, one for each end of the receiver. These were coupled to the absorber tubes via flanges so that they could be disconnected and left in place should the receivers need to be switched. These instrumentation sections were held in position by additional ring holders. They formed the connection between the receiver and the flexible hydraulic hosing at each end of the PTSC.

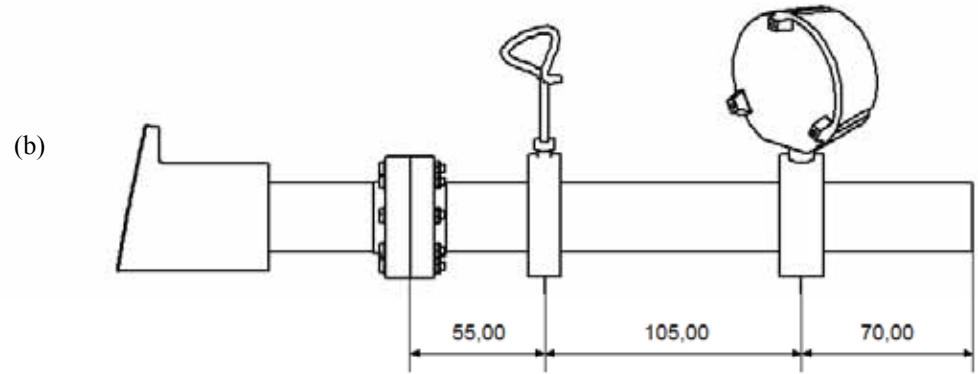
The glass tube of the shielded receiver was manufactured by a chemical glass blower using 4 lengths of Schott Duran borosilicate glass tubing with transmittance of 0.92 and refractive index of 1.473 (Schott, 2004). Each tube had an outer diameter of 44.0 mm, wall thickness of 2.3 mm and length of 1500 mm. This left an annular gap between the absorber and the glass envelope of 5.4 mm, which was the best possible geometry given the diameter of the absorber and the available glass dimensions. The shield was produced in a glass-working lathe with a total length of 5380 mm and a single vent located 50 mm from one end for drawing a vacuum (vent dimensions: length = 15 mm, internal diameter = 7 mm).

A double o-ring arrangement was fabricated to seal the annular gap between the inner absorber tube and the outer glass cylinder of the shielded receiver. A narrow sleeve containing two machined grooves, forming a double-seat, was soldered on to the absorber at each end. Two high-temperature Viton o-rings were slid over the edge of the sleeve and into the recesses formed by the grooves. The o-rings were selected to make contact with the inner surface of the glass envelope when it was slid into position over the absorber, closing the annular gap between the glass and the copper absorber. The arrangement formed a flexible, airtight seal that allowed for expansion of the copper absorber tube within the glass cylinder.

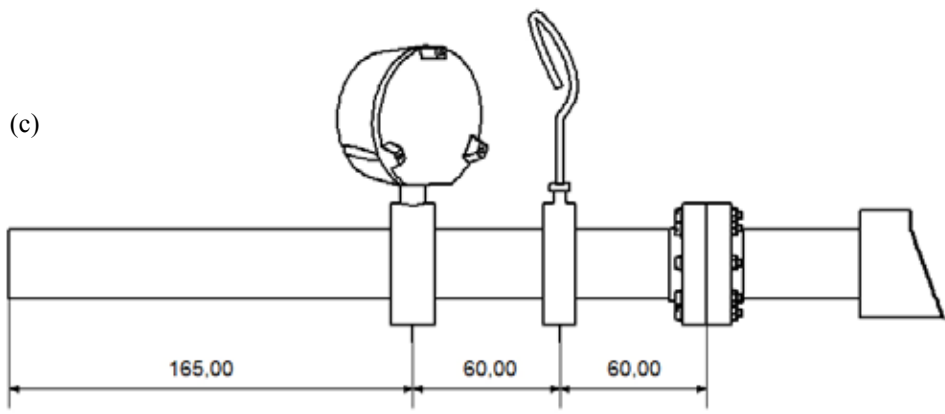
Sketches showing the dimensions of the PTSC receiver and the instrumentation sections are shown in figure A.15. Figure A.16 shows the receiver in place on the trough collector, with the surface of the collector removed. A sketch of one of the ring holders is also shown with its positioning bolts cradling the shielded receiver. Figure A.17 shows the vacuum seal arrangement for the shielded receiver.



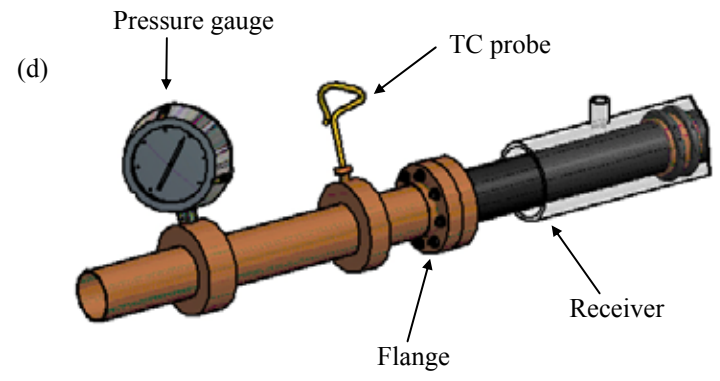
(a)



(b)



(c)



(d)

**Figure A.15** (a) general dimensions of receiver (b) receiver drive end (c) non-drive end with instrumentation sections (d) three-dimensional view of drive end instrumentation section

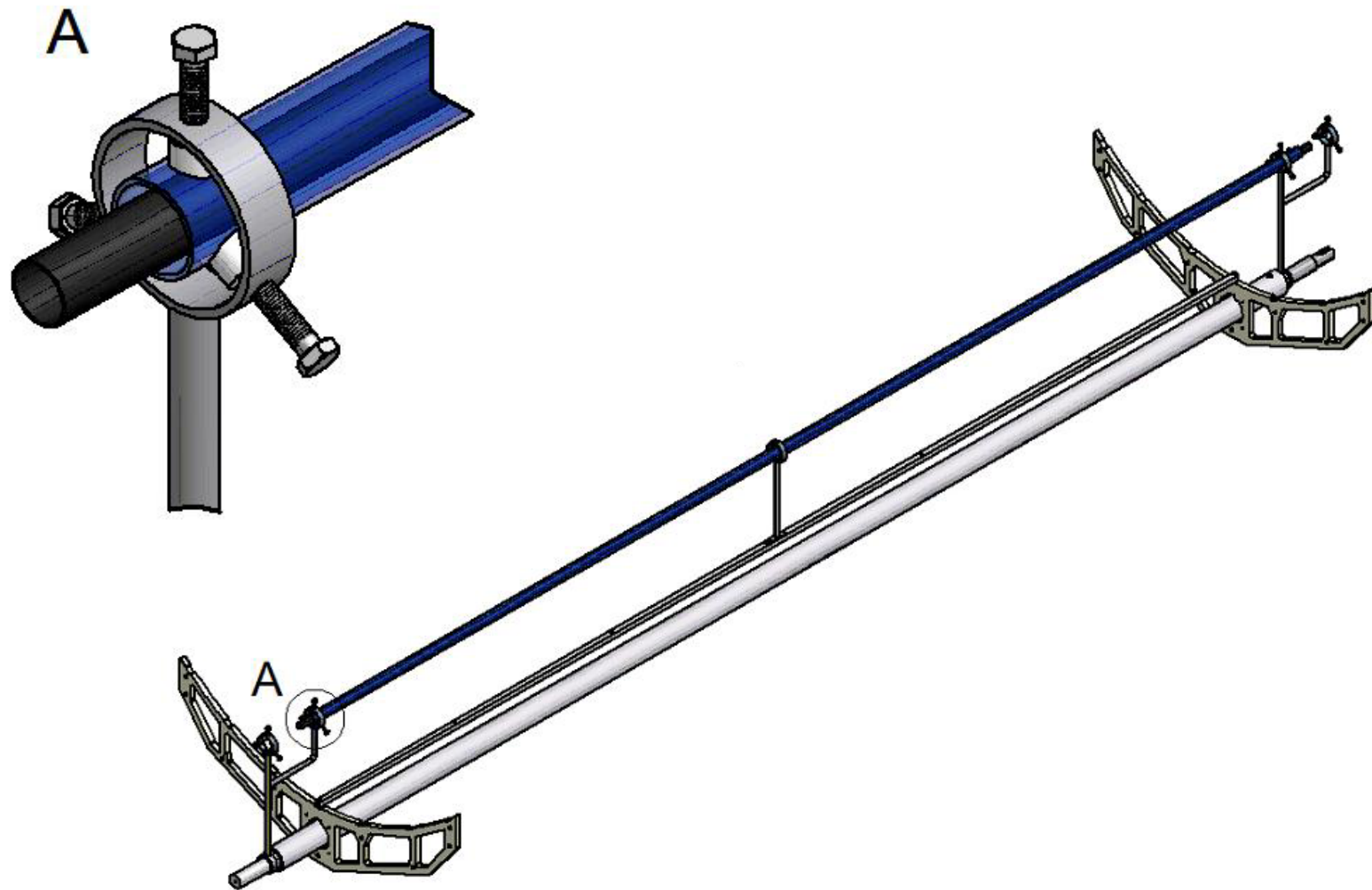


**Figure A.16** (a) detailed view of ring holder and positioning bolts (b) attachment of receiver to the collector structure

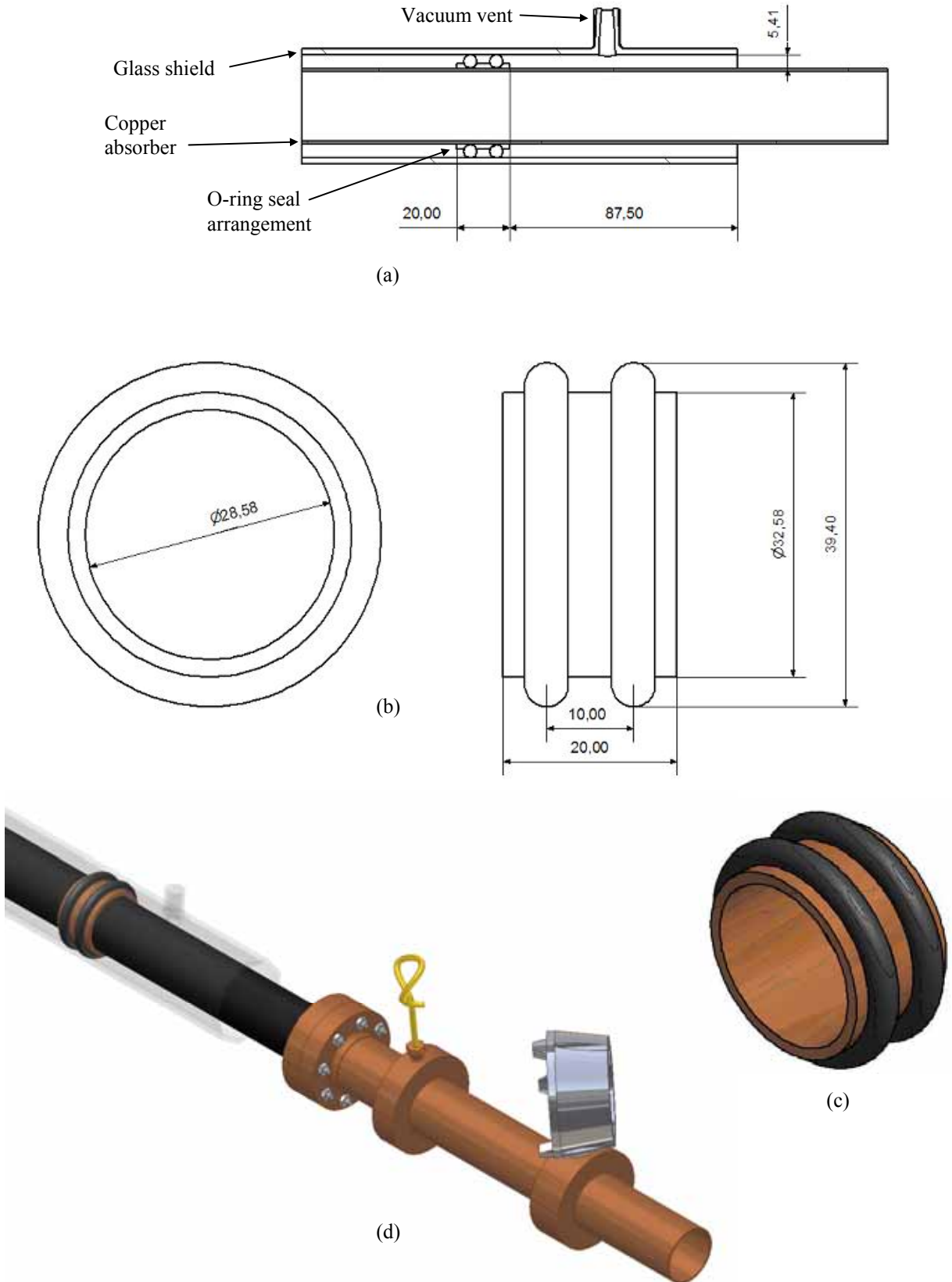


**Figure A.17** (a) glass shield, absorber, vacuum vent and o-ring seal arrangement at drive end (b) and (c) o-ring seal (d) vacuum seal arrangement at drive end of PTSC

Most PTSC absorbers are coated with a low-emittance/high-absorptance selective coating to improve performance. Such a coating was sought, first by experimenting with chemical conversion of the outer surface of the copper tubing, and secondly by application of a commercial spray. Attempts to produce a lasting, absorber-reflector tandem on copper tube samples under laboratory conditions, were not successful. In the first attempt, samples of copper tube were cleaned with acetone and immersed in a commercial solution of ammonium sulphide ( $\text{NH}_4\text{S}$ ) to produce a black copper sulphide ( $\text{Cu}_2\text{S}$ ) coating. The samples were exposed to the sulphide solution for increasing periods of time to test the surface quality. Figure A.18 (a) shows five of the test pieces. Severe peeling of the coating is visible on three of the tubes. Best results were obtained for a tube exposed to the chemical solution for a period of 40 s. This coating appeared reasonably stable though the initial dark, velvet finish was easily rubbed off. The long-term durability of the coating remained questionable. Thermal emittance results were disappointing with none of the samples giving a value below 0.72 up to temperatures of 100 °C. The value of emittance (0.20) reported by Agnihotri and Gupta (1981) could not be reproduced and no South African laboratory could be found to test solar absorptance ( $\alpha$ ), which the above authors give as 0.79.



**Figure A.18** (a) Samples of tube with  $\text{Cu}_2\text{S}$  coating obtained after exposure to  $\text{NH}_4\text{S}$  for (left to right) 20 s, 40 s, 60 s, 120 s and 5 min (b)  $\text{CuO}$  surface coating showing blue-black finish

Attempts were made to produce a copper oxide ( $\text{CuO}$ ) film on sample tubes by immersing them in a bath of sodium hydroxide ( $\text{NaOH}$ ) and sodium chloride ( $\text{NaCl}$ ) at approximately

140 °C for between 3 min and 13 min. These were only partially successful. Whereas the Cu<sub>2</sub>S film had appeared matt-black, the CuO treatment produced only a blue-black surface that was still mostly reflective. The samples were tested for emittance and showed a value of 0.29 at 90 °C, though this was probably due to the weak surface coating. Figure A.18 (b) shows a length of copper tube with the CuO coating applied.

A solution to the coating problem was found with a commercial product called Solkote Hi/Sorb II (Solkote). This is a spray-on liquid specially formulated for solar thermal applications, giving a tested emittance of 0.28 to 0.49 and absorptance of 0.88 to 0.94. Advantages included easy application to the copper absorbers using a standard spray gun, good long-term stability and excellent optical properties (including published values for emittance and absorptance).

#### A.4 Drive, Tracking and Control System (DTCS)

A brief description is given of the design and implementation of a drive, tracking and control system for the PTSC. This was a collaborative work between the author and Naidoo (2005). The author's responsibilities included specifying DTCS requirements selecting the tracking methodology, selecting and analysing a suitable tracking algorithm and specifying the drive hardware.

The requirements of the tracking system were:

- To control the PTSC so as to track the sun accurately about a single axis
- To offer sufficient flexibility to the operator of the system so as to enable the full array of PTSC performance tests to be completed
- To ensure safe operation of the PTSC
- To be upgradeable in time from a pure tracking system to a fully functional control system

Linear imaging concentrators can be tracked about one axis (single-axis tracking) or two axes (double-axis tracking) though in practice, two-axis tracking is not feasible for commercial systems of great length. They are normally aligned along a true north-south (N-S) line or a true east-west (E-W) line, though any alignment is technically possible. In deciding on the

alignment, primary concerns are the amount of energy captured over the course of a year and the demands of the market. For example, in the SEGS plants, the collectors are aligned N-S, which results in slightly less energy captured over a year, but which favours summertime operation when peak power is needed and its sale brings the greatest revenue (Duffie and Beckman, 1991).

The amount of energy captured is largely a function of seasonal changes in sun strength and its angle of incidence ( $\theta_i$ ), which is the angle between the sun's rays and a normal to the collector aperture, when the collector is in focus. Figure A.19 illustrates how  $\theta_i$  changes seasonally for a PTSC aligned N-S and located at the solar energy test facility at Mangosuthu Technikon.

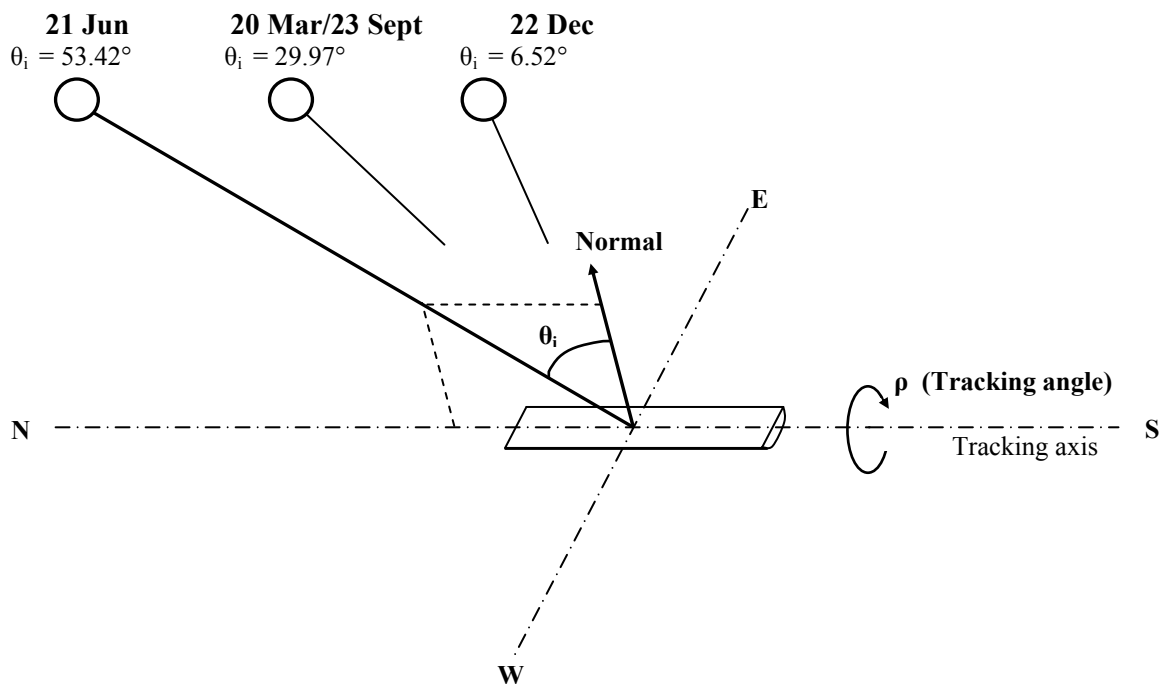


**Figure A.19** Schematic diagram of incidence angle  $\theta_i$  at solar noon on solstices and equinoxes for a PTSC located in Durban, South Africa, and aligned in the N-S direction (adapted from Stine and Harrigan, 1985)

Values of  $\theta_i$  less than zero are possible for Durban during the summer months due to the sun's apparent motion around the outside of an angled disc whose centre shifts along an axis inclined to the horizon by the latitude angle, pointing toward Polaris. Thus in mid-summer the sun will rise behind a Durban-based observer who faces north, only to appear slightly north of the observer at solar noon.

Consideration of the effects of  $\theta_i$  is important because PTSC performance is negatively affected as  $\theta_i$  increases. (This effect is quantified in equations A.1 and 4.1.) It was decided to align this PTSC along an N-S line for the following reasons:

- More stable daily test conditions are possible with respect to  $\theta_i$  with an N-S orientation
- Although  $\theta_i$  changes throughout the day for N-S aligned collectors, this change is less in magnitude than for E-W alignment and the change is relatively slow so that test results are negligibly affected
- The rate of change in angle of incidence for E-W aligned collectors throughout the day is much greater and obtaining test results for a specific angle of incidence is difficult

The operating modes specified in the design of the DTCS are summarised in table A.5.

**Table A.5** Operating modes for the DTCS

<u>Mode</u>	<u>Trough Response</u>	<u>Description</u>
1 a	Jog left slow	Manual positioning using on/off switch
1 b	Jog left fast	Manual positioning using on/off switch
1 c	Jog right slow	Manual positioning using on/off switch
1 d	Jog right fast	Manual positioning using on/off switch
2	Fixed rate tracking	PLC instructs motor to switch on and off to maintain fixed angular velocity of 0.25 °/min
3	PSA tracking	PLC instructs motor to turn through a calculated number of pulses on the encoder to locate the sun using the PSA algorithm. Motor switches on and off to maintain focus according to PSA algorithm
4	Stop/park	Stop all operations and hold as is

To ensure a level of tracking accuracy consistent with the value of the error parameter  $\beta$  adopted in A.3.1, a maximum tracking error of  $0.2^\circ$  was assumed. This was in line with the tracking system described by Kalogirou (1996a) for a smaller research trough. (In table A.3 the value of  $\beta$  was set at  $0.375^\circ$  which includes an allowance for misalignment as well as tracking error.)

For Mode 2, or fixed rate tracking, a control scheme was developed by considering the motion of the sun relative to the PTSC. Figure A.20 shows the sun's movement from A through B to C and the development of the tracking error as the collector stands still between corrective steps.

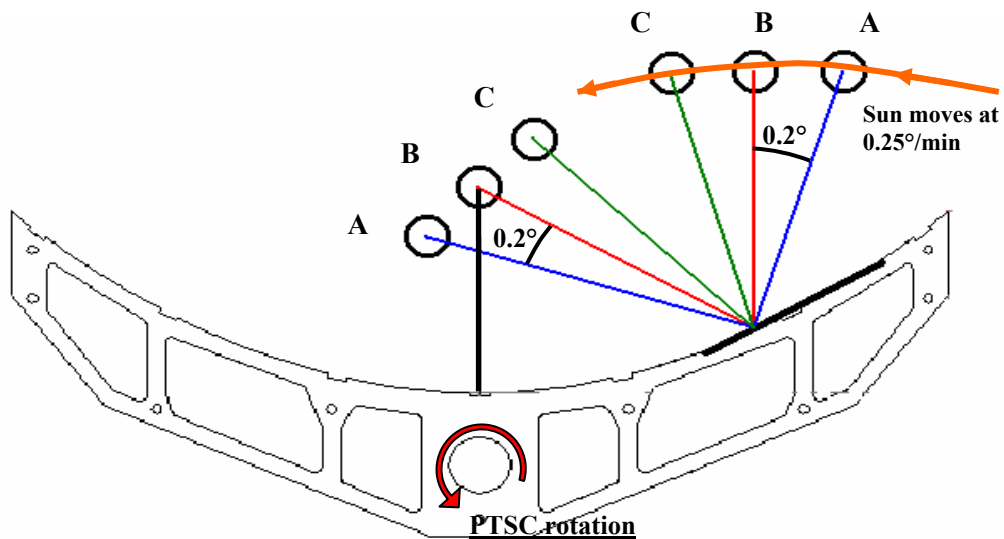


**Figure A.20** Development of tracking error as sun moves through PTSC focus

The collector is correctly focused in position B. For a tracking error of  $0.2^\circ$  either side of B, the trough can be positioned ahead (west) of the sun at A and left standing until the sun moves through a total of  $0.4^\circ$  which would take 96 s. Once the sun reaches C, the DTCS must rotate the trough west through  $0.4^\circ$  to reposition for A. The process is therefore a series of discrete, corrective movements through a fixed angle.

For the rotary encoder used, a rotational movement of  $0.4^\circ$  equated to 2.79 pulses (0.144  $^\circ$ /pulse). Trough corrections were therefore made with 2 pulses to ensure that the maximum

misalignment error was not exceeded. This required a trough angular speed of  $0.288/4 = 0.072$  °/s for a VSD/motor “on-time” of 4 s. Working back through the drive train, the gearbox input speed (equal to the VSD output speed) would be 33.34 °/s or 5.56 rev/min. The time interval between corrective steps was therefore  $(0.288/0.25)60 = 69.12$  s, minus the 4 s required for the trough to rotate into its new position, that is, 65.12 s.

The following is noted:

- Provided the angular error limit of  $0.2^\circ$  was not exceeded, many other combinations of VSD switching-rate and “on-time” would have given the same overall result
- The analysis provided target values for drive speed and motor on-time during the design of the system. Because of added factors such as the VSD ramp time and other drive settings, the values were modified during testing. Counting pulses (instead of time) during each corrective tracking step was found to offer better accuracy (see 5.2.1)

Virtual tracking of the PTSC was accomplished using the PSA Algorithm. This was developed by workers at the Plataforma Solar de Almeria (Blanco-Muriel et al., 2001). The only inputs to the calculation are geographic latitude and longitude (entered in degrees) and Universal Time in year, month, day, hours, minutes and seconds. The algorithm proceeds through the following steps:

- Calculate the Julian Day
- Determine the ecliptic coordinates of the sun
- Convert ecliptic coordinates to celestial coordinates
- Convert celestial coordinates to horizontal Earth-based coordinates and output the solar vector consisting of azimuth and zenith angles ( $A$  and  $\theta_z$ )

Figure A.21 illustrates the relationship between a PTSC aligned in the N-S direction and the angles  $A$ ,  $\theta_z$  and  $\rho_T$ . Sixteen computations are performed to determine the solar vector, consisting of the solar azimuth and zenith angles.

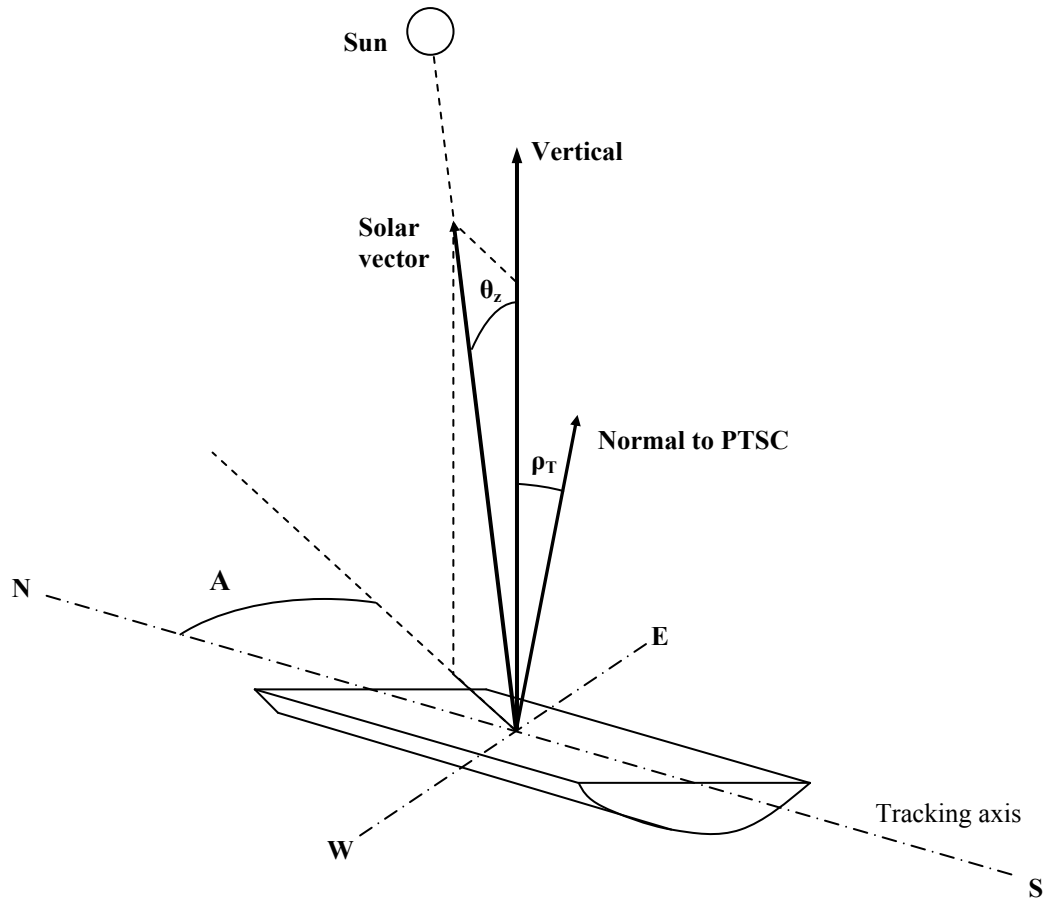


**Figure A.21** Schematic diagram of the solar vector ( $\theta_z$  and A) and tracking angle ( $\rho$ ) for an N-S aligned PTSC rotated through  $\rho_T$  degrees to the east

To ensure correct implementation of the PSA Algorithm, a number of MATLAB programmes were written and the output compared with an online software product of the United States Naval Observatory (USNO) called the Multi-Year Interactive Computer Almanac (MICA), which gives solar data accurate to within half a second of arc (U.S. Naval Observatory, 2003). Results showed that the MATLAB code ran without error (see appendix C). The code was implemented on the system PLC by Naidoo (2005) to enable Mode 3 tracking.

#### A.5 Summary

The key features of the PTSC system designed and constructed for this project are presented in table A.6, together with a brief summary of motivating factors.

**Table A.6** Summary of key features of PTSC

<b><u>Feature</u></b>	<b><u>Motivation</u></b>
Torque-tube concept	<ul style="list-style-type: none"> <li>• Minimal joining and welding of collector structural components</li> <li>• Allows parabolic ribs to be positioned accurately in parallel along the tubular “spine”</li> <li>• Good solution based on cost and simplicity</li> </ul>
Rim angle: $\psi_{rim} = 82$	<ul style="list-style-type: none"> <li>• Rim angles near <math>90^\circ</math> maximise concentration ratio</li> <li>• Rim angles greater than <math>90^\circ</math> are more error-tolerant but produce “deeper” parabolic shape and require more rib material</li> <li>• More ribs of aperture width 1.500 m could be cut from a single sheet of polypropylene with <math>\psi_{rim} = 82^\circ</math> than for higher rim angles</li> <li>• Deeper parabolic ribs are potentially less stiff</li> </ul>
Parabolic ribs water-cut from polypropylene sheet	<ul style="list-style-type: none"> <li>• Polypropylene sheet provides edge thickness for support of the reflective surface without an excessive weight penalty</li> <li>• AWJ machine accepts DXF drawings, simplifying design and manufacture</li> <li>• AWJ technology provides high accuracy</li> <li>• Laser cutting of polypropylene not possible</li> </ul>
Trough dimensions 1.5 m x 5.0 m	<ul style="list-style-type: none"> <li>• Aluminium torque-tube readily available in 6m length</li> <li>• Test module of 5 m x 1.5 m approximated smaller commercial trough modules in aperture area (eg. Acurex 3001 (3.05 m x 1.83 m), IST (2.3 m x 6.1 m), Luz LS-1 (2.5 m x 6 m)), providing more realistic idea of design, manufacturing and material-selection challenges</li> <li>• Polypropylene sheet readily available in 1.5 m x 3.0 m size.</li> <li>• Smaller troughs are easier to make and test but provide less exposure to commercial design challenges</li> </ul>
Stainless steel reflective surface with SA-85 film	<ul style="list-style-type: none"> <li>• Tests showed aluminised acrylic panels distorted when installed</li> <li>• Stainless steel provided stable substrate</li> <li>• SA-85 film was the only practical high-reflectance/low-cost option</li> </ul>
Copper absorber of diameter 28.58 mm with selective coating	<ul style="list-style-type: none"> <li>• Copper reduced thermal gradients in absorber wall</li> <li>• Solkote provided low-cost, easily applied selective coating to maximise absorption and minimise thermal loss</li> <li>• Tests on chemical conversion coatings were only partially successful</li> <li>• Optical error analysis showed absorber diameter between 27 mm and 32 mm would ensure <math>\gamma &gt; 80\%</math> and <math>C &gt; 15</math> for anticipated errors</li> <li>• Final concentration ratio: <math>C = 16.70</math></li> <li>• Final calculated intercept factor: <math>\gamma = 0.8231</math></li> </ul>

**Table A.6 (Continued)** Summary of key features of PTSC

<b><u>Feature</u></b>	<b><u>Motivation</u></b>
Glass-shielded and unshielded receivers	<ul style="list-style-type: none"> <li>• Creating shielded and unshielded receivers allowed for comparison between their performance</li> </ul>
Optical properties	<ul style="list-style-type: none"> <li>• SA-85 surface reflectance <math>\rho = 0.83</math></li> <li>• Schott glass shield transmittance <math>\tau = 0.92</math></li> <li>• Solkote surface absorptance <math>\alpha = 0.88</math> and thermal emittance <math>\varepsilon = 0.49</math></li> <li>• Optical efficiencies: 0.601 (unshielded) and 0.553 (glass-shielded)</li> </ul>
Water circulation system with test flow rate 300 L/hr	<ul style="list-style-type: none"> <li>• Required flexible system to test PTSC according to principles of ASHRAE 93 standard (1991)</li> <li>• Two-tank system enabled high temperature water supply to PTSC</li> <li>• Flow rate of 300 L/hr ensured turbulent flow and reasonable residence time in receiver</li> </ul>
Positive displacement pump with VSD on motor	<ul style="list-style-type: none"> <li>• Helical element pump ensured good performance with regard to flow rate versus pressure in the required operating range</li> <li>• VSD permitted accurate, uncomplicated control of flow rate for testing at reasonable cost</li> </ul>
Tracking system with multiple modes of operation	<ul style="list-style-type: none"> <li>• Manual control of PTSC as well as automatic tracking necessary for completion of collector tests</li> <li>• PSA algorithm highly accurate, relatively simple to implement and superior to existing numerical algorithms</li> </ul>
Drive system with AC motor, VSD and PLC	<ul style="list-style-type: none"> <li>• AC motor provided greater flexibility when coupled to VSD than alternative systems using stepper motors or DC drives</li> <li>• VSD and PLC combination expanded capabilities of system to enable future development of DTCS based on intelligent control principles</li> </ul>

## APPENDIX B

### MATLAB CODE FOR PTSC INTERCEPT FACTOR

## MATLAB code for solving equation A.9 for $\gamma$

### 1. Paracept\_pt.m

%Paracept\_pt solves equation A.9 using MATLAB's 'erf' function (for the error %function) and 'trapz' for the trapezoidal numerical integration technique. The %result is a single point value for the intercept factor (gamma). This code forms %the backbone for the other MATLAB programmes written to analyse the behaviour of %gamma when the universal error parameters sigma\*, beta\* and d\* are changed.

```
clear
clc
clear variables
format long
format compact

%Enter the PTSC data
phrm = input('Enter the Parabolic Trough rim angle in degrees (phi_rim) \n');
fprintf('\n');
sgsta = input('Enter the universal random error parameter \sigma* \n');
fprintf('\n');
bsta = input('Enter the universal non-random error parameter beta* \n');
fprintf('\n');
dsta = input('Enter the universal non-random error parameter d* \n');
fprintf('\n');

%Solve eqn A.9
n = 2*phrm+1;
phrm = phrm*pi/180;

for i = 1:1:n
    phi(i,1) = (i*0.5-0.5)*pi/180;
    efn1(i,1) = erf((sin(phrm)*(1+cos(phi(i,1)))*(1-2*dsta*sin(phi(i,1)))...
        -pi*bsta*(1+cos(phrm)))/(2^0.5*pi*sgsta*(1+cos(phrm))));
    efn2(i,1) = erf(-1*(sin(phrm)*(1+cos(phi(i,1)))*(1+2*dsta*sin(phi(i,1)))...
        +pi*bsta*(1+cos(phrm)))/(2^0.5*pi*sgsta*(1+cos(phrm))));
    itgd(i,1) = (efn1(i,1)-efn2(i,1))/(1+cos(phi(i,1)));
end

mltp = (1+cos(phrm))/(2*sin(phrm));

%Print the result to screen
gd = mltp*trapz(phi,itgd)
```

## 2. Paracept3d3D.m

%Paracept3d2D and Paracept3d3D generate solutions to the closed-form expression %for gamma as given by Guven et al. (1986) and shown in equation A.9. The user %enters a value for sigma\* and the programme produces a solution for gamma in %terms of d\* and beta\*. The graph is a 3-dimensional contour plot (the 2-D plot %is obtained using paracept3d2D). Vector V must be defined so as to enable manual %annotation of the countour lines shown.

```
clear
clc
clg
clear variables
format long
format compact

%Enter the magnitude of the random error, sigma*.

sgsta = 0.0;
phrm = 82;
n = 2*phrm+1;
phrm = phrm*pi/180;

[X,Y] = meshgrid(0:0.05:1,0:0.05:1);

%Solve equation A.9 for a range of beta* and d* values, using the trapezoidal
%numerical integration method. (The 'trapz' and 'erf' MATLAB functions are used.)

for j = 1:1:21
    bsta = 0.05*j-0.05;
    for k = 1:1:21
        dsta = 0.05*k-0.05;
        for i = 1:1:n
            phi(i,1) = (i*0.5-0.5)*pi/180;
            efn1(i,1) = erf((sin(phrm)*(1+cos(phi(i,1)))*(1-2*dsta*...
                sin(phi(i,1)))-pi*bsta*(1+cos(phrm)))/(2^0.5*pi*sgsta*(1+cos(phrm))));
            efn2(i,1) = erf(-1*(sin(phrm)*(1+cos(phi(i,1)))*(1+2*dsta*...
                sin(phi(i,1)))+pi*bsta*(1+cos(phrm)))/(2^0.5*pi*sgsta*(1+cos(phrm))));
            itgd(i,1) = (efn1(i,1)-efn2(i,1))/(1+cos(phi(i,1)));
        end
        mltp = (1+cos(phrm))/(2*sin(phrm));
        gd(j,k,2) = mltp*trapz(phi,itgd);
    end
end
Z = gd(:,:,2);

%Enter the range of values for manually annotating the contour lines
v = [0.1 0.2 0.3 0.4 0.5 0.6 0.7 0.8 0.9 1.0];

%Plot the contour lines of the surface solution
[C,h] = contour3(X,Y,Z,v)
set(gca,'FontSize',10);
clabel(C,h,'manual')
axis([0 1 0 1 0 1])
surface(X,Y,Z,'EdgeColor',[.8 .8 .8],'FaceColor','none')
xlabel('d*','FontSize',13)
ylabel('\beta*','FontSize',13)
zlabel('Intercept factor \gamma*','FontSize',13)
title('Intercept factor \gamma as a function of d* and \beta*','FontSize',14)
colormap winter

%Set the 3-dimensional viewing position
az = 120;
el = 45;
view(az, el);
```

## APPENDIX C

### THE PSA ALGORITHM: CALCULATIONS AND DATA

## C.1 Sample calculation using the PSA Algorithm

### C.1.1 Introduction

A sample calculation is given showing the use of the PSA Algorithm for computing the solar vector. An arbitrary date and time are selected and the algorithm is used to determine the angle through which a parabolic trough must rotate from a stowed position, so as to point at the solar disc.

### C.1.2 Problem statement

A tracking parabolic trough solar collector is aligned in the north-south direction on the flat rooftop area of Mangosuthu Technikon's solar energy test facility, Durban. The trough is in a stowed position with its aperture facing east, corresponding to a trough tracking angle,  $\rho_T$ , of  $+90^\circ$  (assuming east of vertical is positive, west negative).

Find the solar azimuth angle (A) and the zenith angle ( $\theta_z$ ) at 11:25am and 43 seconds South African Standard Time (SAST) on 5 May 2003, and use these values to calculate the PTSC tracking angle,  $\rho_T$ , and the solar angle of incidence,  $\theta_i$ .

### C.1.3 Solution

Two inputs are required for the PSA Algorithm: geographic location and Universal Time (UT). For location, the test facility at Mangosuthu Technikon is at:

$$\begin{array}{ll} \text{Latitude} & \Phi = -29.970233^\circ \\ \text{Longitude} & \text{long} = +30.91502^\circ \end{array}$$

For time, 11:25:43 (SAST) is expressed in UT as a decimal quantity:

$$\begin{aligned} 11:25:43 &= 11 \text{ h} + 25/60 \text{ h} + 43/3600 \text{ h} \\ &= 11.42861111 \text{ h (SAST)} \\ &= 9.42861111 \text{ h (UT)} \end{aligned}$$

For the date, 5 May 2003 is expressed as

$$\begin{array}{llll} \text{Year} & = & y & = & 2003 \\ \text{Month} & = & m & = & 5 \\ \text{Day} & = & d & = & 5 \end{array}$$

With the input values established in the correct format, the PSA Algorithm is implemented:

1. Calculate the Julian Day:

$$\begin{aligned}
 \text{jd} &= (1461(y + 4800 + (m - 14)/12))/4 \\
 &+ (367(m - 2 - 12((m - 14)/12)))/12 \\
 &- (3((y + 4900 + (m - 14)/12)/100))/4 \\
 &+ d - 32075 - 0.5 + \text{hour}/24.0 \quad \text{(C1)} \\
 &= 2\,452\,764.893 \text{ days}
 \end{aligned}$$

Note: Every division in the above equation, except the last, is an integer division. This means that decimal fractions left over from any of the internal division terms, except the last, are dropped. For example, in the first line  $(m - 14)/12 = (5 - 14)/12 = -0.75 = 0$ . Extreme care must be exercised in applying equation C1.

2. Compute the ecliptic coordinates of the sun, noting that all angles are in radians:

$$\begin{aligned}
 n &= \text{jd} - 2451545.0 \quad \text{(C2)} \\
 &= 1219.89286
 \end{aligned}$$

$$\begin{aligned}
 \Omega &= 2.1429 - 0.0010394594(n) \quad \text{(C3)} \\
 &= 0.87487139 \text{ rad}
 \end{aligned}$$

$$\begin{aligned}
 L \text{ (mean longitude)} &= 4.8950630 + 0.017202791698(n) \quad \text{(C4)} \\
 &= 25.880624491 \text{ rad}
 \end{aligned}$$

$$\begin{aligned}
 g \text{ (mean anomaly)} &= 6.2400600 + 0.0172019699(n) \quad \text{(C5)} \\
 &= 27.22461916 \text{ rad}
 \end{aligned}$$

$$\begin{aligned}
 l \text{ (ecliptic longitude)} &= L + 0.03341607\sin(g) \\
 &+ 0.00034894\sin(2g) - 0.0001134 \\
 &- 0.0000203\sin(\Omega) \quad \text{(C6)} \\
 &= 25.90917575 \text{ rad}
 \end{aligned}$$

$$\text{ep (obliquity of the ecliptic)} = 0.4090928 - 6.2140 \times 10^{-9}(n)$$

$$\begin{aligned}
& + 0.0000396\cos(\Omega) && (C7) \\
= & 0.4091106 \text{ rad}
\end{aligned}$$

3. Convert ecliptic to celestial coordinates:

$$\begin{aligned}
\text{ra (right ascension)} & = \text{atan}[\cos(\text{ep})\sin(l)/\cos(l)] && (C8) \\
& = 0.73346270 \text{ rad}
\end{aligned}$$

$$\begin{aligned}
\delta \text{ (declination)} & = \text{asin}[(\sin(\text{ep}))(\sin(l))] && (C9) \\
& = 0.28249216 \text{ rad}
\end{aligned}$$

4. Convert celestial to horizontal coordinates:

$$\begin{aligned}
\text{gmst (Greenwich mean sidereal time)} & = 6.6974243242 \\
& + 0.0657098283(n) + \text{hour} && (C10) \\
& = 96.28498544 \text{ h}
\end{aligned}$$

$$\begin{aligned}
\text{lmst (local mean sidereal time)} & = (\text{gmst}(15) + \text{long})(\pi/180) && (C11) \\
& = 25.74691913 \text{ h}
\end{aligned}$$

Note: “long” is entered in degrees, not radians.

$$\begin{aligned}
\omega \text{ (hour angle)} & = \text{lmst} - \text{ra} && (C12) \\
& = 25.01345643 \text{ rad}
\end{aligned}$$

$$\begin{aligned}
\theta_z \text{ (zenith angle)} & = \text{acos}[\cos(\Phi)\cos(\omega)\cos(\delta) + \sin(\delta)\sin(\Phi)] && (C13) \\
& = 0.81373639 \text{ rad}
\end{aligned}$$

Note: For the geometric arguments in eqn. C13,  $\Phi$  is entered in degrees, the others are entered in radians.

$$\begin{aligned}
A \text{ (solar azimuth)} & = \text{atan}[(-\sin(\omega))/(\tan(\delta)\cos(\Phi) - \sin(\Phi)\cos(\omega))] && (C14) \\
& = 0.15788706 \text{ rad}
\end{aligned}$$

$$\begin{aligned}
\text{Parallax} & = (\text{Earth Mean Radius})/(\text{Astronomical Unit})\sin(\theta_z) && (C15) \\
& = (6371.01 \text{ km})/(149597890 \text{ km})\sin(0.813736392) \\
& = 0.00003096 \text{ rad}
\end{aligned}$$

$$\begin{aligned}\theta_z &= \theta_z + \text{Parallax} \\ &= 0.81376735 \text{ rad}\end{aligned}\tag{C16}$$

The calculation of a corrected zenith angle concludes the PSA Algorithm. For a tracking PTSC, the results from the algorithm can be combined to obtain the angle of incidence or a tracking angle through which the trough must be turned to intercept the sun.

#### C.1.4 Calculation of the collector tracking angle, $\rho_T$

For a horizontal collector orientated in the north-south direction, Stine and Harrigan (1985) give the following equation for determining the tracking angle  $\rho_T$ :

$$\tan \rho_T = \sin(A)/\tan(90 - \theta_z)\tag{C17}$$

$$\begin{aligned}\text{Thus for this example, } \rho_T &= \text{atan}[\sin(A)/\tan(\pi/2 - \theta_z)] \\ &= \text{atan}[(\sin(0.157887058))/\tan(\pi/2 - 0.813767347)] \\ &= + 0.16490476 \text{ rad} \\ &= + 9.448347^\circ\end{aligned}$$

Since the trough is currently pointing east with  $\rho_T = + 90^\circ$ , the angle through which the trough must be rotated in order to intercept the sun,  $\rho_{\text{correction}}$  is:

$$\begin{aligned}\rho_{\text{correction}} &= 90^\circ - 9.448347^\circ \\ &= 80.551653^\circ\end{aligned}$$

#### C.1.5 Calculation of the angle of incidence, $\theta_i$

For an N-S aligned trough collector, Stine and Harrigan (1985) provide a method for determining angle of incidence, using azimuth and zenith angles:

$$\begin{aligned}\theta_i &= \text{acos}\{[1 - \cos^2 A \cos^2((\pi/2) - \theta_z)]^{1/2}\} \\ &= \text{acos}\{[1 + \\ &\quad - \cos^2(0.15788706) \cos^2((\pi/2) - 0.81376735)]^{1/2}\} \\ &= 0.80069262 \text{ rad} \\ &= 45.87630769^\circ\end{aligned}\tag{C18}$$

## C.2 MATLAB code (PSA\_16days.m) for implementing the PSA Algorithm

```
%PSA_16days implements the PSA Algorithm and outputs results for twelve
%16-day periods in a year. The programme outputs solar azimuth and zenith angles
%for the 12th to the 27th of each month, from January to December. The programme is
%configured for the Solar Energy Test Facility at Mangosuthu Technikon and is
%intended to help compare the PSA algorithm with accurate data from other sources,
%such as MICA.

clear
clc
clear variables
format short g

%User enters data
s = input('Enter the SECONDS \n');
fprintf('\n');
mn = input('Enter the MINUTES \n');
fprintf('\n');
h = input('Enter the HOUR \n');
fprintf('\n');
y = input('Enter the YEAR \n');
fprintf('\n');

%The geographic coordinates for the Solar Energy Test Facility at Mangosuthu
%Technikon, Durban.
long = 30.91502*pi/180;
phi = -29.970233*pi/180;

%Start the calculation of the algorithm steps
k = 0;
t = 0;
sts = s/3600+mn/60+h;
st = sts;
for j = 1:1:12
    t = t+1;
    w=15;
    for i = 12:1:(12+w)
        k = k+1;
        d(k,1) = i;
        m(k,1) = j;
        hour = st-2;

%Julian Day calculation
        jd1 = fix((m(k,1)-14)/12);
        jd2 = 1461*(y+4800+jd1);
        jd3 = fix(jd2/4);
        jd4 = 367*(m(k,1)-2-12*(jd1));
        jd5 = fix(jd4/12);
        jd6 = fix((y+4900+jd1)/100);
        jd7 = fix((3*jd6)/4);
        jd8 = d(k,1)-32075-0.5+hour/24;
        jd(k,1) = jd3+jd5-jd7+jd8;

%Algorithm proceeds
        n(k,1) = jd(k,1)-2451545;
        omega(k,1) = 2.1429-0.0010394594*n(k,1);
        L(k,1) = 4.8950630+0.017202791698*n(k,1);
        g(k,1) = 6.24006+0.0172019699*n(k,1);
        lec(k,1) = L(k,1)+0.03341607*sin(g(k,1))+0.00034894*sin(2*g(k,1))-
            0.0001134-0.0000203*sin(omega(k,1));
        lec(k,1) = (rem(lec(k,1), (2*pi)));
        lecdg(k,1) = lec(k,1)*180/pi;
        ep(k,1) = 0.4090928-6.214e-9*n(k,1)+0.0000396*cos(omega(k,1));
        epdg(k,1) = ep(k,1)*180/pi;
```

```

%A series of checks is performed to ensure that the angles obtained
%are located in the correct trigonometric quadrants
    if (cos(ep(k,1))*sin(lec(k,1)))>0 & (cos(lec(k,1))>0)
        ra(k,1) = atan((cos(ep(k,1))*sin(lec(k,1)))/cos(lec(k,1)));
    elseif (cos(ep(k,1))*sin(lec(k,1)))>0 & (cos(lec(k,1))<0)
        prodra(k,1) = -1*(cos(ep(k,1))*sin(lec(k,1)))/cos(lec(k,1));
        raint(k,1) = atan(prodra(k,1));
        ra(k,1) = pi-raint(k,1);
    elseif (cos(ep(k,1))*sin(lec(k,1)))<0 & (cos(lec(k,1))<0)
        prodra(k,1) = (cos(ep(k,1))*sin(lec(k,1)))/cos(lec(k,1));
        raint(k,1) = atan(prodra(k,1));
        ra(k,1) = pi+raint(k,1);
    elseif (cos(ep(k,1))*sin(lec(k,1)))<0 & (cos(lec(k,1))>0)
        prodra(k,1) = -1*(cos(ep(k,1))*sin(lec(k,1)))/cos(lec(k,1));
        raint(k,1) = atan(prodra(k,1));
        ra(k,1) = 2*pi-raint(k,1);
    end
    if ra(k,1)<0
        ra(k,1) = ra(k,1)+2*pi;
    end
    radg(k,1) = ra(k,1)*180/pi;
    decl(k,1) = asin((sin(ep(k,1))*sin(lec(k,1))));
    decldg(k,1) = decl(k,1)*180/pi;
    gmst(k,1) = 6.6974243242+0.0657098283*n(k,1)+hour;
    lmst(k,1) = gmst(k,1)*15*pi/180+long;
    hang(k,1) = lmst(k,1)-ra(k,1);
    hang(k,1) = (rem(hang(k,1),(2*pi)));
    hangdg(k,1) =hang(k,1)*180/pi;
    zen(k,1) = acos(cos(phi)*cos(hang(k,1))*cos(decl(k,1))+
        sin(decl(k,1))*sin(phi));

%Further checks are performed to ensure the correct trigonometric results
    if (-1*(sin(hang(k,1))))>0 & (tan(decl(k,1))*cos(phi)-
        sin(phi)*cos(hang(k,1)))>0
        az(k,1) = atan((-1*(sin(hang(k,1))))/(tan(decl(k,1))*cos(phi)-
            sin(phi)*cos(hang(k,1))));
    elseif (-1*(sin(hang(k,1))))>0 & (tan(decl(k,1))*cos(phi)-
        sin(phi)*cos(hang(k,1)))<0
        prodaz(k,1) = -1*(-1*(sin(hang(k,1))))/(tan(decl(k,1))*cos(phi)-
            sin(phi)*cos(hang(k,1)));
        azint(k,1) = atan(prodaz(k,1));
        az(k,1) = pi-azint(k,1);
    elseif (-1*(sin(hang(k,1))))<0 & (tan(decl(k,1))*cos(phi)-
        sin(phi)*cos(hang(k,1)))<0
        prodaz(k,1) = (-1*(sin(hang(k,1))))/(tan(decl(k,1))*cos(phi)-
            sin(phi)*cos(hang(k,1)));
        azint(k,1) = atan(prodaz(k,1));
        az(k,1) = pi+azint(k,1);
    elseif (-1*(sin(hang(k,1))))<0 & (tan(decl(k,1))*cos(phi)-
        sin(phi)*cos(hang(k,1)))>0
        prodaz(k,1) = -1*(-1*(sin(hang(k,1))))/(tan(decl(k,1))*cos(phi)-
            sin(phi)*cos(hang(k,1)));
        azint(k,1) = atan(prodaz(k,1));
        az(k,1) = 2*pi-azint(k,1);
    end
    para = (6371.01/149597890)*sin(zen(k,1));
    zen(k,1) = zen(k,1)+para;
    zend(k,1) = zen(k,1)*180/pi;
    azd(k,1) = az(k,1)*180/pi;
end
end

%Output the results in column form for the day, month, azimuth and zenith
[d m azd zend]

```

C.3 Comparison of output from PSA\_16days.m with Multi-Year Interactive Computer Almanac (MICA)

**Table C.1** Solar zenith and azimuth data for a range of days covering one year, generated using the PSA Algorithm (MATLAB programme “psa\_16days.m”) and compared with output from the Multi-Year Interactive Computer Almanac (MICA) of the U.S. Naval Observatory

Year	Month	Day	Hour							
			10h00 (SAST)				14h00 (SAST)			
			MICA		PSA_16days.m		MICA		PSA_16days.m	
			Zenith (deg)	Azimuth (deg)						
2003	Jun	18	60.349	31.152	60.349	31.151	60.959	327.635	60.960	327.630
		19	60.391	31.190	60.392	31.190	60.951	327.695	60.951	327.690
		20	60.427	31.233	60.428	31.232	60.936	327.751	60.937	327.750
		21	60.458	31.279	60.458	31.279	60.916	327.804	60.916	327.800
		22	60.482	31.329	60.482	31.329	60.890	327.852	60.890	327.850
		23	60.500	31.383	60.501	31.383	60.858	327.897	60.858	327.900
	Sept	18	41.457	44.499	41.456	44.500	44.386	310.132	44.385	310.130
		19	41.096	44.749	41.094	44.751	44.156	309.668	44.155	309.670
		20	40.735	45.004	40.733	45.005	43.927	309.199	43.926	309.200
		21	40.374	45.263	40.372	45.265	43.700	308.726	43.698	308.720
		22	40.013	45.527	40.011	45.528	43.474	308.250	43.473	308.250
		23	39.653	45.796	39.651	45.797	43.249	307.769	43.248	307.770
	Dec	18	25.943	82.051	25.946	82.055	29.082	275.409	29.079	275.410
		19	26.039	82.201	26.042	82.204	28.967	275.438	28.964	275.440
		20	26.139	82.333	26.141	82.336	28.853	275.484	28.851	275.480
		21	26.242	82.449	26.243	82.451	28.743	275.545	28.741	275.550
		22	26.347	82.547	26.349	82.549	28.634	275.622	28.633	275.620
		23	26.456	82.629	26.457	82.630	28.529	275.715	28.527	275.720
2004	Mar	18	41.538	51.132	41.539	51.131	40.156	311.410	40.157	311.410
		19	41.782	50.651	41.783	50.649	40.505	311.720	40.506	311.720
		20	42.027	50.174	42.028	50.172	40.854	312.025	40.856	312.030
		21	42.274	49.701	42.274	49.698	41.205	312.325	41.207	312.320
		22	42.522	49.232	42.522	49.229	41.556	312.620	41.558	312.620
		23	42.772	48.768	42.771	48.765	41.908	312.910	41.910	312.910

## APPENDIX D

### LABVIEW SOFTWARE: SCATTALOG DATA SAMPLE

Table D.1 contains a 1-minute sample of data from the LabVIEW application SCATTALog for a sampling interval of 6 seconds. The data are from a collector time constant test conducted on 28 December 2003 and have been processed in Microsoft Excel. Table D.2 briefly describes the data in each column. Columns 1 to 9 contain date and time information, columns 10 to 25 contain the conditioned signals from the PTSC TC probes and radiometers, columns 27 to 34 contain air and fluid temperature data, columns 35 to 44 contain thermal efficiency data, columns 45 to 49 contain fluid flow and heat transfer parameters and columns 51 to 62 contain solar position data from the PSA algorithm. SCATTALog was still undergoing development on completion of this project and not all the columns shown in table D.1 contain data that were used or which had been checked for accuracy – such columns are indicated as “under development”.

**Table D.1** Extract from Excel spreadsheet showing processed output from LabVIEW application SCATTALog for collector acceptance angle test

<b>1</b>	<b>2</b>	<b>3</b>	<b>4</b>	<b>5</b>	<b>6</b>	<b>7</b>	<b>8</b>	<b>9</b>	<b>10</b>	<b>11</b>	<b>12</b>	<b>13</b>
YEAR	MNTH	DAY	SAST H (h)	SAST M (min)	SAST S (s)	ST H (h)	ST M (min)	ST S (s)	CH1 MAINS IN (degC)	CH2 VT DOWN (degC)	CH3 VT UP (degC)	CH4 HT (degC)
2003	12	28	10	31	39	10	34	0	27.214	27.697	29.278	28.818
2003	12	28	10	31	45	10	34	6	27.304	27.689	29.297	28.824
2003	12	28	10	31	51	10	34	12	27.332	27.670	29.295	28.806
2003	12	28	10	31	57	10	34	18	27.467	27.687	29.282	28.804
2003	12	28	10	32	3	10	34	24	27.351	27.699	29.299	28.822
2003	12	28	10	32	9	10	34	30	27.212	27.693	29.307	28.835
2003	12	28	10	32	15	10	34	36	27.346	27.709	29.305	28.847
2003	12	28	10	32	21	10	34	42	27.234	27.709	29.311	28.864
2003	12	28	10	32	27	10	34	48	27.418	27.706	29.317	28.874
2003	12	28	10	32	30	10	34	51	27.397	27.716	29.327	28.859
2003	12	28	10	32	33	10	34	54	27.486	27.722	29.349	28.880

<b>14</b>	<b>15</b>	<b>16</b>	<b>17</b>	<b>18</b>	<b>19</b>	<b>20</b>	<b>21</b>	<b>22</b>	<b>23</b>	<b>24</b>
CH5 SUPP MAN (degC)	CH6 PUMP IN (degC)	CH7 PUMP OUT (degC)	CH8 T <sub>n</sub> (degC)	CH9 T <sub>o</sub> (degC)	CH10 RET MAN (degC)	CH11 AMBIENT (degC)	CH12	CH13	CH14	CH15 PYRHELIO (W/m <sup>2</sup> )
28.352	28.640	29.092	29.345	71.003	63.530	28.412	-192.585	-102.866	-99.485	965.944
28.323	28.638	29.121	29.345	71.123	63.589	28.643	-125.021	-101.721	-100.697	966.125
28.342	28.614	29.108	29.343	71.154	63.608	28.538	-108.649	-101.046	-105.587	966.834
28.348	28.652	29.102	29.370	71.178	63.489	28.666	-127.697	-99.171	-102	966.860
28.361	28.642	29.108	29.354	71.182	63.665	28.628	-135.214	-103.246	-106.782	967.659
28.356	28.629	29.123	29.354	71.423	63.669	28.830	-9.9E+37	-111.437	-106.743	967.040
28.388	28.673	29.113	29.371	71.480	63.61	28.910	-9.9E+37	-113.757	-111.76	967.505
28.423	28.677	29.115	29.379	71.480	63.592	28.925	-9.9E+37	-112.866	-106.635	967.131
28.409	28.715	29.128	29.375	70.544	63.330	28.474	-9.9E+37	-111.057	-104.317	966.602
28.428	28.705	29.128	29.365	69.847	63.578	28.482	-9.9E+37	-115.473	-108.561	966.447
28.394	28.732	29.123	29.367	69.097	63.562	28.548	-9.9E+37	-113.916	-103.571	966.138

**Table D.1 (Continued)** Extract from Excel spreadsheet showing output from LabVIEW application  
SCATTAlog for collector acceptance angle test

25	26	27	28	29	30	31	32	33	34	35	36	37
CH16 PYRANO (W/m <sup>2</sup> )	Items.	Flow (l/h)	Mass Flow (kg/s)	t <sub>re,init</sub> (degC)	TCQ	t <sub>a</sub> (degC)	t <sub>ri</sub> - t <sub>a</sub> CORRECTED (degC)	Av. Fl Temp (degC)	Delta Temp (degC)	Th. Eff (%)	t <sub>fi</sub> 50mean (%)	t <sub>fi</sub> 50SD
1023.771	60	100	0.027	70.7	1.007	24.1	4.718	50.174	41.658	66.731	29.31	0.029
1023.576	61	100	0.027	70.7	1.01	24.1	4.724	50.234	41.778	66.706	29.312	0.027
1023.797	62	100	0.027	70.7	1.011	24.1	4.706	50.249	41.811	66.683	29.314	0.026
1024.344	63	100	0.027	70.7	1.012	24.1	4.704	50.274	41.808	66.659	29.316	0.024
1024.799	64	100	0.027	70.7	1.012	24.1	4.722	50.268	41.828	66.635	29.318	0.024
1024.552	65	100	0.027	70.7	1.017	24.1	4.735	50.389	42.069	66.604	29.320	0.023
1024.851	66	100	0.027	70.7	1.019	24.1	4.747	50.425	42.109	66.589	29.322	0.022
1024.435	67	100	0.027	70.7	1.019	24.1	4.764	50.430	42.101	66.575	29.324	0.021
1023.901	68	100	0.027	70.7	0.996	24.1	4.774	49.959	41.169	66.577	29.326	0.022
1023.576	69	100	0.027	70.7	0.979	24.1	4.759	49.606	40.482	66.541	29.328	0.022
1023.510	70	100	0.027	70.7	0.961	24.1	4.780	49.232	39.730	66.491	29.329	0.022

38	39	40	41	42	43	44	45	46	47	48	49
t <sub>fi</sub> 50Var	n <sub>50</sub> mean (%)	n <sub>50</sub> SD	n <sub>50</sub> Var	n <sub>10</sub> mean (%)	n <sub>10</sub> SD	n <sub>10</sub> Var	Re	Pr	fD	Nu	h (W/m <sup>2</sup> K)
0.001	66.858	0.084	0.007	66.808	0.028	0.001	2477.29	1.457	0.049	10.472	626.373
0.001	66.861	0.076	0.006	66.797	0.035	0.001	2479.74	1.456	0.049	10.483	626.965
0.001	66.863	0.072	0.005	66.784	0.042	0.002	2480.34	1.456	0.049	10.486	627.108
0.001	66.863	0.071	0.005	66.769	0.049	0.002	2481.38	1.455	0.049	10.491	627.360
0.001	66.862	0.074	0.005	66.752	0.055	0.003	2481.14	1.455	0.049	10.490	627.301
0.001	66.859	0.079	0.006	66.735	0.062	0.004	2486.07	1.453	0.049	10.512	628.488
0	66.855	0.087	0.008	66.715	0.069	0.005	2487.58	1.452	0.049	10.518	628.852
0	66.85	0.095	0.009	66.694	0.072	0.005	2487.75	1.452	0.049	10.519	628.891
0	66.845	0.102	0.01	66.671	0.070	0.005	2468.52	1.462	0.049	10.433	624.250
0	66.839	0.109	0.012	66.651	0.065	0.004	2454.09	1.470	0.049	10.368	620.733
0.001	66.832	0.117	0.014	66.63	0.063	0.004	2438.84	1.479	0.049	10.299	616.990

50	51	52	53	54	55	56	57	58	59	60	61	62
Pressure (kPa)	DECL (deg)	HANG (deg)	ZENITH (deg)	AZIMUTH (deg)	TRACK (deg)	AOI (deg)	UT (h)	JD (days)	n (days)	l (rad)	ep (rad)	ra (rad)
4	-23.296	-21.497	20.303	75.938	19.742	4.836	8.528	2453002	1456.9	29.953	0.409	4.83
4	-23.296	-21.472	20.282	75.912	19.720	4.840	8.529	2453002	1456.9	29.953	0.409	4.83
4	-23.296	-21.447	20.261	75.885	19.697	4.845	8.531	2453002	1456.9	29.953	0.409	4.83
4	-23.296	-21.422	20.24	75.858	19.674	4.849	8.533	2453002	1456.9	29.953	0.409	4.83
4	-23.296	-21.397	20.219	75.831	19.652	4.853	8.534	2453002	1456.9	29.953	0.409	4.83
4	-23.296	-21.372	20.198	75.804	19.629	4.857	8.536	2453002	1456.9	29.953	0.409	4.83
4	-23.296	-21.347	20.177	75.777	19.606	4.861	8.538	2453002	1456.9	29.953	0.409	4.83
4	-23.296	-21.322	20.156	75.750	19.584	4.866	8.539	2453002	1456.9	29.953	0.409	4.83
4	-23.296	-21.297	20.135	75.723	19.561	4.870	8.541	2453002	1456.9	29.953	0.409	4.83
4	-23.296	-21.284	20.125	75.710	19.550	4.872	8.542	2453002	1456.9	29.953	0.409	4.83
4	-23.296	-21.272	20.114	75.696	19.539	4.874	8.542	2453002	1456.9	29.953	0.409	4.83

**Table D.2** List of columns from table D1 and description of data types

<b>Column</b>	<b>Data description</b>
1	Year
2	Month
3	Day number of the month
4	Clock time - hours (South African Standard Time)
5	Clock time - minutes (South African Standard Time)
6	Clock time - seconds (South African Standard Time)
7	Solar time - hours
8	Solar time - minutes
9	Solar time - seconds
10	Instrument channel 1 – Main water supply manifold temperature
11	Instrument channel 2 – High temperature (HT) tank temperature (lower TC)
12	Instrument channel 3 – High temperature (HT) tank temperature (upper TC)
13	Instrument channel 4 – Low temperature (LT) tank temperature
14	Instrument channel 5 – Main distribution manifold fluid temperature
15	Instrument channel 6 – Pump inlet temperature
16	Instrument channel 7 – Pump outlet temperature
17	Instrument channel 8 – Receiver fluid inlet temperature, $t_{f,i}$
18	Instrument channel 9 – Receiver fluid outlet temperature, $t_{f,o}$
19	Instrument channel 10 – Return manifold fluid temperature
20	Instrument channel 11 – Ambient air temperature (Not used - more accurate value was obtained from the weather station and manually entered)
21	Instrument channel 12 – Unused data logging channel
22	Instrument channel 13 – Unused data logging channel
23	Instrument channel 14 – Unused data logging channel
24	Instrument channel 15 – Normal beam irradiance from NIP
25	Instrument channel 16 – Total global irradiance from PSP
26	Number of programme loop iterations
27	Volumetric flow rate (manually entered)
28	Fluid mass flow rate
29	Initial receiver fluid outlet temperature $t_{f,e,initial}$ (for time constant tests; see equation 5.5)
30	Time constant quotient
31	Ambient air temperature, $t_a$ (manually entered from weather station readout)
32	Temperature difference between receiver fluid at inlet and ambient air temperature, $\Delta t$ (manually corrected to account for software error)
33	Average receiver fluid temperature
34	Fluid temperature difference across receiver, $\Delta t_r$
35	ASHRAE 93 thermal efficiency (see equation 5.4)
36	Under development – 50-point rolling average of receiver fluid inlet temperature, $t_{f,i}$
37	Under development – standard deviation of 50-point rolling average of $t_{f,i}$
38	Under development – variance of 50-point rolling average of $t_{f,i}$
39	Under development – 50-point rolling average of ASHRAE 93 thermal efficiency
40	Under development – standard deviation of 50-point rolling average thermal efficiency
41	Under development – variance of 50-point rolling average thermal efficiency
42	Under development – 10-point rolling average of ASHRAE 93 thermal efficiency
43	Under development – standard deviation of 10-point rolling average thermal efficiency
44	Under development – variance of 10-point rolling average thermal efficiency
45	Reynolds number for receiver flow based on average receiver fluid temperature (Kröger, 1998): ( $Re = \rho v D / \mu$ , where D is the inner diameter of the absorber)
46	Prandtl number for receiver flow based on average receiver fluid temperature (Kröger, 1998): ( $Pr = \mu c_p / k$ )

**Table D.2 (Continued)** List of columns from table D1 and description of data types

<b>Column</b>	<b>Data description</b>
<b>47</b>	Friction factor for receiver flow based on average receiver fluid temperature (Kröger, 1998): $(f = (1.82 \log_{10} Re - 1.64)^{-2})$
<b>48</b>	Nusselt number for receiver flow based on average receiver fluid temperature (Kröger, 1998): $(Nu = \frac{(f/8)(Re - 1000)Pr[1 + (d/L)^{0.67}]}{1 + 12.7(f/8)^{0.5}(Pr^{0.67} - 1)})$
<b>49</b>	Heat transfer coefficient based on average receiver fluid temperature (Kröger, 1998): $(h = (Nu)k/D, \text{ where } D \text{ is the inner diameter of the absorber})$
<b>50</b>	PTSC fluid system pressure
<b>51</b>	Solar declination angle, $\delta$
<b>52</b>	Hour angle
<b>53</b>	Zenith angle, $\theta_z$
<b>54</b>	Azimuth angle, $A$
<b>55</b>	PTSC tracking angle, $\rho_T$
<b>56</b>	Angle of incidence, $\theta_i$
<b>57</b>	Universal time
<b>58</b>	Julian Day
<b>59</b>	Difference between current Julian Day and Julian Day corresponding to 1 January 2000
<b>60</b>	Ecliptic longitude of the sun
<b>61</b>	Obliquity of the ecliptic
<b>62</b>	Right ascension

## APPENDIX E

### SUMMARY OF EXPERIMENTAL TEST DATA

**Table E.1** Summary of data for collector time constant tests

<b>GLASS-SHIELDED RECEIVER</b>									
<b>Cooling tests</b>									
Date	Test time (solar)	Flow rate (L/h)	Time const. (s)	( $t_{fi} - t_a$ ) (°C)	Max. $\Delta(t_{fi})$ (°C)	Ave. $G_{DN}$ (W/m <sup>2</sup> )	Ave. $\theta_i$ (deg)	$t_a$ (°C)	Ave. wind vel. (knots)
15-Feb-04	12:56	75	108.71	4.21	0.11	892.60	16.35	27.00	10.0
15-Feb-04	13:15	150	55.63	3.92	0.05	905.44	15.67	27.00	10.0
15-Feb-04	13:29	300	28.55	4.14	0.05	905.42	15.03	26.70	12.0
15-Feb-04	13:50	450	18.36	3.94	0.08	891.30	14.04	26.92	10.0
15-Feb-04	14:20	600	11.13	7.77	0.25	881.45	12.01	26.60	11.0
15-Feb-04	14:38	750	10.82	1.99	0.03	870.36	10.66	26.70	10.0
			<b>AVERAGE</b>	<b>4.33</b>	<b>0.09</b>	<b>891.10</b>	<b>13.96</b>	<b>26.82</b>	<b>10.5</b>
<b>Heating tests</b>									
Date	Test time (solar)	Flow rate (L/h)	Time const. (s)	( $t_{fi} - t_a$ ) (°C)	Max. $\Delta(t_{fi})$ (°C)	Ave. $G_{DN}$ (W/m <sup>2</sup> )	Ave. $\theta_i$ (deg)	$t_a$ (°C)	Ave. wind vel. (knots)
15-Feb-04	13:04	75	103.21	4.33	0.11	894.67	16.11	27.00	10.0
15-Feb-04	13:19	150	50.21	3.92	0.05	896.70	15.51	27.00	10.0
15-Feb-04	13:33	300	26.40	4.18	0.05	901.29	14.84	26.70	12.0
15-Feb-04	13:52	450	17.85	3.89	0.04	896.08	13.81	27.00	10.0
15-Feb-04	14:14	600	11.95	7.35	0.11	871.37	12.45	26.60	11.0
15-Feb-04	14:39	750	12.29	2.02	0.07	866.46	10.57	26.70	10.0
			<b>AVERAGE</b>	<b>4.28</b>	<b>0.07</b>	<b>887.76</b>	<b>13.88</b>	<b>26.83</b>	<b>10.5</b>
<b>UNSHIELDED RECEIVER</b>									
<b>Cooling tests</b>									
Date	Test time (solar)	Flow rate (L/h)	Time const. (s)	( $t_{fi} - t_a$ ) (°C)	Max. $\Delta(t_{fi})$ (°C)	Ave. $G_{DN}$ (W/m <sup>2</sup> )	Ave. $\theta_i$ (deg)	$t_a$ (°C)	Ave. wind vel. (knots)
28-Dec-03	10:43	75	97.14	5.29	0.06	965.76	4.90	24.10	9.0
28-Dec-03	11:04	150	52.11	4.17	0.06	972.08	5.78	24.20	9.0
28-Dec-03	09:52	300	30.45	3.12	0.05	948.50	2.69	23.70	9.0
28-Dec-03	11:24	450	21.65	2.70	0.04	978.84	6.33	24.60	9.0
29-Dec-03	09:15	600	14.29	1.02	0.04	854.86	0.19	25.80	10.0
29-Dec-03	09:50	750	12.09	2.15	0.05	494.44*	2.61	25.90	13.0
			<b>AVERAGE</b>	<b>3.08</b>	<b>0.05</b>	<b>869.08</b>	<b>3.75</b>	<b>24.72</b>	<b>9.8</b>
* Cloud obstructed pyrheliometer only after PTSC defocused - test unaffected.									
<b>Heating tests</b>									
Date	Test time (solar)	Flow rate (L/h)	Time const. (s)	( $t_{fi} - t_a$ ) (°C)	Max. $\Delta(t_{fi})$ (°C)	Ave. $G_{DN}$ (W/m <sup>2</sup> )	Ave. $\theta_i$ (deg)	$t_a$ (°C)	Ave. wind vel. (knots)
09-Jan-04	11:24	75	98.00	5.24	0.09	925.78	7.44	25.60	9.0
11-Jan-04	11:57	150	51.27	2.89	0.24	910.70	8.09	26.20	9.0
09-Jan-04	10:45	300	27.72	1.81	0.06	885.14	6.43	25.90	9.0
11-Jan-04	12:07	450	19.31	1.51	0.05	913.61	8.09	26.20	9.0
11-Jan-04	12:17	600	16.65	1.38	0.05	900.61	8.03	26.10	9.0
11-Jan-04	12:24	750	15.56	1.31	0.06	910.90	7.95	26.20	9.0
			<b>AVERAGE</b>	<b>2.36</b>	<b>0.09</b>	<b>907.79</b>	<b>7.67</b>	<b>26.03</b>	<b>9.0</b>

**Table E.2** Thermal efficiency test data for glass-shielded receiver (19 February 2004)

COLUMN	A	B	C	D	E	F	G	H	I	J
	Elapsed time	$t_{f,i}$	$t_{f,o}$	$G_{DN}$	$\theta_i$	$G_{bp}$	$m$	$c_p$	$mc_p\Delta t$	$A_a G_{bp}$
ROW	(s)	(°C)	(°C)	(W/m <sup>2</sup> )	(deg)	(W/m <sup>2</sup> )	(kg/s)	(J/kgK)	(W)	(W)
1	6	57.855	66.734	838.094	15.034	809.408	0.082	4185.63	3047.47	6070.56
2	12	57.894	66.736	838.210	15.028	809.543	0.082	4185.65	3034.78	6071.57
3	18	57.894	66.720	838.275	15.022	809.628	0.082	4185.64	3029.28	6072.21
4	24	57.902	66.734	837.320	15.016	808.728	0.082	4185.65	3031.35	6065.46
5	30	57.889	66.714	836.766	15.010	808.216	0.082	4185.64	3028.94	6061.62
6	36	57.904	66.754	835.760	15.004	807.267	0.082	4185.66	3037.53	6054.50
7	42	57.889	66.773	836.224	14.998	807.738	0.082	4185.66	3049.20	6058.03
8	48	57.887	66.759	837.449	14.992	808.944	0.082	4185.65	3045.08	6067.08
9	54	57.914	66.757	836.714	14.986	808.257	0.082	4185.66	3035.13	6061.92
10	60	57.920	66.793	836.779	14.980	808.342	0.082	4185.68	3045.44	6062.56
11	66	57.924	66.785	836.662	14.974	808.252	0.082	4185.67	3041.32	6061.89
12	72	57.930	66.816	837.823	14.968	809.396	0.082	4185.69	3049.91	6070.47
13	78	57.955	66.791	838.404	14.962	809.980	0.082	4185.69	3032.75	6074.85
14	84	57.951	66.816	838.287	14.956	809.889	0.082	4185.69	3042.71	6074.17
15	90	57.949	66.834	838.158	14.949	809.791	0.082	4185.70	3049.58	6073.43
16	96	57.935	66.820	838.171	14.943	809.826	0.082	4185.69	3049.57	6073.70
17	102	57.947	66.859	838.442	14.937	810.111	0.082	4185.71	3058.85	6075.83
18	108	57.961	66.879	838.068	14.931	809.772	0.082	4185.72	3060.92	6073.29
19	114	57.969	66.887	837.488	14.925	809.234	0.082	4185.73	3060.92	6069.26
20	120	57.978	66.892	837.307	14.919	809.082	0.082	4185.73	3059.55	6068.12
21	126	57.998	66.916	836.972	14.913	808.781	0.082	4185.75	3060.94	6065.86
22	132	57.992	66.873	837.204	14.907	809.028	0.082	4185.73	3048.22	6067.71
23	138	57.988	66.916	836.611	14.901	808.477	0.082	4185.74	3064.36	6063.58
24	144	57.986	66.912	835.566	14.895	807.490	0.082	4185.74	3063.68	6056.17
25	150	57.992	66.906	834.883	14.889	806.852	0.082	4185.74	3059.56	6051.39
26	156	57.994	66.937	834.315	14.882	806.329	0.082	4185.75	3069.52	6047.47
27	162	58.000	66.935	833.555	14.876	805.617	0.082	4185.75	3066.78	6042.13
28	168	58.006	66.896	834.225	14.870	806.287	0.082	4185.74	3051.32	6047.15
29	174	57.986	66.877	834.586	14.864	806.659	0.082	4185.73	3051.66	6049.94
30	180	57.980	66.908	835.399	14.858	807.467	0.082	4185.74	3064.36	6056.00
31	186	57.986	66.855	836.224	14.852	808.287	0.082	4185.72	3044.10	6062.15
32	192	57.984	66.857	834.186	14.846	806.339	0.082	4185.72	3045.47	6047.54
33	198	57.982	66.840	833.065	14.839	805.282	0.082	4185.71	3040.32	6039.61
34	204	57.996	66.885	831.685	14.833	803.970	0.082	4185.73	3050.97	6029.78
35	210	57.976	66.873	830.859	14.827	803.194	0.082	4185.72	3053.71	6023.95
36	216	57.986	66.869	830.975	14.821	803.328	0.082	4185.72	3048.91	6024.96
37	222	58.002	66.857	830.189	14.815	802.591	0.082	4185.73	3039.30	6019.43
38	228	57.990	66.812	831.079	14.809	803.473	0.082	4185.71	3027.96	6026.05
39	234	57.994	66.822	830.485	14.802	802.925	0.082	4185.71	3030.02	6021.94
40	240	57.994	66.814	830.485	14.796	802.947	0.082	4185.71	3027.27	6022.10
41	246	58.000	66.799	830.640	14.790	803.119	0.082	4185.71	3020.06	6023.39
42	252	58.004	66.838	830.421	14.784	802.930	0.082	4185.72	3032.09	6021.97
43	258	57.986	66.892	830.279	14.778	802.815	0.082	4185.73	3056.81	6021.11
44	264	58.015	66.826	829.428	14.771	802.018	0.082	4185.72	3024.19	6015.13
45	270	58.000	66.826	828.461	14.765	801.105	0.082	4185.71	3029.34	6008.28
46	276	58.017	66.855	828.267	14.759	800.939	0.082	4185.73	3033.47	6007.04
47	282	58.023	66.847	827.700	14.753	800.413	0.082	4185.73	3028.66	6003.10
48	288	57.996	66.883	826.965	14.747	799.724	0.082	4185.73	3050.29	5997.93
49	294	57.982	66.916	826.036	14.740	798.851	0.082	4185.74	3066.42	5991.39
50	300	57.980	66.865	825.598	14.734	798.450	0.082	4185.72	3049.59	5988.37
<b>SUM TOTAL</b>									<b>152289.58</b>	<b>302303.17</b>



For the calculation of thermal efficiency over the required 5-minute period, equation 4.5 is used:

$$\eta_g = \frac{\sum_{n=1}^{50} m_n (c_p)_n (\Delta t_r)_n}{A_a \sum_{n=1}^{50} G_n} \quad (4.5)$$

From table E.2, column I represents the numerator in equation 4.5 and column J the denominator. The totals of these columns are 152 289.58 W and 302303.17 W respectively, giving a single thermal efficiency point for the PTSC with glass-shielded receiver (see table E.4):

$$\begin{aligned} \eta_g &= (152\,289.58/302303.17) \\ &= 50.38\% \end{aligned}$$

#### Instantaneous efficiency, $\eta_{inst,T}$

The instantaneous efficiency of the collector, as defined in equation E.3 and used in the calculation of the tracking efficiency factor (equation 5.1), is determined by dividing the thermal power absorbed by the working fluid, by the rate of energy input to the PTSC system. Using the values from the above sample calculation for row 1:

$$\begin{aligned} \eta_{inst,T} &= (mc_p \Delta t) / (A_a G_{bp}) \quad (5.3) \\ &= (3047.47) / (6070.56) \\ &= 50.20\% \end{aligned}$$

To determine the tracking efficiency factor (equation 5.1), the same calculation is repeated for each time interval to find the maximum instantaneous efficiency. This becomes the denominator in equation 5.1, from which the remaining data are obtained. In a similar way, for the collector acceptance angle results given in 5.4.2, 10 instantaneous efficiency points are used to give a 1-minute average. Each of these values is then divided by the maximum efficiency to yield a single datum point.

**Table E.3** Summary of data for thermal efficiency tests with unshielded receiver

Date	Test time	$t_a$ (°C)	$(t_{r,i} - t_a)$ (°C)	Ave. $G_{DN}$ (W/m <sup>2</sup> )	$(t_{r,i} - t_a)/G_{bp}$ (m <sup>2</sup> °C/W)	Max. $\Delta(t_{r,i})$ (°C)	Max. $\Delta(G_{DN})$ (W/m <sup>2</sup> )	Efficiency (%)	Ave. $\theta_i$ (deg)	Max. $\Delta(\theta_i)$ (deg)	Ave. wind vel. (knots)
	(solar)										
02-Jan-04	10:10	27.50	2.66	901.60	0.0030	0.07	10.20	54.75	4.03	0.26	*
02-Jan-04	10:30	28.40	0.63	905.58	0.0007	0.06	11.86	53.92	5.04	0.21	*
02-Jan-04	13:51	26.20	2.86	899.68	0.0032	0.09	10.69	54.49	3.91	0.27	*
02-Jan-04	13:19	26.00	3.30	900.85	0.0037	0.09	7.63	54.52	5.42	0.19	*
26-Jan-04	14:28	26.80	22.40	918.33	0.0245	0.65	29.27	50.63	5.47	0.36	13.0
12-Jan-04	09:34	29.40	16.71	925.05	0.0181	0.07	7.69	50.82	3.05	0.34	12.0
13-Jan-04	11:56	28.30	21.64	930.87	0.0235	0.28	5.21	51.26	8.41	0.01	8.0
13-Jan-04	12:04	28.40	21.80	925.66	0.0238	0.21	16.40	52.62	8.41	0.01	8.0
25-Jan-04	09:42	26.70	29.31	951.93	0.0310	1.24	3.10	49.24	6.19	0.33	7.0
02-Jan-04	14:50	26.00	33.70	871.89	0.0387	0.30	12.47	47.87	0.10	0.38	*
25-Jan-04	09:50	26.89	30.81	954.92	0.0325	1.14	5.44	47.93	6.71	0.31	7.0
11-Jan-04	14:44	27.60	30.59	876.66	0.0349	0.45	16.35	47.66	1.49	0.37	9.0
25-Jan-04	10:59	26.70	44.76	979.37	0.0464	1.52	2.70	45.71	9.96	0.25	10.0
25-Jan-04	11:08	27.20	45.52	984.95	0.0470	1.22	5.47	45.58	10.17	0.13	8.0
25-Jan-04	13:09	27.00	45.49	974.61	0.0473	0.28	10.55	44.31	9.62	0.18	10.0
25-Jan-04	12:59	27.20	45.52	981.06	0.0471	0.55	12.26	47.55	9.95	0.15	9.0
25-Jan-04	12:29	26.50	55.97	985.29	0.0578	0.48	9.63	43.51	10.67	0.08	10.0
25-Jan-04	12:39	26.80	56.43	981.20	0.0585	0.69	7.75	44.77	10.53	0.10	10.0
27-Jan-04	11:24	26.30	49.61	912.06	0.0554	0.71	32.25	44.60	11.04	0.09	8.0
28-Jan-04	11:37	26.50	56.56	981.79	0.0588	0.40	13.36	41.05	11.52	0.06	11.0
<b>AVERAGE</b>		<b>27.12</b>		<b>937.17</b>		<b>0.52</b>	<b>11.51</b>		<b>7.08</b>	<b>0.20</b>	<b>9.3</b>

\* No wind data available due to weather station failure

**Table E.4** Summary of data for thermal efficiency tests with glass-shielded receiver

Date	Test time	$t_a$ (°C)	$(t_{r,i} - t_a)$ (°C)	Ave. $G_{DN}$ (W/m <sup>2</sup> )	$(t_{r,i} - t_a)/G_{bp}$ (m <sup>2</sup> °C/W)	Max. $\Delta(t_{r,i})$ (°C)	Max. $\Delta(G_{DN})$ (W/m <sup>2</sup> )	Efficiency (%)	Ave. $\theta_i$ (deg)	Max. $\Delta(\theta_i)$ (deg)	Ave. wind vel. (knots)
	(solar)										
13-Feb-04	15:09	26.00	2.20	809.05	0.0027	0.22	15.20	52.97	7.26	0.44	10.0
11-Feb-04	15:51	27.60	2.81	792.44	0.0036	0.05	21.07	54.21	2.71	0.50	10.0
11-Feb-04	10:17	27.30	38.09	889.88	0.0439	1.15	6.80	47.42	12.59	0.28	7.0
19-Feb-04	13:55	26.60	31.37	834.14	0.0389	0.17	12.84	50.38	14.89	0.30	10.0
11-Feb-04	09:01	25.80	26.00	825.11	0.0318	0.49	10.66	49.93	7.53	0.42	7.0
11-Feb-04	09:21	26.40	27.94	847.77	0.0334	0.54	6.60	50.88	9.26	0.19	7.0
11-Feb-04	10:37	27.80	43.11	899.31	0.0494	1.04	7.21	48.22	13.96	0.22	9.0
11-Feb-04	10:50	27.80	44.75	898.75	0.0514	0.55	7.47	48.81	14.54	0.18	9.0
11-Feb-04	12:04	28.80	50.70	909.18	0.0580	0.70	5.89	47.54	15.80	0.01	10.0
11-Feb-04	12:19	28.60	53.99	910.19	0.0616	0.33	7.39	48.01	15.68	0.06	10.0
<b>AVERAGE</b>		<b>27.27</b>		<b>861.58</b>		<b>0.52</b>	<b>10.11</b>		<b>11.42</b>	<b>0.26</b>	<b>8.9</b>

**Table E.5** Summary of data for collector acceptance angle tests with unshielded and glass-shielded receiver

Date	Test time (solar)	$t_a$ (°C)	$(t_{fi} - t_a)$ (°C)	Ave. $G_{DN}$ (W/m <sup>2</sup> )	$(t_{fi} - t_a)/G_{bp}$ (m <sup>2</sup> °C/W)	Max. $\Delta(t_{fi})$ (°C)	Max. $\Delta(G_{DN})$ (W/m <sup>2</sup> )	Ave. $\theta_i$ (deg)	Ave. wind vel. (knots)	Coll. acc. angle (deg)
Unshielded 28-Dec-03	12:14	25.4	2.62	969.75	0.0027	0.08	16.89	6.62	8.0	0.43
Glass-shielded 17-Feb-04	12:33	29.9	3.38	899.43	0.0039	0.18	16.30	17.52	11.0	0.52
<b>AVERAGE</b>		<b>27.65</b>	<b>3.00</b>	<b>934.59</b>	<b>0.0033</b>	<b>0.13</b>	<b>16.60</b>	<b>12.07</b>	<b>9.5</b>	

**Table E.6** Summary of data for incidence angle modifier tests with unshielded receiver

Date	Test time (solar)	$t_a$ (°C)	$(t_{fi} - t_a)$ (°C)	Ave. $G_{DN}$ (W/m <sup>2</sup> )	$(t_{fi} - t_a)/G_{bp}$ (m <sup>2</sup> °C/W)	Max. $\Delta(t_{fi})$ (°C)	Max. $\Delta(G_{DN})$ (W/m <sup>2</sup> )	Efficiency (%)	Ave. $\theta_i$ (deg)	Max. $\Delta(\theta_i)$ (deg)	Ave. wind vel. (knots)	$K_{tr}$
01-Jul-04	11:32	22.00	2.05	806.37	0.0042	0.71	15.42	44.70	52.74	0.11	4.0	0.81
01-Jul-04	11:45	22.00	3.33	800.33	0.0069	0.36	33.04	45.15	52.98	0.05	4.0	0.82
11-Jun-04	12:01	23.00	1.18	850.92	0.0023	0.10	5.92	47.69	53.09	0.01	3.0	0.86
12-Jul-04	09:36	19.00	2.35	818.42	0.0040	0.56	10.92	49.32	44.30	0.47	1.0	0.89
29-Jul-04	15:04	19.00	5.53	772.98	0.0090	0.14	6.15	50.66	37.30	0.52	10.0	0.92
02-Jan-04	13:19	26.00	3.30	900.85	0.0037	0.09	7.63	54.52	5.42	0.19	*	0.99
02-Feb-04	08:05	24.60	2.83	810.69	0.0035	0.27	9.20	55.74	0.32	0.50	8.0	1.01
02-Feb-04	15:43	25.20	5.18	814.63	0.0064	0.11	17.77	55.13	0.89	0.48	10.0	1.00
02-Feb-04	15:55	24.90	1.83	789.93	0.0023	0.80	27.58	55.28	0.22	0.44	10.0	1.00
02-Jan-04	10:10	27.50	2.66	901.60	0.0030	0.07	10.20	54.75	4.03	0.26	*	0.99
<b>AVERAGE</b>		<b>23.32</b>	<b>3.02</b>	<b>826.67</b>		<b>0.32</b>	<b>14.38</b>			<b>0.30</b>	<b>6.25</b>	

\* No wind data available due to weather station failure

**Table E.7** Summary of data for incidence angle modifier tests with glass-shielded receiver

Date	Test time (solar)	$t_a$ (°C)	$(t_{fi} - t_a)$ (°C)	Ave. $G_{DN}$ (W/m <sup>2</sup> )	$(t_{fi} - t_a)/G_{bp}$ (m <sup>2</sup> °C/W)	Max. $\Delta(t_{fi})$ (°C)	Max. $\Delta(G_{DN})$ (W/m <sup>2</sup> )	Efficiency (%)	Ave. $\theta_i$ (deg)	Max. $\Delta(\theta_i)$ (deg)	Ave. wind vel. (knots)	$K_{tr}$
22-May-04	11:12	24.73	2.46	768.44	0.0049	0.10	17.72	41.82	49.54	0.19	3.0	0.78
09-Jun-04	12:08	21.00	4.74	873.41	0.0090	0.09	3.13	40.17	52.91	0.04	10.0	0.75
01-May-04	11:34	26.50	2.27	839.03	0.0038	0.38	3.98	44.88	45.20	0.02	6.0	0.83
19-Apr-04	12:17	28.30	3.16	892.58	0.0047	0.54	17.44	43.78	41.22	0.06	5.0	0.81
21-Apr-04	09:38	25.20	2.47	865.15	0.0035	0.55	5.79	47.93	35.37	0.43	2.0	0.89
21-Apr-04	10:05	25.36	4.28	862.57	0.0063	0.09	7.96	47.94	37.62	0.36	3.0	0.89
28-Mar-04	12:09	30.00	2.26	886.14	0.0031	0.49	15.67	48.24	33.14	0.03	12.0	0.90
03-Mar-04	11:28	26.50	1.83	943.59	0.0021	0.66	7.21	49.79	25.01	0.09	12.0	0.93
15-Feb-04	11:45	27.03	2.37	878.53	0.0028	0.27	15.82	53.84	17.09	0.04	9.0	1.00
28-Feb-04	09:22	27.50	3.30	851.25	0.0040	0.10	29.18	53.42	15.04	0.40	9.0	0.99
11-Feb-04	15:50	27.60	2.81	792.44	0.0036	0.05	21.07	54.21	2.71	0.50	10.0	1.01
<b>AVERAGE</b>		<b>26.34</b>	<b>2.90</b>	<b>859.37</b>		<b>0.30</b>	<b>13.18</b>			<b>0.20</b>	<b>7.36</b>	

## APPENDIX F

### THERMAL MODEL DATA

**Table F.1** Output from MATLAB thermal modelling programme for unshielded receiver (wind speed of 4.8 m/s, inlet temperature of 27.12 °C and beam irradiance of 928.23 W/m<sup>2</sup>)

End position (m)	Ext. wall temp. (°C)	Air film temp. (°C)	Air Re	$h_{ce}$ (W/m <sup>2</sup> K)	Temp. in (°C)	Temp. out (°C)	Bulk temp. (°C)	Water Re	$h_{ci}$ (W/m <sup>2</sup> K)	U (W/m <sup>2</sup> K)
0.143	38.33	32.73	8424.19	63.64	27.12	27.43	27.27	4715.68	813.21	811.28
0.286	38.33	32.73	8424.19	63.64	27.43	27.73	27.58	4715.68	813.21	811.28
0.429	38.56	32.73	8424.19	63.64	27.73	28.04	27.89	4747.47	817.60	815.65
0.571	38.79	32.84	8418.71	63.63	28.04	28.35	28.19	4779.32	821.82	819.85
0.714	39.02	32.96	8413.17	63.63	28.35	28.65	28.50	4811.21	826.03	824.04
0.857	39.25	33.07	8407.63	63.62	28.65	28.96	28.81	4843.12	830.21	828.20
1.000	39.48	33.19	8402.08	63.62	28.96	29.26	29.11	4875.06	834.38	832.35
1.143	39.72	33.30	8396.53	63.62	29.26	29.57	29.42	4907.02	838.54	836.49
1.286	39.95	33.42	8390.97	63.61	29.57	29.87	29.72	4939.02	842.67	840.60
1.429	40.18	33.53	8385.42	63.61	29.87	30.17	30.02	4971.04	846.79	844.70
1.571	40.42	33.65	8379.86	63.60	30.17	30.48	30.33	5003.08	850.88	848.78
1.714	40.65	33.77	8374.29	63.60	30.48	30.78	30.63	5035.14	854.97	852.84
1.857	40.88	33.88	8368.73	63.60	30.78	31.08	30.93	5067.23	859.03	856.88
2.000	41.12	34.00	8363.16	63.59	31.08	31.38	31.23	5099.34	863.08	860.91
2.143	41.35	34.12	8357.60	63.59	31.38	31.68	31.53	5131.47	867.11	864.92
2.286	41.59	34.24	8352.03	63.58	31.68	31.98	31.83	5163.62	871.12	868.91
2.429	41.82	34.35	8346.46	63.58	31.98	32.28	32.13	5195.79	875.11	872.88
2.571	42.06	34.47	8340.90	63.58	32.28	32.58	32.43	5227.98	879.09	876.84
2.714	42.29	34.59	8335.33	63.57	32.58	32.88	32.73	5260.18	883.05	880.78
2.857	42.53	34.71	8329.77	63.57	32.88	33.18	33.03	5292.40	886.99	884.70
3.000	42.76	34.82	8324.20	63.56	33.18	33.47	33.32	5324.64	890.92	888.60
3.143	43.00	34.94	8318.64	63.56	33.47	33.77	33.62	5356.89	894.83	892.49
3.286	43.24	35.06	8313.08	63.56	33.77	34.07	33.92	5389.15	898.72	896.36
3.429	43.47	35.18	8307.52	63.55	34.07	34.36	34.21	5421.43	902.59	900.22
3.571	43.71	35.30	8301.97	63.55	34.36	34.66	34.51	5453.72	906.45	904.05
3.714	43.95	35.41	8296.41	63.54	34.66	34.95	34.80	5486.01	910.29	907.87
3.857	44.18	35.53	8290.86	63.54	34.95	35.24	35.10	5518.32	914.11	911.68
4.000	44.42	35.65	8285.32	63.54	35.24	35.54	35.39	5550.64	917.92	915.46
4.143	44.66	35.77	8279.78	63.53	35.54	35.83	35.68	5582.97	921.71	919.23
4.286	44.89	35.89	8274.24	63.53	35.83	36.12	35.98	5615.30	925.48	922.98
4.429	45.13	36.01	8268.70	63.52	36.12	36.41	36.27	5647.64	929.23	926.72
4.571	45.37	36.13	8263.17	63.52	36.41	36.71	36.56	5679.99	932.97	930.44
4.714	45.60	36.24	8257.65	63.52	36.71	37.00	36.85	5712.34	936.70	934.14
4.857	45.84	36.36	8252.13	63.51	37.00	37.29	37.14	5744.70	940.40	937.83
5.000	46.08	36.48	8246.61	63.51	37.29	37.58	37.43	5777.06	944.09	941.49
<b>AVERAGE</b>	<b>42.08</b>	<b>34.49</b>	<b>8340.44</b>	<b>63.58</b>	<b>32.25</b>	<b>32.55</b>	<b>32.40</b>	<b>5229.76</b>	<b>878.32</b>	<b>876.07</b>

**Table F.2** Loss output from MATLAB thermal modelling programme for unshielded receiver (wind speed of 1.34 m/s, inlet temperature of 29.77 °C, ambient temperature of 21.2 °C and zero beam irradiance)

Position (m)	Ext. wall temp. (°C)	Air film temp. (°C)	Air Re	$h_{ce}$ (W/m <sup>2</sup> K)	Temp. in (°C)	Temp. out (°C)	Bulk temp. (°C)	Water Re	$h_{ci}$ (W/m <sup>2</sup> K)	U (W/m <sup>2</sup> K)
0.143	29.17	25.17	2456.80	29.72	29.77	29.75	29.76	4975.41	854.82	852.69
0.286	29.17	25.17	2456.80	29.72	29.75	29.74	29.74	4975.41	854.82	852.69
0.429	29.15	25.17	2456.80	29.72	29.74	29.72	29.73	4973.58	854.58	852.45
0.571	29.14	25.16	2456.92	29.72	29.72	29.70	29.71	4971.76	854.35	852.22
0.714	29.12	25.15	2457.04	29.72	29.70	29.68	29.69	4969.93	854.11	851.99
0.857	29.10	25.14	2457.16	29.72	29.68	29.67	29.67	4968.11	853.88	851.75
1.000	29.09	25.14	2457.29	29.72	29.67	29.65	29.66	4966.29	853.65	851.52
1.143	29.07	25.13	2457.41	29.72	29.65	29.63	29.64	4964.47	853.41	851.29
1.286	29.05	25.12	2457.53	29.72	29.63	29.61	29.62	4962.66	853.18	851.06
1.429	29.03	25.11	2457.65	29.72	29.61	29.60	29.61	4960.85	852.95	850.83
1.571	29.02	25.10	2457.77	29.72	29.60	29.58	29.59	4959.04	852.72	850.60
1.714	29.00	25.09	2457.89	29.72	29.58	29.56	29.57	4957.23	852.49	850.37
1.857	28.99	25.09	2458.01	29.72	29.56	29.55	29.55	4955.42	852.25	850.14
2.000	28.97	25.08	2458.13	29.72	29.55	29.53	29.54	4953.62	852.02	849.91
2.143	28.95	25.07	2458.24	29.72	29.53	29.51	29.52	4951.82	851.79	849.68
2.286	28.94	25.06	2458.36	29.72	29.51	29.49	29.50	4950.02	851.56	849.45
2.429	28.92	25.05	2458.48	29.72	29.49	29.48	29.49	4948.22	851.33	849.22
2.571	28.90	25.04	2458.60	29.72	29.48	29.46	29.47	4946.43	851.10	848.99
2.714	28.89	25.04	2458.72	29.72	29.46	29.44	29.45	4944.64	850.87	848.76
2.857	28.87	25.03	2458.84	29.72	29.44	29.43	29.44	4942.85	850.64	848.53
3.000	28.85	25.02	2458.96	29.72	29.43	29.41	29.42	4941.06	850.41	848.30
3.143	28.84	25.01	2459.08	29.72	29.41	29.39	29.40	4939.28	850.18	848.08
3.286	28.82	25.00	2459.20	29.72	29.39	29.38	29.38	4937.50	849.95	847.85
3.429	28.80	25.00	2459.31	29.72	29.38	29.36	29.37	4935.72	849.73	847.62
3.571	28.79	24.99	2459.43	29.72	29.36	29.34	29.35	4933.94	849.50	847.39
3.714	28.77	24.98	2459.55	29.72	29.34	29.33	29.33	4932.17	849.27	847.17
3.857	28.75	24.97	2459.67	29.72	29.33	29.31	29.32	4930.40	849.04	846.94
4.000	28.74	24.96	2459.79	29.72	29.31	29.29	29.30	4928.63	848.81	846.71
4.143	28.72	24.95	2459.90	29.72	29.29	29.28	29.28	4926.86	848.59	846.49
4.286	28.71	24.95	2460.02	29.72	29.28	29.26	29.27	4925.09	848.36	846.26
4.429	28.69	24.94	2460.14	29.72	29.26	29.24	29.25	4923.33	848.13	846.03
4.571	28.67	24.93	2460.26	29.72	29.24	29.22	29.23	4921.57	847.90	845.81
4.714	28.66	24.92	2460.37	29.72	29.22	29.21	29.22	4919.81	847.68	845.58
4.857	28.64	24.91	2460.49	29.72	29.21	29.19	29.20	4918.05	847.45	845.36
5.000	28.62	24.91	2460.61	29.72	29.19	29.17	29.18	4916.30	847.23	845.13
<b>AVERAGE</b>	<b>28.90</b>	<b>25.04</b>	<b>2458.61</b>	<b>29.72</b>	<b>29.48</b>	<b>29.46</b>	<b>29.47</b>	<b>4946.50</b>	<b>851.11</b>	<b>849.00</b>

**Table F.3** Output from MATLAB thermal modelling programme for glass-shielded receiver (wind speed of 4.6 m/s, inlet temperature of 27.27 °C and beam irradiance of 841.73 W/m<sup>2</sup>)

Position (m)	Ext. wall temp. (°C)	Air film temp. (°C)	Air Re	$h_{ce}$ (W/m <sup>2</sup> K)	Temp. in (°C)	Temp. out (°C)	Bulk temp. (°C)	Water Re	$h_{ci}$ (W/m <sup>2</sup> K)	U (W/m <sup>2</sup> K)	Glass temp. (°C)
0.143	37.92	30.52	12622.68	52.20	27.27	27.56	27.42	4730.43	815.52	813.58	33.76
0.286	38.21	30.52	12622.68	52.20	27.56	27.86	27.71	4730.43	815.52	813.58	33.76
0.429	38.45	30.52	12622.68	52.20	27.86	28.15	28.00	4760.75	819.50	817.54	33.77
0.571	38.69	30.52	12622.25	52.20	28.15	28.44	28.29	4791.15	823.51	821.53	33.78
0.714	38.94	30.53	12621.97	52.20	28.44	28.73	28.59	4821.63	827.51	825.51	33.79
0.857	39.18	30.53	12621.65	52.20	28.73	29.03	28.88	4852.19	831.50	829.49	33.80
1.000	39.42	30.53	12621.35	52.20	29.03	29.32	29.17	4882.82	835.48	833.45	33.81
1.143	39.66	30.54	12621.03	52.20	29.32	29.61	29.47	4913.53	839.45	837.40	33.82
1.286	39.91	30.54	12620.72	52.20	29.61	29.91	29.76	4944.32	843.41	841.34	33.83
1.429	40.15	30.55	12620.41	52.20	29.91	30.20	30.05	4975.18	847.37	845.27	33.83
1.571	40.40	30.55	12620.09	52.20	30.20	30.49	30.34	5006.12	851.31	849.20	33.84
1.714	40.64	30.56	12619.78	52.20	30.49	30.78	30.64	5037.13	855.24	853.11	33.85
1.857	40.89	30.56	12619.46	52.20	30.78	31.08	30.93	5068.22	859.16	857.01	33.86
2.000	41.14	30.57	12619.14	52.20	31.08	31.37	31.22	5099.39	863.08	860.91	33.87
2.143	41.39	30.57	12618.82	52.20	31.37	31.66	31.52	5130.63	866.98	864.79	33.88
2.286	41.63	30.57	12618.50	52.20	31.66	31.96	31.81	5161.94	870.88	868.67	33.89
2.429	41.88	30.58	12618.17	52.20	31.96	32.25	32.10	5193.32	874.76	872.53	33.90
2.571	42.13	30.58	12617.85	52.20	32.25	32.54	32.40	5224.78	878.64	876.39	33.90
2.714	42.38	30.59	12617.52	52.20	32.54	32.83	32.69	5256.32	882.50	880.23	33.91
2.857	42.63	30.59	12617.19	52.20	32.83	33.13	32.98	5287.92	886.36	884.07	33.92
3.000	42.88	30.60	12616.86	52.20	33.13	33.42	33.27	5319.60	890.21	887.90	33.93
3.143	43.13	30.60	12616.53	52.20	33.42	33.71	33.57	5351.35	894.04	891.72	33.94
3.286	43.38	30.61	12616.20	52.20	33.71	34.01	33.86	5383.16	897.87	895.52	33.95
3.429	43.63	30.61	12615.86	52.20	34.01	34.30	34.15	5415.06	901.69	899.32	33.96
3.571	43.89	30.61	12615.53	52.20	34.30	34.59	34.45	5447.02	905.50	903.11	33.97
3.714	44.14	30.62	12615.19	52.20	34.59	34.88	34.74	5479.05	909.30	906.89	33.98
3.857	44.39	30.62	12614.85	52.20	34.88	35.18	35.03	5511.15	913.09	910.66	33.99
4.000	44.64	30.63	12614.51	52.20	35.18	35.47	35.32	5543.32	916.87	914.42	34.00
4.143	44.90	30.63	12614.17	52.20	35.47	35.76	35.62	5575.56	920.64	918.17	34.01
4.286	45.15	30.64	12613.83	52.20	35.76	36.06	35.91	5607.86	924.40	921.91	34.02
4.429	45.41	30.64	12613.49	52.20	36.06	36.35	36.20	5640.24	928.15	925.64	34.03
4.571	45.66	30.65	12613.14	52.20	36.35	36.64	36.50	5672.68	931.89	929.36	34.03
4.714	45.92	30.65	12612.80	52.20	36.64	36.94	36.79	5705.20	935.62	933.07	34.04
4.857	46.17	30.66	12612.45	52.20	36.94	37.23	37.08	5737.77	939.34	936.77	34.05
5.000	46.43	30.66	12612.10	52.20	37.23	37.52	37.37	5770.42	943.05	940.46	34.06
<b>AVERAGE</b>	<b>42.15</b>	<b>30.58</b>	<b>12617.76</b>	<b>52.20</b>	<b>32.25</b>	<b>32.54</b>	<b>32.40</b>	<b>5229.36</b>	<b>878.27</b>	<b>876.01</b>	<b>33.91</b>